



Measurements and improvements of the
response of the $\bar{\text{P}}\text{ANDA}$ -EMC prototype
PROTO 60 to high energetic particles and
photons in accelerator experiments

Dissertation zur Erlangung des Doktorgrades (Dr. rer. nat)

im Fachgebiet Experimentalphysik

Prof. Dr. Volker Metag

II. Physikalisches Institut

Universität Giessen

vorgelegt von

Dipl.-Phys. Markus Moritz

aus Biedenkopf

Gießen, 2013

Contents

Kurzdarstellung	1
Abstract	3
1 Introduction and motivation	5
1.1 Used Units	6
1.2 FAIR overview	7
1.3 Accelerator facility	8
2 The $\bar{\text{P}}\text{ANDA}$ experiment	11
2.1 $\bar{\text{P}}\text{ANDA}$ Physics program	13
2.2 Antiproton production	16
2.3 HESR	17
2.4 Detector setup	19
2.4.1 Electromagnetic target-calorimeter	20
2.4.1.1 Specifications	20
2.4.1.2 Design	22
2.4.1.3 Scintillator as active detection material	25
2.4.1.4 Large area avalanche photo diodes	31
2.4.1.5 Parametrization of the calorimeter energy resolution	33
2.4.2 Further target spectrometer components	34
2.4.3 Forward spectrometer	40
2.5 Triggerless data acquisition	44
3 PROTO 60	47
3.1 Design	47
3.2 Preamps	50

Contents

4	GEANT4	55
4.1	The PROTO 60 model	57
4.1.1	Implementation of non-uniform light collection	57
4.2	Cosmic radiation	60
5	Experiment at MAMI	65
5.1	The electron accelerator MAMI	66
5.1.1	Production of energy tagged photons	68
5.2	Experimental setup	69
5.2.1	Data acquisition	71
5.2.2	LAAPD high voltage adjustments	73
5.3	Experimental procedure	75
5.4	Data Analysis	78
5.4.1	Raw data	78
5.4.2	Energy calibration	82
5.4.2.1	Simulations of cosmic radiation	87
5.4.3	Line-shapes	96
5.5	Results	102
5.5.1	Linearity verification	102
5.5.2	Multiplicity	103
5.5.3	Influence of dead material	105
5.5.3.1	Experimental data	105
5.5.3.2	Simulations	108
5.5.4	Energy resolution	112
6	Experiment at CERN	115
6.1	The accelerator facility	115
6.2	Experimental setup	116
6.2.1	Data acquisition	118
6.3	Experimental procedure	119
6.4	Data analysis	120
6.4.1	PROTO 60 raw data	122
6.4.2	Calibration	122
6.4.2.1	Calibration with cosmic radiation	123
6.4.2.2	Calibration with 150 GeV muon beam	123

6.4.2.3 Absolute calibration alignment to GEANT	126
6.4.3 Line-shapes	127
6.5 Results	129
7 Optimum APD gain measurements	133
7.1 Voltage to gain relation	133
7.2 Setup	137
7.3 Procedure	140
7.4 Analysis	142
7.4.1 Equivalent energy determination	145
7.5 Results	146
8 Discussion and Outlook	149
8.1 Discussion	149
8.2 Outlook	160
Appendix	VII
List of Figures	XI
List of Tables	XXIII
Bibliography	XXV
Danksagung	XXXI

Kurzdarstellung

Das $\bar{\text{P}}\text{ANDA}$ -Experiment bei FAIR stellt eine Möglichkeit dar, ein besseres Verständnis von komplexen hadronischen Systemen zu erlangen. Die Messungen werden mit Hilfe von Antiprotonen in einem Fixed-Target-Experiment durchgeführt. Für die Rekonstruktion der meisten Reaktionen ist ein genauer Nachweis von elektromagnetischen Proben sowie die Messung ihrer Energien entscheidend. Aufgrund dessen ist das elektromagnetische Kalorimeter eine wichtige Komponente des $\bar{\text{P}}\text{ANDA}$ Detektors. Generell sind solche anspruchsvollen, komplexen und hoch spezialisierten Detektorsysteme nicht kommerziell erhältlich. Für dessen Realisierung sind somit umfangreiche Forschungsarbeiten nötig, welche unter anderem die Entwicklung, das Testen sowie die Optimierung von Prototypen beinhalten. Die Hauptzielsetzung dieser Arbeit ist die Untersuchung des Ansprechverhaltens des Prototypen eines homogenen elektromagnetischen Kalorimeters. Dieser Prototyp wird als PROTO 60 bezeichnet und besteht aus 60 pyramidenstumpfförmigen PWO-II Kristallen welche auf -25°C gekühlt und jeweils mit einer Large-Area-Avalanche Photodiode (LAAPD) ausgelesen werden. Er repräsentiert einen kleinen zentralen Ausschnitt aus dem fassförmigen Teil des $\bar{\text{P}}\text{ANDA}$ Kalorimeters. Im Rahmen mehrerer Experimente wurde zum ersten mal sein Ansprechen über einen umfangreichen Energiebereich von 52 MeV bis 15 GeV mittels energiemarkierten Photonen bzw. Positronen für die höchste Energie, untersucht. Es konnte gezeigt werden, dass dieser Detektorprototyp prinzipiell funktioniert und linear auf Photonen anspricht. Die erzielte Energieauflösung über den kompletten gemessenen Energiebereich kann durch

$$\frac{\sigma}{E} = \sqrt{\left(\frac{1.86\%}{\sqrt{E/\text{GeV}}}\right)^2 + \left(\frac{0.25\%}{E/\text{GeV}}\right)^2 + 1.46\%^2}$$

parametrisiert werden. Aufgrund der Verwendung von nur einer 1 cm^2 großen LAAPD pro Kristall und einer nicht linearisierten Lichtsammlung stellen die erzielten Ergeb-

Kurzdarstellung

nisse lediglich eine obere Grenze für die Energieauflösung dar. Ein detailliertes Simulationsmodell des Prototypen wurde in GEANT 4 erstellt um dessen Kalibration mittels kosmischer Strahlung und eines 150 GeV Myonenstrahls zu untersuchen, sowie den Einfluss der komplexen Geometrie und der Lichtsammlung auf dessen Ansprechen.

Ferner wurde mittels eines Lichtpulsers der Einfluss der APD Verstärkung auf die Energieauflösung untersucht. Insbesondere für niedrige Energien zeigte sich, dass ein Verstärkungsfaktor von 50, welcher von dem elektromagnetischen Kalorimeter des CMS Detektors verwendet wird, nicht optimal ist.

Abstract

The $\bar{\text{P}}\text{ANDA}$ experiment at FAIR will provide an opportunity to achieve a better understanding of complex hadronic systems. Measurements will be performed with antiprotons using a fixed-target setup. In order to reconstruct most of the reactions, a precise measurement of electromagnetic probes and their energies are crucial. An important and major component of the detector is therefore the electromagnetic calorimeter. Due to the lack of commercial availability of such ambitious, complex and highly specialized detector systems, detailed research and development are necessary, including prototype development, testing and optimization. The investigation of the response of a homogeneous electromagnetic calorimeter prototype is the main scope of the present thesis. This prototype, called PROTO 60, is composed out of 60 truncated pyramidal shaped PWO-II crystals, cooled down to -25°C and read out with one Large Area Avalanche Photodiode (LAAPDs). The PROTO 60 represents a small section of the central barrel part of the $\bar{\text{P}}\text{ANDA}$ calorimeter. Its response is being investigated for the first time over an extensive energy range from 52.34 MeV up to 15 GeV within several experiments measuring the response to energy marked photons or positrons at the highest energy, respectively. The study verified the principle detector concept. A linear response was observed. The achieved overall resolution can be parameterized as:

$$\frac{\sigma}{E} = \sqrt{\left(\frac{1.86\%}{\sqrt{E/\text{GeV}}}\right)^2 + \left(\frac{0.25\%}{E/\text{GeV}}\right)^2 + 1.46\%^2}.$$

Due to the use of only one single LAAPD per crystal with the effective surface of 1 cm^2 and a not linearized light collection within the crystals, these parameters represent an upper performance limit of the final $\bar{\text{P}}\text{ANDA}$ calorimeter. A detailed GEANT based model of the prototype was developed in order to investigate the calibration based on cosmic radiation or a 150 GeV muon beam and to understand the impact of the detailed geometry and light collection on the achieved performance.

Abstract

Furthermore, the influence of the APD gain on the energy resolution was examined with a light pulser system. The performed measurements revealed that a gain of 50, as used for the CMS electromagnetic calorimeter, does not apply for the PANDA electromagnetic calorimeter in particular in the low energy regime.

Chapter 1

Introduction and motivation

The spectroscopy of compound objects is a main tool to investigate the nature of particles. The basic concept is to identify and describe the fundamental forces between their elementary particles. In hadron-physics, composed objects made out of quarks are investigated. These objects, called hadrons, are characterized by their rest mass, lifetime, spin and further quantum numbers. Depending on the amount of so-called valence quarks, hadrons can be baryons or mesons. Baryons consist of 3 quarks (qqq) and mesons of a quark and an antiquark ($q\bar{q}$) in their simplest form. Besides leptons like electrons or bosons like the gluon, quarks form an own group of elementary particles in the Standard Model. Within this group there are three families of elementary quarks and antiquarks (tab.1.1). They are fermions (particles with spin 1/2) and have 2/3 or -1/3 of the elementary charge of an electron. The difference between quarks and antiquarks is their conjugated electric charge. The fundamental force between

Quark flavor	up	down	charm	strange	top	bottom
Charge / e	2/3	-1/3	2/3	-1/3	2/3	-1/3
Mass ¹	$2.3^{+0.7}_{-0.5}$	$4.8^{+0.7}_{-0.3}$	1.275 ± 0.025	95 ± 5	173.5 ± 0.6	4.18 ± 0.03
	MeV	MeV	GeV	MeV	GeV	GeV

Table 1.1: Properties of quarks [PDG12].

quarks is the strong interaction. The gluons are the corresponding exchange bosons. The strong interaction introduces a new property, called color. Quarks and antiquarks can have one out of three types of color or anticolor charges, respectively. The gluons

¹See section 1.1

Chapter 1 Introduction and motivation

can have any combination of one color and anticolor. In all observed strongly bound systems, the color blends to white objects. As a consequence we can observe gluonic self interaction, the confinement of quarks and Hybrids. These Hybrids are mesons with an excited gluon flux between the quarks. The existence of Glueballs is predicted. Glueballs are composed out of gluons without valence quarks. The typical range of the strong interaction is in the order of 10^{-15} m, the size of a nucleon. The quantitative theoretical description of a hadronic system is not fully understood. Some of the problems can be successfully simplified with a model consisting only of valence quarks. Nevertheless many problems demand a deeper understanding of the complex inner structure. In detail, a hadronic object represents an intrinsic many body system with many gluons and quark-antiquark pairs besides the valence quarks. The $\bar{\text{P}}\text{ANDA}^2$ experiment at FAIR³ provides an opportunity to achieve a better understanding of the complex hadronic systems. For reconstructing most of the reactions a precise measurement of energies is crucial. An important and major component of the experiment is therefore the electromagnetic calorimeter. Due to the lack of commercial availability of such ambitious, complex and highly specialized detector systems, detailed research and development are necessary, including prototype developing, testing and optimizing.

1.1 Used Units

The common unit of energy in the field of particle and high energy physics is the electron Volt (eV). One electron Volt is the energy which a single charged particle, like an electron, obtains when it is accelerated through a potential of 1 Volt. This energy is equivalent to $1.602 \cdot 10^{-19}$ Joule. Due to the equations $E = m \cdot c^2$ and $E = p \cdot c$ the unit of mass is $\frac{\text{eV}}{c^2}$ and $\frac{\text{eV}}{c}$ is the unit for the momentum. The speed of light c is a well known value. In this thesis mostly natural units are used, which sets $c=1$. Thus the electron Volt is the given unit for mass, energy and momentum.

² $\bar{\text{P}}\text{ANDA}$ = Antiproton annihilation at Darmstadt

³FAIR = Facility for Antiproton and Ion Research

1.2 FAIR overview

The present research facility of GSI⁴ will be expanded. Within the FAIR project, a next generation accelerator complex will be created. The new facility, where various physics programs can be operated in parallel, will offer outstanding research opportunities. The present GSI accelerator in combination with a new linear accelerator will be used as beam injectors. Within the new accelerator complex, primary and secondary beams can be injected, cooled and stored in a system of rings with internal targets and in-ring experiments (fig.1.1). The main pillars are APPA⁵ Physics, CBM⁶, NUSTAR⁷ and PANDA. A summary of the main FAIR projects can be found in [BTDR] and [HEN08].

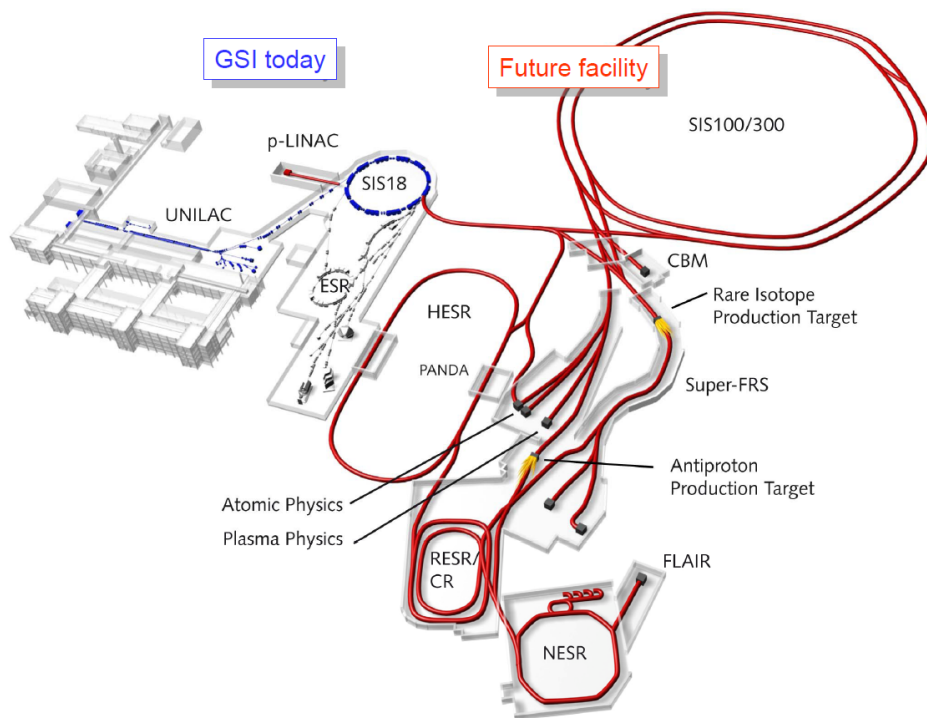


Figure 1.1: Present GSI facility together with the planned FAIR complex.

⁴GSI = Gesellschaft für Schwerionenforschung

⁵APPA = Atomie, Plasma Physics and Applications

⁶CBM = Compressed Baryonic Matter experiment

⁷NUSTAR = Nuclear Structure, Astrophysics and Reactions

1.3 Accelerator facility

In the start-up period the main part of the new accelerator will be the double-ring heavy ion synchrotron SIS100 with a circumference of 1100 m. Later on, an additional synchrotron SIS300 will be installed in the same tunnel. The two synchrotron accelerator rings will have maximum magnetic rigidities of 100 Tm and 300 Tm, respectively. For minimizing operating and construction costs, superconducting magnet structures are chosen. To obtain highest intensities, the SIS100 will operate at a repetition rate of 1 Hz. Therefore, ramp rates of the bending magnets of up to 4 Tesla per second are needed. The synchrotron will be able to create for example intense pulsed uranium (charge state $q = 28+$) or proton beams with $5 \cdot 10^{11}$ ions per pulse at 1 GeV and $4 \cdot 10^{13}$ at 29 GeV, respectively. The length of the bunches will be compressed down to 60 ns for heavy ions and 25 ns for protons. These short intense ion bunches are required for the production, subsequent storage and efficient cooling of exotic nuclei, antiprotons and for plasma physics experiments. The accelerator facility is completed by a system of storage rings [ACCEL].

- The collector ring (CR) provides fast stochastic cooling of radioactive ions and antiprotons from the production targets. This ring can operate in an isochronous mode for mass measurements of short lived nuclei.
- The accumulator ring (RESR) accumulates the antiprotons to produce more intense beams after they have been cooled in the CR, and is used for the fast deceleration of short-lived nuclei.
- The new experimental storage ring (NESR) will house a variety of experiments with ions and antiprotons, including a precision mass spectrometer, internal target experiments with atoms and electrons, and an electron-nucleus scattering facility. It is equipped with stochastic and electron cooling and capable to further decelerate ions and antiprotons and to extract them for the FLAIR⁸ experiments.
- The high-energy storage ring (HESR) is designed for the \bar{P} ANDA experiment. It will deliver an antiproton beam from 1.5 up to 15 GeV. It will be equipped with a high-energy electron cooler (up to 5 MeV electron energy) and a stochastic cooling system to compensate for beam degradation due to target interaction

⁸FLAIR = Facility for Low-Energy Antiproton and Ion Research

1.3 Accelerator facility

and intra-beam scattering. Due to the relevance for the $\bar{\text{P}}\text{ANDA}$ experiment a more detailed description is given in 2.3.

Chapter 2

The \bar{P} ANDA experiment

Nowadays Quantum Chromodynamics (QCD) is the state of art for the description of strong interactions. Conceptually, QCD is a relativistic quantum field theory of interacting quarks and gluons according to the forces between color charges. The gluons are the exchange bosons for the strong interaction. They carry color charge and therefore they can interact among themselves. This makes each strong interacting system like hadrons a complex many-body problem. As part of the Standard Model of particle physics, QCD is well verified at high energies or at short distances (shorter than the nucleon size), respectively. In these energy regimes the coupling constant becomes small and therefore perturbation theory becomes applicable. For distances in the order of the nucleon size the coupling plays a major role. The binding energies increase rapidly with the distance until new hadrons are generated. Therefore free quarks should not exist. The perturbation approach fails at the corresponding energies. Many aspects in this regime are not yet understood. The \bar{P} ANDA experiment is designed as a multi purpose experiment. The main focus will be on detailed studies of the strong interaction. Phenomena like the confinement of quarks, existence of glueballs and hybrids, the origin of the masses of hadrons in the context of the breaking of chiral symmetry are perspectives for a better understanding of the nature of the strong interaction and hadronic matter. Therefore, many measurements are foreseen with \bar{P} ANDA. The experiment will use the HESR antiproton beam interacting with various internal targets. The high energy and intensity beam with a momentum range from 1.5 GeV up to 15 GeV gives access to a broad range of states of matter. In $\bar{p}p$ annihilations, all quantum numbers can be directly produced. This allows high precision resonance scans (fig.2.1) for all directly accessible states.

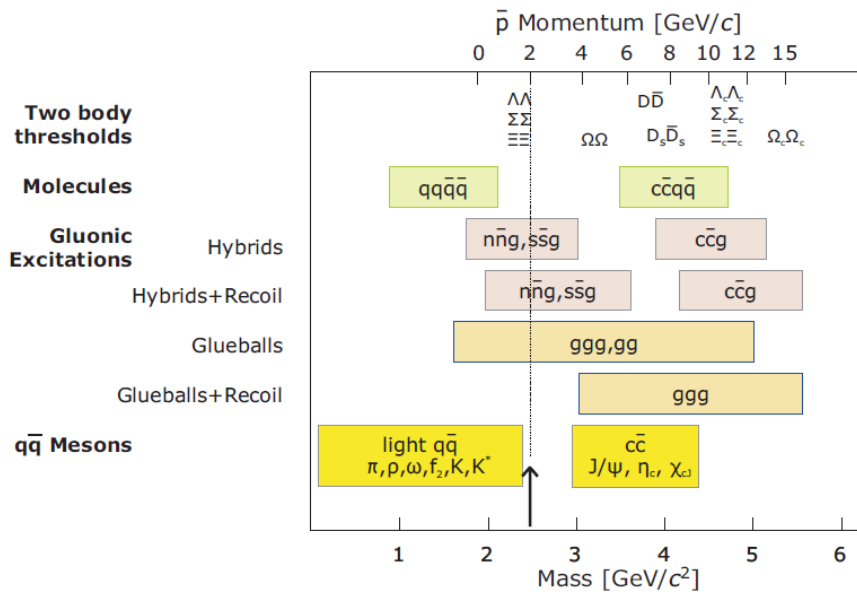


Figure 2.1: Overview over the mass and momentum regime. The upper scale represents the antiproton momentum and the lower one the hadron mass. The vertical line shows the upper limit of the former $\bar{p}p$ annihilation experiment at the Low Energy Antiproton Ring (LEAR) at CERN. All states between 1.5 GeV and 15 GeV \bar{p} -momentum are accessible with \bar{P} ANDA.

2.1 $\bar{\text{P}}\text{ANDA}$ Physics program

For the physics program the main topics are:

Charmonium spectroscopy Due to the quantum numbers, all $c\bar{c}$ states can be formed directly in $\bar{p}p$ annihilation not just 1^{--} as in the e^+e^- experiments. By utilizing the accelerator for fine energy scans, it will be possible to measure masses with accuracies in the order of 100 keV and widths to 10 % or better. Current theoretical QCD calculations predict not yet measured states. Some of the in other experiments already discovered $c\bar{c}$ states are not consistent with present theoretical calculations. Therefore, especially high precision charmonium spectroscopy will deliver a deeper insight into QCD. With $\bar{\text{P}}\text{ANDA}$ the entire energy region below and above the open charm threshold can be explored, for example the charmonium ground state η_c , measured by several experiments in the past with poor agreement on the mass and the width. High statistics will be generated to obtain precise values. Furthermore, the η'_c , first discovered by Belle [CHOI02] in the $\eta'_c \rightarrow K\bar{K}\pi$ channel in 2002, is known with an uncertainty in the width of 40 %. Another interesting candidate is for instance the $X(3872)$, discovered by Belle 2003 [CHOI03]. Today there are several hypotheses to explain this narrow state. It is not clear if it is an excited charmonium (1^3D_2 or 1^3D_3), a D^0D^{*0} molecule or even a $c\bar{c}g$ hybrid.

Search for gluonic excitations QCD theory predicts that gluons can act as a principal component in hadrons. They should be able to form states of pure glue or hybrids for example made out of a $q\bar{q}$ and a constituent gluon. The properties of glueballs and hybrids are determined by the long-distance effects of QCD and will yield fundamental insight into the structure of the QCD vacuum. These gluonic excitations are not yet verified. There are a few already observed states like the $f_0(1500)$ which are possible candidates [ABEL96]. LQCD¹ predicts in total 15 glueball states with masses accessible to $\bar{\text{P}}\text{ANDA}$. For example the first 2^{+-} state is predicted at 4.3 GeV. Glueballs decay color blind in $u\bar{u} d\bar{d} s\bar{s}$ and $c\bar{c}$ and can mix with normal hadronic resonances in the same mass range. The expected glueballs to be studied with $\bar{\text{P}}\text{ANDA}$ will be decaying mostly into $\phi\phi$ or $\phi\eta$ if their mass is < 3.6 GeV or into $J/\psi\eta$ or $J/\psi\phi$

¹LQCD= Lattice quantum chromodynamics

Chapter 2 The $\bar{\text{P}}\text{ANDA}$ experiment

if the mass is above. $\bar{\text{P}}\text{ANDA}$ will have the best chance to detect the $c\bar{c}g$ states with exotic quantum numbers since they are predicted to be very narrow with masses in the region above 3.5 GeV. If they exist $\bar{\text{P}}\text{ANDA}$ will have access to tetraquarks and pentaquarks up to ~ 5.5 GeV. The reaction $p\bar{p} \rightarrow \Theta^+\Theta^-$ could be studied near threshold [BOCA].

Besides these main topics $\bar{\text{P}}\text{ANDA}$ will give the opportunity to perform further investigations. Some of them are listed below.

Study of hadrons in nuclear matter So far all experiments have investigated in-medium modifications of hadrons in hadronic matter with light quarks. With $\bar{\text{P}}\text{ANDA}$ these measurements can be extended to heavier hadrons containing charm quarks due to the high-intensity antiproton beam with beam momentum up to 15 GeV. These studies will give a better understanding of the origin of hadron masses in the context of spontaneous chiral symmetry breaking in QCD.

Open charm spectroscopy With the high luminosity and at beam momenta larger than 6.4 GeV produced by the HESR the experiment will generate D meson pairs with high statistics. For example 100 charm pairs per second around the $\Psi(4040)$ are expected. The $p\bar{p}$ annihilation can create these meson states directly. The high yield and the well defined production kinematics can carry out a significant charmed meson spectroscopy program. This will include studies on the direct CP violation and T violation of the D meson, the determination of branching ratios or new Cabibbo forbidden decays.

Hypernuclear physics A phenomenon in nuclear physics is the existence of nuclei containing strange baryons. By replacing an up or down quark by a strange quark the nucleus obtains the quantum number strangeness. With $\bar{\text{P}}\text{ANDA}$ it will become possible to explore the level scheme of low-mass isotopes of double hypernuclei for the first time [ACH12].

Electromagnetic Processes By investigating electromagnetic processes, like $\bar{p}p \rightarrow e^+e^-$ it will be possible to measure the time-like electromagnetic form factor of the proton over an extended q^2 region.

2.1 PANDA Physics program

To fulfill the experimental detector requirements defined by the different research fields, an electromagnetic calorimeter with a high energy resolution over a large energy range plays a major role. Especially for an effective background suppression, the energy resolution and a low energy threshold are essential. For example, for the measurement of the h_c , a singlet state of a P wave charmonium (1^1P_1) created by $\bar{p}p$ annihilation, the signature has to be distinguished from at least 3 major background contributions. The background channels

- $\bar{p}p \rightarrow K^+K^-K^+K^-\pi^0$
- $\bar{p}p \rightarrow \phi K^+K^-\pi^0$
- $\bar{p}p \rightarrow \phi\phi\pi^0$

can be easily misidentified as

- $\bar{p}p \rightarrow h_c \rightarrow \eta_c\gamma \rightarrow \phi\phi\gamma \rightarrow K^+K^-K^+K^-\gamma$

if one γ from the π^0 decay is not detected or mismatched. Therefore, for reconstructing all π_0 's to separate the h_c signal from the background the γ threshold and energy resolution have to be as low as possible. Another detector benchmark is given by Lattice-QCD and fluxtube model calculations. They predict the J^{PC} exotic 1^{-+} hybrid to be the lightest charmonium hybrid within an expected mass region between 4-4.4 GeV. The expected cross section of $\sigma(\bar{p}p \rightarrow H_c\chi) \approx 100$ pb leads to a small amount of reactions compared to the background which is in the order of $2 \cdot 10^7 s^{-1}$. The search for the hybrid state $X(1^{-+})$ requires an unambiguous assignment of many final states. The channels in fig.2.2 ending up with the detection of $\bar{p}p \rightarrow e^+e^-\gamma$ or $\bar{p}p \rightarrow 2\pi^+2K^-\gamma$, respectively, which will pose a challenge for the detector.

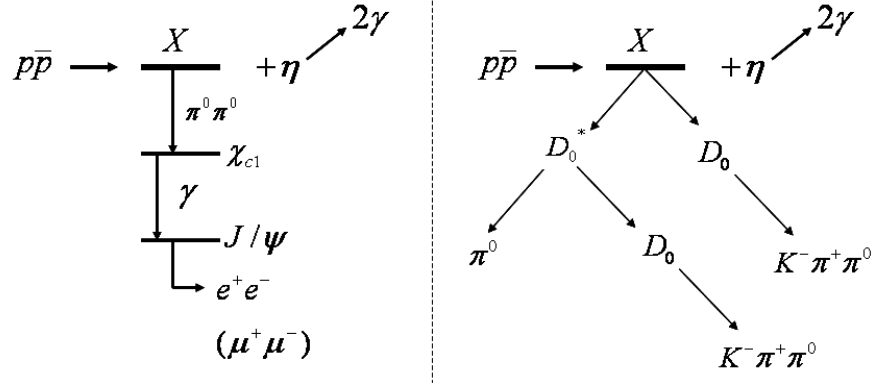


Figure 2.2: Main decay channels of the $X(1^{-+})$. Due the high amount of decay products a calorimeter with high energy resolution is necessary.

2.2 Antiproton production

Antiprotons (\bar{p}) can be generated by inelastic collisions of accelerated protons with nucleons of a target nucleus at rest by the process $pA \rightarrow \bar{p}X$, where X represents all the other secondary particles. By taking into account the kinetic energy of the center of mass of the interacting nucleons, the antiproton production threshold requires a minimum kinetic proton energy of $6m_p c^2 = 5.6$ GeV, with m_p being the rest mass of the proton and antiproton respectively. The accelerator facility at FAIR will produce high quality antiproton beams within a considerable large momentum range. For the creation of antiprotons, in a first step 70 MeV protons will be injected from the planned proton linear accelerator (LINAC) with pulses of 70 mA into the SIS18 synchrotron of the present GSI with a repetition rate of 5 Hz. The LINAC pulses have to be accumulated over 15 cycles within the SIS18 to attain the required number of $5 \cdot 10^{12}$ protons per SIS18 cycle. After acceleration up to 2 GeV, the protons are transferred into the synchrotron SIS100. Here the protons can be further accumulated up to $4 \cdot 10^{13}$ per SIS100 cycle and accelerated to the envisaged antiproton production energy of 29 GeV. Before impinging on the target, the proton beam circulating within the SIS100 has to be compressed to a single bunch of approximately 7.5 m or 25 ns, respectively. This ensures, that a fast reduction of the momentum spread is achieved required for injection into the accumulation in the CR. A target made out of metal for antiproton production is foreseen. The yield per proton will be $5 \cdot 10^{-6}$, resulting in a maximum yield of $1 \cdot 10^8$ per cycle. For separating antiprotons from all other particles, a magnetic

separator will be placed behind the production target. The collector ring with a large aperture will cool the hot secondary antiproton beam with 3 GeV mean energy and large momentum spread $\Delta p/p = \pm 3\%$ (full width, half maximum) down to $\Delta p/p = \pm 0.1\%$ and transfer the antiprotons to the RESR for accumulation for high luminosity experiments. During the accumulation, the beam will be further cooled stochastically. The accumulation rate increases up to $7 \cdot 10^{10}$ antiprotons per hour, depending on the requirements for the experiments. From here, the antiprotons can be transferred to the NESR or the HESR. Basically, there are two main applications for antiprotons at FAIR: experiments with low energetic antiprotons at FLAIR and the study of high energetic antiproton collisions at PANDA. The appropriate storage rings for these experiments are the HESR and the NESR for the high and low momentum domain, respectively.

2.3 HESR

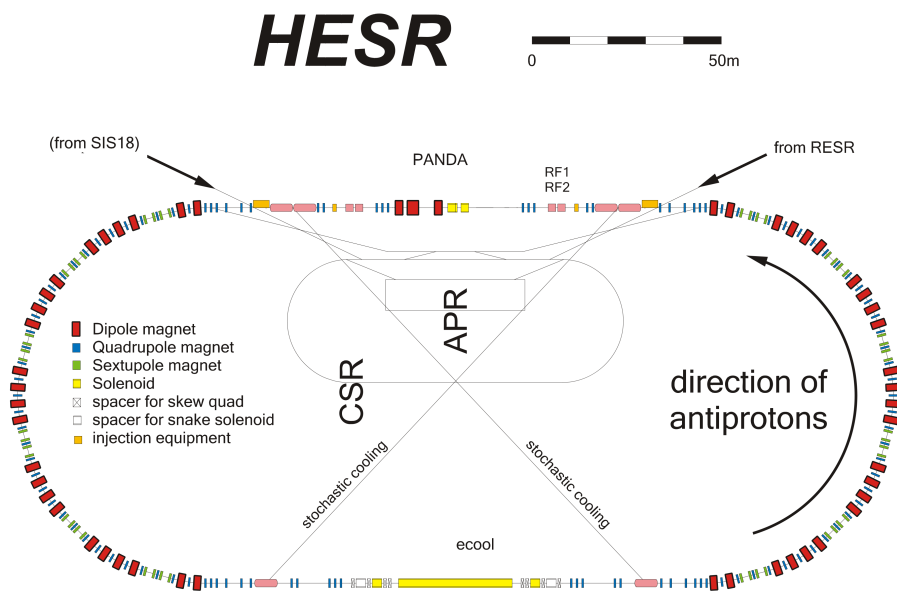


Figure 2.3: Schematic view of the HESR ring. Equipment for experiment, stochastic and electron cooling, compensation solenoids, and injection is included. Picture taken from [ACCEL].

Chapter 2 The $\bar{\text{P}}\text{ANDA}$ experiment

The HESR is a racetrack-shaped storage ring with 574 m circumference, housing $\bar{\text{P}}\text{ANDA}$ as an internal experiment (fig.2.3). It will cover an area of about 120 m by 250 m. The magnetic bending power is about 50 Tm. The purpose of the HESR is to supply the $\bar{\text{P}}\text{ANDA}$ experiment with a high quality antiproton beam in a broad momentum range from 1.5 GeV up to 15 GeV. Therefore, the precooled antiprotons from the RESR are injected into the HESR and accelerated or decelerated, respectively, to the desired beam momentum. Afterwards, the HESR serves as a storage ring for internal target experiments. The beam preparation will be completed by focusing on the target region. Two operation modes are foreseen: the high luminosity mode with intensities up to 10^{11} antiprotons over the whole energy range, will deliver a peak luminosity of $\mathcal{L} = 2 \cdot 10^{32} \text{ cm}^{-2}$ at a rms momentum spread of about $\Delta p/p = 10^{-4}$. The high resolution mode will deliver 10^{10} particles between 1.5 GeV and 8.9 GeV and provides a peak luminosity of $\mathcal{L} = 2 \cdot 10^{31} \text{ cm}^{-2}$ at a momentum spread of $\Delta p/p = 10^{-5}$. In order to reach the high beam quality in the straight section opposite to the experiment, electron cooling is foreseen, surrounded by compensation solenoids. Therefore, an electron beam will be used with a current up to 1 A and energies up to 8 MeV. The electron cooling will be applicable for beam momenta between 1.5 GeV and 8.9 GeV. In addition, for stochastic cooling, pickup and kicker devices with a bandwidth of 2 - 4 GHz are located in the straight sections opposite to each other. The stochastic cooling is available above 3.8 GeV [PPR]. The straight section at the $\bar{\text{P}}\text{ANDA}$ side will accommodate the microwave cavities as well as the beam injection systems. The accelerator arc is formed out of 6 unit cells (fig.2.4). 4 dipoles with 7.5° bending angle are defining one cell.

2.4 Detector setup

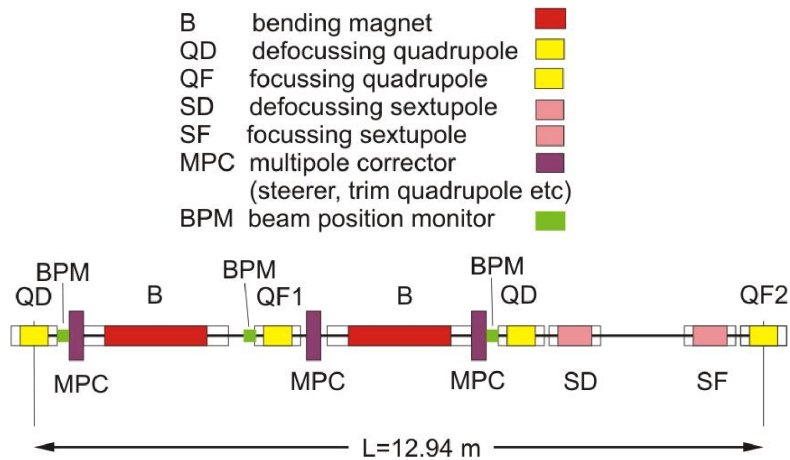


Figure 2.4: One half of the unit cell in the HESR arc. One arc is formed by 6 unit cells. Picture taken from [ACCEL].

2.4 Detector setup

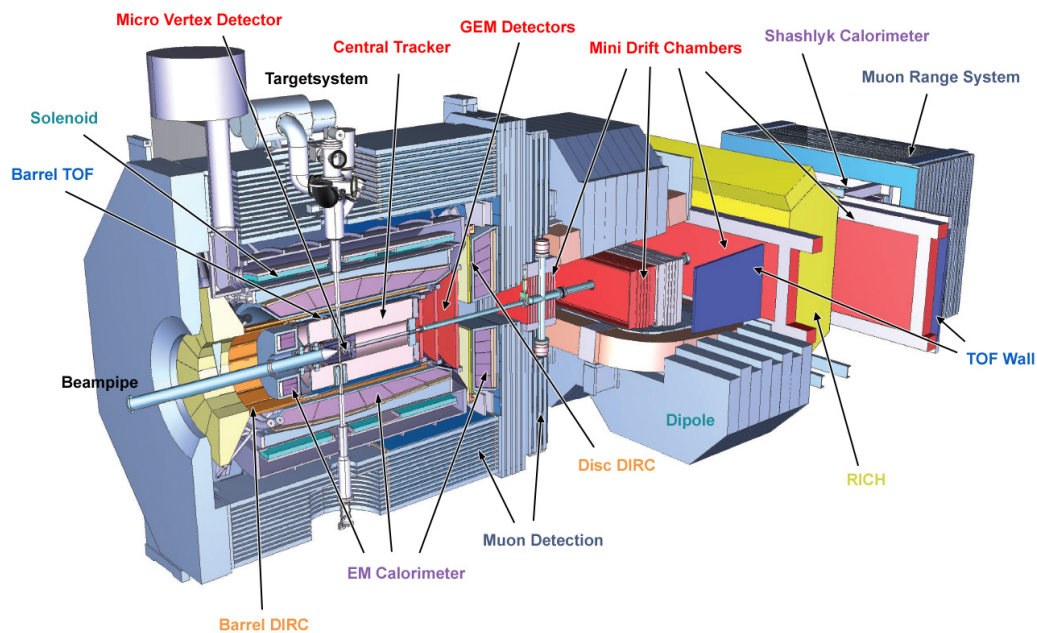


Figure 2.5: The PANDA Detector. Picture taken from [PWEB].

The main goal are completely exclusive measurements, which require a nearly full coverage of the solid angle. The detector has to handle interaction rates up to 10^7 Hz to achieve the desired luminosity. Due to the high beam intensities, all detectors

must withstand a high radiation dose. High energy and angular resolution for charged particles and photons over the full energy range are required. For tracking slow particles with momenta of about 100 MeV and detecting photons as low as a few MeV, a low material budget of dead material is indispensable. The $\bar{\text{P}}\text{ANDA}$ experiment is designed as a fixed target experiment. Because of the strong Lorentz boost of decay products along the beam direction, the detector is subdivided into two parts. One part is the target spectrometer within a superconducting 2 T solenoid which covers the interaction region. The target spectrometer consists of a target system, a micro vertex detector, a straw tube tracker, a Cherenkov detector, a time-of-flight detector, an electromagnetic calorimeter and a muon detector. The forward spectrometer is utilizing a dipole magnet with an integrated field of 2 Tm to analyze the forward-going particles (fig.2.5). It consists of a tracking system, a Ring Imaging Cherenkov, an electromagnetic calorimeter and a muon detector. A more detailed description of the components will follow. To underline the relevance for this thesis, the electromagnetic target-calorimeter, short EMC², will be described first and in more detail compared to the other detector components.

2.4.1 Electromagnetic target-calorimeter

2.4.1.1 Specifications

In an experiment which produces a hadron rich environment, the measurement of photons and leptons plays a major role for the selection and identification of specific physical reactions of interest as well as the reduction or separation of background events. In association with the tracking system, the EMC can be even utilized for the identification of charged particles. For example, the electromagnetic calorimeter will be the main device for the discrimination between electrons and pions. $\bar{\text{P}}\text{ANDA}$ can not rely on the typically used threshold Cherenkov detector for that purpose. Therefore, a precise E/p measurement, where the uncertainty of the electron energy is negligible compared to the momentum error in the order of 1% from the tracking detectors, determines the needed energy resolution at high energies. In general, the planned measurements require a high energy resolution over the total dynamic range necessary for a sufficient resolving power of final states with multiple electrons,

²EMC = Electromagnetic Calorimeter

positrons and photons. In particular, the low energy threshold affects the sensitivity. For example, simulations of the channel $p\bar{p} \rightarrow \eta_{c1}\eta$ show that the signal to background ratio depends almost quadratically on the minimum detectable photon energy. Furthermore, experiments like Crystal Barrel, CLEO, BaBar or BES with comparable detector structure have proven that a invariant mass width for π^0 of less than 8 MeV and for η of less than 30 MeV is necessary for a reasonable final state decomposition. The required resolution and the necessary lower edge of the energy range puts the limit on the acceptable noise of a single detector unit. A maximum of 1% random hits due to electronic noise should be acceptable which corresponds to $3\sigma_{noise}$. Based on simulations, the required resolution can be achieved if the noise level remains below 1 MeV deposited energy.

All components of the detector, which includes electronics and of course the active detection material, have to sustain a high radiation dose. Simulations estimate dose rates up to 125 Gy per year and single detector rates up to 500 kHz in the most forward region [TDREMC]. An overview of the most important calorimeter requirements is given in table 2.1. Besides the technical requirements for the calorimeter a fundamental

Properties	Necessary value		
energy resolution $\frac{\sigma(E)}{E}$	$\frac{\leq 2\%}{\sqrt{E/GeV}} \oplus \leq 1\%$		
energy threshold	≤ 10 MeV		
individual crystal threshold	≤ 3 MeV		
noise equivalent $\sigma_{E,noise}$	≤ 1 MeV		
solid angle coverage 4π / %	99%		
Subunit properties	backward ($\geq 140^\circ$)	barrel ($\geq 22^\circ$)	forward ($\geq 5^\circ$)
dynamic Range	0,7 GeV	7,3 GeV	14,6 GeV
position resolution σ_θ	0,5°	0,3°	0,1°
maximum signal rate	100 kHz		500 kHz
shaping time	400 ns (LAAPD)		100 ns (VPT)
radiation hardness (annual dose)	10 Gy		125 Gy

Table 2.1: Overview over the main requirements for the PANDA EMC [TDREMC].

aspect is the radial compactness to reduce costs. The cost of a scintillator and the

surrounding superconducting magnet scales with the cube of their dimension.

To come close to all listed requirements PbWO_4 was chosen as scintillator material. It is fast and radiation hard with a very short radiation length below 1 cm. A description of PbWO_4 can be found in chapter 2.4.1.3.

2.4.1.2 Design

The EMC is subdivided into three parts. The backward end-cap, the forward end-cap and the barrel (fig. 2.5 & 2.6). The barrel covers polar angles between 22° and 140° , respectively and consists of 11360 crystals. The basic crystal shape is a

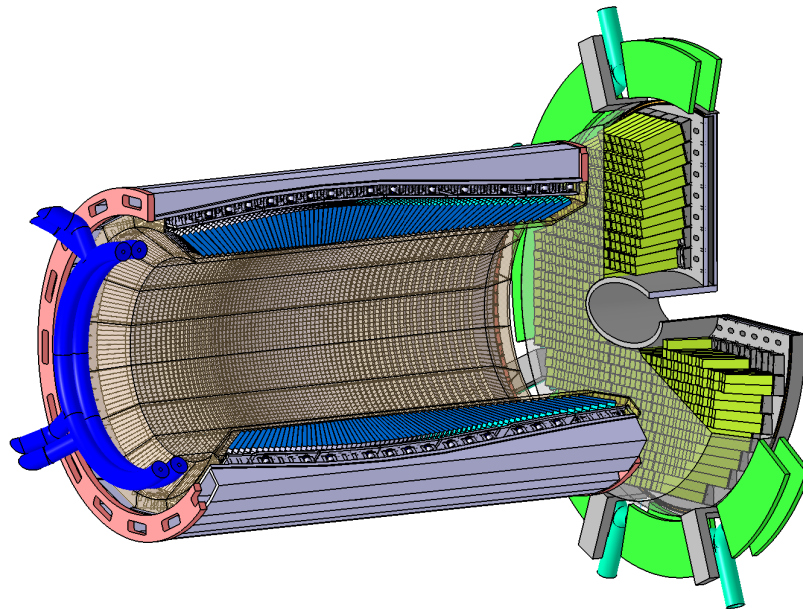


Figure 2.6: Schematic drawing of the target calorimeter without the backward end cap.

tapered parallelepiped. To obtain the barrel geometry, eleven different shapes are designed in two mirrored geometries (fig.2.7). Right angle corners are introduced in order to simplify the CAD design and the mechanical manufacturing process. Each crystal will be wrapped with a Radiant Mirror Film ESR (former VM2000) from 3M (Neuss, Germany) as reflective material in order to optimize the light collection. Two rectangular LAAPDs³ per crystal serve as photosensor. Besides an enhanced light collection, two LAAPDS allow to discard direct interaction with particles in the

³LAAPD = Large Area Avalanche Photodiode

2.4 Detector setup

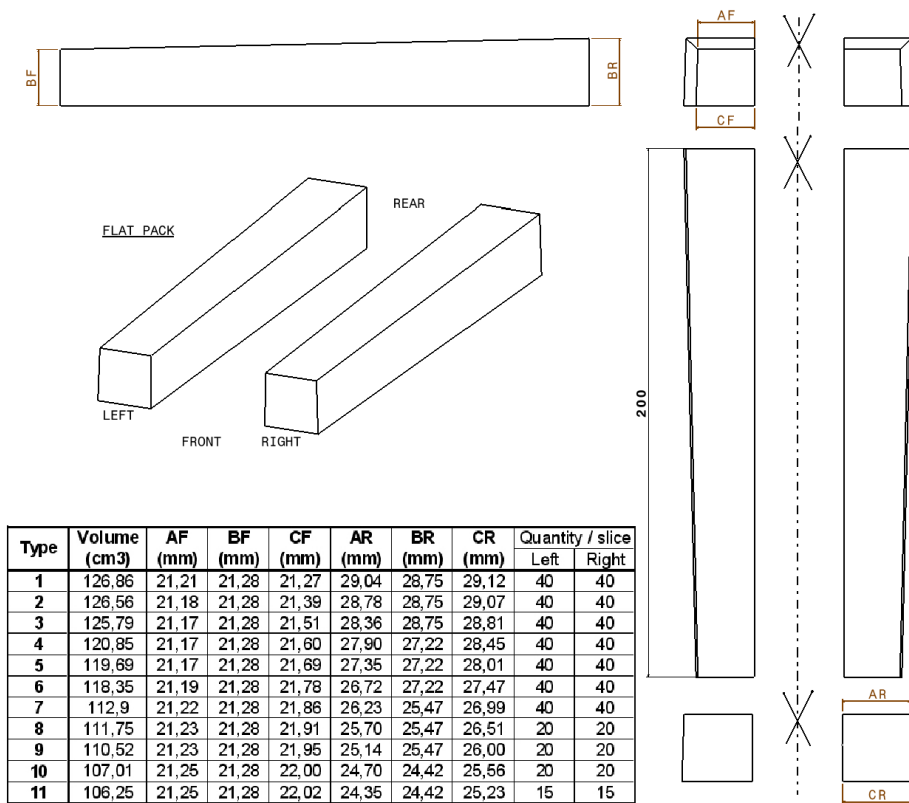


Figure 2.7: The shape of the barrel scintillator crystals and the definition of geometrical parameters. Pictures taken from [TDREMC].

Chapter 2 The \bar{P} ANDA experiment

sensor. Photomultipliers cannot be used due to the high magnetic field of the solenoid. Each crystal is positioned in a thin but stiff carbon fiber alveole and fixed by a metal insert, which is glued into the alveole. The latter provides the necessary stiffness and the fixation to a back plane supporting each of the 16 slices of the barrel (fig.2.8). The

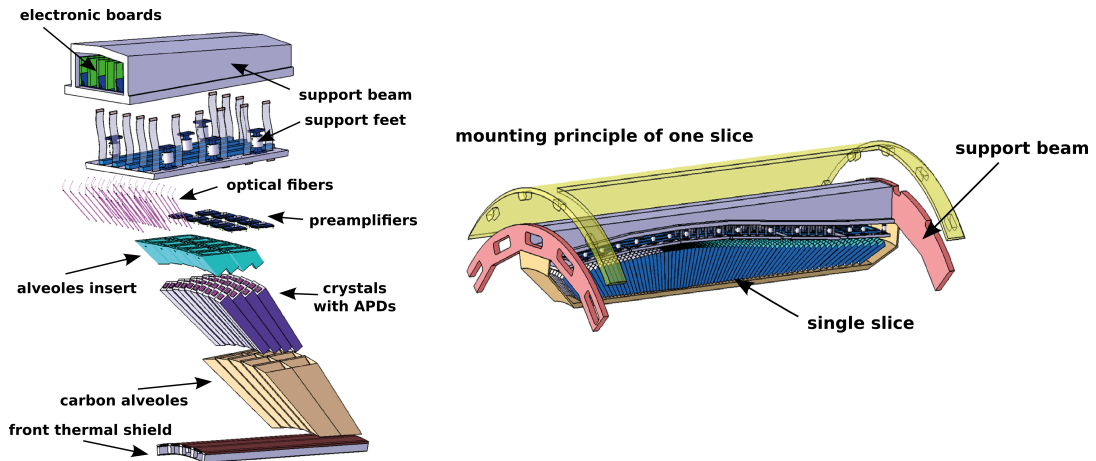


Figure 2.8: Schematic view of the barrel calorimeter.

considered photon detection from 10 MeV up to 15 GeV is a challenge especially for the electronics due to the high dynamic range. Instead of a design based on discrete components, the preamplifier for the pair of APDs is accomplished by an ASIC⁴. Amplified outputs of two different gains are provided including signal shaping. The signals of each output will be digitized by sampling ADCs⁵ with a samplingrate below 100 MHz. In order to compensate changes of the optical transmission of the crystals due to radiation damage, pulsed LED light will be distributed into the crystals via optical fibers. The barrel is subdivided symmetrically into 16 identical slices parallel to the beam pipe. Each crystal is slightly tilted by 4° to 4 cm off the target to avoid that photons can pass undetected between two crystals. The crystals of both endcaps are not pointing towards the interaction point as well. The backward end cap is composed up to 592 and the forward end cap of 3600 20 cm long crystals. The forward end cap crystals are nearly rectangular with a front face of 24.4×24.4 and a back face of 26×26 mm. The backward end cap crystals are rectangular with front and back surfaces of 24.4×24.4 mm. In contrast to the barrel the photon detection in the forward endcap has to deal with much higher single crystal rates up to 500

⁴ASIC = Application Specific Integrated Circuit

⁵ADC = Analog to digital converter

kHz in a magnetic field up to 1.2 T. VPTs⁶ or VPTTs⁷ are considered as photosensors with a bialkali photocathode with enhanced quantum efficiency for the innermost 25% crystals. In contrast to the barrel region, the magnetic field is oriented in the axial direction of the sensors and thus makes it feasible to use VPTs or VPTTs for the endcap.

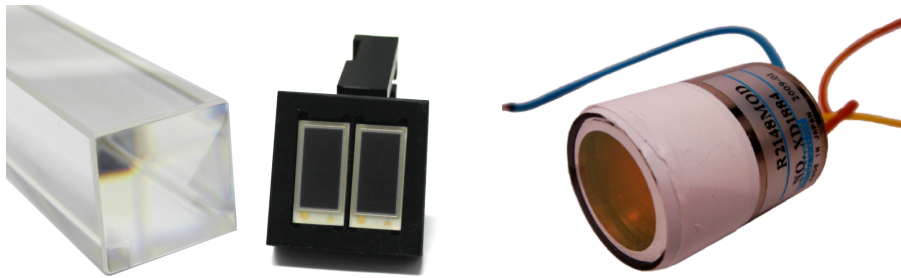


Figure 2.9: Left picture: LAAPD photo-sensors for the barrel. By using 2 LAAPDs on one crystal, nearly the whole surface is covered. Right picture: considered photo-sensor for the forward end cap.

2.4.1.3 Scintillator as active detection material

Calorimetry is the measurement of energy via complete absorption.

Photons can transfer their energy mainly via three fundamental processes:

- Photoelectric effect - The photon can be absorbed completely by a bound electron. The effect is dominated by the most strongly bound electrons in the inner shells of an atom. If the absorbed energy is larger than the binding energy, the atom will be ionized. The kinetic excess energy of the electron can cause further ionization or excitation respectively. This effect dominates at low energies. The cross section has a strong dependence on the absorber material ($\sim Z^{4-5}$).
- Compton Scattering - In case of an incident photon interacting with a weakly bound electron from outer shells, only a part of the energy is transferred to the electron. The photon will be deflected with respect to its original direction. The absorption coefficient has a linear dependence on the atomic number.

⁶VPT = Vacuum Photo-Triode

⁷VPTT = Vacuum Photo-Tetrolodes

Chapter 2 The PANDA experiment

- Pair Production - Photons cannot lose their energy by Coulomb interactions as charged particles do. If the photon energy exceeds twice the rest mass of an electron (1.022 MeV) it can be converted into an electron-positron pair within a coulomb field, mainly from the nucleus. For high energies this effect is dominating.

The attenuation of the radiation intensity follows:

$$I(x) = I_0 \cdot e^{-\mu \cdot x}, \quad (2.1)$$

with the absorption coefficient composed of the coefficients for the photoelectric effect, the Compton scattering and the pair production.

$$\mu = \tau + \sigma + \kappa. \quad (2.2)$$

The energy dependence of these effects can be seen in fig. 2.10. The radiation length X_0 of a photon is a fraction of 7/9 from the mean free path due to pair production. It can be approximated with [PDG08]:

$$X_0 = \frac{716.4 \text{ g} \cdot \text{cm}^{-2} \cdot A}{Z(Z+1) \ln\left(\frac{287}{\sqrt{Z}}\right)}. \quad (2.3)$$

Besides inelastic coulomb scattering described by the Bethe Bloch equation:

$$-\frac{dE}{dx} = \frac{4\pi}{m_e c^2} \frac{n z^2}{\beta^2} \left(\frac{e^2}{4\pi\epsilon_0}\right)^2 \left[\ln \frac{2m_e c^2 \beta^2}{I \cdot (1 - \beta^2)} - \beta^2 \right], \quad (2.4)$$

with $\beta = v/c$, z the particle charge, n the electron density of the target and I the mean excitation potential of the target, a charged particle can lose energy via radiation. It is known as Bremsstrahlung and is generated due to deflection and therefore acceleration by the coulomb field of the absorber. The cross section scales with $1/m^2$ of the penetrating particle, the process is only relevant for electrons and positrons in the considered energy regime. Above the critical energy of $E_c \approx 550 \text{ MeV}/Z$, Bremsstrahlung is the dominating process for electrons and positrons. The generated radiation is depending on its energy finally subject to photoelectric effect, Compton scattering or pair production again. The energy loss of the charged particle due to Bremsstrahlung can be described by

$$-\frac{dE}{dx} = \frac{E}{X_0}, \quad (2.5)$$

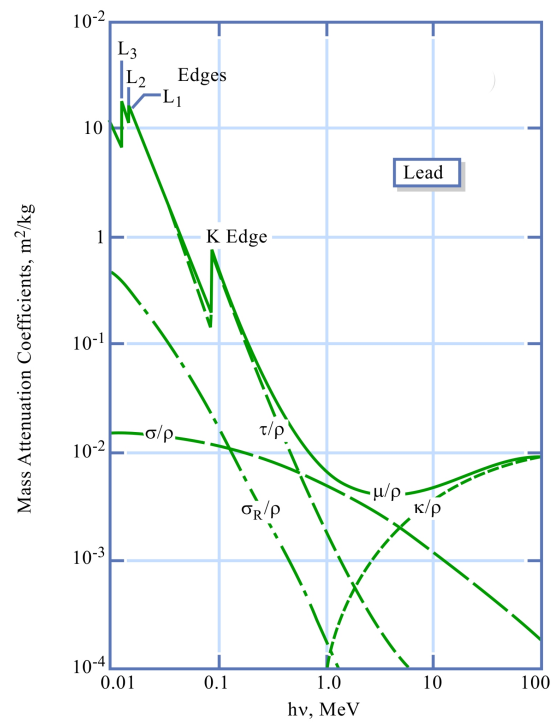


Figure 2.10: Exemplary mass attenuation coefficients for lead. With τ/ρ for the photoelectric effect, σ/ρ Compton Scattering, κ/ρ pair production, σ_R/ρ Rayleigh (coherent) scattering and μ/ρ their sum [MIT].

Chapter 2 The PANDA experiment

with [LE09]

$$X_0 = \frac{A}{4\alpha N_a Z^2 r_e^2 \ln(183Z^{-\frac{1}{3}})}. \quad (2.6)$$

X_0 is the radiation length of a high energetic charged particle as well, but where its energy is reduced by a factor of $1/e$. With N_a the Avogadro constant, r_e the classical electron radius and α the Sommerfeld's fine-structure constant.

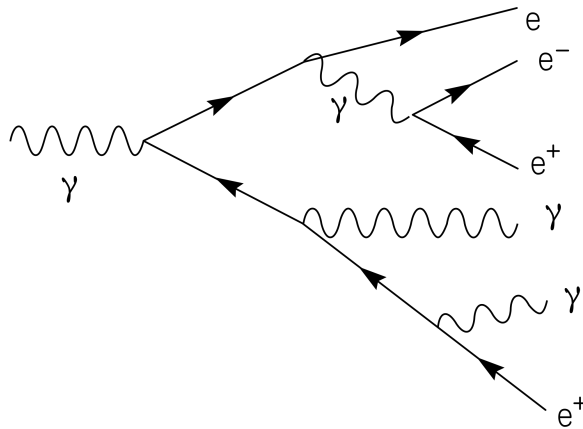


Figure 2.11: Development of an electromagnetic shower.

The combination of these interaction effects leads to the development of an electromagnetic shower. For example, an impinging photon converts into an electron-positron pair. These charged particles might emit new photons due to the Bremsstrahlung process, which can convert again into electron-positron pairs (fig.2.11).

The transversal spread of the electromagnetic shower due to multiple scattering processes of the electrons can be quantified by the Molière Radius:

$$R_M \approx \frac{21 \text{ MeV}}{E_c} \cdot X_0. \quad (2.7)$$

On average, only 10% of the energy lies outside the cylinder with radius R_M . About 99% is contained inside of $3.5 R_M$.

The energy loss probability distribution for charged particles like high energetic muons, which are completely traversing any absorber with a moderate thickness, is described by the asymmetric Landau distribution. The most probable energy loss for an absorber

with a thickness x in g/cm^2 can be calculated with:

$$\Delta_p = \xi \left(\ln \frac{2mc^2\beta^2\gamma^2}{I} + \ln \frac{\xi}{I} + j - \beta^2 - \delta(\beta\delta) \right), \quad (2.8)$$

with I the mean excitation energy,

$$\xi = \left(\frac{K}{2} \right) \left\langle \frac{Z}{A} \right\rangle \left(\frac{x}{\beta^2} \right) \text{ MeV}, \quad (2.9)$$

$j = 0.2$, $\delta(\beta\delta)$ the density effect correction to ionization energy loss and

$$K = 4\pi N_A r_e^2 m_e c^2. \quad (2.10)$$

For higher energies than $\beta\gamma = 100$ eq. 2.8 gets simplified due to the behavior of $\delta(\beta\delta)$. The energy loss reaches the Fermi plateau and can be calculated via:

$$\Delta_p(\beta\gamma \geq 100) = \xi \left(\ln \frac{2mc^2\xi}{(\hbar\omega_p)^2} + j \right), \quad (2.11)$$

where the plasma energy is given by

$$\hbar\omega_p = 28.816 \sqrt{\rho \left\langle \frac{Z}{A} \right\rangle} \text{ eV} \quad (2.12)$$

for ρ in g/cm^{-3} . The plasma energy for PbWO_4 is equal to 53.36 eV and $K = 0.307 \text{ MeV}\cdot\text{cm}^2$. For very thick absorbers the asymmetric distribution becomes more symmetric, but never approaches a Gaussian shape. [PDG08].

Besides pure electromagnetic interactions, an impinging hadron creates a cascade of inelastic hadronic interactions with the nuclei and nucleons of the absorber material. These reactions can lead to new hadrons like pions, kaons, protons or neutrons. The decay of the secondary hadrons, for example $\pi^0 \rightarrow \gamma\gamma$, can initiate an electromagnetic shower. The hadronic absorption length λ_{Had} is described by:

$$\lambda_{Had} = \frac{A}{N_A \rho \sigma_\mu} \quad (2.13)$$

with A the atomic mass number, ρ the absorber density and σ_μ the cross section for inelastic interactions.

Scintillators are generally used to convert the energy deposited by radiation into visible or near visible light which can be quantitatively measured with photosensors. The

Chapter 2 The $\bar{\text{P}}\text{ANDA}$ experiment

mechanism of inorganic scintillators is a lattice effect. As described before, the energy of the radiation can be absorbed by electrons of the scintillator. If sufficient energy is transferred to the electrons, they will be lifted into the conduction band leaving a hole in the valence band. Inside the conduction band the electrons are freely moving. If a free electron from the conduction band reaches an activation center, the center will be transformed into an excited state. The energy of these centers is located between the conduction and valence band in the energetically forbidden zone. The decay of this excited states finally produces the scintillation light [LE09]. Each calorimeter part of the target spectrometer utilizes lead tungstate (PbWO_4 or PWO for short) as scintillation material. In PbWO_4 the light is produced by transitions from Pb^{2+} Ions to WO_4^{2-} , WO_4^{3-} and WO_3 centers. The material was developed originally for the CMS⁸ experiment at CERN [CMSWEB]. For $\bar{\text{P}}\text{ANDA}$, PWO-II was developed. Due to the lower energy regime of the γ -rays to be studied, this material had to provide an improved light yield compared to the PWO crystals used by CMS. The concentration of lattice defects could be reduced. Therefore, in order to maintain the radiation hardness, the co-doping with Lanthanum and Yttrium could be achieved with a lower concentration. As a result, the light yield increased by a factor of two. Since the dopants lead to shallow traps which reduce the luminescence efficiency. In addition, the $\bar{\text{P}}\text{ANDA}$ crystals are cooled down to -25°C . The reduced so called thermal quenching effect increases the light yield further by a factor of ~ 4 compared to a crystal temperature of $+25^\circ$. A summary of the main PWO-II properties can be found in table 2.2.

Decay time	$\tau = 6 \text{ ns}$
Density	$\rho = 8.28 \text{ g}\cdot\text{cm}^{-3}$
Radiation length	$X_0 = 0.89 \text{ cm}$
Molière Radius	$R_M = 2.0 \text{ cm}$
MIP energy loss (dE/dx)	$10.2 \text{ MeV}\cdot\text{cm}^{-1}$
Light yield (LY) @ 18° within 100 ns	$17\text{-}22 \text{ phe}\cdot\text{MeV}^{-1}$
LY temp. dependence	$3\%/\text{C}$
Emission wavelength (peak)	420 nm

Table 2.2: Some properties of PWO-II. The light yield of full size crystals was measured with a photomultiplier with a bi-alkali photocathode (quantum efficiency $\sim 20\%$) [TDREMC].

⁸CMS = Compact Muon Solenoid

2.4.1.4 Large area avalanche photo diodes

In spite of the improvement, PWO-II remains a scintillator material with moderate light output. Therefore, in order to obtain an electric signal from the scintillation photons above the noise of any preamplifier, a sensor with intrinsic amplification is needed. As mentioned before, photomultipliers cannot be used for the target calorimeter due to the strong magnetic field. PIN⁹-photodiodes have no internal gain mechanism. Therefore, at least for the barrel part of the calorimeter, LAAPDs are foreseen. To optimize the light collection efficiency, first LAAPDs in the size of 10 x 10 mm² (type no. S8664-1010SPL) were developed for \bar{P} ANDA in collaboration with Hamamatsu (Herrsching am Ammersee, Germany). In the effort to collect even more light, an increase in the capacity and noise was observed by increasing the sensitive area of the LAAPD. This introduced the development of 14 x 6.8 mm² LAAPDs (type no. S11048, specifications: tab.:2.3). By using two of them, nearly 40% of the end face of

Parameter	Rating ($T = 25^\circ$)
Window material	Epoxy resin
Active area	14.0 x 6.8 mm
Spectral response range	320 - 1000 nm
Peak sensitivity	580 nm
Quantum efficiency ($\lambda = 420$ nm)	70
Terminal capacitance ($M = 50, f = 100$ kHz)	270 pF
Excess noise index ($M = 50, \lambda = 420$ nm)	0.2

Table 2.3: Some of the S11048(X2) LAAPD properties for \bar{P} ANDA, as written in the data sheet.

a crystal can be covered. A schematic of an APD can be found in fig.2.12. A reverse voltage has to be applied to the p-n junction. High doped p^{++} and n^{++} layers are serving as electrodes. The photons are absorbed inside a thin p^+ doped layer and generate electron-hole pairs. The electrons drift towards the n^+ side while the holes drift towards the p^+ side. The strong electric field across the p-n junction accelerates the charge carriers. If the reverse voltage reaches a certain value, some of the carriers create new electron-hole pairs when they collide with the crystal lattice. These new electron-hole pairs create additional electron-hole pairs which can again collide with

⁹PIN = positive intrinsic negative

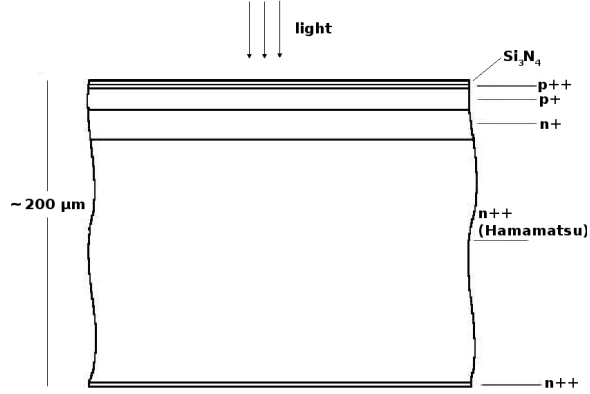


Figure 2.12: Schematic of a APD.

the lattice. Typical values of the electric field are in the order of $10^6 \text{ V}\cdot\text{m}^{-1}$ at a reverse voltage of 400 V. The intrinsic gain due to the avalanche effect depends on the applied voltage. To designate the gain M , the current I with (I_l) and without (I_d) illumination can be measured:

$$M = \frac{I_l(U) - I_d(U)}{I_l(M=1) - I_d(M=1)}. \quad (2.14)$$

In addition, the effective gain depends strongly on the temperature. The crystal lattice vibration can moderate the charge carriers and therefore impeded ionization. In general, the APD multiplication process is subject to statistical fluctuations. This non-uniform multiplication for each charge carrier is known as excess noise. Therefore the APD shot noise is larger than the PIN photodiodes shot noise and given by the following equation:

$$I_n = [2q(I_{DS} + I_{DB}M^2F)B]^{1/2}, \quad (2.15)$$

with: q the electron charge, I_{DS} surface leakage current, I_{DB} bulk leakage current, B system bandwidth and F excess noise factor. The Poisson statistics describes the variance of primary generated electron-hole pairs N_{phe} , often mentioned as number of photoelectrons with respect to the quantum efficiency:

$$\sigma = \sqrt{N_{phe}}. \quad (2.16)$$

Including the statistical APD gain fluctuations eq. 2.16 can be written as:

$$\sigma = \sqrt{FN_{phe}}. \quad (2.17)$$

F can be calculated by [INT66]:

$$F = kM + (1 - k) \left(2 - \frac{1}{M} \right), \quad (2.18)$$

with the carrier ionization ratio k defined by the ratio of hole to electron ionization probability ($k < 1$). Therefore, the lower the values of k and M , the lower the excess noise factor. According to [HAM] equation 2.18 can be simplified by the empirical formula:

$$F = M^x. \quad (2.19)$$

The exponent x represents the excess noise index. For example, σ of a photo peak with a Gaussian shape, including σ_{pre} , the noise of the preamplifier can be described by:

$$\sigma_E = \sqrt{(FN_{\text{phe}})^2 + \sigma_{pre}^2}. \quad (2.20)$$

The influence of the excess noise on the total energy resolution can be written as:

$$\frac{\sigma_E}{E} = \sqrt{\frac{F}{N_{\text{phe}}}} = \sqrt{\frac{F}{LY \cdot E}}. \quad (2.21)$$

As mentioned before, the excess noise and the photo current are increasing with the gain. This means that an optimum signal to noise ratio exists at a certain gain value (fig.2.13).

2.4.1.5 Parametrization of the calorimeter energy resolution

The total energy resolution is not only photon statistic dependent ($1/\sqrt{E}$). The read-out electronics including the LAPPDs affect the resolution as well. On one hand the excess noise factor affects the stochastic term a/\sqrt{E} , on the other hand the electronic noise will contribute a b/E part to the total parametrization. Furthermore, inhomogeneities in the detector, inter-calibration inaccuracies or shower losses in longitudinal and transverse direction contribute to a energy independent constant term. In total the resolution can be described with:

$$\frac{\sigma(E)}{E} = \sqrt{\left(\frac{a}{\sqrt{E}} \right)^2 + \left(\frac{b}{E} \right)^2 + c^2}. \quad (2.22)$$

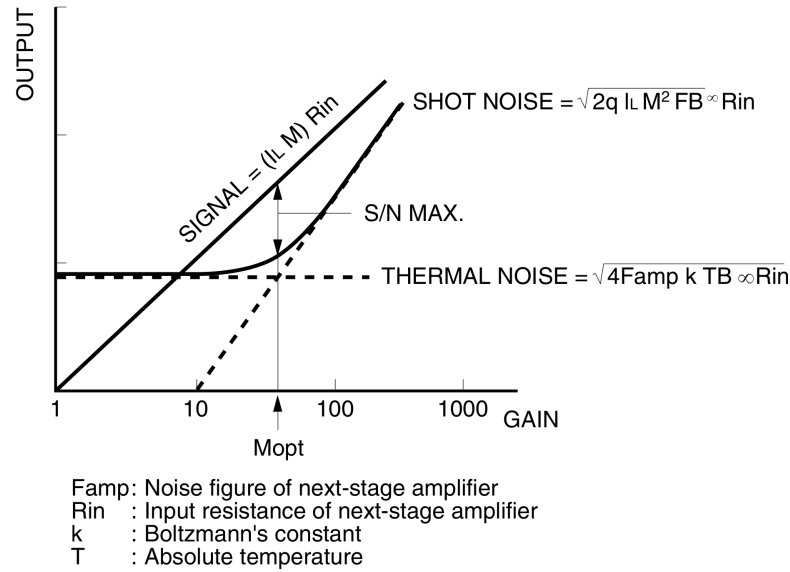


Figure 2.13: APG gain vs output example for a certain APD. The optimum APD gain depends on the ratio of signal to noise. Picture taken from [HAM].

2.4.2 Further target spectrometer components

Target system Depending on the experimental requirements, two target systems are being developed. A cluster-jet target and a complementary pellet target are considered. Both techniques are capable of providing sufficient densities at the interaction point. Besides the primarily considered hydrogen, both systems can utilize heavier gases like deuterium, nitrogen or argon as target material. For the experiment, the main difference of the two target systems is the impact on the beam quality and the vertex definition of the interaction point. The pellet target system provides frozen hydrogen pellets traversing the antiproton beam perpendicularly. The pellet size is in the order of 15-40 μm , depending on the size of the injection nozzle. The pellets can be produced far away from the interaction point and transported through a narrow pipe which gives minor restrictions on detectors close to the target. The in-beam position of the pellets can be measured with the micro-vertex detector. By traversing the beam the pellet will create hundreds of nuclear interactions with the antiproton beam. By averaging over many events it will be possible to determine the pellet position. Furthermore pellet tracking systems are under development. They will utilize a laser or high speed line scan cameras. With these additional devices, a pellet posi-

tion resolution better than $100 \mu\text{m}$ will be achievable. Due to the pellet structure of the target, the luminosity will have a high variation. Therefore a cluster jet target is considered as well. Here cooled hydrogen gas, under high pressure, is expanded into the vacuum through a micron-sized Laval-type nozzle. This creates a supersonic beam which condensates and creates nano-particles. The size of these clusters amounts to the order of $10^3 - 10^5$ atoms. The density achieved so far is below the value achieved for a pellet target. The ongoing developments lead to the conclusion that the luminosity requirements can be fulfilled. The advantages are a homogeneous volume density distribution, a sharp boundary, and a constant angular divergence determined by the collimators used at the cluster-jet source.

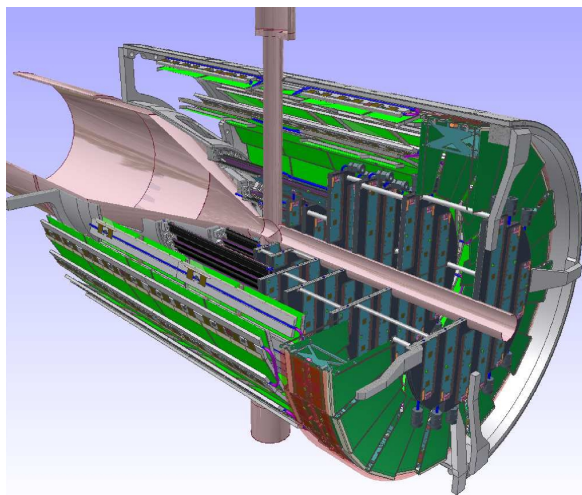


Figure 2.14: The microvertex detector has 4 barrel layers and 6 discs of silicon detectors in forward direction around the interaction point. Picture taken from [TDRMVD].

Microvertex detector The Microvertex detector (MVD) is the innermost detector surrounding the interaction point. It is a tracking device for charged particles to determine vertex points close to the interaction point. A typical example relevant for $\bar{\text{P}}\text{ANDA}$ are D_s mesons with a momentum of 4 GeV. They decay on average after a range of $300 \mu\text{m}$. For the reconstruction of the secondary vertex, a high position resolution is necessary. A vertex resolution better than $100 \mu\text{m}$ is envisaged. The obtained 3 dimensional track and time information provides an important input for the event reconstruction. Furthermore due to the magnetic field of the solenoid the track gives access to the particle momentum. The MVD has a barrel geometry with

Chapter 2 The PANDA experiment

4 layers of silicon detectors and 6 discs in forward direction (fig.2.14). Silicon hybrid pixel detectors are foreseen for the innermost MVD layers. The total number of channels which are required to cover larger surfaces increases rapidly. Therefore, the increasing material budget with increasing numbers of channels requires double-sided silicon micro-strip detectors for the outer parts of the MVD. Two additional silicon disk layers are considered further downstream at around 40 cm and 60 cm to achieve a better acceptance for hyperon cascades [TDRMVD]. Generally, these silicon detectors work with a reverse bias voltage over a p-n junction. When a charged particle propagates through the active volume, energy will be deposited due to ionization. The amount of deposited energy can be calculated with the the Bethe-Bloch formula. Due to the electric field within the p-n junction, the created electron-hole pairs drift apart in opposite directions. While conduction electrons move towards the n-side, holes propagate towards the p-side. An electric signal can be detected due to the resulting currents until free charge carriers are completely collected at the boundaries of the active volume.

Central tracker The central tracker is made out of straw tubes (STT¹⁰) combined with 3 planar stations in forward direction. The 10 mm diameter straw tubes are made out of 27 μm thick aluminized Mylar foil filled with a gas mixture of Argon and CO₂ as quencher. By applying an overpressure of 1 bar these tubes will be stiffened and self supporting. Each tube is equipped with a 20 μm thick gold plated tungsten anode wire. In total, there will be 4636 straws arranged in planar layers. These layers are mounted in a hexagonal shape around the MVD. A position resolution in x and y coordinates of less than 150 μm is expected [TDRSTT]. The task of the SST is the precise spatial reconstruction of the helical trajectories of charged particles from a few 100 MeV/c up to 8 GeV traveling accross the magnetic field. Based on these trajectories the particle momentum can be calculated. Particles are identified via measuring the specific energy loss dE/dx . In particular, protons, kaons and pions can be separated in the momentum region below 1 GeV. In principle, an electric field between the wire and the outer conductor separates the electrons and positive ions, which are generated by a traversing charged particle. The electric field near the thin anode wire accelerates the generated electrons fast enough to create further gas ionizations by collisions. The now amplified signal can be read out electronically. Particles emitted at angles below

¹⁰STT = Straw Tube Tracker

22° will be tracked by the planar stations. These stations are equipped with Gas Electron Multiplier (GEM) foils as amplification stages. The working principle of a GEM detector can be found in fig. 2.15. By having an individual small anode opposite of every hole in the GEM foil, the position resolution can be better than 100 μm .

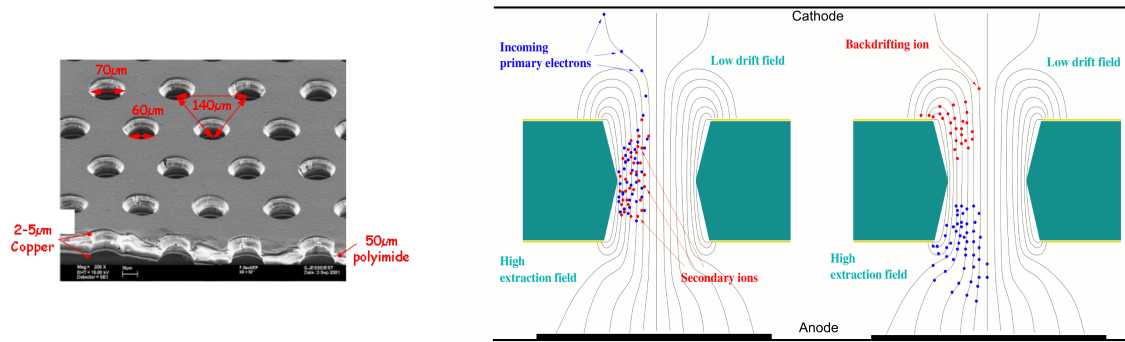


Figure 2.15: Working principle of a GEM detector: electrons are guided into the holes by the low drift field, where avalanches of electron-ion pairs are generated. The asymmetric field configuration of low drift field and higher extraction field together with the small ion mobility leads to efficient back flow suppression. Adapted from [TDSTPC].

Cherenkov detectors The mass of a particle can be obtained by combining the momentum information from the tracking detectors with the velocity information from Cherenkov detectors:

$$p = \frac{m_0 \cdot v}{\sqrt{1 - \frac{v^2}{c^2}}} \Rightarrow m_0 = \frac{p}{v} \cdot \sqrt{1 - \frac{v^2}{c^2}}. \quad (2.23)$$

If a charged particle with the velocity $\beta = v/c$ propagates through a dielectric medium with the index of refraction n and the condition $\beta < 1/n$ is fulfilled, Cherenkov radiation will be emitted. The opening angle Θ of the emitted light cone is velocity dependent and can be described by

$$\Theta = \arccos(1/\beta n). \quad (2.24)$$

The PANDA detector uses so called DIRC¹¹ detectors. A schematic drawing of the detector principle is shown in figure 2.16. The rectangular cross section of the radiator

¹¹DIRC = Detection of Internally Reflected Cherenkov light

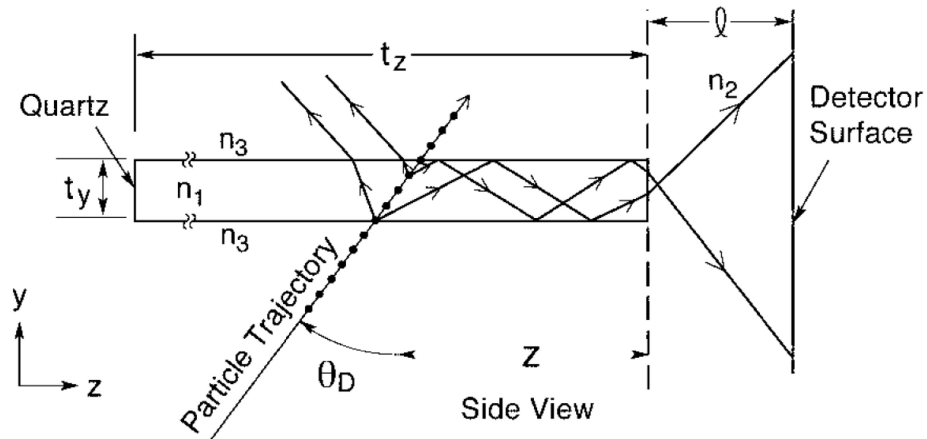


Figure 2.16: Imaging principle of the DIRC detector. A particle traverses the quartz bar and emits Cherenkov light. The light is reflected internally until it exits the quartz bar where the light is detected [TPR].

maintains the angles of the reflected Cherenkov light at its surfaces. The portion of the Cherenkov cone that lies inside the total internal reflection angle is transported undistorted down the bar to the end. When it reaches the end, the light either reflects or emerges into a volume with the refractive index n_2 . After a distance l it hits a two dimensional detection surface, where it forms characteristic images on the surface. Out of these images the opening angle Θ of the light cone can be reconstructed [COY94].

The Cherenkov detector in $\bar{\text{P}}\text{ANDA}$ will be made out of fused silica with a refractive index of 1.47. This gives the possibility to separate for example pions from kaons in the momentum range of 800 MeV up to 5 GeV. Slower particles can be measured with TOF¹² detectors. The Cherenkov detector in the target spectrometer is divided into two parts. The barrel DIRC detector covers angles from 22° to 140°, surrounding the beamline at a distance of 45-54 cm, right in front of the electromagnetic calorimeter. It will consist of 1.7 cm thick quartz slabs. Fused quartz (SiO_2) has a radiation length of $X_0=12.295$ cm ($X_0=27.05$ g/cm⁻², $\rho=2.2$ g/cm⁻³ [PDG12]). The Cherenkov light patterns are intended to be focussed by lenses onto Micro-channel plate photomultiplier tubes or digital Silicon photomultiplier. The concept in forward direction is comparable. The Disc-DIRC detector in forward direction will be sensitive for particles between 5° and 22°, 2 cm thick and will have a radius of 110 cm.

¹²TOF = Time Of Flight

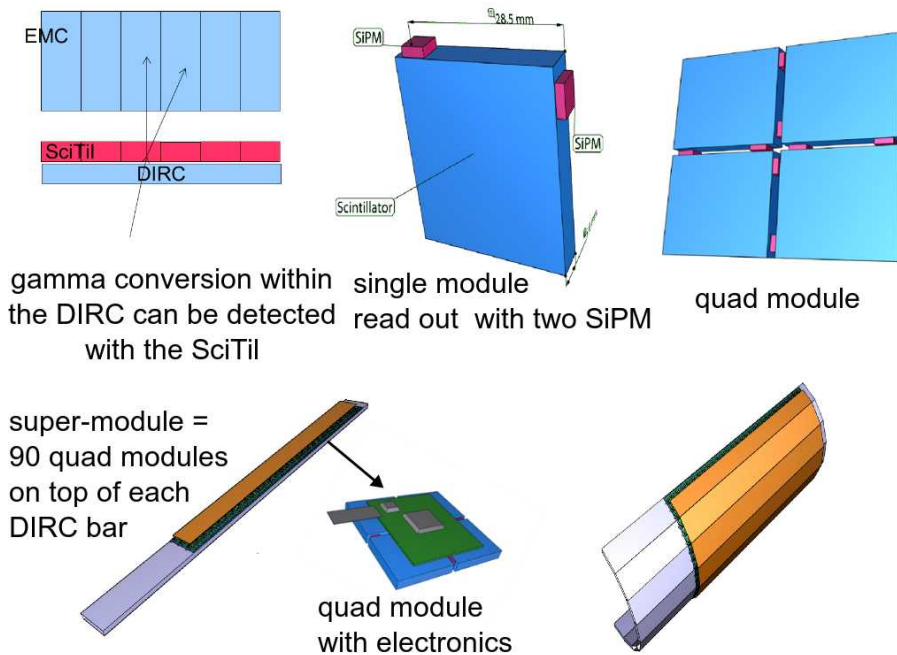


Figure 2.17: The TOF detector between the EMC and the DIRC. It will utilize scintillator-tiles (SciTil) as active material. Pictures taken from [SCHW13].

Time of flight For low momenta charged particle identification, a TOF-barrel is currently under discussion. It will increase redundancy for other sub-detector systems. As detector, scintillator-tiles (SciTil) of $28.5 \times 28.5 \text{ mm}^2$ size are presently foreseen. They are individually read out by two silicon photomultipliers per tile. In total, 5760 tiles are located in the barrel part and 1000 tiles in forward direction. They are sensitive for particles at polar angles from 22° to 140° . They will be located between the EMC and the DIRC. As disadvantage, this detector adds more material in front of the EMC and increases the probability for conversion. On the other hand, the SciTils can be used to identify gamma conversion within the DIRC detector, by detecting the lepton pair.

The muon detectors The detection of muons is important for example for the investigation of J/ψ decays, Drell-Yan processes (fig.2.18) and semi-leptonic D -meson decays. The strongest background contribution to these reactions are pions and their decay daughter muons. For a good identification of primary muons a range tracking system will be implemented in the yoke of the solenoid. The yoke itself is used as absorber. It is finely segmented with interleaving tracking detectors made out of

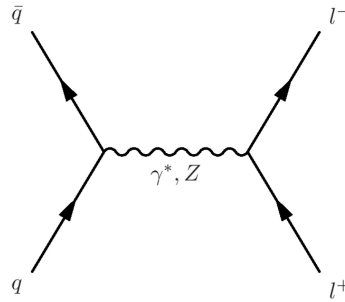


Figure 2.18: Feynman diagram of the Drell-Yan process. A quark of one hadron and an antiquark of another hadron annihilate. This creates a virtual photon or Z boson which decays into a pair of oppositely-charged leptons like e^+e^- .

aluminum drift tubes. These tubes are equipped with additional capacitively coupled strips, read out on both ends to obtain the longitudinal coordinate. There are 13 sensitive layers in total, each 3 cm thick, alternating with 3 cm thick iron absorbers. In the forward end cap more material is needed due to the higher momenta of the particles. Six detection layers will be placed here. The corresponding iron layers therefore will have a thickness of 6 cm.

Detector for hypernuclear physics The production and spectroscopic investigation of hypernuclear particles requires a change of the $\bar{\text{P}}\text{ANDA}$ detector. Due to the modular design, the backward end cap of the calorimeter can be removed and a dedicated nuclear target together with high resolution γ detectors can be installed. In $p\bar{p}$ annihilation, $\Xi\bar{\Xi}$ pairs can be created. Very slow Ξ particles can be absorbed in a secondary target nearby and produce double hypernuclei via nuclear reactions. The secondary target consists of 25-30 mm thick sandwich structured silicon micro strip detectors, alternating with absorbing material. The tracking by the silicon detectors allows to detect the weak decay cascade of the hypernucleus. With an additional germanium array, γ spectroscopy will be done.

2.4.3 Forward spectrometer

The forward spectrometer of the $\bar{\text{P}}\text{ANDA}$ detector has an angular acceptance of $\pm 10^\circ$ in the horizontal direction and $\pm 5^\circ$ in the vertical direction. It makes use of a conventional 2 Tm dipole magnet for the deflection and therefore momentum determination

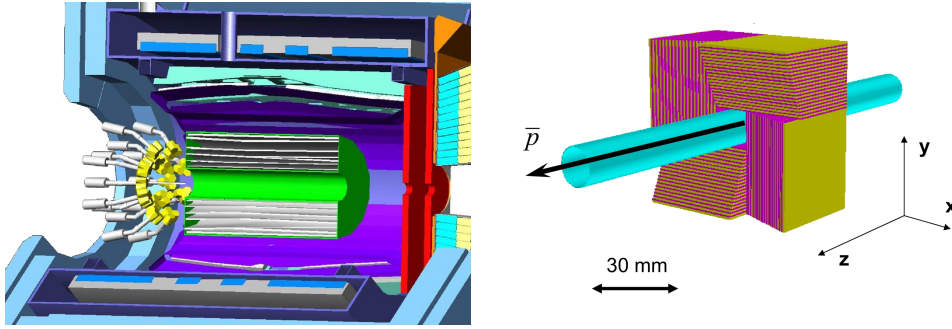


Figure 2.19: Detector setup for hypernuclear physics. Left picture: beam entering from the left. The backward end cap is replaced by a set of germanium detectors. Right picture: the sandwich structured active secondary target for slow backscattered Ξ s. Pictures taken from [TPR].

of charged particles. The impact on the antiproton beam of the accelerator will be compensated by two correcting dipole magnets placed around the \bar{P} ANDA apparatus. For example at the maximum momentum of 15 GeV, a beam deflection of 2.2° has to be corrected. The detector components are arranged downstream the beam pipe.

Forward tracker The deflection of charged particle trajectories due to the magnetic field will be measured by three pairs of mini drift chambers. The first pair for tracking is placed right in front, the second within and the third behind the dipole magnet. Inside the chambers, straw tubes are foreseen. They will be arranged in four double layers. The pair inside the dipole magnet will be able to track even particles with low momenta whose tracks are tightly twisted. All single chambers can reconstruct tracks individually which might be relevant for multi track events. For 3 GeV protons a momentum resolution of $\Delta p/p = 0.2\%$ is expected.

Forward Particle Identification For particle identification especially at highest momenta, a RICH¹³ detector is proposed. The favored design is based on the HERMES RICH detector (fig.2.20). It will use two different radiators to obtain particle separation over a broad momentum range. With silica aerogel ($n=1.0304$) and C_4F_{10} gas ($n=1.00137$), the separation of pions, kaons and protons from 2 to 15 GeV can be

¹³Ring Imaging Cherenkov

provided. The Cherenkov light will be reflected by focusing mirrors outside the active volume on an array of photo sensors.

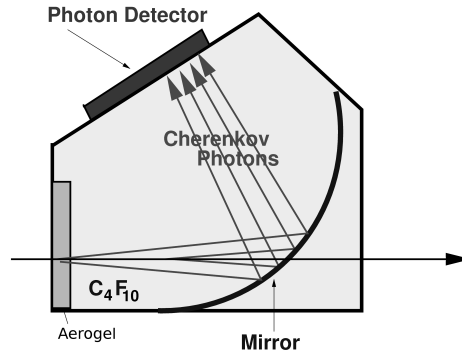


Figure 2.20: Schematic side view of the upper half of the proposed RICH detector.

A TOF wall acts as a stop counter 7 m downstream from the target. The TOF detector will be based on plastic scintillators, read out with photomultiplier tubes on both ends. The time resolution is expected to be approx. 50 ps. Furthermore, similar detectors will be placed inside the dipole magnet. This will give the possibility to detect low momentum particles which do not exit the dipole.

Forward electromagnetic calorimeter The electromagnetic calorimeter in forward direction is based on a Shashlyk-type detector. The principle is based on alternating lead and plastic-scintillator sheets. The design results in a compact detector, which reduces material costs. Furthermore, a plastic scintillator is a very fast active detector material. The fast response will be necessary in the forward region. The scintillation light is collected by several wave-length shifting fibers passing through all the sheets inside the detector block and coupled into photomultipliers. The lateral dimension of one supermodule is 110 mm x 110 mm with a length of 680 mm. This corresponds to 20 radiation lengths ($X_0 = 34.9$ mm). The Molière Radius inside the detector is $R_M = 59.8$ mm. The lead absorbers have a thickness of 0.275 mm and the scintillators of 1.5 mm, respectively. For a better spatial resolution, each supermodule is subdivided into 4 modules. Each module is equipped with an individual photomultiplier. For covering the desired forward acceptance, 351 such modules arranged in 13 rows and 27 columns at a distance of 7.5 m from the target are foreseen. With such

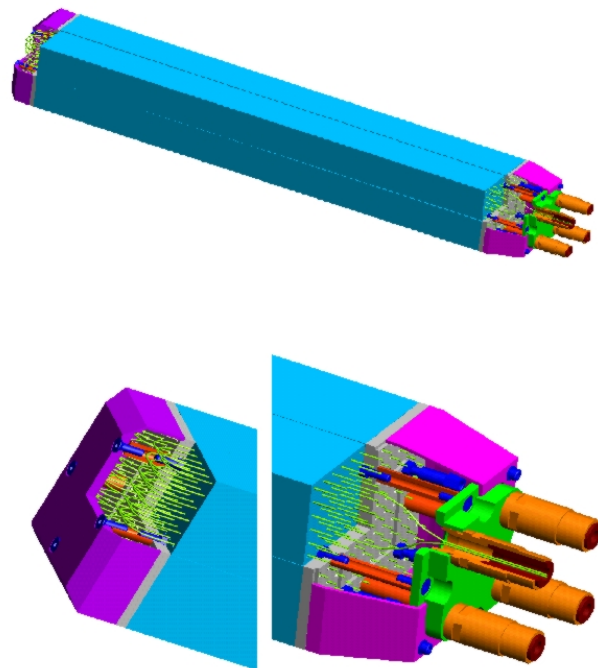


Figure 2.21: A single Shashlyk supermodule is comprised of 4 modules. Each module guides the scintillation light through fibers to a photomultiplier.

a type of detector previous experiments achieved energy resolutions in the order of $\sigma(E)/E = 4\%/\sqrt{E}$ [ATO04][ATO08].

Muon detectors For the detection of forward going muons, a further range tracking system is considered. It consists of interleaved absorber layers and rectangular aluminum drift tubes. The design is comparable to the muon detectors in the target spectrometer, but optimized for higher momenta. This detector will discriminate pions from muons, detect pion decays and will measure with moderate resolution the energy of neutrons and anti-neutrons. The muon system will be located 9 m away from the target.

Luminosity monitor Precise measurements of cross sections require a well defined luminosity for normalizing the reaction rate. For measuring the luminosity, elastic $\bar{p}p$ scattering events are considered. At small polar angles the cross section is dominated by the Coulomb component which simplifies calculations. Due to the finite size of the target, the position of the primary vertex is not exactly known. Therefore, the trajectory instead of a point must be measured. The luminosity monitor will consist of four sensor planes. Each plane is equipped with double sided silicon microstrip detectors placed inside a vacuum chamber. They will be sensitive in the range of 3-8 mrad. The luminosity monitor will be located 10-12 m downstream of the $\bar{\text{P}}\text{ANDA}$ target.

2.5 Triggerless data acquisition

The $\bar{\text{P}}\text{ANDA}$ data acquisition system is extremely ambitious. The basic conceptual design of the $\bar{\text{P}}\text{ANDA}$ detector offers a broad range of versatile experiments. Common trigger systems are fixed hierarchic structured. A subset of detectors is generating the first level trigger decision. The generated event may be passed to the next higher order trigger and finally to the data storage system. The main drawback of these hard wired structures is the lack of flexibility. Therefore a new DAQ¹⁴ concept is being developed, matched to the complexity of the experiment. In the new approach each detector component operates independently self triggered. The signals are preprocessed by

¹⁴DAQ = Data Acquisition

2.5 Triggerless data acquisition

FPGAs¹⁵ within the individual detector. After event detection, noise suppression and clustering, only the physically relevant information with a precise time stamp is passed on through buffers to the computing nodes. The final trigger selection is done by the computing nodes which access the buffers via a high speed network. The new concept provides high flexibly trigger algorithms beyond standard approaches. To enable this scheme, a continuous on-line calibration of all detectors is required. The data taking for experiments is therefore interleaved with calibration runs.

¹⁵FPGAs = Field programmable Gate Arrays

Chapter 3

PROTO 60

3.1 Design

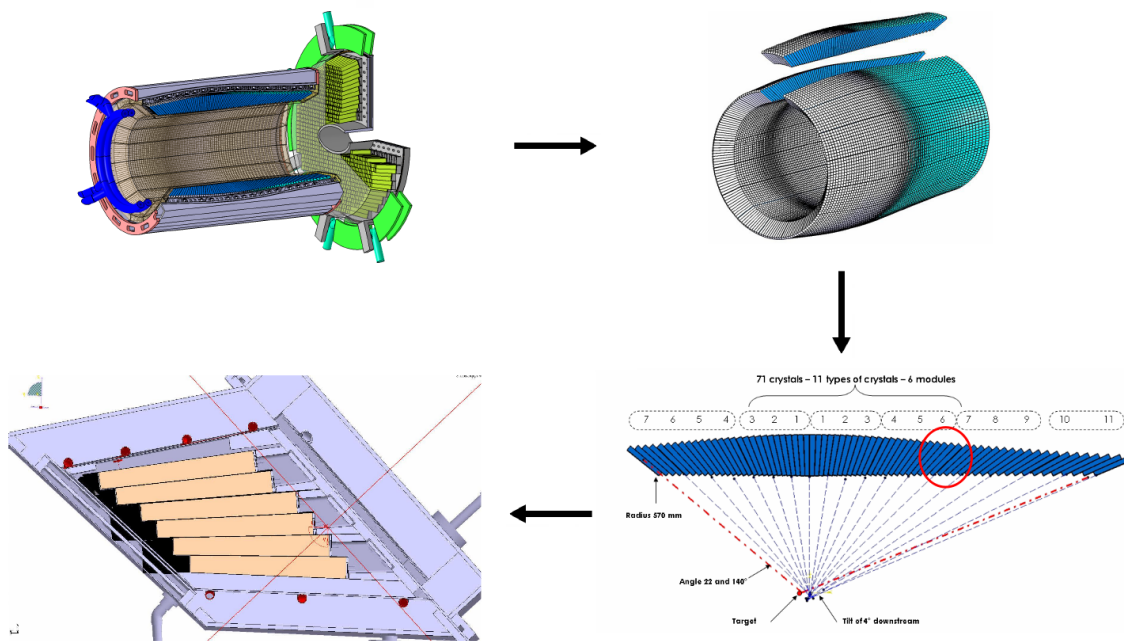


Figure 3.1: The prototype PROTO 60 (lower left picture) is derived from the barrel calorimeter design (upper left picture). The setup of the prototype crystal matrix corresponds to the red circle on the lower right picture.

The recent prototype of a selected part of the barrel calorimeter is the PROTO 60. The prototype consists of 60 type-6 L & R shaped PWO-II crystals (fig.2.7) arranged

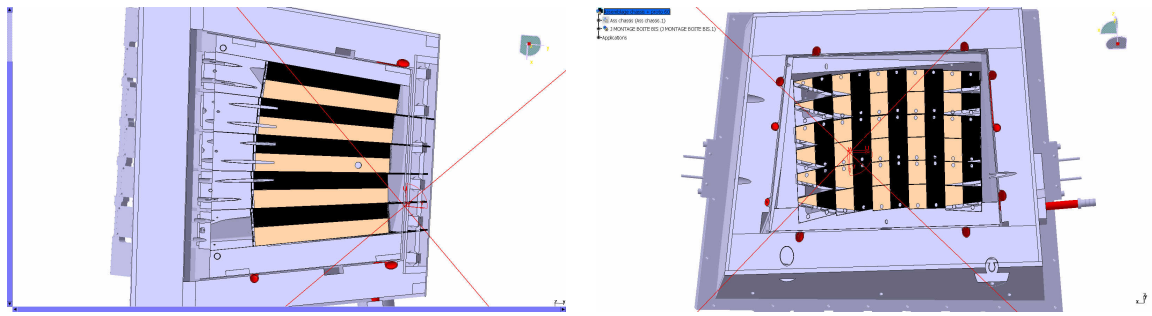


Figure 3.2: Schematic profile view of the PROTO 60 crystal arrangement from the top and front side. Due to the geometry of the barrel calorimeter, the PROTO 60 matrix has a convoluted arrangement.

similar to the corresponding barrel area (fig.3.1). The tapered crystals are staggered against each other (fig.3.1 and 3.2). The crystals are wrapped with a $63.5 \mu\text{m}$ thick reflective VM2000 foil for increasing the light output and assembled together to a group of four with polyethylene terephthalate tape. The scintillation light of each crystal is measured with a single $10 \times 10 \text{ mm}^2$ Hamamatsu LAAPD (S8664-1010SPL). The sensors are optically coupled to the crystal with the silicon grease Baysilone M300000 from Bayer (Leverkusen, Deutschland). This minimizes light loss due to transition between materials of different refractive indices. The LAAPD is held by a black plastic capsule which is fixed with adhesive tape (fig.3.3).

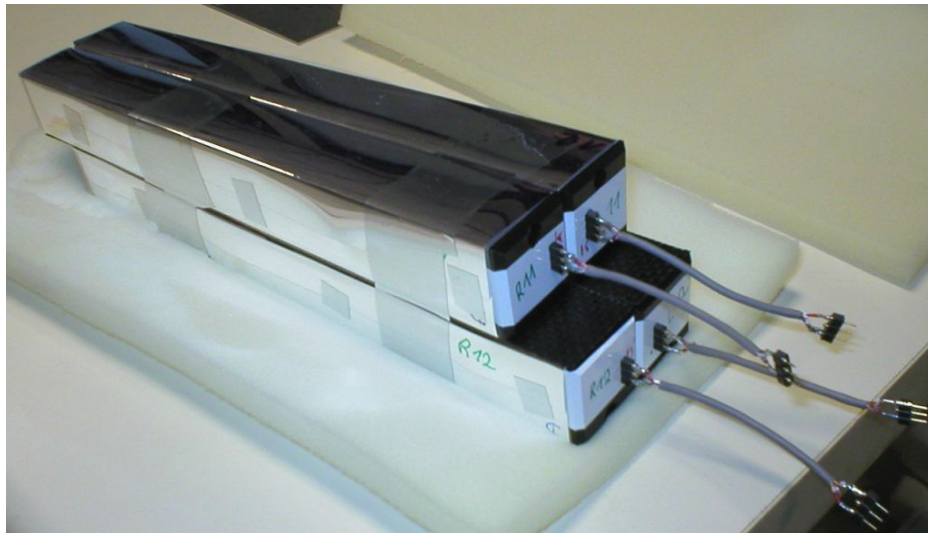


Figure 3.3: A group of 4 wrapped crystals is shown. The LAAPDs are hidden behind plastic capsules.

An overview of the used LAAPD properties can be found in tab. 3.1. Each crystal

Property	Value
Active area	10x10 mm ²
Quantum efficiency QE , $\lambda = 420$ nm	70 %
Dark current I_d , $M = 50$, $+25^\circ\text{C}$	≈ 50 nA*
Dark current I_d , $M = 50$, -25°C	≈ 5 nA*
Capacitance C	270 pF
Excess noise index F	0.2

Table 3.1: PROTO60 LAAPD properties (Hamamatsu S8664-1010SPL) [HAMP60], *[WIL].

group is placed in a stiff carbon fiber alveole with a wall thickness of 200 μm in order to avoid mechanical stress on the crystals. Including mechanical tolerances, the distance between the crystals summarizes to 0.68 mm. The structure, except the front and backside, is surrounded by aluminium panels followed by copperplates with mounted winding copper pipes for cooling. As a next layer, a 40 mm thick coating with styrene foam as insulating material is placed within the plastic chassis of the whole detector. A removable copper plate with glued rubber hoses for cooling and minimizing radiation interaction is used on the front face or the beam entrance side respectively. For temperature insulation on that side, vacuum can be created between two thin aluminum panels supported by carbon fiber structures within a plastic frame for mounting on the plastic chassis. This prototype for a vacuum insulation panel reduces the isolation thickness down to 20 mm. It has a thermal conduction coefficient lower than 2 mW/mK and keeps the outside well above the dew point.

The backside of the PROTO 60 is accessible as well. A picture of the opened detector can be found in fig. 3.4. In that picture on the lower left side, three of the aluminium inserts can be seen. In the final calorimeter, these flanges are glued to the alveoles, creating the connection to the mainframe for carrying the weight and place the crystals exactly inside their alveoles. The preamplifiers are mounted on top of the inserts. Each circuit board houses 4 preamplifiers which are connected to the LAAPDs by 25 mm long twisted pair wires. An elaborated description of the preamplifiers can be found in the next section. The circuit boards are still within the cooled volume to minimize the length of the wires and to reduce the electronic noise. Aluminium back plates screwed on the inserts and link the whole structure to the support frame. They have a

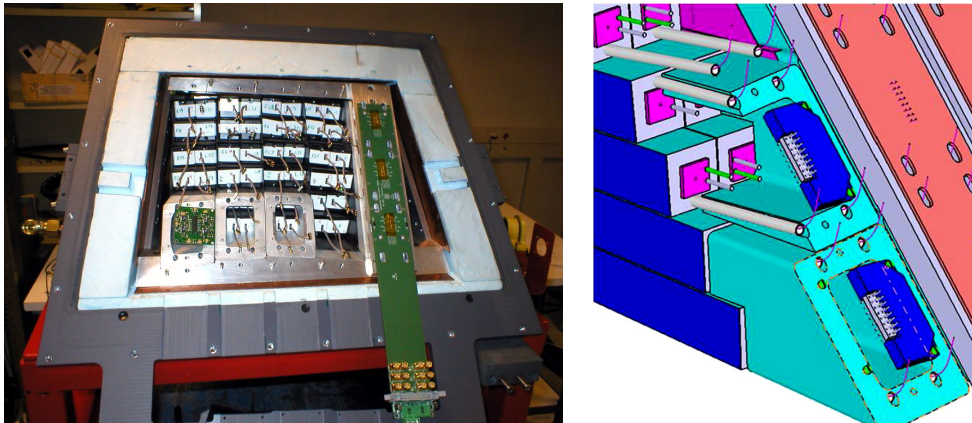


Figure 3.4: Backside of the opened and partly disassembled PROTO 60.

slot to pass the pin connectors of the circuit boards to backplanes. These backplanes feed the signals outside the cooled volume and pass the voltages for the LAAPDs and preamplifiers inside through narrow sealed slots in the insulation. The backside of the PROTO 60 case is closed by a plastic faceplate which contains winding copper pipes for cooling and insulating material as well.

A FP50-HL Julabo (Seelbach, Germany) cooling unit pumps a mixture of water and alcohol through all the cooling pipes and houses. The whole detector is constructed vacuum tight and during operation at typically -25°C flushed with dry nitrogen to avoid vapor condensation. Due to the temperature dependence of the light yield and LAAPD gain, the temperature is monitored by 13 sensors which are spread within the detector. During long term test measurements the obtained variation was in the order of $\pm 0.05^{\circ}\text{C}$ and is therefore negligible.

3.2 Preamps

Preamps are necessary to convert the weak charge pulses from the LAAPDs into voltage signals suitable for digitization. The conversion has to be linear. Due to the location inside the cooled volume, a low power consumption or power dissipation, respectively is needed. On one hand this will reduce the needed cooling power and on the other hand ensures a small temperature gradient within the crystal. To obtain a low energy threshold in the order of a few MeV the electronic noise has to be low.

3.2 Preamps

For this purpose the discrete charge preamplifier LNP¹ SP883a has been developed. For the PROTO 60 four of them are combined on one circuit board. A picture of the circuit board can be found in fig. 3.4 on the lower left side on top of a insert. The preamp has a 50 Ω output. It uses commercially available low-noise J-FET² transistors of type BF862 from NXP Semiconductors (Munich, Germany) combined with a low power, high speed current feedback operational amplifier AD8011AR made by Analog Devices (Munich, Germany). The circuit diagram can be found in fig. 3.5. The J-FETs are typically used in preamplifiers of car radio receivers. The noise level can be

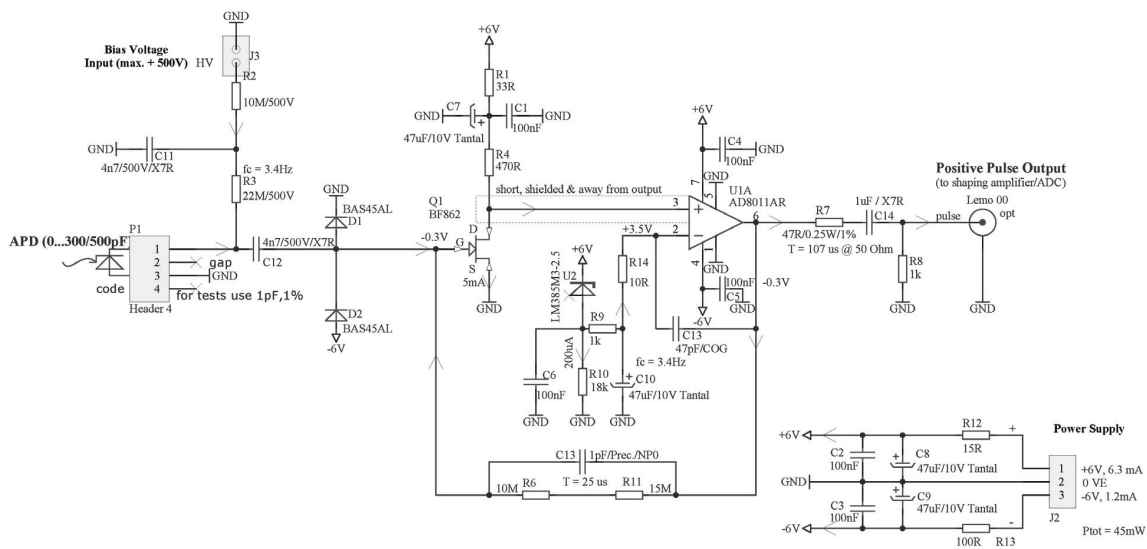


Figure 3.5: Circuit diagram of the SP883a. Picture taken from [PREAMP].

declared in detector signal equivalent noise charge (ENC). The PROTO 60 preamp produces an ENC of 1250 e_{RMS}^- at -25°C . Combined with a Hamamatsu S8664-1010SPL LAAPD at a gain of 50, measurements show in total 1700 e_{RMS}^- at -25°C . The LNP amplification corresponds to 0.5 V/pC. The maximum input charge of 4 pC will produce an output pulse of 2 V at 50 Ω [PREAMP]. Depending on the APD gain, the values of the dynamic range and the noise are equal to signals of different energy depositions in the crystal, which can be calculated.

The average type 6 crystal light yield of 18.7 phe/MeV at 18°C will increase to 67.32 phe/MeV at -25°C measured with a 2 inch bialkali photo cathode photomultiplier tube. This

¹LNP = Low-Noise low-Power charge preamplifier

²J-FET = Junction gate field-effect transistor

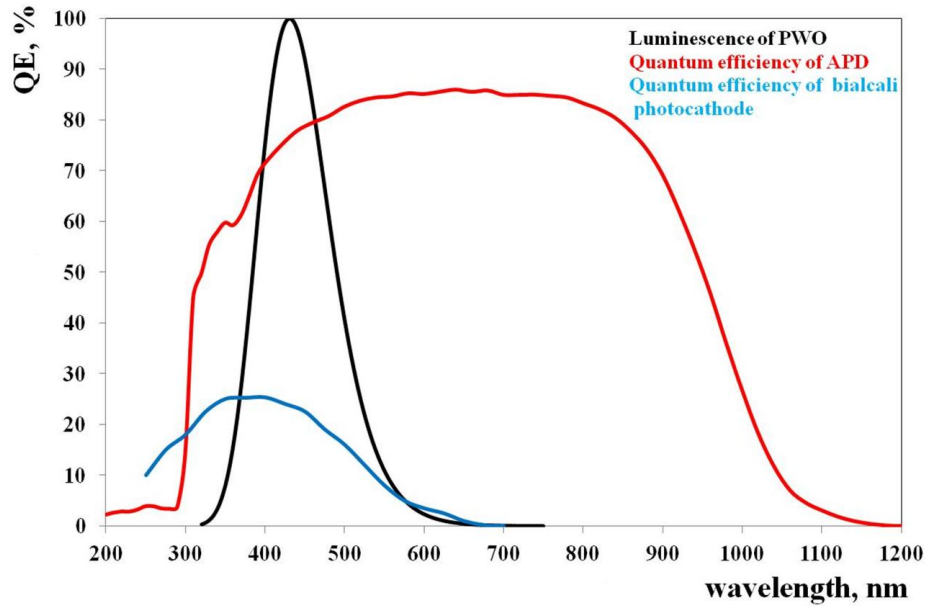


Figure 3.6: Comparison of the luminescence spectrum of lead tungstate with the quantum efficiencies of the PANDA LAAPD and the Photomultiplier used for the light yield measurements [HAMP] [HAMP60] [TDREMC].

tube has an quantum efficiency of 20% and covers the whole crystal endface. To derive a good approximation for the number of photoelectrons inside a LAAPD per MeV deposited energy in the crystal, the spectral distribution of scintillation light and quantum efficiency of the photo-sensors are taken into account. The integrals of the overlapping areas in fig.3.6 leading to an increased LAAPD quantum efficiency of

$$\int_{300nm}^{700nm} QE_{APD}(\lambda) \cdot LU_{PWO}(\lambda) d\lambda \div \int_{300nm}^{700nm} QE_{PMT}(\lambda) \cdot LU_{PWO}(\lambda) d\lambda = 3.5 \quad (3.1)$$

compared to the photomultiplier. Their active area covering only $\sim 13.6\%$ of the full endface which leads to 32.04 phe/MeV for the LAAPD at -25°C . Recent measurements indicate a quantum efficiency up to 80% [WIL] which will lead to 36.62 phe/MeV in this calculation. Depending on the LAAPD gain the values for the noise and dynamic range of the preamp is summarized in table 3.2. As a trade-off between noise and pile-up probability, the rise time of the output signal is 18 ns and the feedback time constant 25 μs .

Gain	Preamp noise / MeV		Max. single crystal en. / GeV	
	QE=70%	QE=80%	QE=70%	QE=80%
50	1.06	0.93	15.58	13.63
100	0.53	0.46	7.79	6.82
150	0.35	0.31	5.19	4.54
200	0.27	0.23	3.9	3.41

Table 3.2: Preamp estimations concerning noise and dynamic range.

Chapter 4

GEANT4

GEANT4¹ is a toolkit environment for simulating the passage of particles through matter with Monte Carlo methods. These methods are based on random sampling of physical interactions with respect to their probability. It is developed within an international collaboration mainly at CERN, utilizing the object oriented C++ language. The simulation includes optical, hadronic and electromagnetic processes based on theory, data or parameterization. Furthermore, a comprehensive set of particles, elements and materials is included. It is used for a broad range of applications such as medical physics, high energy physics, astrophysics, nuclear physics, accelerator design, space engineering and radiation protection in the energy range from a few hundred eV up to the PeV range. GEANT is a standard instrument for the development of new detector systems like $\bar{\text{P}}\text{ANDA}$. On the one hand, design considerations can be optimized easily and cost effective, for example the influence of absorbing material from other detector components on the calorimeter performance. On the other hand GEANT is an useful aid for the data interpretation obtained within real experiments. Therefore a detector design process is an iterative interplay between the simulation models and prototype experiments.

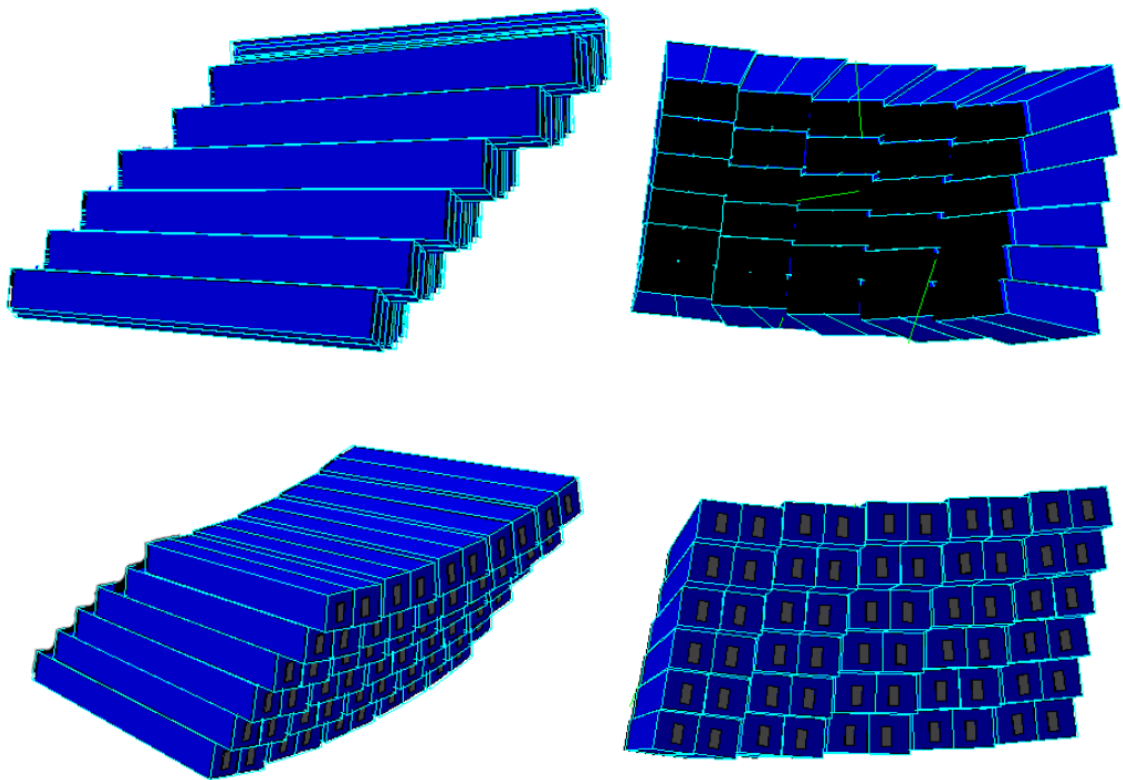


Figure 4.1: PROTO60 GEANT model

4.1 The PROTO 60 model

The PROTO60 GEANT geometry is manually derived from CAD² drawings. The crystal type 6 geometry was created once as described in fig. 2.7 with the G4Trap class. Within GEANT its material is composed out of three components: four oxygen, one lead and one tungsten atom with their individual molar masses and a total density of 8.28 g/cm. As an approximation for the reflector material and the alveole, the crystal is wrapped with a 264 μm thick layer of carbon with a density of 2 g/cm³. The obtained module is copied, rotated and placed precisely to the 60 positions taken out of the provided CAD drawings. The setup is placed inside a large experimental hall filled with air to mimic real experiment conditions. The air is composed as an approximation out of 70% nitrogen and 30% oxygen with a density of 1.29 mg/cm³. This will take into account pair production by high energetic gammas traversing the air between the end of an accelerator beam pipe and the detector.

4.1.1 Implementation of non-uniform light collection

Due to the tapered crystal shape, a focusing effect causes that the collected fraction of the scintillation light created near the smaller crystal front is larger than the collected fraction near the photo sensor. This feature has an impact on the detector characteristic and therefore needs to be implemented into simulations. Especially for the PROTO60 detector calibration with cosmic radiation for beam test measurements, the influence becomes relevant. The cosmic radiation traverses the entire crystal in contrast to a photon-beam of lower energy which deposits its energy mostly in the frontsection of the crystals. GEANT provides the ability to simulate the scintillation process and the corresponding optical photon tracing through the materials. Such simulations are intensive in computing time, especially for high energies. Besides the long computing time, PbWO_4 is a birefringent material which is not yet supported by the software. Furthermore, macro defects have to be considered for the optical photon tracing. They are indicated by scattered light from a laser shining through the material (fig.4.3). To obtain however a simulation model with properties close to realistic crystals, a more practical approach was considered. A experimental program

¹GEANT = Geometry and Tracking

²CAD = Computer-aided Design

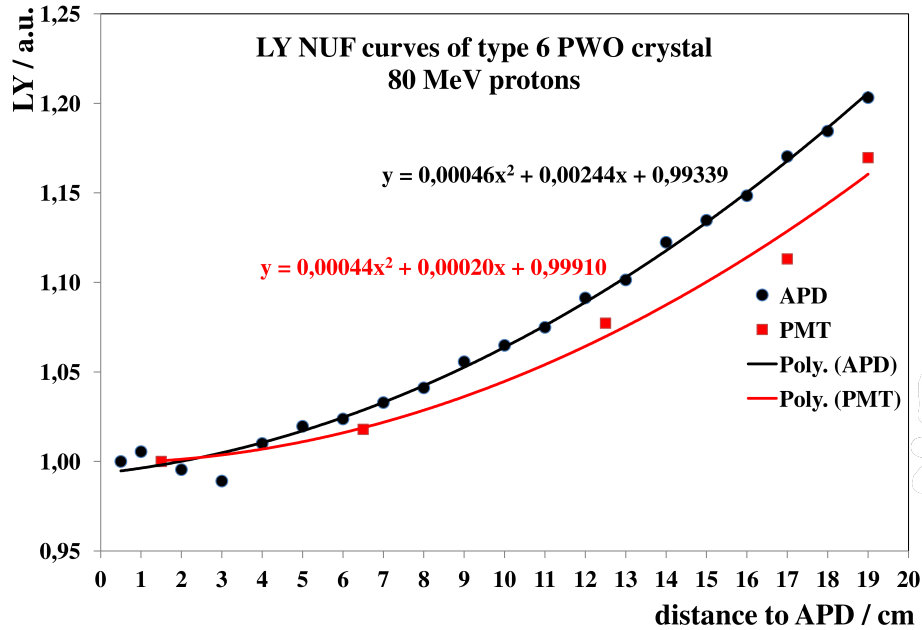


Figure 4.2: Measurement of nonuniform light collection of a type 6 crystal at KVI. Adapted from [BRE13].

was performed which investigated in detail the light collection for all PANDA crystal shapes. The closest approach with respect to the PROTO60 was performed at KVI³ Groningen. A 80 MeV proton beam with 2 mm diameter was used to scan a type 6 crystal perpendicularly to the crystal axis with respect to the light collection. The crystal was equipped with a LAAPD as used for the PROTO60 and wrapped with the similar reflector material VM2000. The obtained data (fig.4.2) shows a signal increase of $\sim 22.6\%$ between the two ends of the crystal. If the signal (LY_n) is normalized to 1 at the LAAPD side, the non uniformity can be fitted with:

$$LY_n(d) = 0.00046 \cdot d^2 + 0.00244 \cdot d + 0.99339, \quad (4.1)$$

and d given in cm. Within GEANT the simulation of an event, like a single photon impinging on the detector, is basically divided into many interaction steps. Among other information for each step the information about position and the local energy deposition $E_{step}(z)$ can be received. Combined with an aligned coordinate system within the crystal, the deposited energy of each step can be weighted according to the formula 4.1 depending on the crystal depth. By summing up E_{step}^* , the weighted

³KVI = Kernfysisch Versneller Instituut

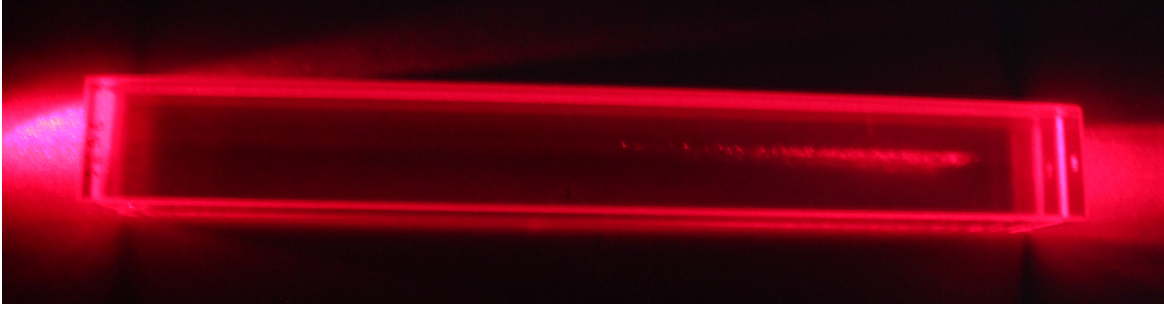


Figure 4.3: A laser beam through a PANDA PWO-II crystal. The inside scattered photons indicate macro defects within the crystal.

energy of each step within a single crystal, the total weighted crystal energy can be retrieved:

$$E_{crystal}^* = \sum E_{step}^* = \sum E_{step}(cm) * LY_n(cm). \quad (4.2)$$

The number of photoelectrons can be obtained with

$$N_{phe} = E_{crystal}^* \cdot \frac{32.04 \text{ phe/MeV}}{LY_n(20 \text{ cm})}. \quad (4.3)$$

The second factor of the product 4.3 gives the light yield at the side of the photo-sensor, after the normalization. This simulation model referred to as PROTO60-NUF⁴-model can for example be used to obtain a better relative detector calibration. To reproduce the real detector response, the excess noise of the LAAPD and electronic noise of the preamp have to be considered in addition. For implementing photon statistics, the LAAPD excess noise and the preamp noise within the simulation, N_{phe} are weighted with a Gaussian distribution according to eq. 2.20. The precise relation between the operation voltage and the gain for the PROTO60 LAAPDs and the resulting excess noise factor is unknown at -25° C. As described in chapter 5.3 the gain can be estimated to be in the order of 150, which corresponds to an excess noise factor of 2.72 (eq. 2.19). The preamplifier noise is equal to $\sigma_{pre} = 0.25 \text{ MeV}$ deposited energy, in anticipation of chapter 5.4.3. By including this signal broadening the PROTO60-NUF-NOISE model is obtained.

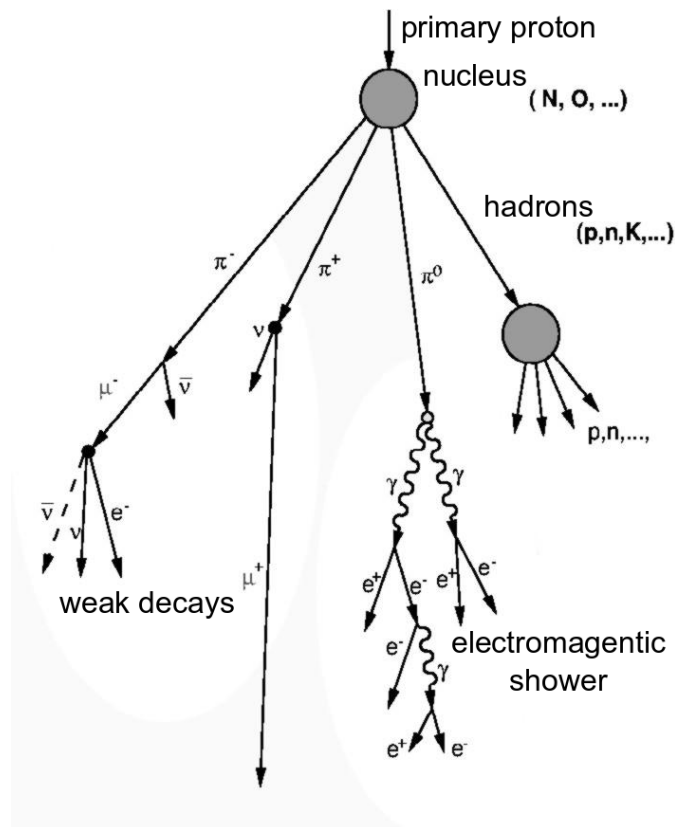


Figure 4.4: Cosmic shower generated by a high energetic proton interacting with a nucleus of the atmosphere.

4.2 Cosmic radiation

As mentioned before, the everywhere available cosmic radiation can be considered to calibrate a calorimeter. Due to their complex energy and angular distribution in combination with a sophisticated detector geometry like the tapered crystals in the PROTO60 with a non uniform light collection, a precise simulation is needed. The cosmic radiation is generated by high energetic particles like electrons, protons or complete nuclei accelerated at astrophysical sources, interacting with the terrestrial atmosphere (fig.4.4). The major fraction of about 79% are protons and 70% of the remaining particles are helium nuclei. Due to diffusion in galactic magnetic fields, this radiation is nearly isotropically distributed in outer space. The distribution of its energy per nucleon in the range from several GeV up to a few hundred TeV energy

⁴NUF = Non-uniformity

per nucleon (including rest mass) can be approximated by:

$$I_N(E) \approx 1.8 \cdot 10^4 \left(\frac{E}{1 \text{ GeV}} \right)^{-\alpha} \frac{\text{nucleons}}{\text{m}^2 \cdot \text{s} \cdot \text{sr} \cdot \text{GeV}} \quad (4.4)$$

where $\alpha = 2.7$ is the differential spectral index of the cosmic ray flux [PDG12]. If a high energetic cosmic particle interacts with the atmosphere through elastic and inelastic scattering, particles like pions, kaons or neutrons are created.

At sea level, muons are the predominant charged particles besides electrons or protons. They are generated via the decay of the charged mesons:

$$\pi^+ \rightarrow \mu^+ + \nu_\mu \quad (4.5)$$

$$\pi^- \rightarrow \mu^- + \bar{\nu}_\mu. \quad (4.6)$$

Most of the muons are typically produced at about 15 km above sea level. Their mean lifetime is $2.2 \cdot 10^{-6}$ s within their rest frame. Due to relativistic effects, a large part can reach sea level. A created muon with 2.4 GeV energy traverses 15 km in vacuum. Due to energy loss via ionization of the atmosphere, the mean path is reduced to 8.7 km. The mean energy of muons reaching the sea level is about 4 GeV. The measured velocity distribution can be found in figure 4.5. Below 1 GeV, which is not shown, the distribution is nearly flat. Well above 100 GeV the pions can lose their energy by interaction with the atmosphere before they decay into muons, therefore the velocity distribution decreases. Low energetic muons decay before they arrive at the surface at large angles (\diamond in fig.4.5). Therefore the average muon velocity increases here. Generally the angular distribution of the muons follows $\cos^2 \theta$.

The energy distribution and angular dependence for electrons depends on the altitude. Their main origin at sea level are muon decays. They provide mostly low energetic electrons. At high altitudes, π^0 are the main source. Occasionally a primary cosmic proton reaches the surface with energies above 1 GeV. About 1/3 of the nucleons found at sea level are neutrons.

To simulate the total energy deposited in the crystal for various particles, a cosmic ray shower generator (CRY) was implemented in GEANT. It allows to simulate full cosmic ray particle shower distributions at sea level in the energy range of 1 MeV up to 100 TeV for muons, neutrons, protons, electrons, photons and pions. The latitude can be specified due to the impact of the earth's magnetic field on primary cosmic

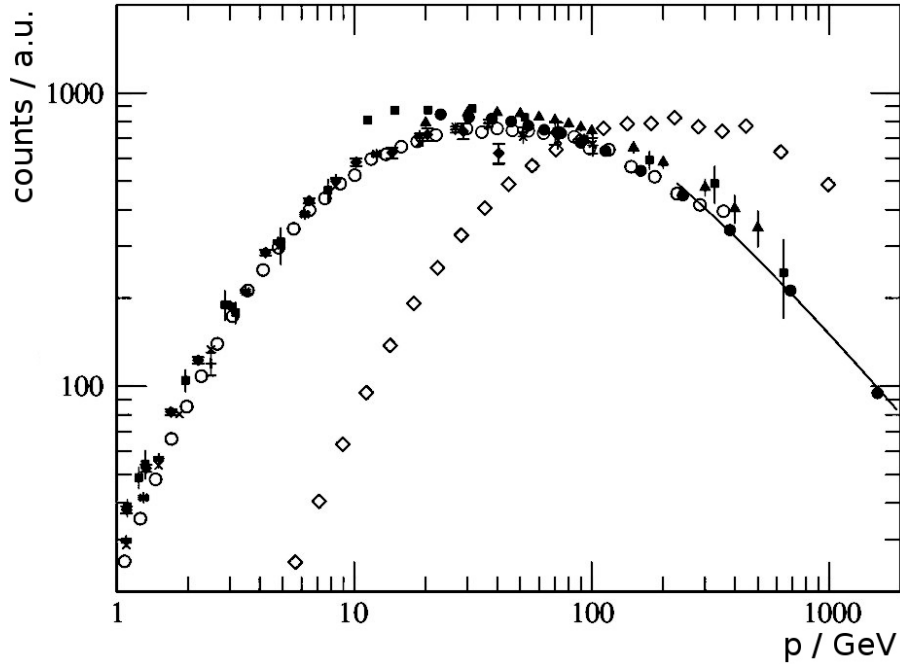


Figure 4.5: All data points showing the velocity spectrum of muons at $\theta = 0^\circ$, except \diamond which are for $\theta = 75^\circ$. Data taken from [PDG12].

particles in particular in case of the low energy spectrum of the primary cosmic-ray particles. It is implemented as a cutoff (E_{min}) on the energy of the primary cosmic protons. The latitude L dependence of E_{min} , where L is in degrees and the zenith angle is 90° , is given by the approximation from [CO83] and [DO09]:

$$E_{min} = 18.8 \cos^4(\pi L / 180^\circ). \quad (4.7)$$

The generator is based on lookup tables. These tables are generated by full simulations of protons hitting the earth's atmosphere, starting at an altitude of 31 km in the range of 1 GeV - 100 TeV. The atmosphere is approximated by 42 constant-density layers. Each layer is composed out of 78% N_2 , 21% O_2 , and 1% Ar of the volume. The density of the layers are derived from the 1976 US Atmosphere Model. Lookup tables for discrete quadratic boxes on the surface with the size of 1, 3, 10, 100 and 300 m^2 are generated. For box sizes in between, the next largest table will be utilized. Particles outside of the specified window are ignored. The obtained simulation is in good agreement to published experimental data (fig.4.6) [CRY].

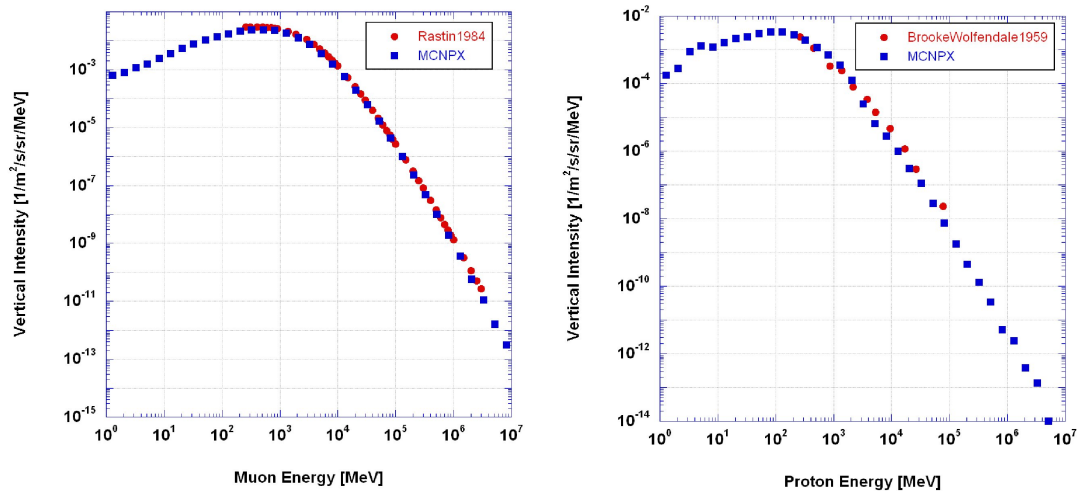


Figure 4.6: Comparison of the full atmosphere simulation of muons and protons at sea level (blue data points) with published data. Pictures are taken from [CRYP].

Chapter 5

Experiment at MAMI

In order to investigate the performance of the planned \bar{P} ANDA barrel calorimeter, two test measurements in the A2 experimental hall at MAMI¹ were performed. Due to similarities, both experiments will be presented together within this chapter.

The first experiment served to verify the principle detector concept over the full available MAMI energy range up to 1.5 GeV to confirm the required energy resolution.

The second similar experiment at a lower energy regime was investigating in addition the impact of the material budget of other detector components in front of the \bar{P} ANDA barrel calorimeter on the performance of the detector, in particular in the lower MAMI energy regime down to 52 MeV. The main contribution is expected from the DIRC detector due to the 1.7 cm thick SiO₂ bars for the barrel or the 2 cm disc DIRC at forward direction. The degradation of the energy resolution due to a proposed TOF detector (7% X_0) was included as well.

The high quality electron beam from the accelerator in combination with the Glasgow Tagged Photon spectrometer (Tagger) was used to generate an energy tagged bremsstrahlung photon beam. The measurements were performed with the PROTO 60 in combination with tagged gammas in the energy range of 52.34 MeV and 1.5 GeV, respectively .

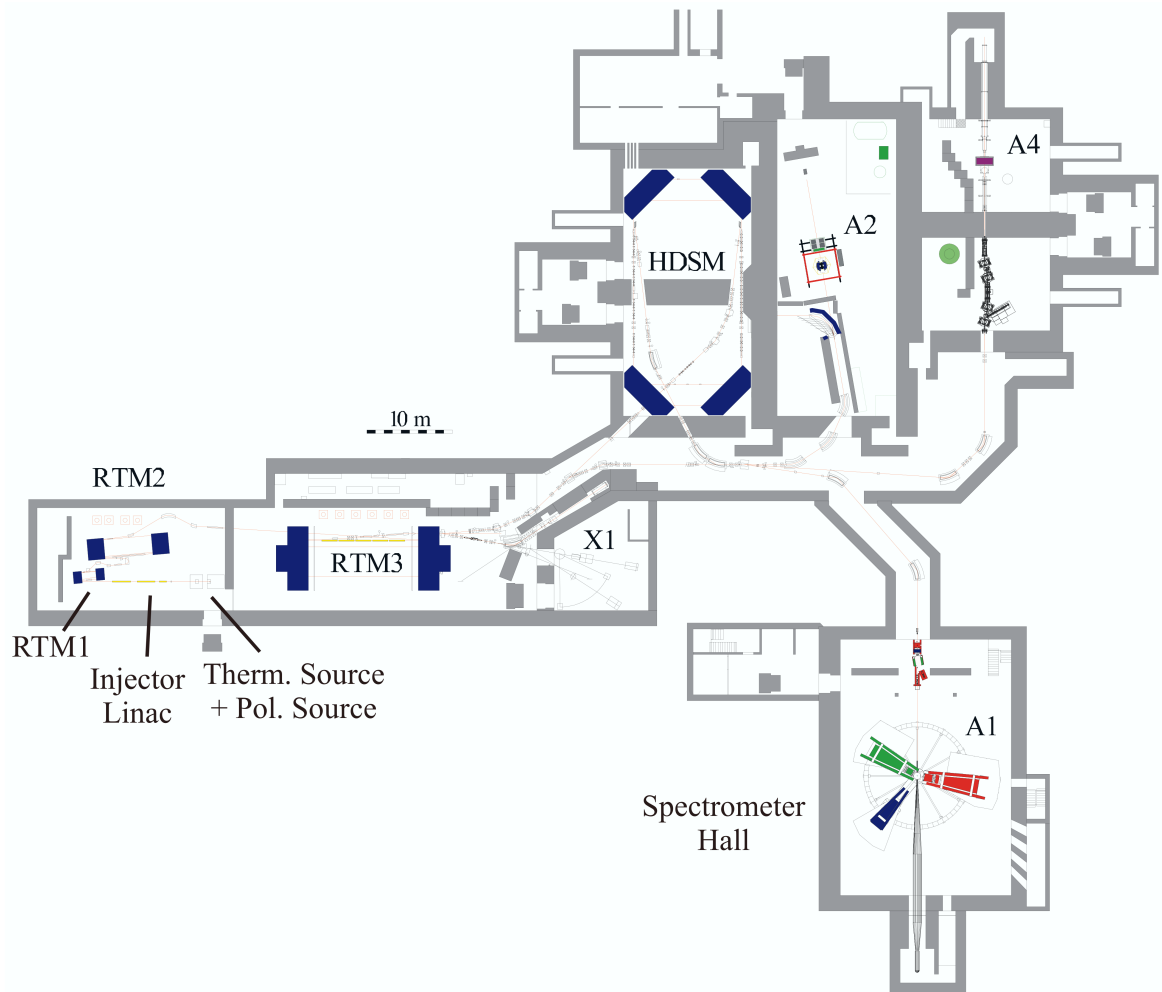


Figure 5.1: Floor plan of the MAMI-C accelerator facility including the experimental halls A1, A2, A4 and X1. Picture taken from [JAN06].

5.1 The electron accelerator MAMI

As a result of a recent upgrade of MAMI (MAMI-C), the accelerator provides electrons up to 1.508 GeV as a continuous beam current up to $100 \mu\text{A}$ with a duty factor of nearly 100 %. The beam can be delivered to the experimental halls A1, A2, A4 and X1, situated at the KPH-Mainz research facility. For the injection of electrons, a thermoionic 100 keV DC-gun is used followed by a 3.46 MeV linear accelerator. The electrons are accelerated by three racetrack microtrons arranged in series followed by a

¹MAMI = Mainzer Mikrotron

5.1 The electron accelerator MAMI

harmonic double-sided microtron. Figure 5.1 shows the floor plan of the facility. Inside a racetrack microtron (fig.5.2) the electron beam is deflected by two dipole magnets with a constant magnetic field. Each magnet deflects the beam approx. 180° . In each turn the recirculating beam is guided through a single linear accelerator. It uses high frequency of about 2.45 GHz within normal conducting structures to provide an energy gain of several MeV per cycle. According to the stepwise increase of the electron energy the radius of curvature of the circulating beam rises. To ensure that the electrons stay within the same phase of the alternating voltage in the linear accelerator section, the traveling time for each cycle has to match an integer multiple of the period of the accelerator frequency. Racetrack microtrons have an inherent phase correction. If the energy of individual particles is slightly higher or lower than the energy of their corresponding cycle, their deviating path length leads to a difference in the arrival time at the linear accelerator section. This time difference causes an energy correction due to the fact that the electrons enter the high frequency with a different phase. The electrons are accelerated depending on the phase.

Finally, when the electrons reach a certain energy, a small so called kicker magnet ejects them out of the microtron into the beam handling system. 180 MeV are ob-

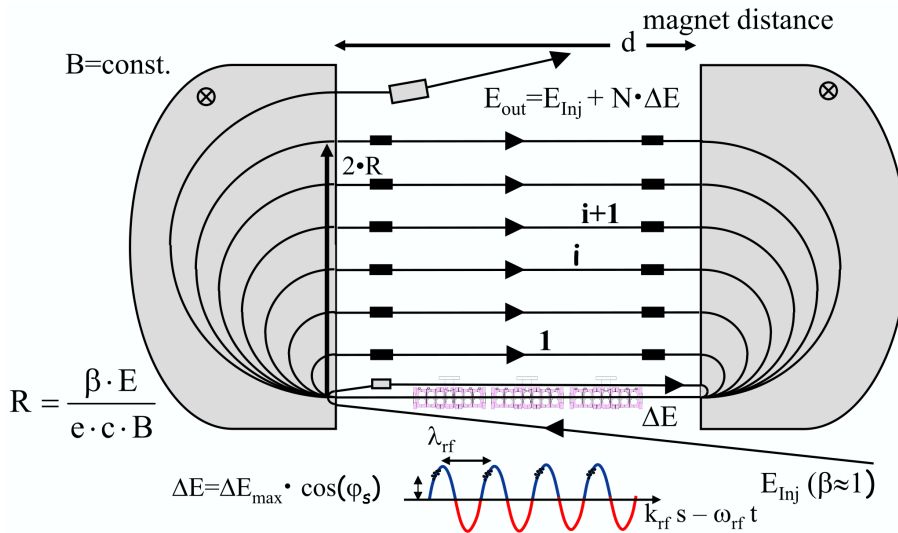


Figure 5.2: Basic setup of a racetrack microtron. Picture taken from [JAN06].

tained by the electrons after the second microtron and 855 MeV after the third. The double-sided microtron, not used for the second experiment, increases the energy up to the maximum facility energy. The working principle is comparable to the racetrack

microtron. The differences are that the two dipole magnets are split into four in order to decrease their weight and 2 linear accelerators, one operated at 2.45 GHz and the other at 4.9 GHz opposing each other.

5.1.1 Production of energy tagged photons

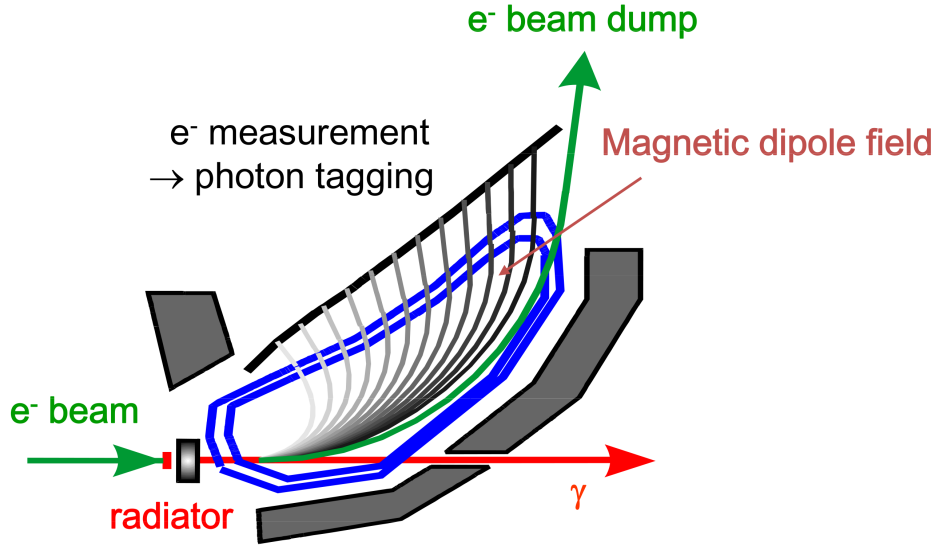


Figure 5.3: The Glasgow Tagging system. Picture taken from [BERG10].

At the MAMI facility photons can be created by the electron beam passing through a thin metal foil. Due to the Coulomb field of the nuclei, the momentum of the electron changes and bremsstrahlung is generated. The energy distribution follows $\frac{1}{E_\gamma}$. According to Leroy et al. [LE09], these photons are emitted in the original beam direction with an opening angle of the beam cone of approximately

$$\Theta \approx \frac{m_e}{E_e} \quad (5.1)$$

with m_e the rest mass and E_e the energy of the electron. In order to ensure a small diameter a set of collimators can be placed 2509 mm downstream the radiator. After passing the radiator foil, the remaining momentum of the electron is measured with the Glasgow photon tagging spectrometer, short Tagger (fig.5.3). The spectrometer uses a magnetic dipole field. Due to the Lorentz force the trajectory of the electrons is bend towards a focal plane or in case of no interaction with the radiator into a beam

dump. The point of impact depends on the remaining momentum. The momentum p_e of the electron with the charge q can be calculated with:

$$p_e = R \cdot q \cdot B \quad (5.2)$$

if the magnetic field B and the curvature R is known. To measure the point of impact, the focal plane is equipped with a ladder composed of 353 plastic scintillators. Each detector, 24 mm wide and 2 mm thick, is overlapping with half of its neighbor and read out with a photomultiplier tube. By demanding a coincidence of two scintillators, the background can be suppressed. The energy E_γ of the photon can be calculated from the energy of the deflected electron E_{e^-} and the initial beam energy E_0 with:

$$E_\gamma = E_0 - E_{e^-}. \quad (5.3)$$

This assumes that no energy is transferred to the radiator atoms. The probability of transferring less than 2.5 keV is 99 % [KRU95]. Via a coincidence between the detector of an experiment (the PROTO 60 for example) and the individual channels of the Tagger, nearly mono energetic photons are selectable out of the bremsstrahlung spectrum. The energy resolution of the Tagger, and therefore the width of the tagged photons is in the order of ≤ 3 MeV depending on the energy.

5.2 Experimental setup

For the first beam-time, the PROTO 60 setup including data acquisition, power supply, nitrogen for detector flushing and a vacuum pump was placed downstream of the local detectors Crystal-Ball and TAPS². For the second beam-time, a comparable setup (fig.5.4) was placed in-between the Crystal-Ball and TAPS. The PROTO 60 was mounted on top of a computer controlled movable table. By using fixed reference points together with a laser, the detector was positioned parallel to the beam line with respect to the center axis of the PROTO 60 crystal matrix. The center is located between the crystals 25, 26, 35 and 36 (fig.5.5).

Within the Coulomb field of any nucleus on the trajectory of the photon-beam, charged particles can be created by the reaction $\gamma \rightarrow e^+e^-$. For their detection a plastic detector wrapped with reflector material and shrinking tube was placed in front and

²TAPS = Two Arms Photon Spectrometer

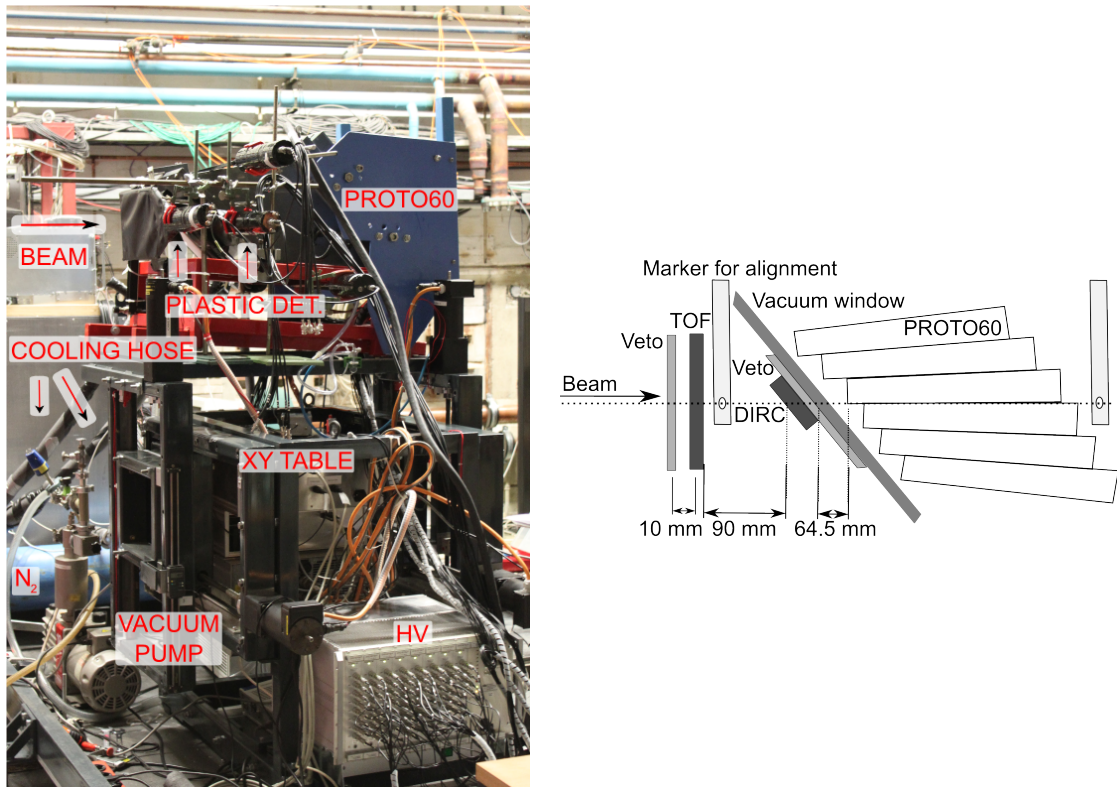


Figure 5.4: Experimental setup at MAMI A2. In order to measure the impact of insensitive material on the PROTO 60 energy resolution a 24.5 mm Plexiglas, simulating the material budget of a TOF detector, and an original piece of DIRC quartz are placed between two plastic detectors.

10	9	8	7	6	5	4	3	2	1
20	19	18	17	16	15	14	13	12	11
30	29	28	27	26	25	24	23	22	21
40	39	38	37	36	35	34	33	32	31
50	49	48	47	46	45	44	43	42	41
60	59	58	57	56	55	54	53	52	51

Figure 5.5: The numbering of the PROTO 60 crystals from the beam perspective.

read out with a photomultiplier tube. In the second experiment, 2 plastic detectors were used. The first one measured conversion caused by the air between the tagger radiator and the PROTO 60 and served as a veto detector. The second one, which was placed directly on the vacuum insulation panel, detects additional conversion within the optional passive material between the two plastic detectors. For the material, a sample of the DIRC quartz bar (SiO_2 , 20 mm thick) was provided by the corresponding working group. The distance between the crystals of the PROTO 60 and the vacuum insulation panel is larger than the distance within the final \bar{P} ANDA detector between the DIRC detector and the barrel calorimeter crystals. The DIRC detector has a distance of 50 mm to the barrel calorimeter crystals. The vacuum insulation panel has already a distance of 64.5 mm. Therefore the quartz bar was mounted directly on the second plastic detector. A 24.5 mm thick Plexiglas sheet ($\rho = 1.19 \text{ g/cm}^{-3}$, $X_0 = 40.55 \text{ g/cm}^{-2}$) with a radiation length of 7.2 % was used to simulate the material budget of a proposed TOF detector. It was placed right before the alignment marker due to space limitations.

5.2.1 Data acquisition

Figure 5.6 depicts the schematic of the data acquisition. The digitization of the energy information is started by a gate-signal. This signal can be generated by a test pulser,

Chapter 5 Experiment at MAMI

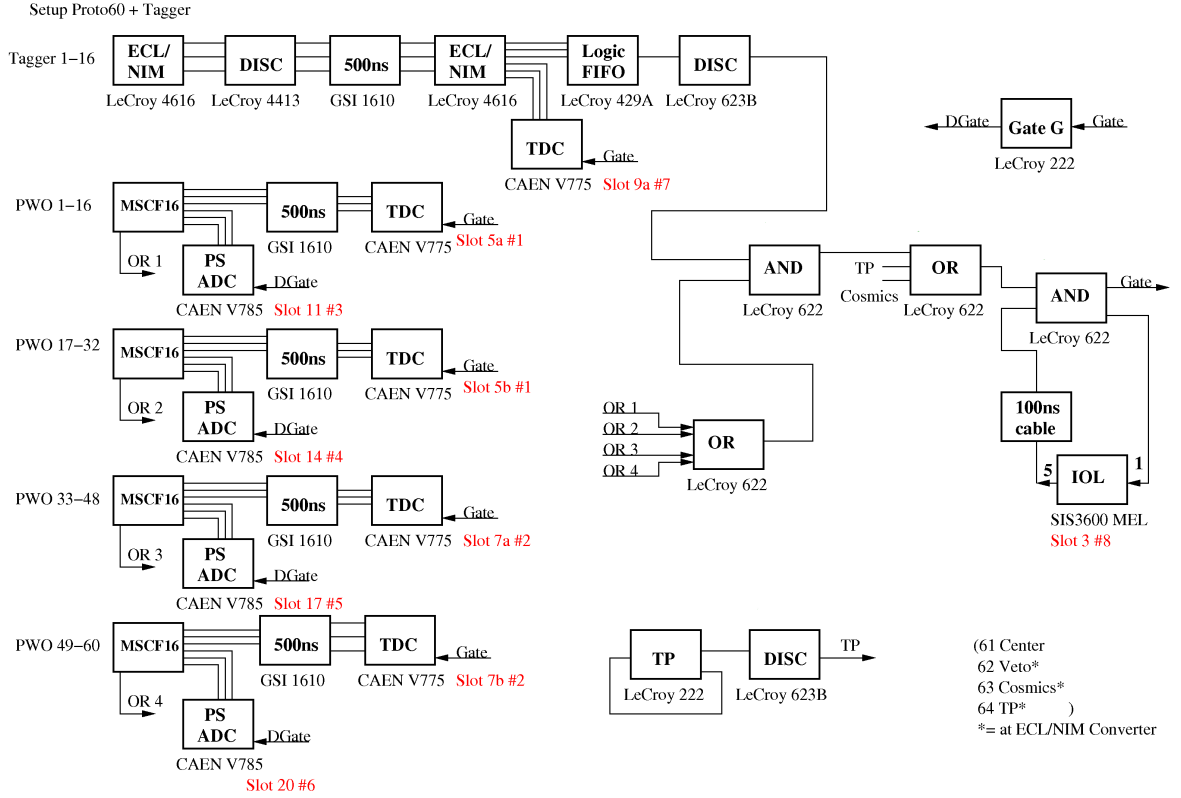


Figure 5.6: Schematic of the data acquisition at MAMI during the second beamtime. The only difference during the first beamtime was a coincidence between the tagger and exclusively the central crystal.

a cosmic trigger or a coincidence between any PROTO 60 crystal and an logical OR of all chosen tagger channels.

- The test pulser with a selectable rate serves for the measurement of the noise level (Pedestal), in order to obtain the zero level within the energy calibration.
- The cosmic trigger is generated by an logical AND between any crystal out of the top and any one out of the bottom row of the crystal matrix.
- In order to obtain the energy information by the Tagger, all chosen Tagger signals are split into two branches. One branch feeds the Tagger OR for the gate generation, the other branch is fed into TDCs³. These TDCs digitize the time difference between the gate and the tagger signal.

³TDC = Time to Digital Converter

The signals of the PROTO 60 preamplifiers are treated inside MSCF16 modules which are a combination of spectroscopy amplifiers and CFDs⁴. The signals of the spectroscopy amplifiers, integrated over an integration time of $\tau = 1 \mu\text{s}$, are fed into the CAEN (Viareggio, Italy) V785 peak sensing ADCs⁵. The dynamic range of each input corresponds to 3860 channels. The time difference between the CFD signals and the gate signal is measured by additional TDCs. The signals of the plastic detectors are processed similarly, except they are excluded from the gate generation. For each event, the following parameters are recorded onto the hard disc:

- Energy information of each crystal and both plastic detectors.
- Time information for the same detectors and the Tagger channels.

5.2.2 LAAPD high voltage adjustments

The high voltage settings for the LAAPDs were similar during both beamtimes. They were once adjusted using a stabilized light pulser system and the energydeposition of cosmic radiation. A description of the light pulser will be given in chapter 7. The light pulses are fed into the crystals via optical fibers (fig.5.7). The LAAPD manufacturer Hamamatsu provides the individual voltages for a gain of 50 at room temperature. By comparing the signals of the light pulses after the PROTO 60 preamps and subtracting the Pedestals, the voltages at -25°C for a gain of 50 and 150 are determined. As a next step, cosmic radiation was measured for both gains. The most probable value of the energy deposition of the cosmic radiation within a few modules indicated inconsistencies. The deviations of the peak positions are much larger than expected due to the typical differences in the crystal light yield. Therefore, and with respect to the transversal shower of 1.5 GeV photons, the voltages of each LAAPD was set to cover a dynamic range of approximately 200 MeV with the DAQ. The adjustment delivers a rough pre-calibration of the detector. On average, the cosmic peak position for the measured gain of 150 and the cosmic peak position for the desired dynamic range are comparable (tab.8.3). Therefore, the used gain can be specified with 150. A principal description of the cosmic data analysis is given in chapter 5.4.2.

⁴CFD = Constant Fraction Discriminator

⁵ADC = Analog to Digital Converter

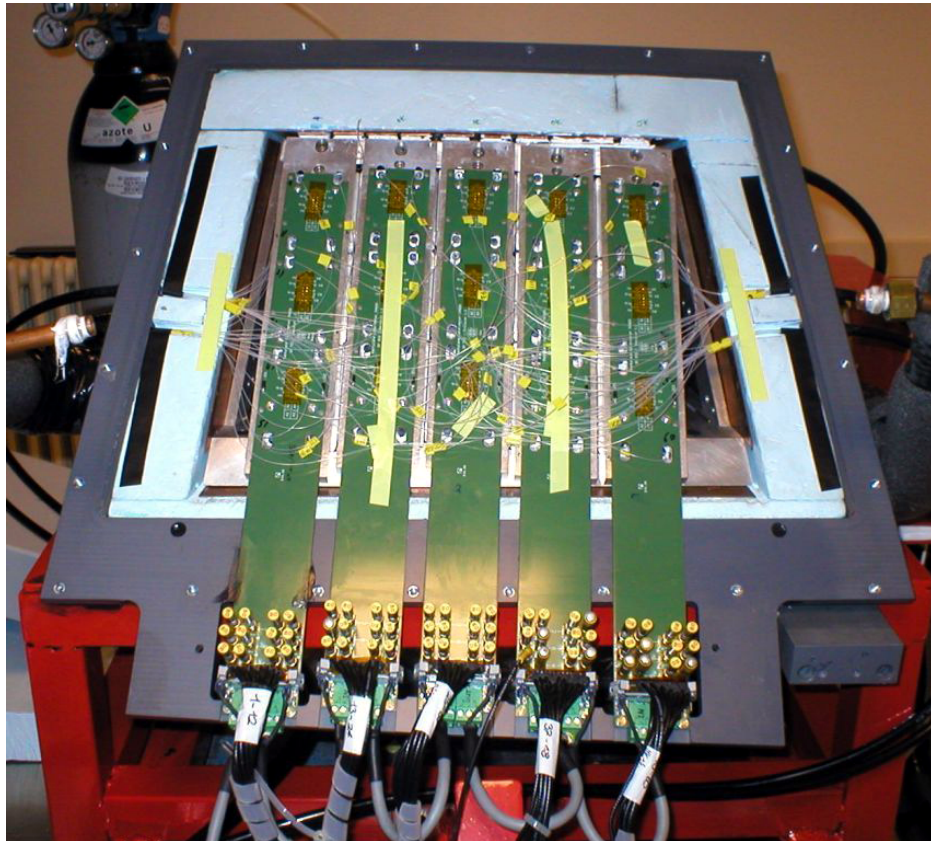


Figure 5.7: Partly assembled PROTO 60 with additional optical fibers. They are fed through a hole of the crystal's plastic capsules and connected to the crystal's backside.

5.3 Experimental procedure

In order to obtain a stable operating state of the PROTO 60 at $-25\text{ }^{\circ}\text{C}$, the whole setup was put into operation a few days before. For the beam measurements, the PROTO 60 was moved with the XY table until the beam impinged on the center of crystal 35. Due to the limited dynamic range of the data acquisition, a -15 dB attenuator was inserted after the preamp of crystal 35. Out of the bremsstrahlung spectrum the energies are chosen by coincidence between the corresponding Tagger channels and the PROTO 60. In both experiments, the accelerator current was adjusted to a rate of 7.5 kHz of the OR of all read out Tagger channels. The thresholds of the plastic detectors were set just above the noise level. The noise and signals of all channels have been checked. The timing of the detector against the Tagger was verified.

During the first experiment, data for beam energies between 158.31 MeV and 1.44 GeV were collected. After 150 minutes of data taking, the detector was moved 5 mm to the side. Due to the increased deposited energy in the neighbor module, an additional attenuator reduced the signal after the preamp of crystal 36. 90 minutes later the detector was moved further until the beam impinged between the crystal 35 and 36. The measurement took again 90 minutes. For calibration, cosmic radiation was measured afterwards two times. One run was performed with the additional attenuator after the preamp of crystal 36 for 3 days, and one run without that attenuator for one day. In addition, two short measurements of the noise level, with a high rate pulse generator for triggering the read out, were performed. Again one with and one without the attenuator.

In total, 3 measurements with the photon beam (52.34 MeV - 685.58 MeV) were performed during the second beam-time. A first run was only used for checking the whole setup and adjusting the alignment with a beam-position reconstruction algorithm. Details of the algorithm can be found in [BRE13]. During the second run, the complete insensitive material was mounted. For the third run, the Plexiglas sheet was removed and the last run excluded all additional material. For collecting data, each run had a duration of about 3 hours. For calibration, cosmic radiation was measured for 25 hours afterwards. Furthermore, cosmic radiation was measured in-house over a period of three weeks with the PROTO 60 vertically aligned. For measuring the noise level, a pulser with a rate of 1 Hz was used during all measurements.

Chapter 5 Experiment at MAMI

An overview over the performed beam measurements at MAMI is given in table 5.1. The corresponding tagged energies are given in table 5.2.

Exp.	Run num.	Mat. in front	Beam pos.	Energy / MeV
1	1.1	no mat.	center of 35	
	1.2	no mat.	5 mm away from the center	158.31 - 1441.06
	1.3	no mat.	between 35 & 36	
2	2.1	test	center of 35	
	2.2	DIRC+TOF	center of 35	52.34 - 685.58
	2.3	DIRC	center of 35	
	2.4	no mat.	center of 35	

Table 5.1: MAMI procedure overview for the beam experiments.

5.3 Experimental procedure

Tagger channel	Energy ^{1st} / MeV	Energy ^{2nd} / MeV
1	1441.06	685.58
2	1356.89	650.81
3	1257.31	601.77
4	1156.56	579.10
5	1057.7	509.88
6	956.16	443.77
7	857.98	387.38
8	756.58	339.67
9	657.34	269.95
10	556.97	200.35
11	456.26	152.72
12	355.88	107.98
13	256.41	93.97
14	158.31	84.67
15	-	61.54
16	187.99	52.34

Table 5.2: Chosen energies during the first and second experiment at MAMI. During the first beam-time the wires for the TDC channels 14 and 16 are inverted. TDC channel 15 was not used.

5.4 Data Analysis

5.4.1 Raw data

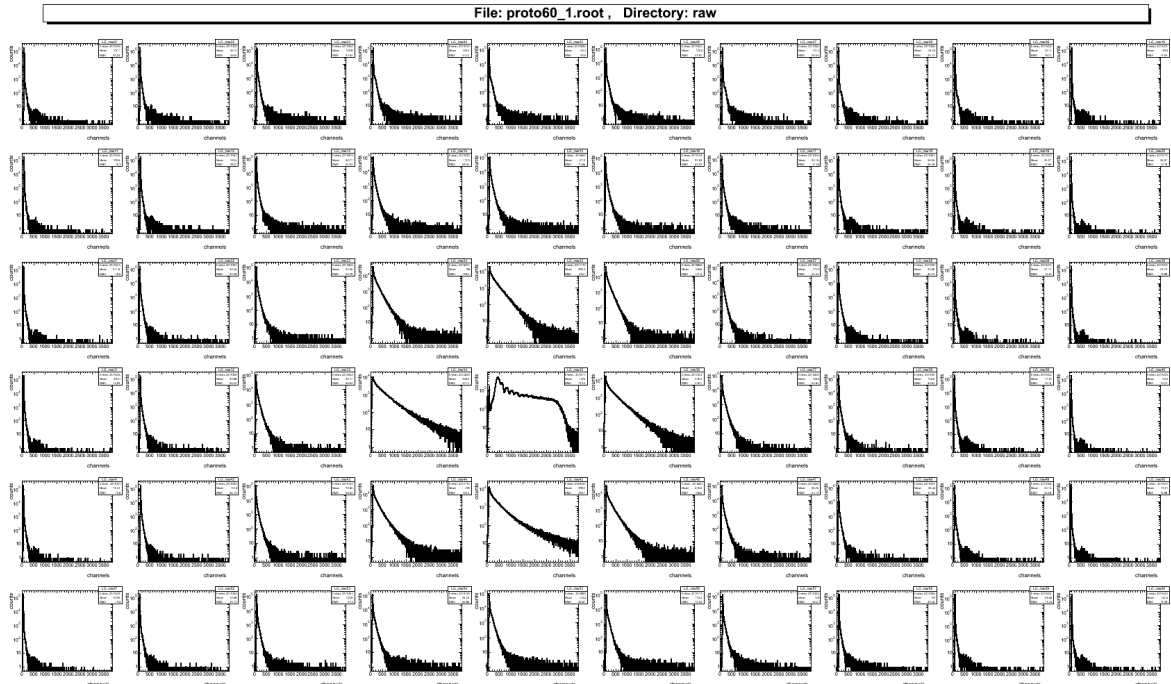


Figure 5.8: Raw data of all 60 crystals in run 1.1. The events are plotted in logarithmic scale versus the energy in ADC channels. The crystal number 1 can be found in the upper left corner.

In the figures 5.8, 5.9 and 5.10 the uncalibrated raw data of all crystals are shown. The modules are numbered as seen from the detector back side. Figure 5.8 shows the data of run 1.1. The distribution of the lateral electromagnetic shower over the full 60 crystals can be seen. With increasing distance from the beam entry point, the energy deposition decreases. Even the outermost crystals obtain an appreciable energy deposition. Due to the pre-calibration via adapting the dynamic range of all 60 crystals, it can be assumed that the beam entry point was not precisely the center of crystal 35. By comparison of the deposited energy in the crystals around the central crystal, it can be seen that the entry point was shifted towards the direction of crystal 45 and additional slightly towards crystal 44. For comparison see also the raw data of run 1.3 in fig.5.9, where the detector was moved 5 mm horizontally. The shift towards

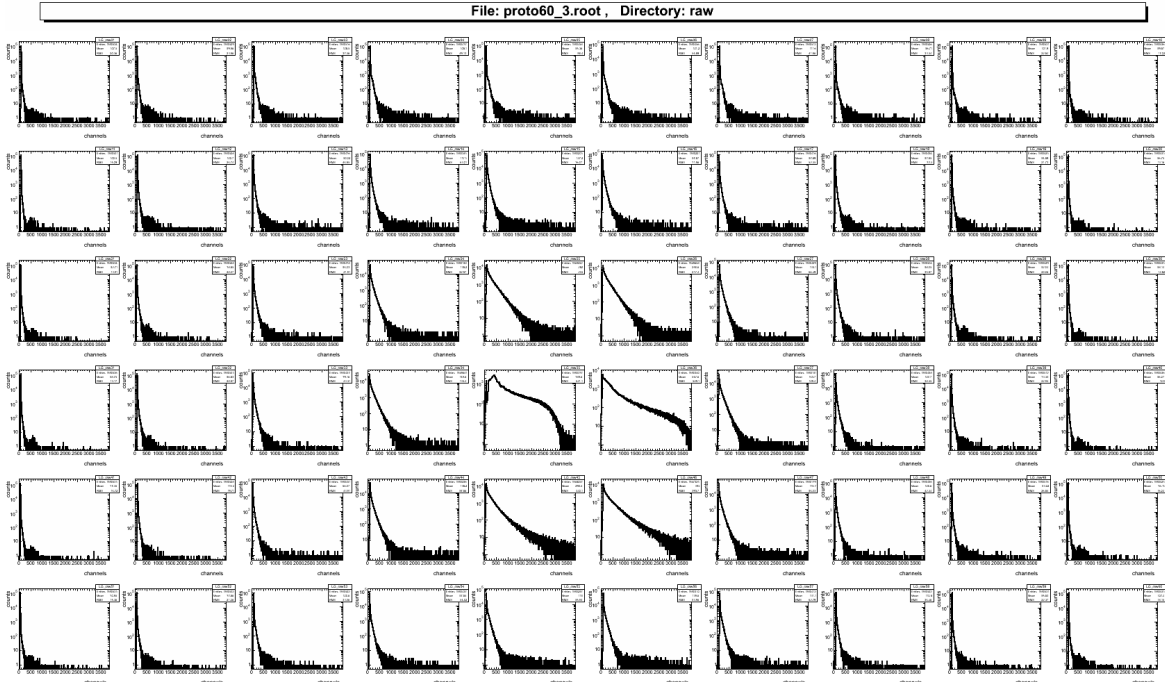


Figure 5.9: Raw data of all 60 crystals in run 1.3 (beam between crystal 35 and 36). The events are plotted in logarithmic scale versus the energy in ADC channels.

crystal 45 can be seen here as well, but the focus of the electromagnetic shower moved between crystal 35 and 36, with a slight shift towards crystal 36. For a complete picture, the raw data of run 2.4 can be seen in fig. 5.10. For this experiment, the setup was reestablished and therefore new aligned. Due to the lateral shower distribution and within a first approximation, the entry point of the beam was accurately the center of crystal 35. Through the superposition of several peaks in the energy spectrum of crystal 35 within all three shown raw data pictures, the coincidence of the read out with the chosen tagger channels is indicated. In figure 5.11 the raw data of crystal 35 in the second experiment, plotted in different colors, can be seen in more detail for all runs. The difference of the runs, and therefore the effect of material, becomes more visible at lower channel numbers. Coming from the high energy side, the curves separate at lower energies. On the right side above channel number 500, the differences almost vanish. By comparing the first two peaks, especially on the right picture, it can be noticed that there is a discrepancy between the peak height relation from the first to the second peak within different runs. For example, the red curve (TOF+DIRC in front) of the left peak is approximately three times higher than the black curve of the

Chapter 5 Experiment at MAMI

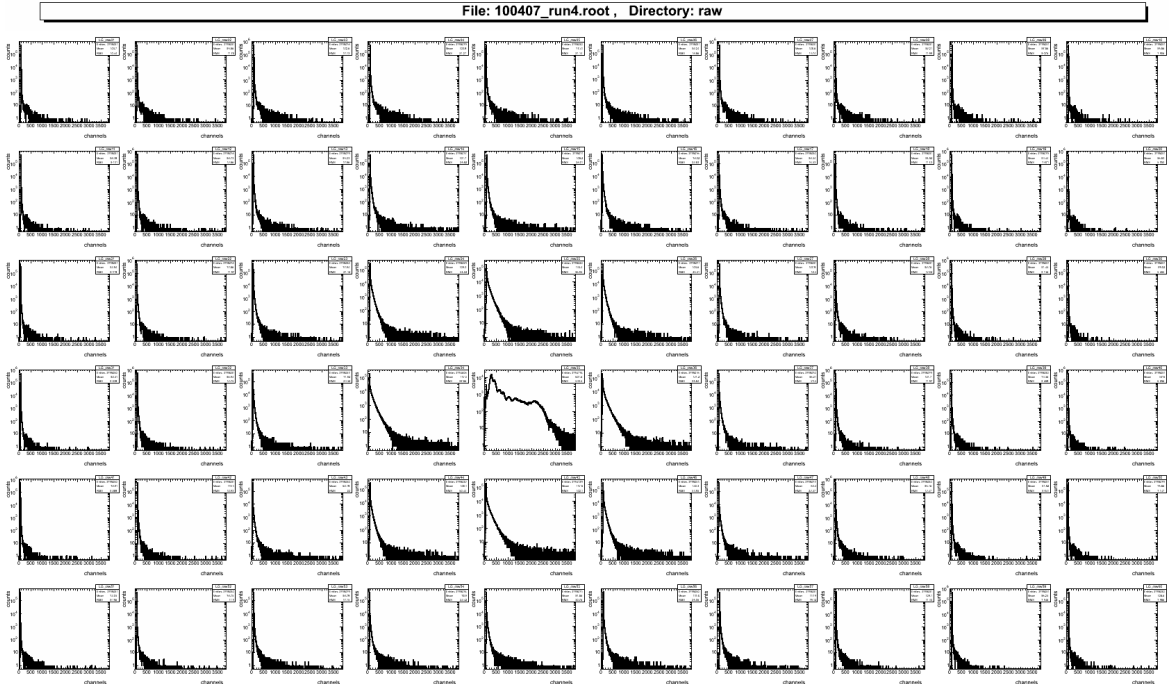


Figure 5.10: Raw data of all 60 crystals run 2.4, the experiment without any additional dead material in front. The events are plotted in logarithmic scale against the energy in ADC channels.

data without additional material in front.

Within the data analysis, the chosen energies can be separated off-line (fig.5.12) by demanding a coincidence between the PROTO 60 and a single Tagger TDC channel (fig.5.13). A short time window in the width of a few bins was set individually around the peak in every Tagger TDC data.

Besides the actual photo-peak, the low energetic peak can be found in each single tagged energy spectrum. As mentioned before, it increases on one hand with the amount of insensitive material and on the other hand for lower photon energies in relation to the corresponding photo-peak height (fig.5.14). The raw TDC data of both plastic detectors of run 2.3 can be found in picture 5.15. In this run the DIRC sample was placed in between. By using the definition of X_0 (chapter 2.4.1.3), the probability $P_{e^+e^-}(\gamma)$ of pair production of the primary photon within 2 cm of SiO_2 can be calculated to:

$$P_{e^+e^-}(\gamma) = 1 - e^{-\frac{7}{9} \frac{X}{X_0}} = 12\%. \quad (5.4)$$

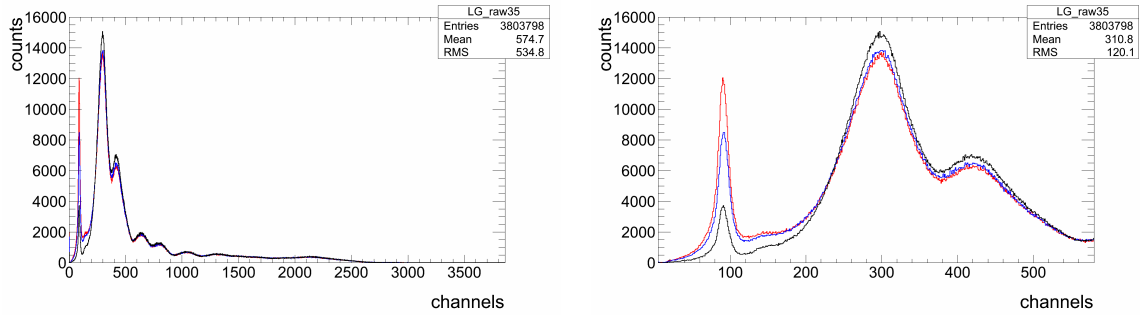


Figure 5.11: Raw data of crystal 35 from the second experiment. Run 2.2 with DIRC+TOF in front is plotted in red. Run 2.3 (DIRC only) is plotted in blue and run 2.4, without any additional material in front, in black.

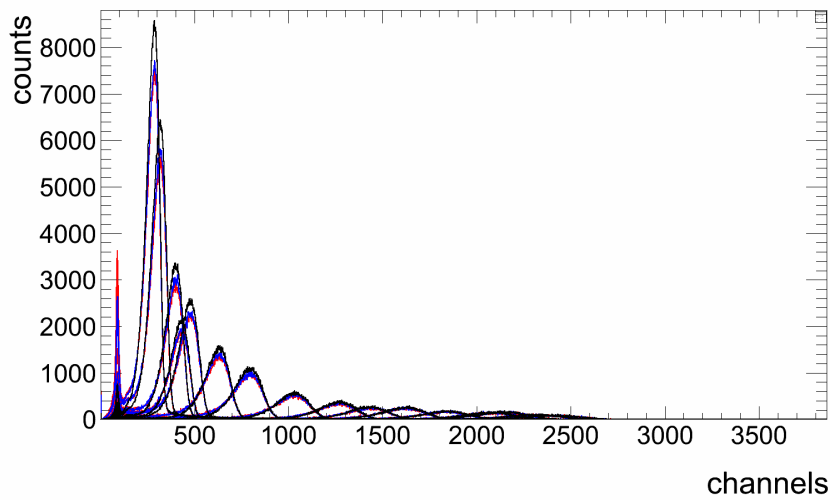


Figure 5.12: Data from figure 5.11 separated by an individual coincidence with every single tagger channel.

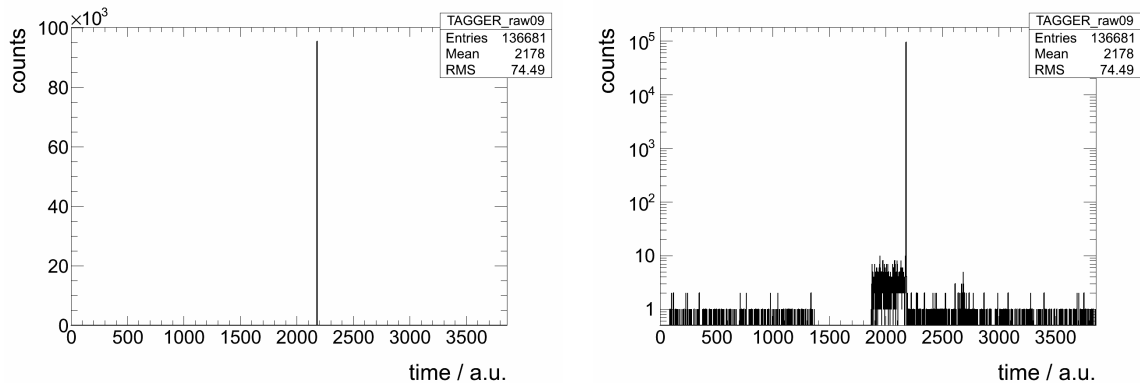


Figure 5.13: Raw data of the Tagger TDC channel 09 in linear and logarithmic scale from the second experiment run 2.4.

In total, only 2175 conversion events are registered due to the difference of measured events within the plastic detectors. On the other hand, according to figure 5.11, more than $3.8 \cdot 10^6$ tagged photons are measured. The discrepancy between the expected and measured conversions indicates technical problems with the plastic detectors.

5.4.2 Energy calibration

Due to the distribution of the deposited energy over several crystals, the response of the detector modules needs to be aligned. In principle one has to distinguish between two kinds of calibrations. On the one hand the relative calibration, where the signal caused by a certain energy is aligned for all crystals and given in arbitrary units. This calibration is sufficient to determine the energy resolution and evaluate the principle detector performance of prototypes. On the other hand the absolute calibration, which is needed to measure energies deposited within the detector and investigate its response in more detail.

For the calibration of the different runs within the two experiments, the corresponding cosmic radiation and noise measurements were used. Furthermore, GEANT simulations were performed.

The signals of the detector modules are a superposition of the signal due to the energy deposition and the electronic noise. Therefore the measured noise level has to be subtracted. It delivers a calibration point for the zero value in the energy scale of both

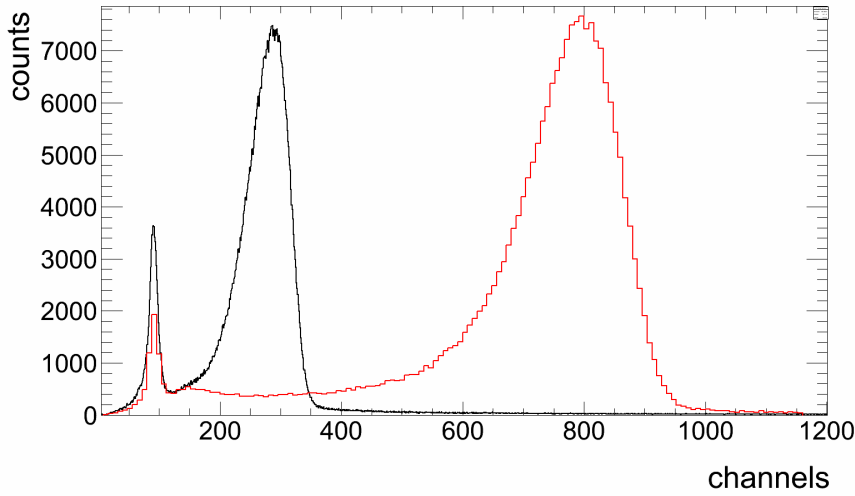


Figure 5.14: Raw energy data of crystal 35 from run 2.2 for 52.34 MeV (black) and 200.35 MeV (red) photons. For a better comparison of the low energetic peak, the bin-size of the higher energy plot was increased until the photo-peak height becomes comparable.

calibration cases. For each module, the obtained data of the test pulser measurements are fitted with a Gaussian distribution and the value for the peak position is taken into account (fig.5.16).

For the calibration of the detector with cosmic radiation, only events which are exclusively caused by traversing cosmic muons are of interest. In order to work out the interpenetration of the complete detector, and in favor of background suppression a coincidence between any crystal out of the top row and any crystal out of the bottom row is chosen via the DAQ system as a trigger (fig.5.17). Furthermore, a restriction to events where only crystals of the same column contribute a signal above a threshold well above the noise, assures almost complete suppression of the background. This condition will be referred to as column cut. The obtained line shape can be fitted with a Landau distribution without any fit-range restrictions (fig.5.18). For crystals within the first and second row from the top and from the bottom of the crystal matrix, a low energetic background remains. The figure 5.19 gives an overview of the calibrated cosmic radiation data under the column cut condition. The relative calibration coefficient F , to align all cosmic peak positions Δ_p to the value X , can be obtained

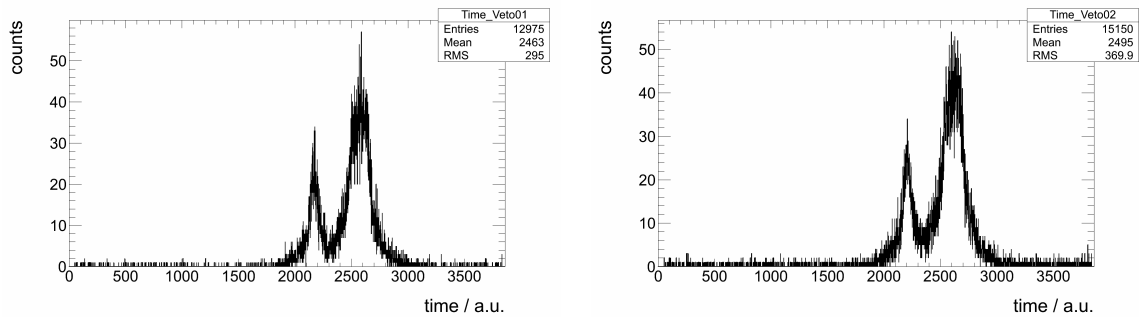


Figure 5.15: Exemplary raw data from the TDCs of the plastic detectors from the run 2.3. The DIRC sample was placed between the first and second plastic detector. The data of the first is shown on the left, and of the second plastic detector on the right side.

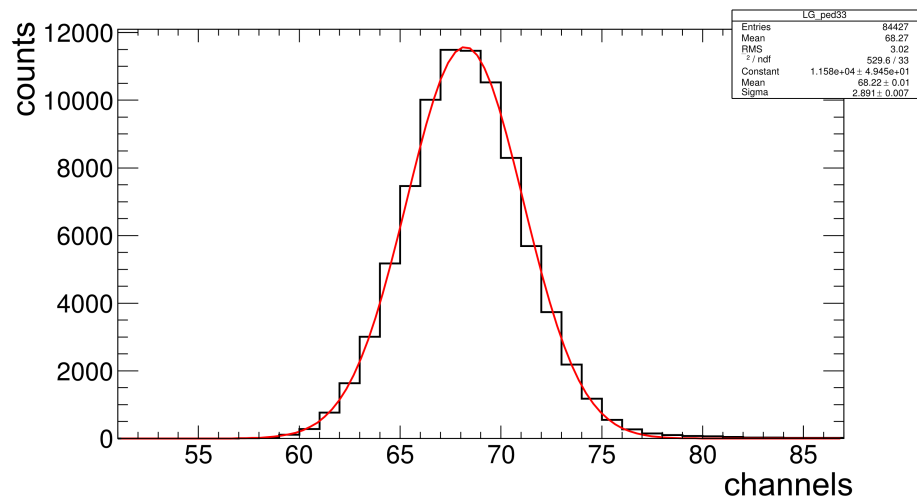


Figure 5.16: Exemplary noise distribution of crystal 33 fitted with a Gaussian distribution.

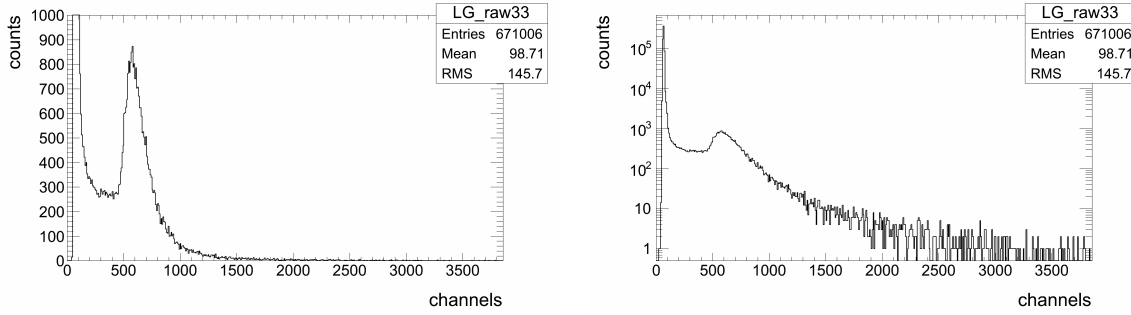


Figure 5.17: Exemplary raw cosmic data of crystal 33.

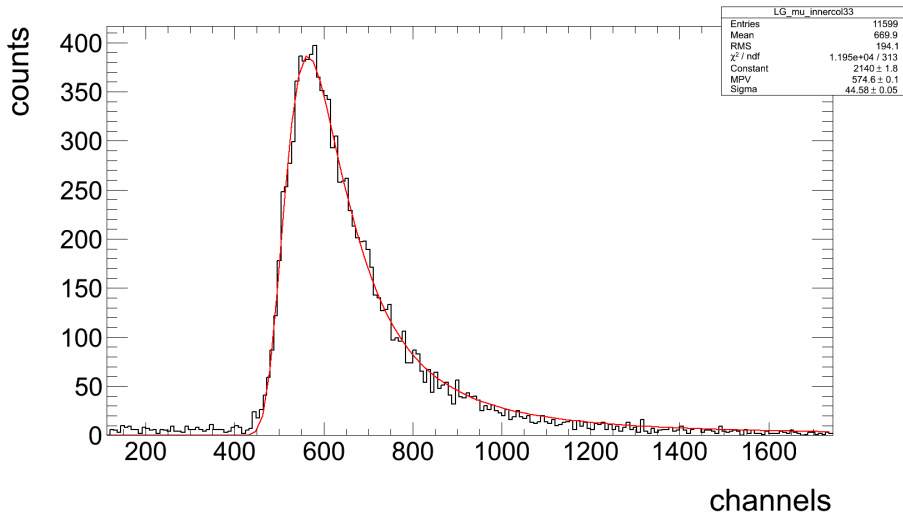


Figure 5.18: Deposited energy spectrum of cosmic radiation radiation in crystal 33 after the column cut. The most probable value Δ_p is determined with a Landau fit-function.

with:

$$F = \frac{X}{\Delta_p - \text{ped}_p}. \quad (5.5)$$

To obtain an absolute energy calibration an energy has to be assigned to the value X . In the literature it can be found that minimum ionizing particles deposit $10.2 \text{ MeV}\cdot\text{cm}^{-1}$ inside lead tungstate [PDG08]. As a first approximation, this value can be considered for the cosmic radiation. The average vertical path length through a horizontally aligned type 6 crystal is 24.032 mm, which corresponds to a deposition of 24.513 MeV. In order to verify the relative calibration, the histograms are fitted again with a Landau distribution. The largest deviation of a single crystal from the

Chapter 5 Experiment at MAMI

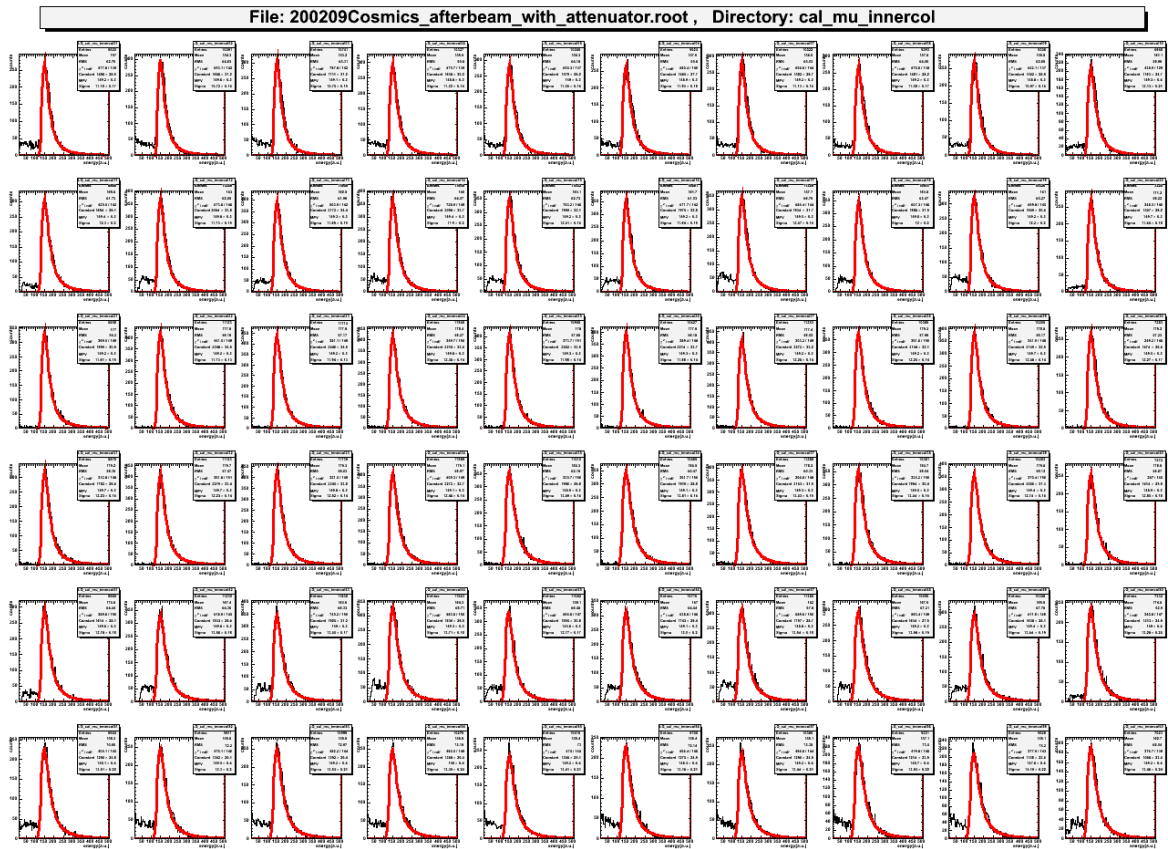


Figure 5.19: Calibrated cosmic radiation data with the column cut condition. A fit with a Landau distribution (red) is applied in order to verify the alignment.

calibration value was 0.6%.

5.4.2.1 Simulations of cosmic radiation

Due to the nonlinearity, the measured signal of a certain deposited energy differs with the location of origin within the crystal. Especially, the difference of an accelerator beam impinging frontally versus the cosmic radiation is of interest. In order to obtain a better understanding of the measured cosmic radiation data, with respect to the nonlinearity and calibration, three dedicated GEANT simulations are performed. The simulation of cosmic radiation is generally performed for a latitude of 50° for Germany and at sea level. For each simulation $1.34993 \cdot 10^8$ events were simulated. The simulation environment is filled with air as explained in chapter 4.1.

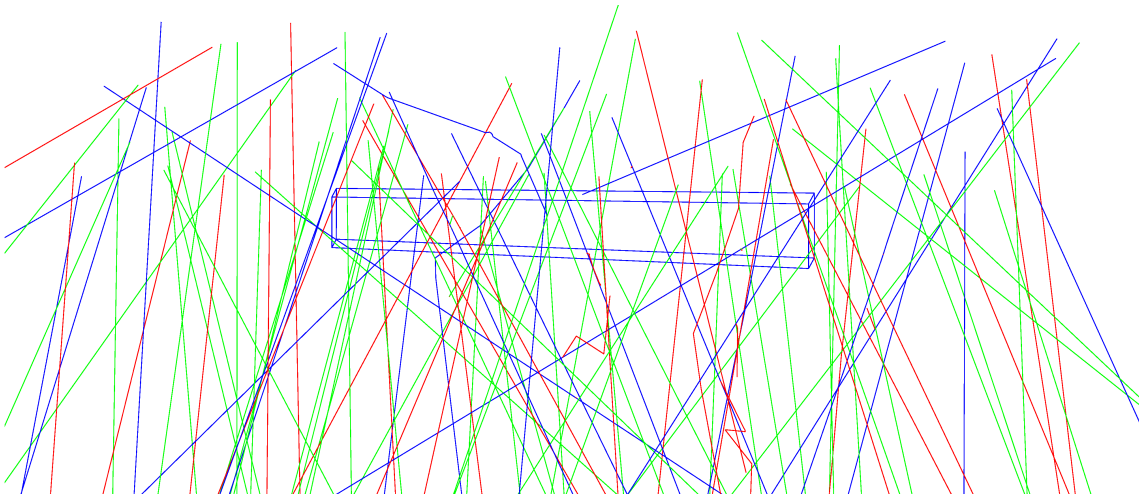


Figure 5.20: Cosmic simulation via CRY with a single type 6 crystal. The track of positive charged particles are drawn in blue, negative in red and neutral in green color.

Single Crystal A simulation with a single, horizontally aligned type 6 crystal of the PROTO 60 model was performed (fig.5.20). The cosmic radiation was generated through a window of $0.4 \times 0.4 \text{ m}^2$, 5 cm above the center of the crystal. The amount of measured events decreases with the deposited energy and covers the whole energy range up to 2 GeV. Applying a fit with a Landau function on the muon peak, a MPV⁶ of deposited energy of $27.97 \pm 0.03 \text{ MeV}$ is deduced (fig.5.21). If the simulation is restricted to muons low energy contributions are reduced, in particular below 20 MeV. Including the non linearity of the PROTO60-NUF-NOISE model, the MPV expressed

⁶MPV = most probably value

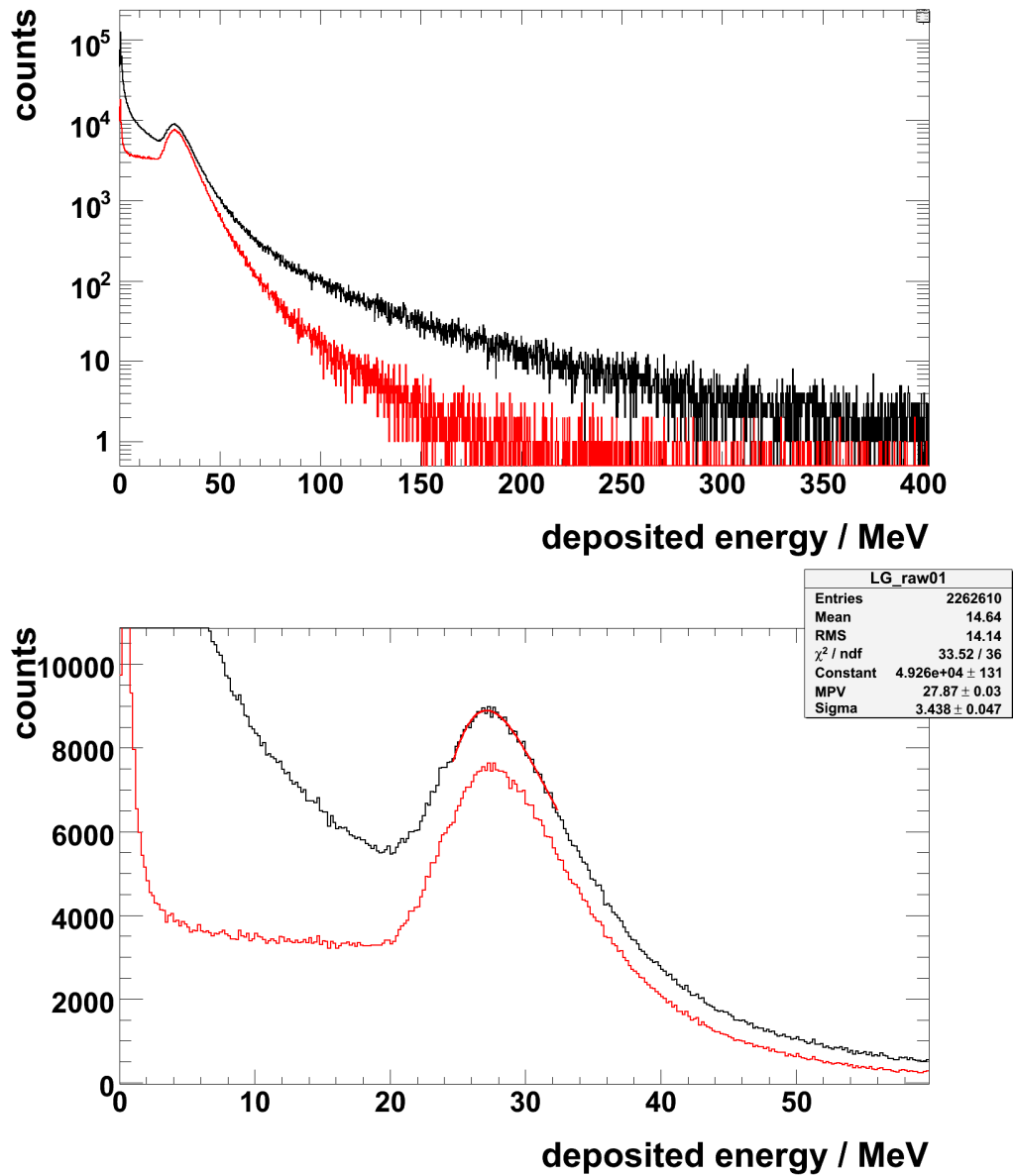


Figure 5.21: Cosmic radiation simulation of a horizontally aligned type 6 crystal. The data for the red curves are restricted to generated muons. The black curves are obtained by the full simulation. The peak due to muons in the full simulation was fitted with a Landau function in the lower picture.

in the number of photo-electrons amounts to 782.3 ± 0.9 registered in a LAAPD (fig.5.22).

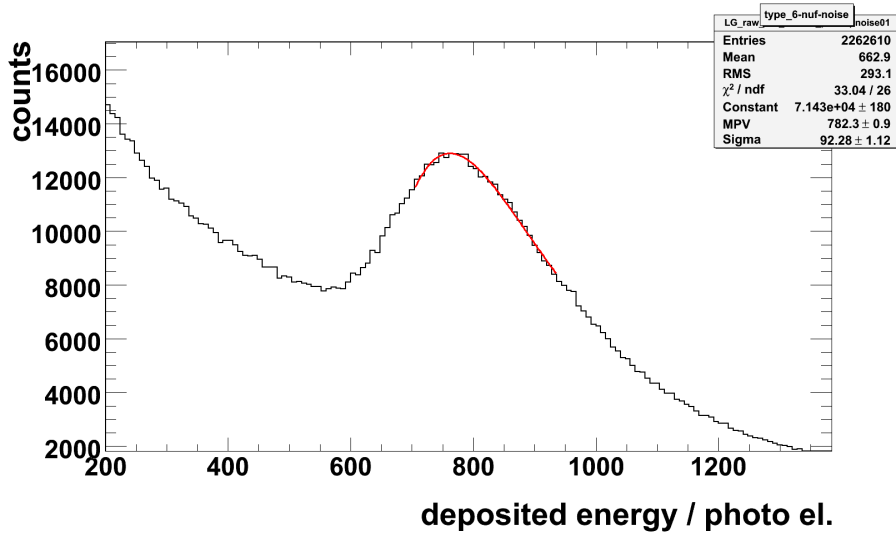


Figure 5.22: Cosmic radiation simulation with a single type 6 crystal. Adapted from the PROTO60-NUF-NOISE model.

PROTO60 For a full simulation with 60 crystals, cosmic radiation was generated through a window of $0.6 \times 0.6 \text{ m}^2$, 10 cm above the upper crystal row. An example for 100 events can be seen in figure 5.23. The crystals are labeled as seen in beam direction. Crystal number 1 is located at the upper left corner and crystal number 60 at the lower right corner. The MPV for the deposited energy within the muon peak is similar for all crystals in the order of $28 \pm 0.2 \text{ MeV}$ (fig.5.24). As used in the DAQ of the PROTO 60, the trigger condition via coincidence between any crystal out of the top row and any crystal out of the bottom row is implemented within the simulation. Furthermore, the column cut is realized using a 10 MeV threshold for each crystal. As shown in fig. 5.25, the column cut reduces the background within the simulation. For crystals at the top and bottom row of the matrix this is not the case, a reduced background remains (fig.5.26). On the other hand, the simulated trigger condition influences the muon peak position. The shift direction of the values depends on the position of the crystal within the detector matrix (fig.5.27). For example, the crystal number 5 shows a MPV of 27.96 MeV for the cosmic radiation raw data. Including the coincidence between any crystal out of the top row and any crystal out of the bottom row the

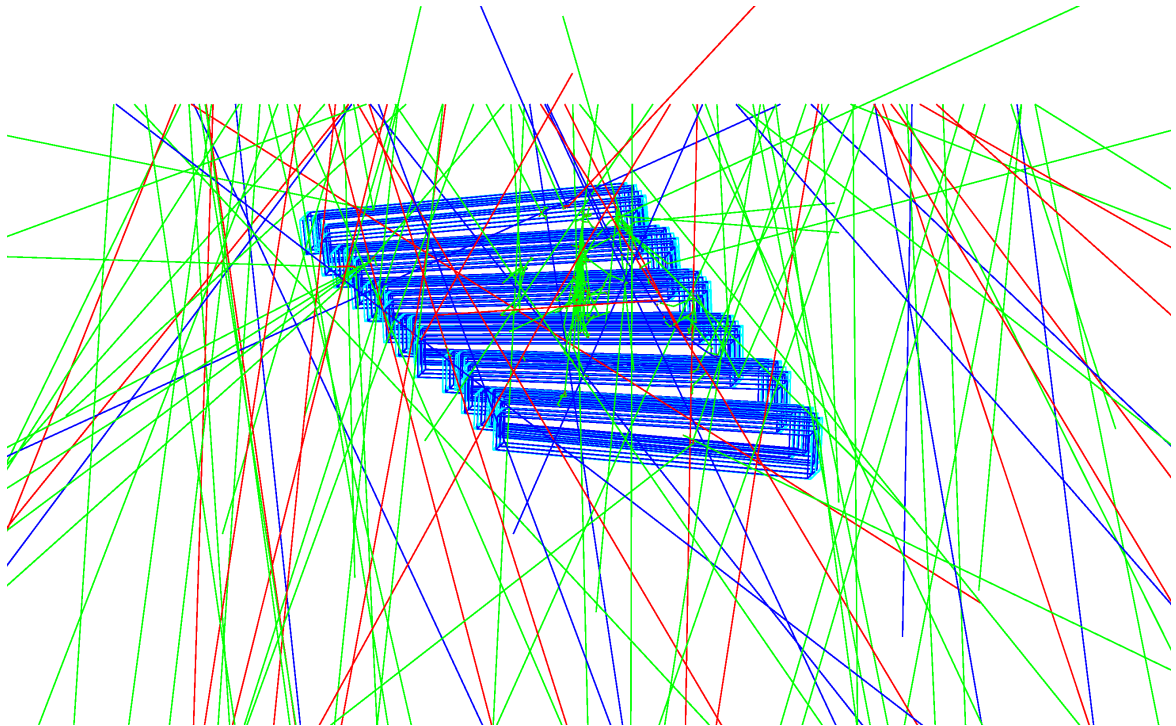


Figure 5.23: PROTO60 CRY simulation with 100 events. The track of positive charged particles are drawn in blue, negative in red and neutral in green color.

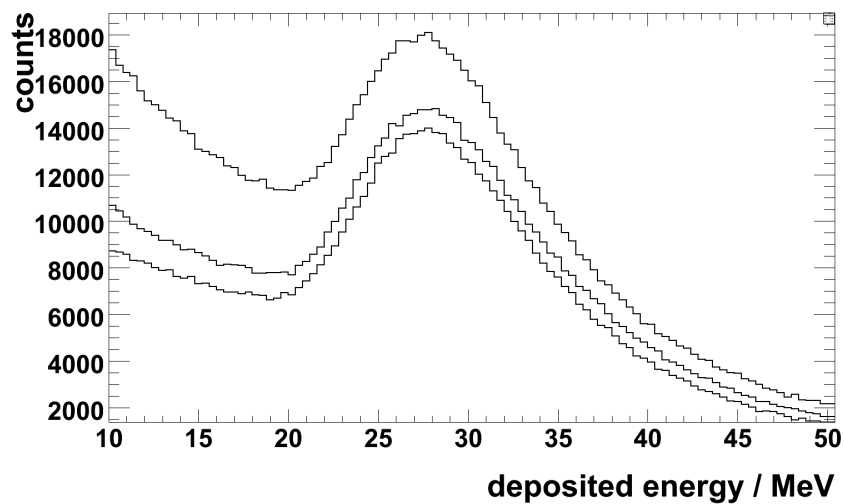


Figure 5.24: PROTO60 cosmic radiation simulation. The pure energy deposition for crystals in the middle of the upper, of the middle and the lowest row is shown.

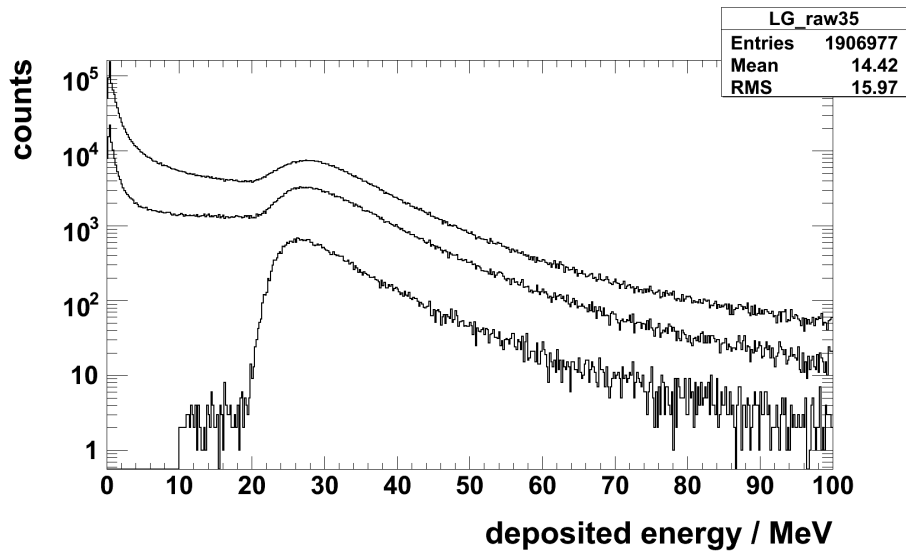


Figure 5.25: Cosmic simulation for a central crystal out of the PROTO 60 matrix under different trigger conditions. The upper curve represents the raw data, the middle one the result of a coincidence between any crystal out of the top row and any crystal out of the bottom row and the lower curve includes the column cut.

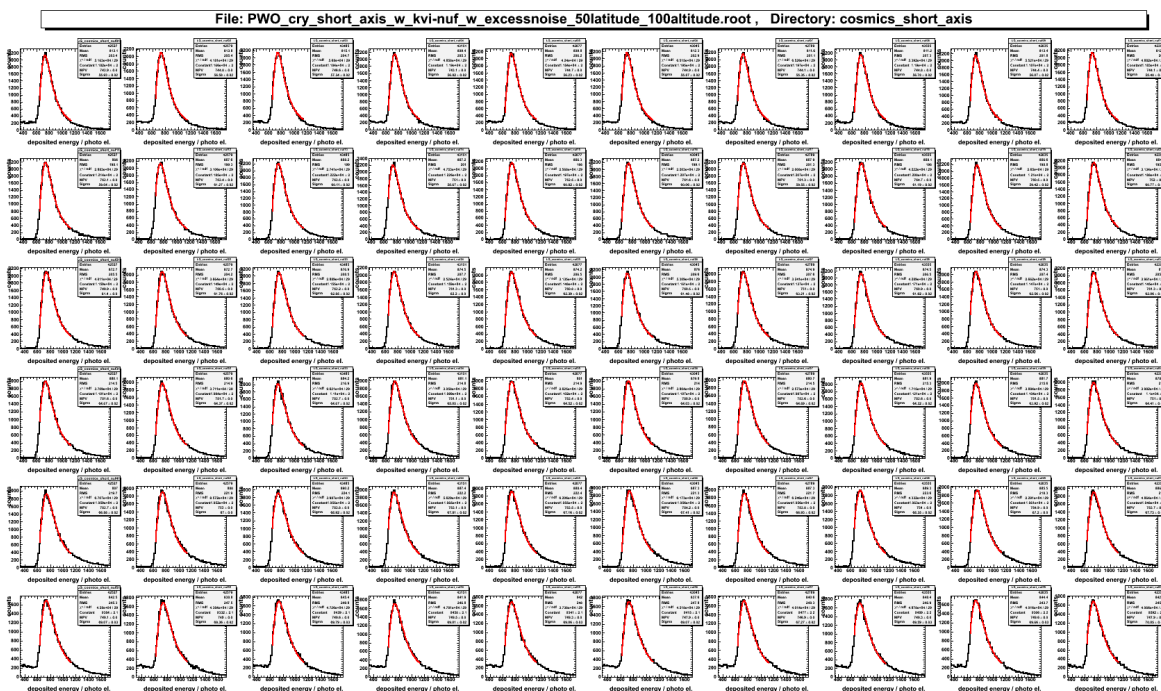


Figure 5.26: Landau fit of all crystals under simulated cosmic radiation including the column cut.

peak shifts to 28.9 MeV. The result applying the column cut amounts to 28.03 MeV. Both trigger conditions lead to an increased peak value compared to the raw data. For comparison, for crystal 55 the corresponding MPVs are: 28.11 MeV, 26.17 MeV and 25.22 MeV, respectively showing the opposite trend. Due to the staggered arrangement of the matrix geometry, the coincidence conditions of the different trigger versions select muon tracks across the crystal closer to the LAAPD side in case of the top row and vice versa for the bottom row (fig.5.28). This will lead to different energy depositions in every row. Furthermore, the non planar crystal alignment within a row has to be considered. The cosmic radiation simulation including the column

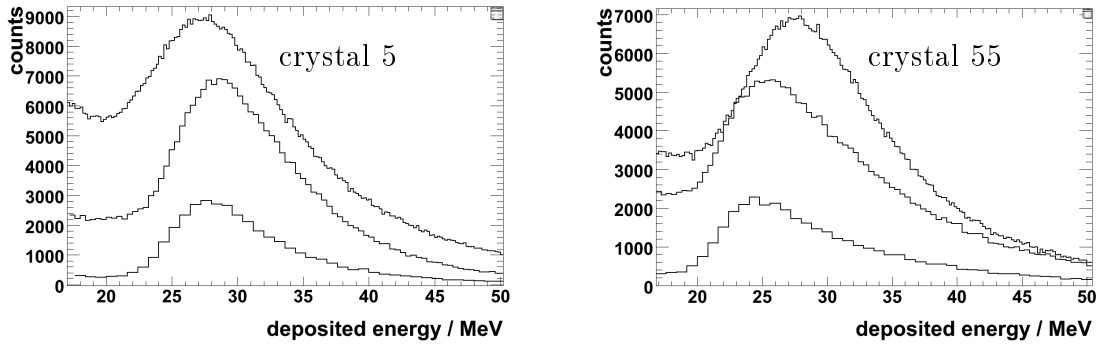


Figure 5.27: PROTO 60 cosmic simulation for different trigger conditions. The upper curve in both pictures represents a self triggered DAQ (raw-data). The curves in the middle includes the condition of a coincidence between any crystal from the top and any from the bottom layer. The lowest curves corresponds to the condition, that all crystals in the same column responded simultaneously.

cut gives most probably values from 25.221 ± 0.002 MeV up to 28.208 ± 0.001 MeV for the 60 different crystals, which corresponds to a difference of 11.8% (fig.5.29). Within the individual rows, the differences are less than 0.2 MeV. Major variations appear with the transition from one row to another. However, including the light collection with the PROTO60-NUF model, the MPVs vary only between 743.13 ± 0.02 and 754.87 ± 0.03 photo electrons in total. This corresponds to an increase of 1.6%. The individual values of all crystals are plotted in figure 5.30. The average amount of photo electrons is 750.31. For comparison this value is equal to a signal caused by:

$$E_{dep}(0 \text{ cm}) \approx \frac{750.31 \text{ phe}}{32.04 \text{ phe/MeV}} = 23.42 \text{ MeV} \quad (5.6)$$

energy deposition within the first few mm of the crystals front-face.

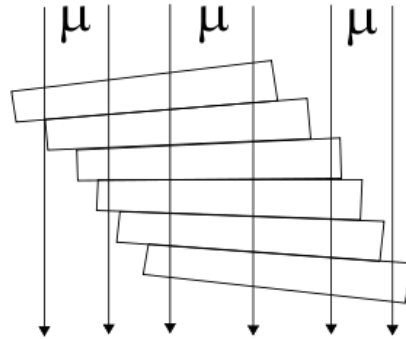


Figure 5.28: The picture serves to illustrate the mean cosmic paths. It is not true to scale. By applying trigger conditions, the cosmic paths are restricted to the overlapping parts of the crystal volumes.

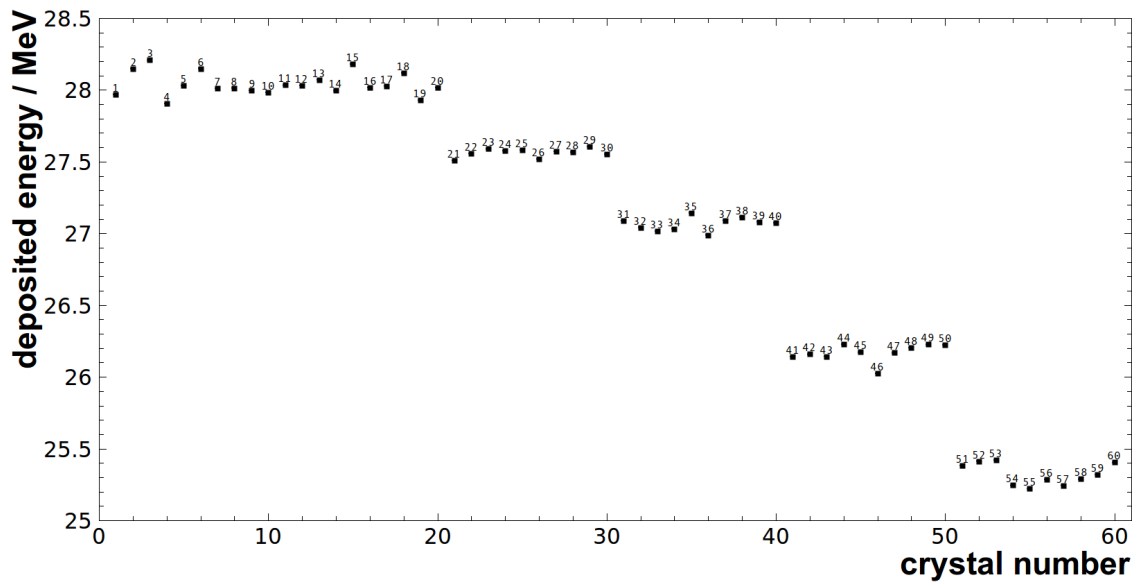


Figure 5.29: Summary of the cosmic radiation simulation with the PROTO60 model under the column cut condition. The most probable values of the deposited energy are plotted. The error bars are smaller than the size of the data points. The data can be found in the appendix (tab.8.4).

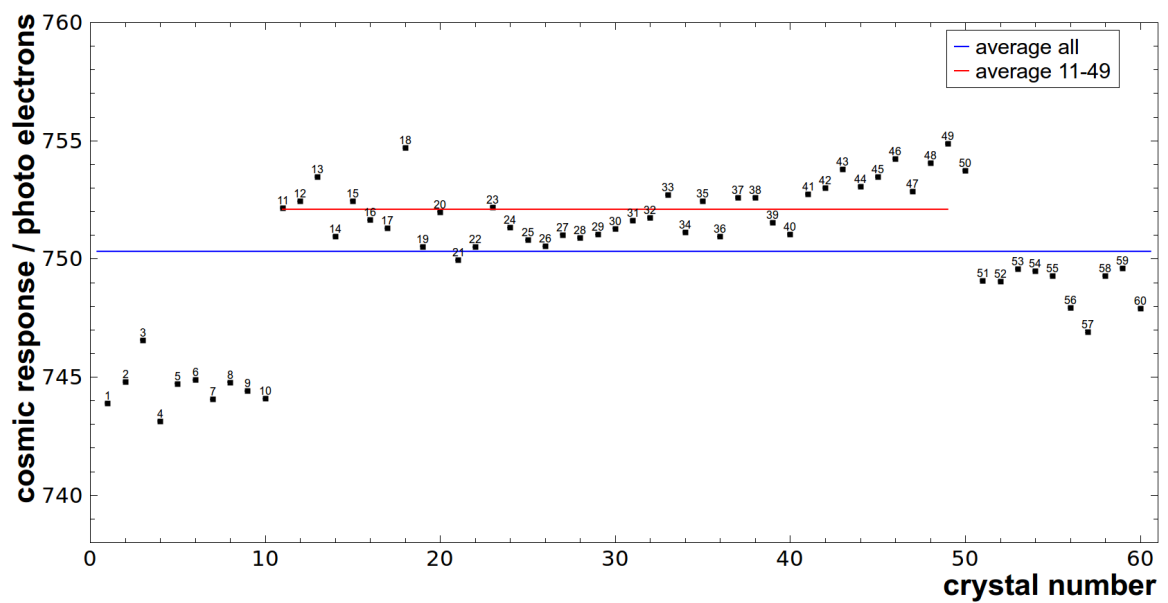


Figure 5.30: Summary of the cosmic radiation simulation with the PROTO60-NUF model under the column cut condition. The most probable values are plotted. The error bars are smaller than the size of the data points. 750.31 is the total average of the most probable value and 752.09 for the crystals 11-49. The data can be found in the appendix (tab.8.4).

In order to obtain another calibration point besides the cosmic radiation peak of the horizontally aligned crystal, cosmic muons which traverses the entire 20 cm of a crystal are of interest. Therefore a simulation with a vertically aligned PROTO 60 was performed. The line shape of a typical crystal is shown in figure 5.31. The entries in the histogram decrease with increasing energies. Structures are visible around 34 MeV and 220 MeV, respectively. To select muons which pass trough a full single crystal, an energy deposition larger than 100 MeV in one crystal and less than 10 MeV in all neighbors was required. The result is plotted as shaded area. The peak position corresponds to 218.4 MeV or 6153 photo electrons with the PROTO60-NUF-NOISE model, respectively (fig.5.32). For comparison this value is equal to a signal of:

$$E_{dep}(0 \text{ cm}) \approx \frac{61531 \text{ phe}}{32.04 \text{ phe/MeV}} = 192.04 \text{ MeV} \quad (5.7)$$

energy deposition within the first few mm of the crystals front-face.

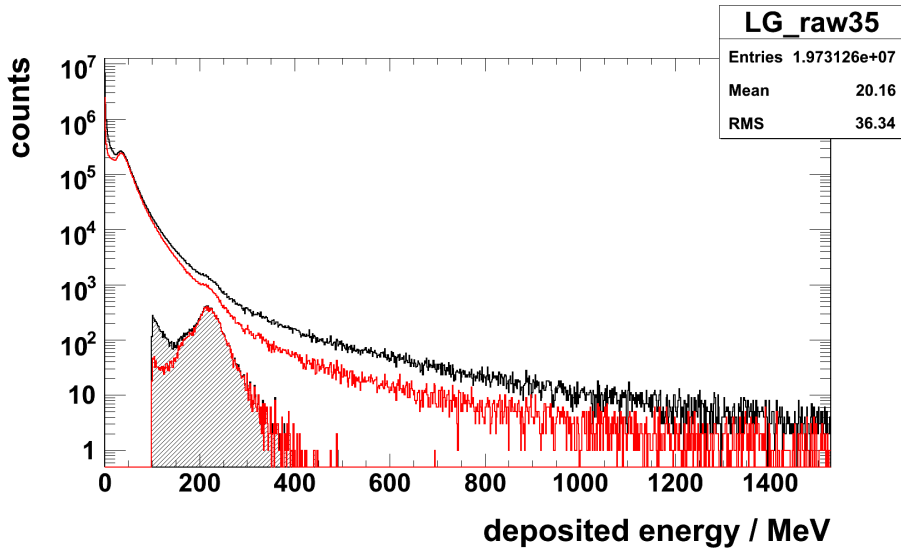


Figure 5.31: Cosmic radiation simulation with the vertically aligned PROTO 60. The red curves are restricted to muons. The shaded area includes a cut. The conditions are an energy deposition larger than 100 MeV in one crystal and less than 10 MeV in all others.

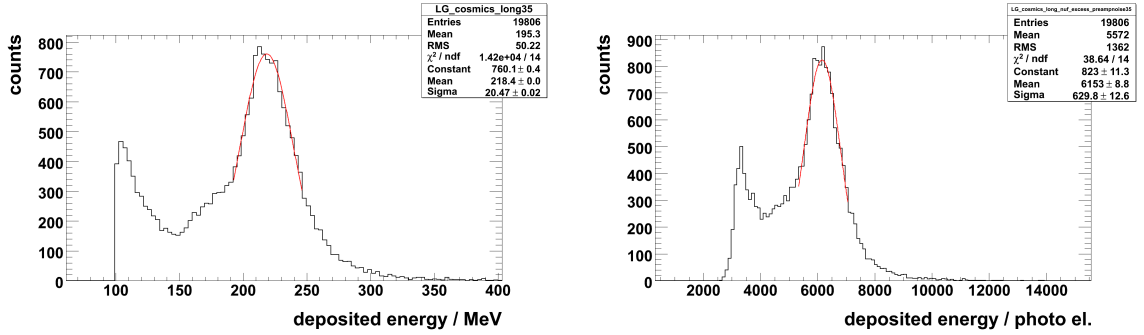


Figure 5.32: Cosmic radiation simulation of a vertically aligned PROTO 60. An energy deposition larger than 100 MeV in one crystal and less than 10 MeV in all others was required. The peaks of the pure energy deposition and the PROTO60-NUF-NOISE model are fitted with a Gaussian distribution.

5.4.3 Line-shapes

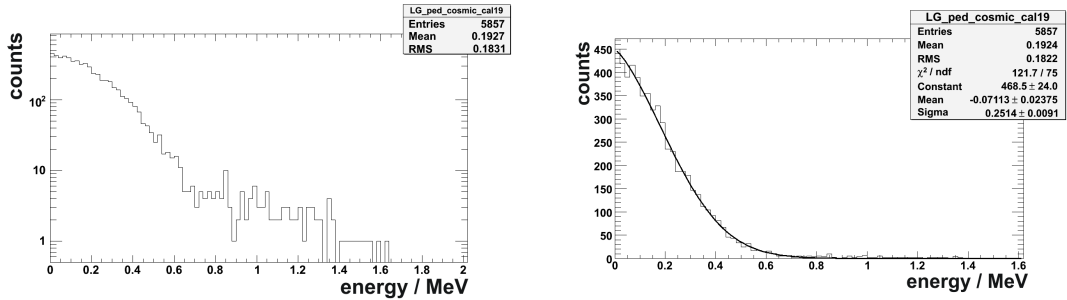


Figure 5.33: Typical calibrated noise spectrum of the module 19. For the evaluation of $\sigma_{(E,noise)}$, the right picture was fitted with a Gaussian distribution.

An example of the calibrated noise distribution is plotted in the two pictures of figure 5.33. The noise can be quantified with a fit of a Gaussian distribution. The width of the distribution corresponds to an energy equivalent of $\sigma_{(E,noise)} = 0.25$ MeV. For the reconstruction of the energy deposit in the whole detector, the distributed deposition over several crystals needs to be added. The incomplete energy deposition within the crystals, due to absorption within dead material or energy leakage out of the detector, leads to an asymmetric line shape for the reconstructed energy. For its parameterization, the Novosibirsk function

$$f(E) = Ae^{-0,5 \ln^2[1+\Lambda\tau\cdot(E-E_0)]/\tau^2+\tau^2} \quad (5.8)$$

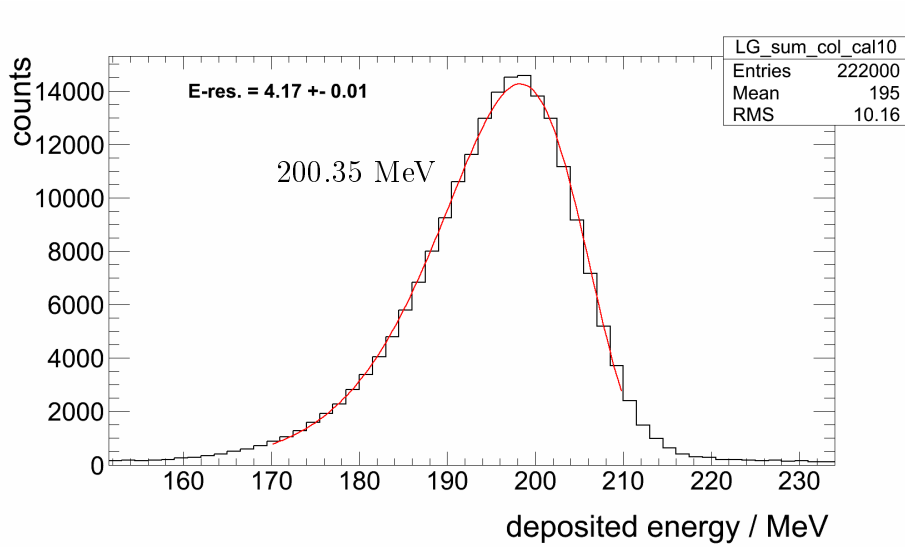


Figure 5.34: Exemplary energy sum fitted with the Novosibirsk function. The impinging photon had an energy of 200.35 MeV. Data taken from run 2.4.

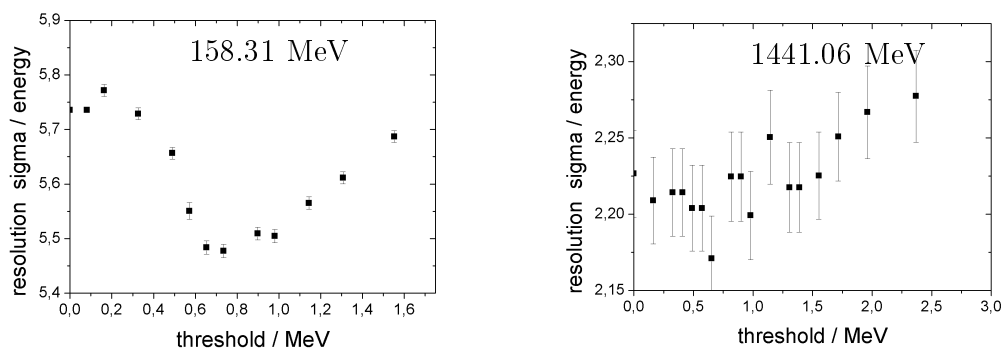


Figure 5.35: Determination of the optimum threshold with the data of run 1.1.

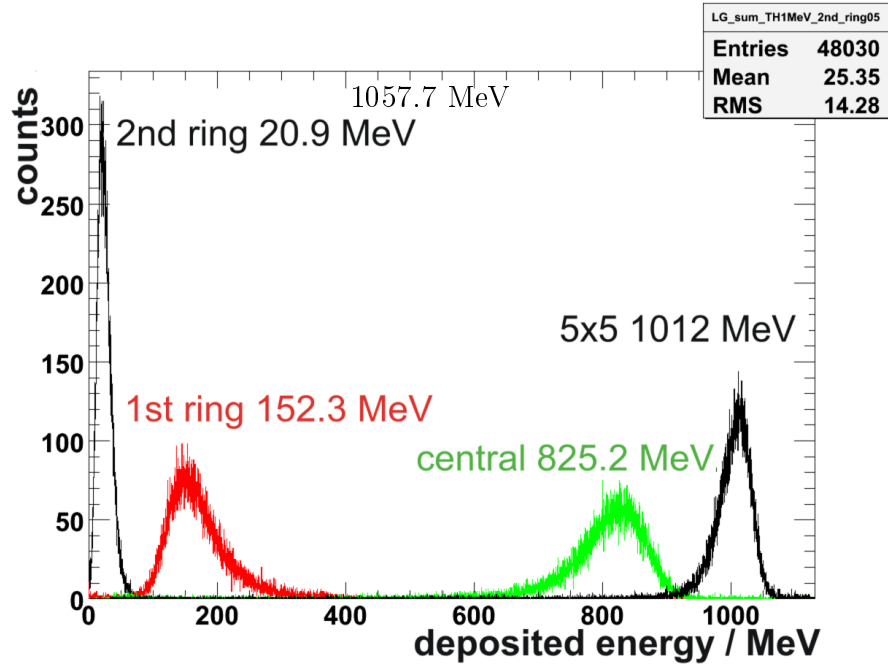


Figure 5.36: Lineshape for run 1.1.

will be used, with:

$$\Lambda = \frac{\sinh(\tau\sqrt{\ln 4})}{\sigma\tau\sqrt{\ln 4}}, \quad (5.9)$$

and

$$\sigma = \frac{FWHM^7}{2,36}. \quad (5.10)$$

E_0 represents the peak position and τ the parameter for the asymmetric tail. For $\tau \rightarrow 0$, the Novosibirsk function becomes a symmetric Gaussian-like shape. An example of a fit with this function can be found in figure 5.34.

Due to the common gate read out of the PROTO 60 modules, a certain amount of noise can be summed up together with the actual signal. Especially in case of lower impinging photon energies their energy will be distributed over a few modules only. By adding up the signal of all 60 modules the resolution will be deteriorated. Therefore a threshold has to be set. The influence of the threshold on the energy resolution can be

⁷FWHM = Full Width at Half Maximum

seen in figure 5.35. Here the energy sum of all 60 crystals is investigated. At the energy of 1441.06 MeV, the influence of a threshold within the investigated range is negligible. At a lower energy of 158.31 MeV there is a clear impact. The optimum threshold can be found between 0.6 MeV and 0.9 MeV. The value $3\sigma_{(E,noise)}$ corresponds to 0.75 MeV and is compatible with the optimum range. For the energy sum, this threshold value will be used unless otherwise specified. The energy distribution of photons with an energy of 1057.7 MeV is contained to 78% in the central crystal, 14.4% in the first ring and around 2% in the second ring (fig.5.36). The total remaining energy of 158.31 MeV and 1441.06 MeV photons, outside the 5×5 matrix but still within the PROTO 60 matrix, is shown in figure 5.37. For the 1441.06 MeV photons, the peak of the remaining energy can be determined with the Novosibirsk function and specified with 4.27 MeV. The mean value corresponds to 7.48 MeV. For the 158.31 MeV photons only the mean value of 2.44 MeV can be specified due to the exponentially decreasing shape. For a complete picture, the line shapes of the central crystal together with the

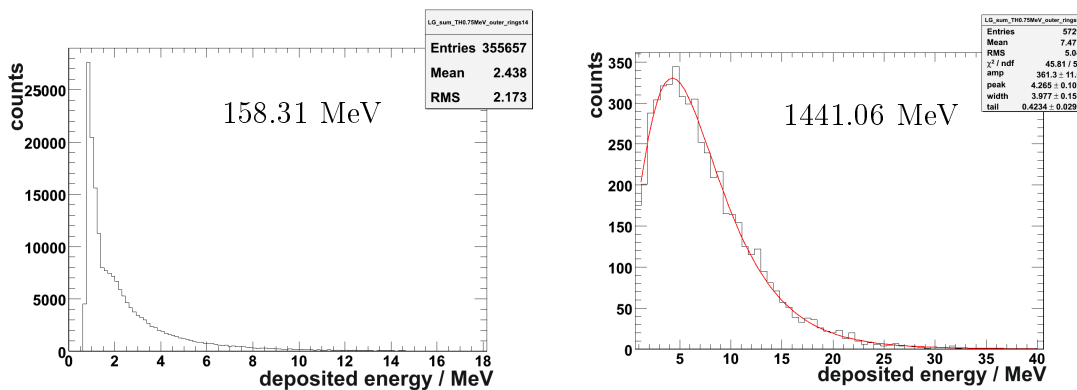


Figure 5.37: Energy sum of the remaining crystals outside the inner 5×5 matrix.

energy sum of different matrices for the energies 158.31 MeV and 1441.06 MeV are shown in figure 5.38. Adding up the total PROTO 60 matrix instead of a 5×5 matrix leads to an improved response even for the lower energy.

The example figure 5.39 shows the influence of the point of impact on the full energy sum. In comparison of the different beam positions, the detector response decreases when moving away from the crystal center towards the edge. The reconstructed energy of 1057.7 MeV photons drops from 1018 MeV down to 988 MeV.

An example for the measurements with dead material in front is shown in figure 5.40.

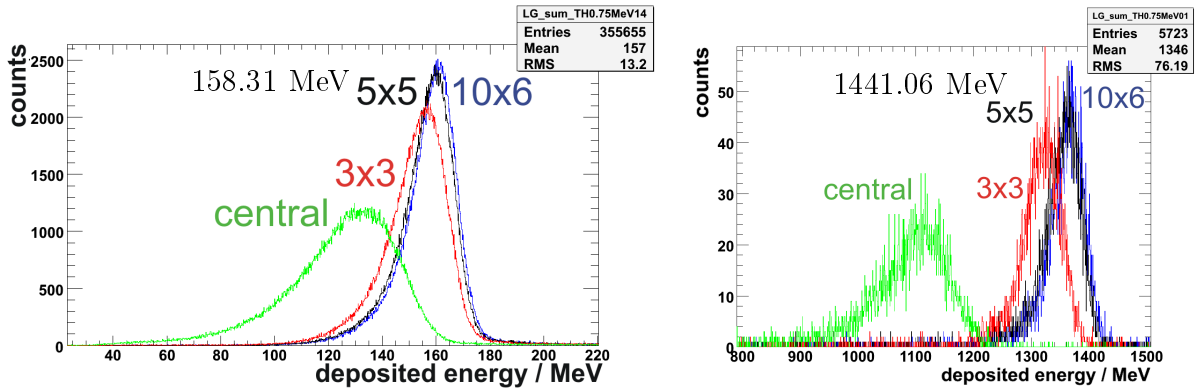


Figure 5.38: Response of different PROTO 60 subunits of run 1.1.

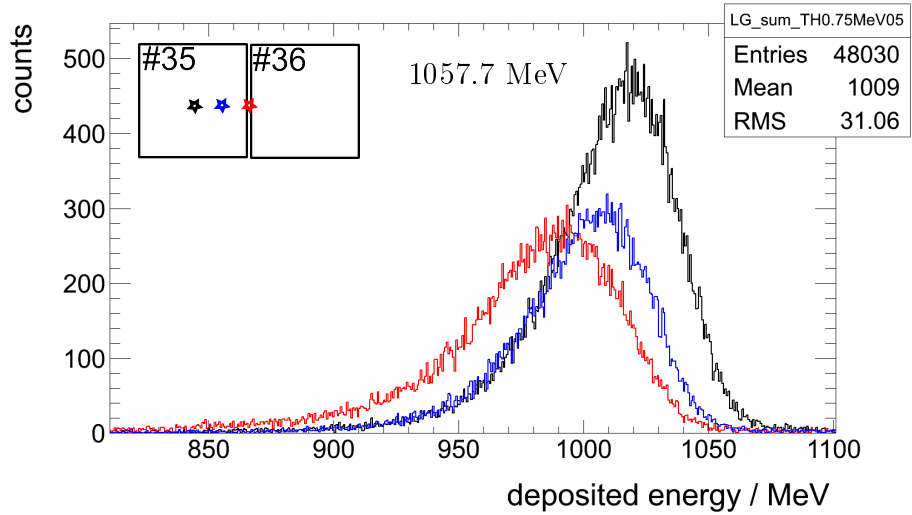


Figure 5.39: Full energy-sum for different beam positions. 1018 MeV, 1005 MeV and 988 MeV are the peak values. The data is taken from run 1.1, 1.2 and 1.3.

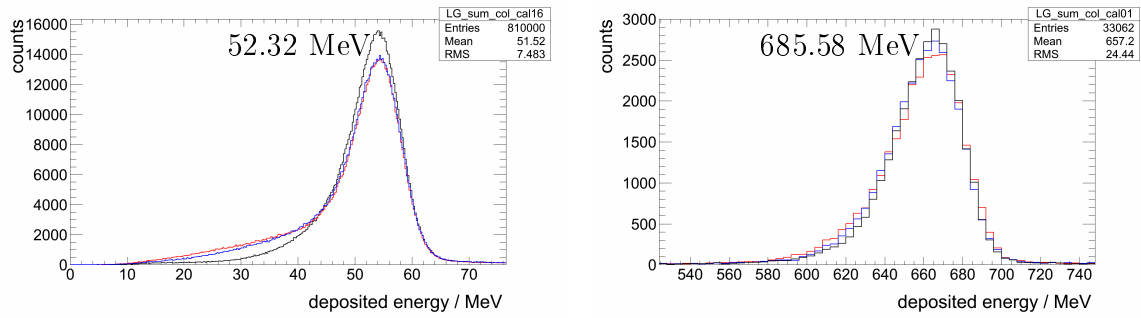


Figure 5.40: Combined runs of the second experiment. The energy sum over the PROTO 60 is shown (run 2.2: black, run 2.3: blue, run 2.4: red).

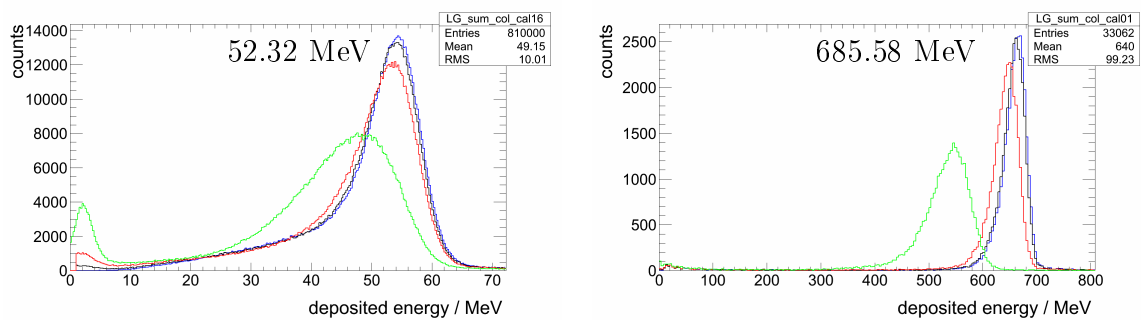


Figure 5.41: Data of run 2.2 (DIRC+TOF in front). The energy sum over the full PROTO 60 is plotted in blue, the sum over the inner 25 crystals in black, the sum over the inner 9 crystals in red and the central crystal in green.

The plotted data is normalized to 810000 events at 52.32 MeV. The line shape difference between the runs 2.2, 2.3 and 2.4 at the highest measured energy are negligible. A marginal increase of a tail to lower reconstructed energies can be seen after placing additional material in front of the detector. This effect gets even more pronounced at low energetic photons as shown for an energy of 52.32 MeV. The peak height decreases, and the tailing to lower energies increases with the amount of dead material in front. In figure 5.41 the data of run 2.2 at the same energies are plotted for different detector sizes. For 52.32 MeV the low energetic peak at 2.34 MeV is prominent in the line shape of the center crystal. Its peak height decreases with increasing detector size. For the full energy sum it becomes insignificant. For the 685.58 MeV photons, this low energetic peak is negligible even in the single crystal line shape.

5.5 Results

5.5.1 Linearity verification

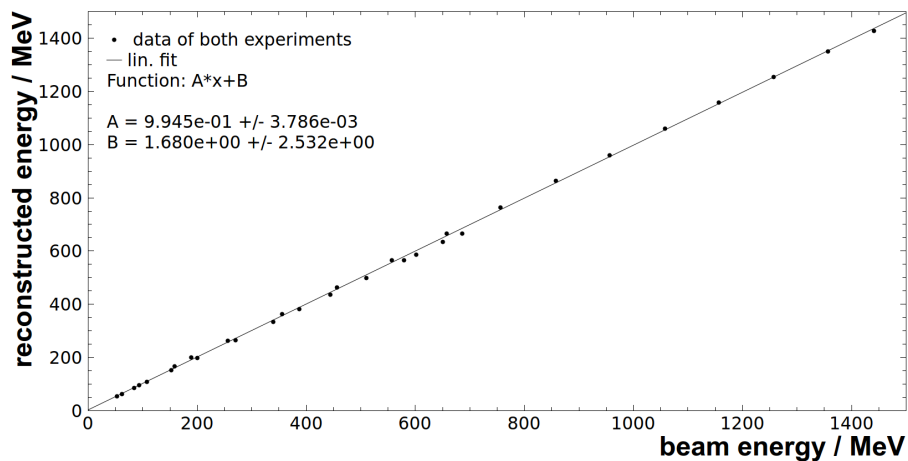


Figure 5.42: Linear response verification with the energy sum over all 60 crystals. The error bars are smaller than the size of the drawn data points.

A linear response is essential for reliable energy measurements. Possible reasons for a nonlinear response are for example a saturating preamplifier, inhomogeneities in the crystal material or the nonlinear light collection. For the verification of the linear

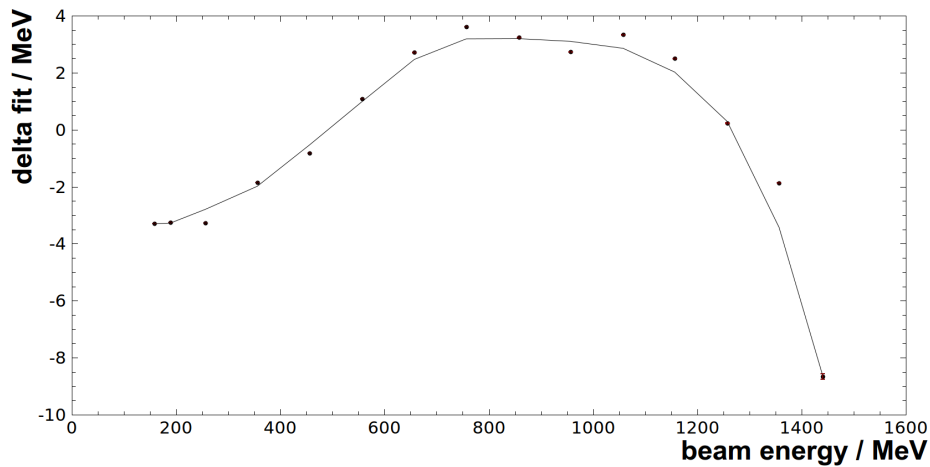


Figure 5.43: Difference between data and fit of run 1.1. The error bars are still within the size of the drawn data points.

response, the reconstructed energy is plotted against the incident beam energy. In figure 5.42 the data of run 2.4 and 1.1 is shown. For a better evaluation, the difference between a linear fit on the data of run 1.1 and the data itself are plotted against the beam energy (fig.5.43). The maximum deviation of -8.7 MeV from the ideal linear response can be found at the highest measured energy. This difference corresponds to 0.6%. Between 500 and 1200 MeV the reconstructed energy is larger and for energies below 500 MeV the reconstructed energies stay below the linear fit function.

5.5.2 Multiplicity

The multiplicity is the number of crystals which create a signal above the threshold for an event like an impinging photon. Its value depends on the particle energy, the threshold value and is subject to statistical fluctuations. The mean values are determined assuming a Gaussian distribution fit (fig.5.44). At the highest measured energy of 1441.06 MeV a mean multiplicity of 22 and 32 at maximum is obtained. At 52.34 MeV, the lowest measured energy, there are only 4 crystals delivering a signal above the threshold. A difference between the two experiments can be observed (fig.5.45). The data of the second experiment shows lower multiplicity values for similar energies.

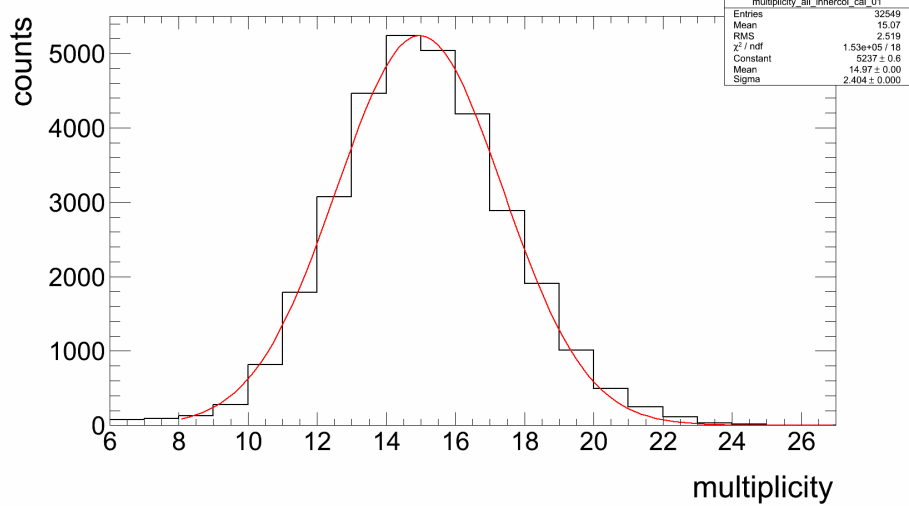


Figure 5.44: Exemplary multiplicity for 685.58 MeV photons.

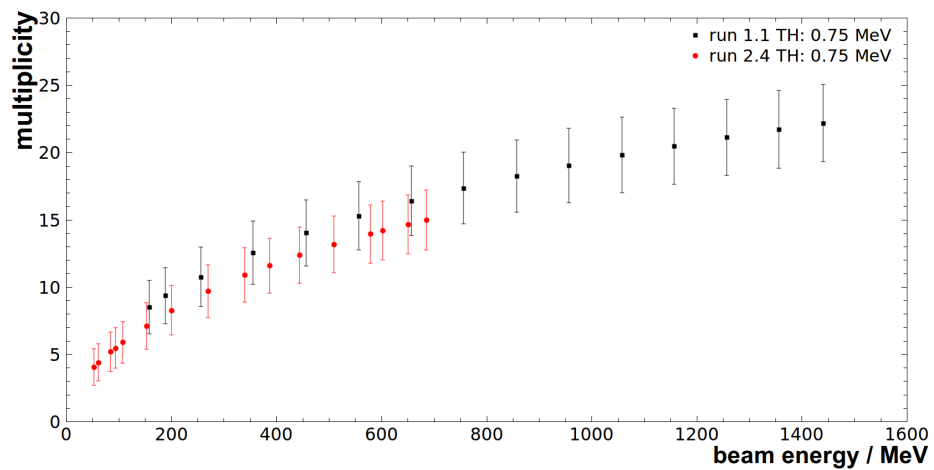


Figure 5.45: Multiplicity against the energy. The error-bars are the width σ of the distribution.

5.5.3 Influence of dead material

In the following chapter the analysis concerning the influence of the dead material will be presented. Due to the malfunction of the plastic detectors, GEANT simulations are presented afterwards for a more complete picture.

5.5.3.1 Experimental data

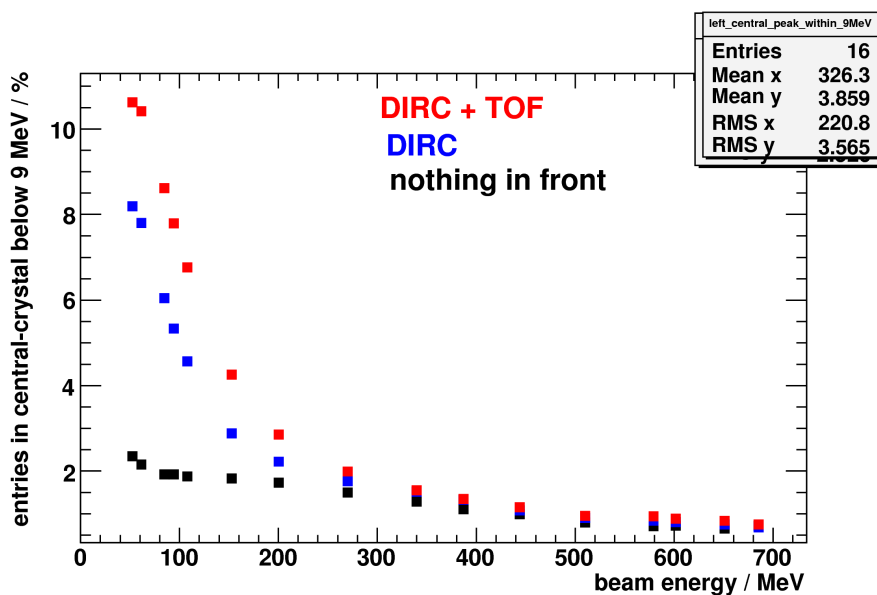


Figure 5.46: Percentage of the number of events with an energy deposition less than 9 MeV in the central crystal for the runs 2.2, 2.3 and 2.4.

In order to quantify the effect, the characteristics of low energy deposits over the full energy range is shown in figure 5.46. Here the percentage of the number of events with an energy deposition below 9 MeV in the central crystal can be seen. The entire absorber material in front causes a complete energy misidentification in 10.6% of all 52.32 MeV photons by using only a single matrix module. On the other hand only 2.4% of the 52.32 MeV photons are lost due to misidentification if the additional material is removed totally. The DIRC alone in front causes an 8.1% photon loss at the lowest energy. Above 300 MeV photon energy this effect is negligible within the single crystal. Summing up the deposited energy of several crystals reduces this complete

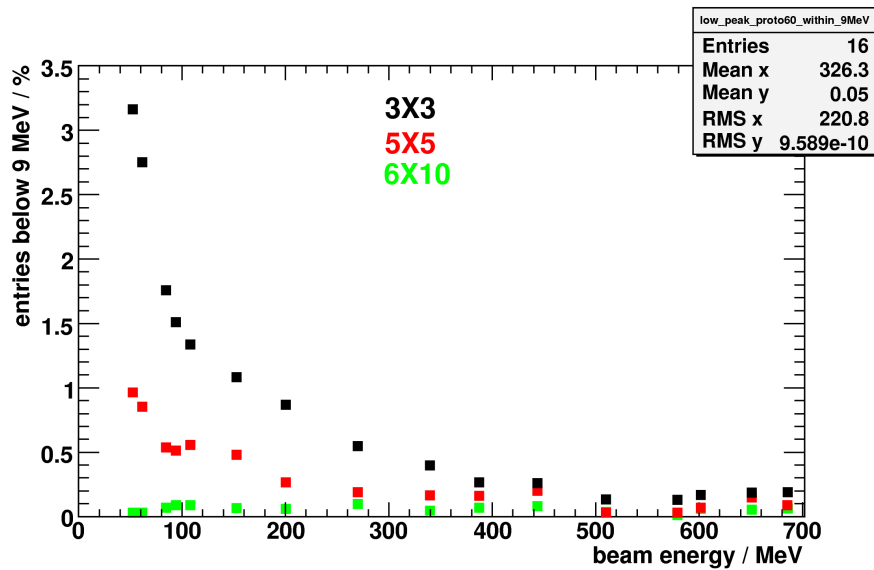


Figure 5.47: Percentage of the number of events with an energy deposition less than 9 MeV in different matrices for run 2.2 (DIRC+TOF in front). The 100% reference is given by the corresponding tagger response.

photon loss. The loss values for different matrix sizes with the complete absorber material in front, are shown in figure 5.47. Increasing the detector matrix reduces the effect. The values at the lowest energy are 3.15% for a 3×3 matrix, 0.95% for a 5×5 and close to 0% for the complete PROTO 60. Nevertheless, the additional material deteriorates the line-shape of the photo-peak. The most significant deformation arises in those events where less than 9 MeV of the incident photon energy are deposited within the central crystal (fig.5.48). In order to quantify the distortion, the following procedure is applied. The peak positions of the energy sum of all runs during the second experiment are similar within the error margin for the same incident energy. Therefore the peak and σ values for run 2.1 were determined with the Novosibirsk function (sec.5.5.4) and used as cuts in all data of the second experiment. An example is given in figure 5.49. 34.92% of the entries remain in the low energy tail below σ , 21.15% below 2σ and 14.12% below 3σ , respectively. The histogram entries below 3σ over the measured energy range are shown in figure 5.50. Without additional absorber material in front for 6% out of all events an energy less than 3σ below the peak energy are reconstructed. This value increases slightly at high energies. In case of placing the DIRC in front, 12% of all 52.35 MeV events shift below 3σ . This value increases

until 100 MeV up to 13% and falls of towards 7.5% for the highest measured energy. Adding in addition the TOF dummy, the values starting with 11.8%, reach almost 16% at 100 MeV and approaching to 8.5% at the highest energy.

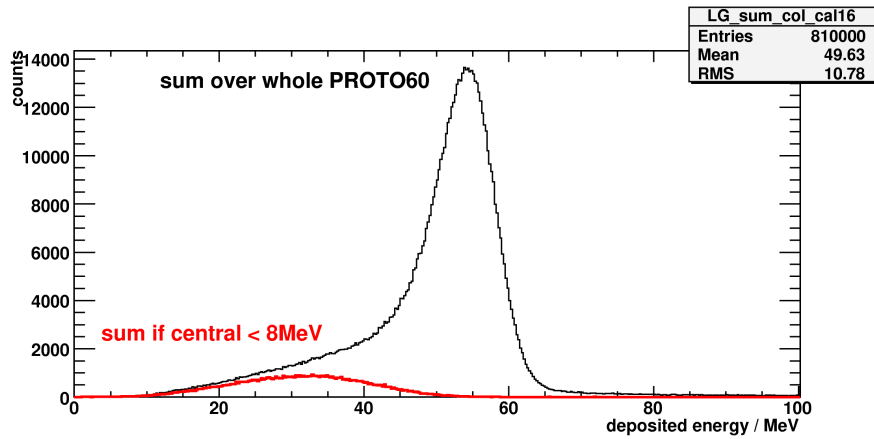


Figure 5.48: Energy sum over the 10×6 matrix of run 2.2.

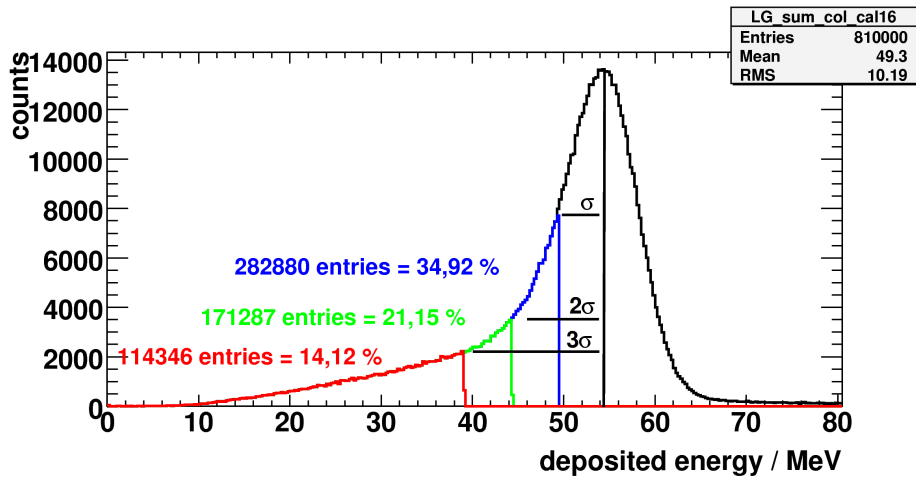


Figure 5.49: Example for quantifying the line-shape deformation due to the additional material in front. The 10×6 energy sum of run 2.2 is shown.

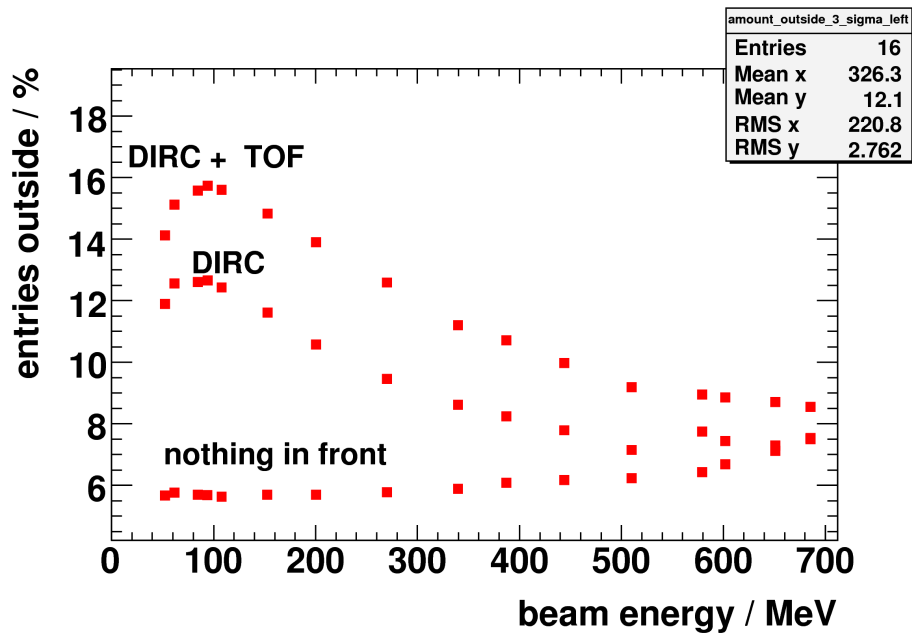


Figure 5.50: Low energetic histogram entries below 3σ , as shown in figure 5.49.

5.5.3.2 Simulations

In the simulation, a cuboid of $30 \times 30 \times 2$ cm SiO_2 was added in the same position as the DIRC bar during the experiments. A homogeneous beam with a radius of 4 mm was shot in the middle of crystal 35. 50000 events were simulated. The PROTO 60 model without the nonuniform light collection was used in order to study the pure influence of the additional material. In figure 5.51, two simulation examples based on a few events are shown. Only tracks of charged particles are drawn. They are created within the DIRC or the crystals due to conversion. Disregarding the backscattered particles, the difference in the opening angles of charged particles created in the DIRC material can be seen by comparing the two pictures. The mean opening angle follows equation 5.1. In case of 52.32 MeV photons, a few charged particles even pass the 6×10 matrix. Many of them require at least a 5×5 matrix for their detection. For 1 GeV photons, most of the charged particles can be collected even within the central crystal. In the line shape of the central crystal, the low energetic peak can be found in the simulation as well (fig.5.52). Its peak position is in the order of 0.5 MeV. In case of conversion in the DIRC, the measured energy is distributed over the complete range up to the incident photon energy. In the energy sum over the

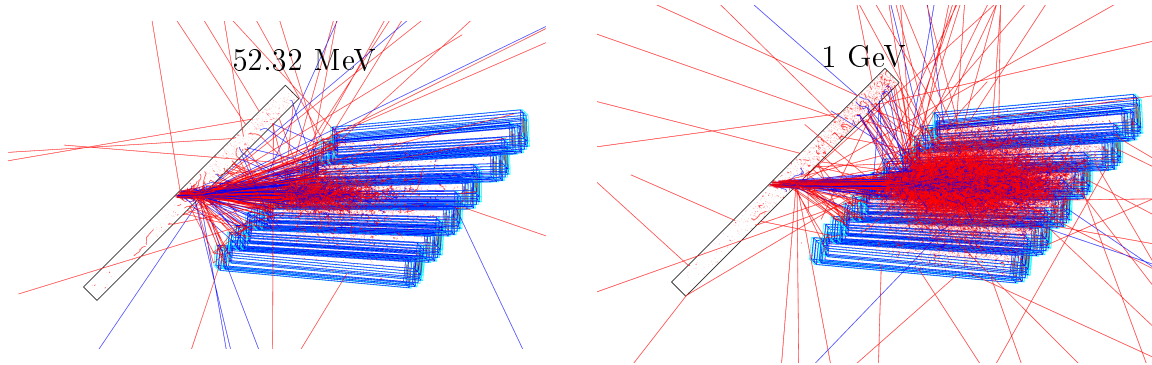


Figure 5.51: GEANT simulation of the experiment with the DIRC sample. Only charged particles are drawn. 1000 photons with 52.32 MeV and 500 photons with 1 GeV were simulated.

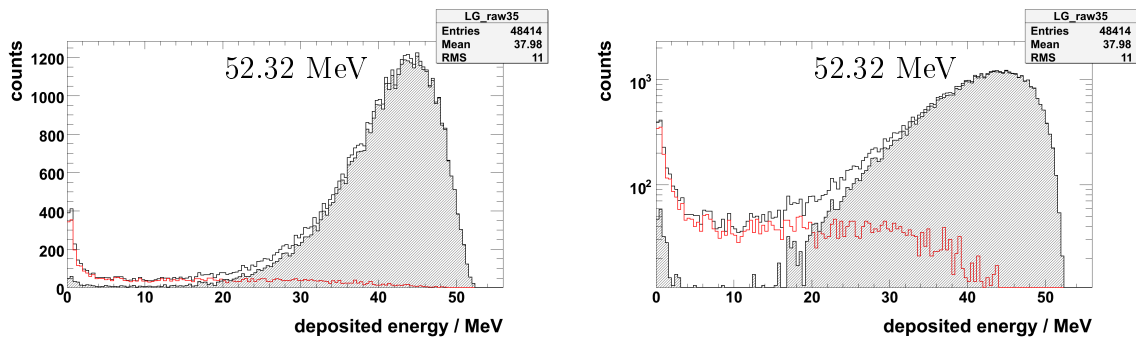


Figure 5.52: GEANT simulation of the experiment with the DIRC sample. The energy deposition in the central crystal is plotted. The red curve represents the deposited energy when conversion in the DIRC occurred, the black curve with the shaded area when no conversion occurred and the black curve all events.

Chapter 5 Experiment at MAMI

full detector, the low energetic peak disappears in the spectrum (fig.5.53). A broad distribution can still be observed. This distribution approaches the line shape, which excludes conversion within the DIRC, at high energies. The probability of the observed

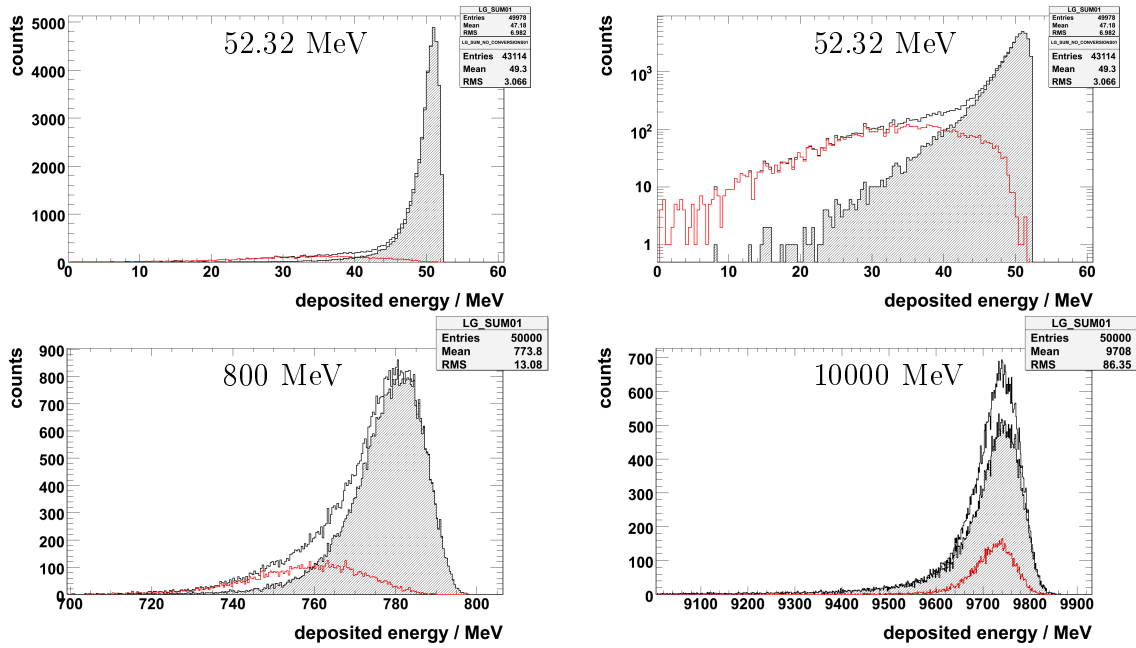


Figure 5.53: GEANT simulation of the experiment with the DIRC sample. The energy sum over 60 crystals is plotted. The red curve represents the deposited energy when conversion in the DIRC occurred, the black curve with the shaded area when no conversion occurred and the black curve all events.

conversion within the DIRC material is in the order of 19% for high energies. Its value decreases with decreasing energy. The characteristic is plotted in figure 5.54. Similar as in chapter 5.5.3.1, a measure for the line shape deterioration can be stated. 4σ is chosen as a limit due to the analysis of the pure energy deposition. In figure 5.55 the reconstructed events within the chosen limit are shown. The largest impact can be found near 100 MeV photon energy. For lower and for higher energies the efficiency increases.

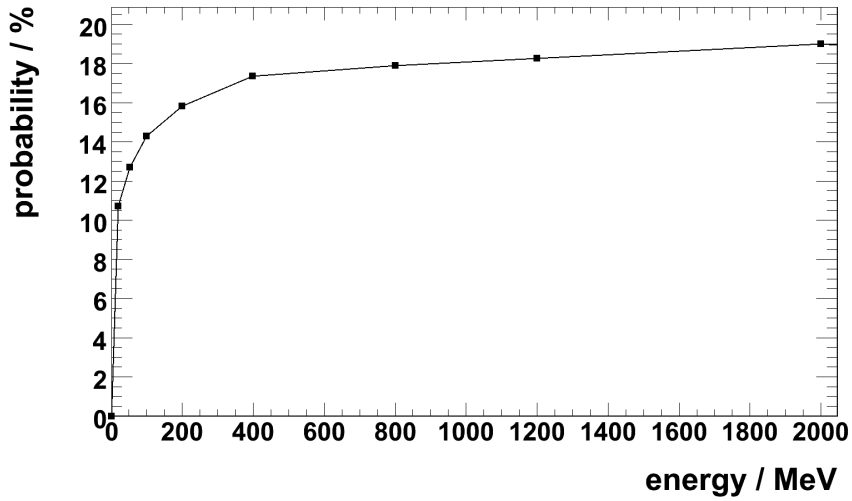


Figure 5.54: Conversion probability within the DIRC.

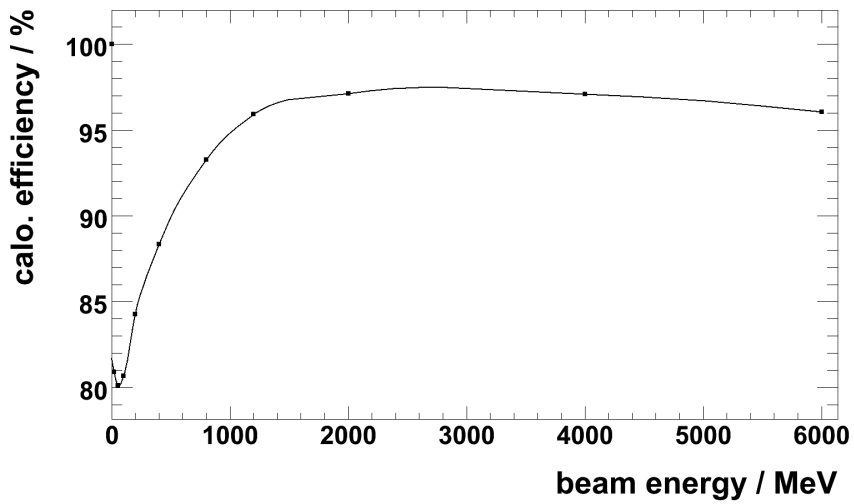


Figure 5.55: Calorimeter efficiency with the SiO₂ cuboid in front. As a limit, 4σ of the unaffected line-shaped was considered.

5.5.4 Energy resolution

It is well known that the fit result, and therefore the determined resolution, depends on the chosen bin width of the histogram. According to Knuth [KNU06], the optimum binning for a Gaussian distribution are 5 bins within the FWHM and 14 bins for the complete distribution, respectively. Due to the more complex Novosibirsk function and with respect to the low energetic tailing, approximately 10 bins within the FWHM are considered for the analysis. The individual results of all six measurements are summarized in figure 5.56 and 5.58. The data is always shown for the complete prototype energy sum with a threshold of 0.75 MeV per module. Without any dead material in front and a beam impact point in the center of the crystal front-face (run 1.1 and 2.4), the resolution in the second experiment appears better. Moving the beam spot away from a crystal center deteriorates in addition the resolution (run 1.1, 1.2 and 1.3). Mainly the constant term of the resolution parametrization is affected. For energies below 250 MeV the resolution for the runs with dead material in front (run 2.2 and 2.3) could not be determined, since the distorted line shape cannot be described with the standard fit function (fig.5.57).

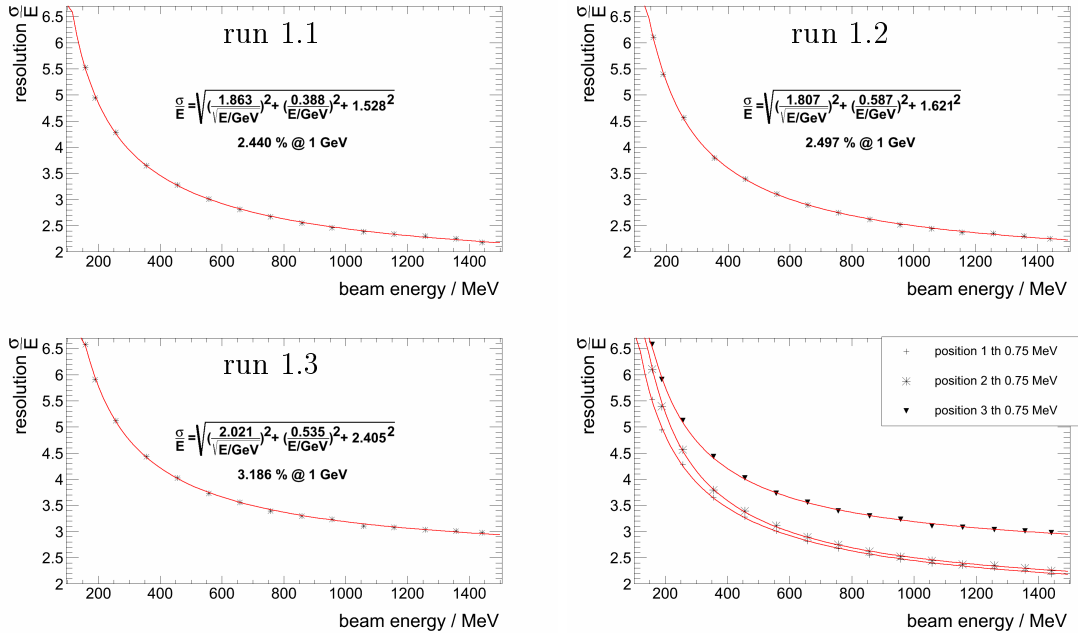


Figure 5.56: Obtained resolution for the full energy sum from the analysis of the first experiment.

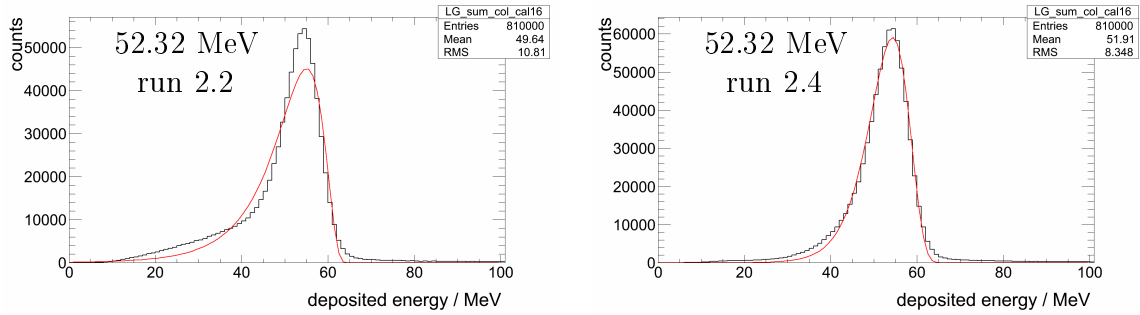


Figure 5.57: Comparison of the fit accuracy. For low energies, the fit function does not sufficiently reproduce the line shape in case of dead material in front of the detector (run 2.2).

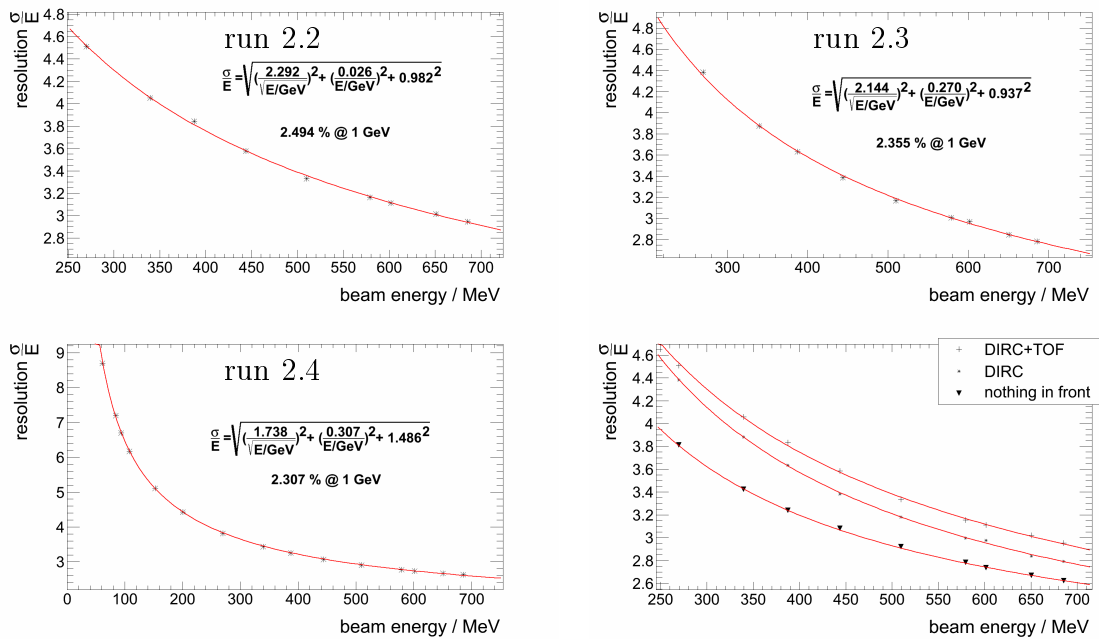


Figure 5.58: Obtained resolution for the full energy sum from the analysis of the second experiment.

Chapter 6

Experiment at CERN

In order to investigate the response of the prototype PROTO 60 at the highest design energy, an experiment at the north area (H4,NA57) of CERN was performed. Runs using 15 GeV positrons and for calibration a 150 GeV muon beam were taken together with cosmic radiation. For the data-acquisition, exclusively sampling ADCs were chosen. The experiment was done in conjunction with prototype tests of the micro vertex detector of PANDA. The provided data will furthermore be analyzed within the work of D. Bremer [BRE13], investigating aspects of position reconstruction of the electromagnetic shower.

6.1 The accelerator facility

A detailed description of the whole CERN accelerator facility (fig.6.1) can be found in [LHC1], [LHC2] and [LHC3]. A brief overview of the components relevant for this work, will be given in this section. The utilized beams start with the production of protons. Hydrogen gas is passing through an electric field to strip off its electrons and the obtained protons are accelerated to 50 MeV inside the LINAC¹. As a next step, the protons are injected into the Proton Synchrotron Booster. It consists of 4 beam-rings above each other with a radius of 25 m each and accelerates the protons up to 1.4 GeV. A magnet system guides the particles into the next synchrotron (PS)². It is a ring accelerator with a circumference of 628.3 m and releases a beam of 25 GeV into the

¹LINAC = Linear Accelerator

²PS = Proton Synchrotron

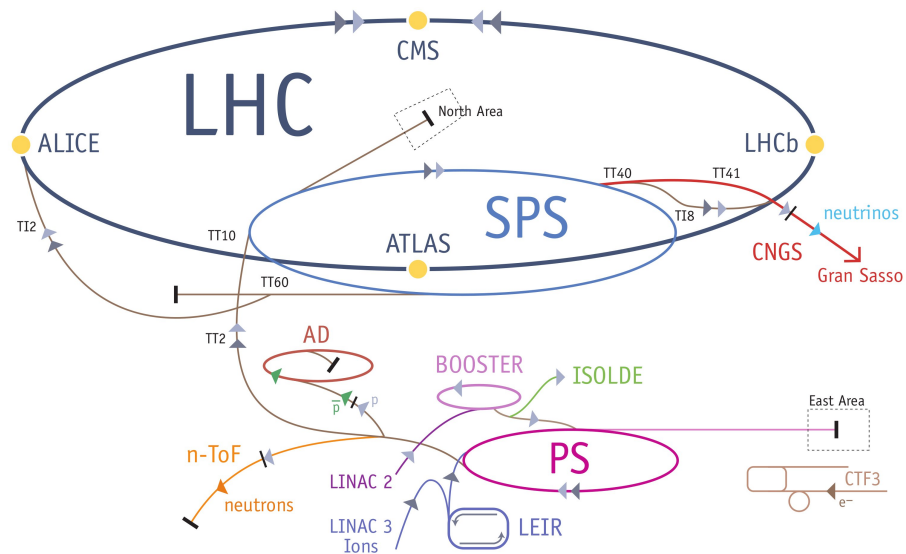


Figure 6.1: CERN accelerator complex overview. Picture taken from [LEV08].

Super Proton Synchrotron (SPS). This synchrotron has a circumference of 6912 m. Within 21.6 seconds, the particles are accelerated further to 450 GeV. From there the beam can be extracted into the two collector rings of the Large Hadron Collider (LHC). Each ring has a circumference of 26659 meters and accelerates the protons up to an envisaged energy of 7 TeV before they collide. For the measurements in the context of this work, the protons are extracted from the SPS into the north area where they can be distributed to several beam lines. Via target interactions and a selective magnet system, various leptons and hadrons with certain energies can be created inside every beam line. The new generated beams are referred to as secondary and tertiary beams, depending on the number of intermediate steps for their creation.

6.2 Experimental setup

For the present experiment, the PROTO 60 setup including data acquisition, power supply, nitrogen for detector flushing and a vacuum pump was placed in the area NA57 of the H4 beamline, behind the Goliath [NA57] magnet. The detector was mounted again on top of the computer controlled XY table and aligned to the beam axis with lasers. A coincidence of two plastic detectors was used to generate a trigger-signal for the data acquisition. Two \bar{P} ANDA MVD silicon strip prototypes were placed in

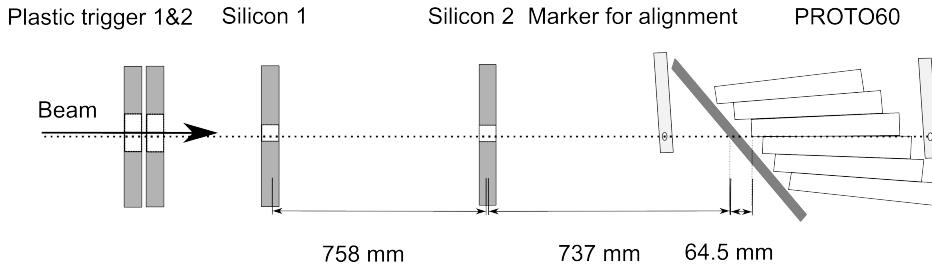


Figure 6.2: Detector setup at CERN.

front of the PROTO 60. They had a distance of 1495 mm and 737 mm respectively, measured from the center of the PROTO 60 front face (fig.6.2). A detailed description of the MVD readout is given by M. Becker et al. [BE11].

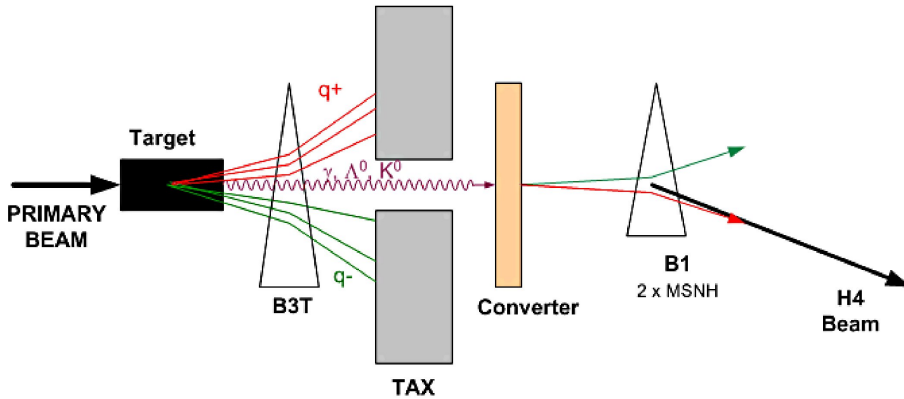


Figure 6.3: Simplified schematic of the H4 beam-line for the positron beam production. The triangles represents magnets. TAX are motorized beam-dump and collimator modules. Not all available magnets, targets and TAX modules are drawn. Picture taken from [EFT03].

The used positrons were produced as a tertiary beam. For production, protons from the SPS interact first with a target. Afterwards all charged particles are removed with the help of a magnetic field and absorbed in a motorized beam-dump and collimator module (TAX) (fig.6.3). A second target is used to convert the created γ s among the neutral particles into e^+e^- pairs. An additional magnet separates the positrons from the electrons. Finally magnets and collimators in the beamline select 15 GeV positrons with a momentum spread of $\frac{\Delta p}{p} = 0.7\%$. Positrons were chosen due to the superior beam quality with respect to momentum spread and mixture of background particles. The 150 GeV muons were obtained by stopping all other secondary particles in a closed collimator before the last bending magnets of the beam line.

6.2.1 Data acquisition

The signals of all PROTO 60 preamps, except the first and last detector matrix column, were read out with SIS3302 SADCs³ made by Struck Innovative Systeme (Hamburg, Germany). Their inputs have a dynamic range of 5 V (PROTO 60 preamp. output max. 2 V), with 16-bit resolution. A sampling rate of 50 MHz was used. The signal shape was sampled at 250 consecutive positions. The digitized pulse shapes were treated with feature extraction algorithms. Due to the long decay constant of the preamps of $\tau = 25 \mu s$, a Moving Window Deconvolution (MWD) was applied. This algorithm reduces the width of the pulse and can be described by the expression:

$$MWD_M(n) = x(n) - x(n - M) + \frac{\ln 2}{\tau} \sum_{i=n-M}^{n-1} x(i). \quad (6.1)$$

The parameter M defines the desired pulse length and $x(n)$ is the signal value of the input sample number n out of the 250 samples. The noise level can be reduced with a Moving Average (MA) filter. This algorithm smooths the signal difference of L samples and can be described by the following expression:

$$MA_L(n) = \sum_{i=n-L}^n x(i). \quad (6.2)$$

According to M. Kavatsyuk et al. [KAV11], for an optimum energy resolution the length of the MWD parameter M should be larger than the signal rise time ($M > 200$ ns) and the length L should be between 80 ns and 400 ns, depending on the event rate and the desired or tolerated noise level, respectively. Therefore $M = 240$ ns and $L = 100$ ns were chosen for this analysis (fig.6.4). After the MWD and MA algorithms, the energy information was extracted from the difference of the highest signal within the 250 samples and the baseline BA :

$$BA = \frac{1}{60} \sum_{n=40}^{100} x(n). \quad (6.3)$$

The read out numbering of the 8×6 matrix, as used in this experiment, is shown in figure 6.5.

³SADC = Sampling analog to digital converter

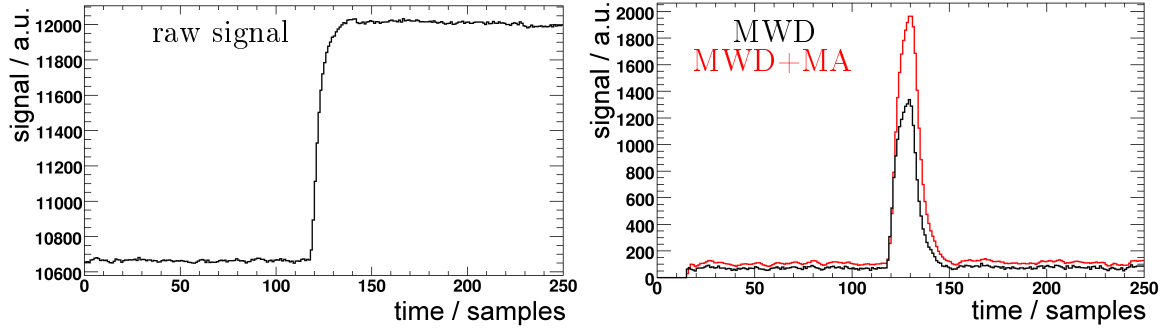


Figure 6.4: Example of recorded and processed PROTO 60 preamp signal digitized with a SADC.

	8	7	6	5	4	3	2	1	
	16	15	14	13	12	11	10	9	
	24	23	22	21	20	19	18	17	
	32	31	30	29	28	27	26	25	
	40	39	38	37	36	35	34	33	
	48	47	46	45	44	43	42	41	

Figure 6.5: The numbering of the read out channels from the beam perspective at CERN.

6.3 Experimental procedure

In order to obtain a stable operating state of the PROTO 60 at -25°C , the whole setup was put into operation a day before the experiments. For the beam measurements, the detector was moved by the XY table until the beam axis was located in the center of crystal 28. The crystal with the number 28 was labeled 35 during the previous experiments at MAMI. At first, all LAAPD high voltages were set to the same values as used in the previous measurements. These values produce a gain of approximately 150 (chapter 5.2.2). According to the estimations of the dynamic range of the PROTO 60 preamps (table 3.2) in chapter 3.2, this gain corresponds to a dynamic range of approximately 5 GeV. The minimum dynamic range needed is shown

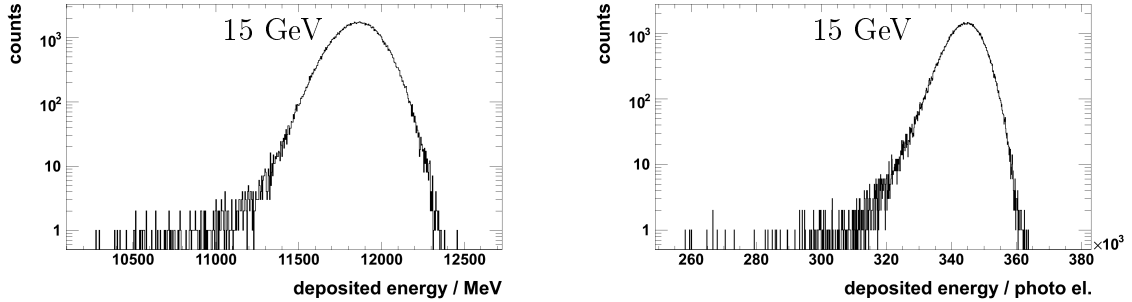


Figure 6.6: GEANT simulation of 15 GeV positrons with the PROTO60 and PROTO60-NUF-NOISE model. The central crystal is shown.

in figure 6.6. A GEANT simulation with a 15 GeV positron beam in the center of a PROTO 60 crystal indicates a maximum energy deposition of 12.4 GeV in the center crystal and 1.4 GeV in its neighboring crystals. The PROTO60-NUF model delivers at maximum $3.65 \cdot 10^5$ photoelectrons within the same simulation. With respect to the maximum preamp input charge of 4 pC, the LAAPD gain has to be less than 68.5 in order to process the simulated $3.65 \cdot 10^5$ photoelectrons of the central crystal. Due to the unknown correlation of the voltage and gain, the voltages were adjusted during first test beam measurements with respect to the planned measuring program of two different positions. Adapting to the maximum deposit the HV of the LAAPD was reduced to exclude saturation of the preamplifier. For the actual measurements, data were collected for two detector positions. On the first position the beam was centered at crystal 28 and shifted in between crystal 28 and 29 in the second run. Finally a broad 150 GeV muon beam illuminated the whole PROTO 60. A standard calibration with cosmic radiation was taken for several hours.

6.4 Data analysis

The size of the 15 GeV positron beam spot can be approximated with the silicon prototypes (fig.6.2) with an active area of 2×2 cm. The beam spot radius in the order of 10 mm was verified with the silicon detector placed in front of the PROTO 60 (fig.6.7).

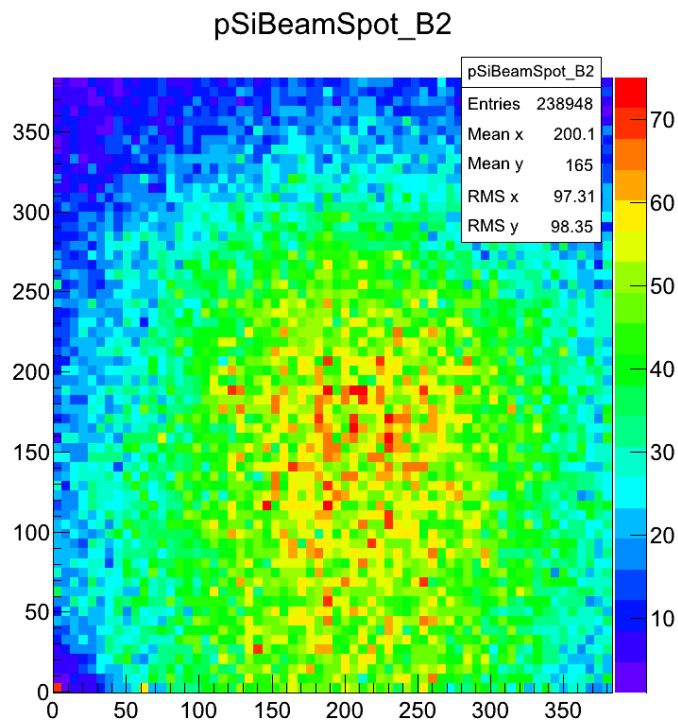


Figure 6.7: Beam-spot data of the second silicon detector. Each prototype had an active area of 2×2 cm.

6.4.1 PROTO 60 raw data

The raw data of the 15 GeV positron beam, hitting the center of crystal 28, is shown in figure 6.8. Due to the different gains of the inner crystals, the line-shapes are not directly comparable. However, a low-energetic structure in the central crystal besides the actual peak is clearly visible.

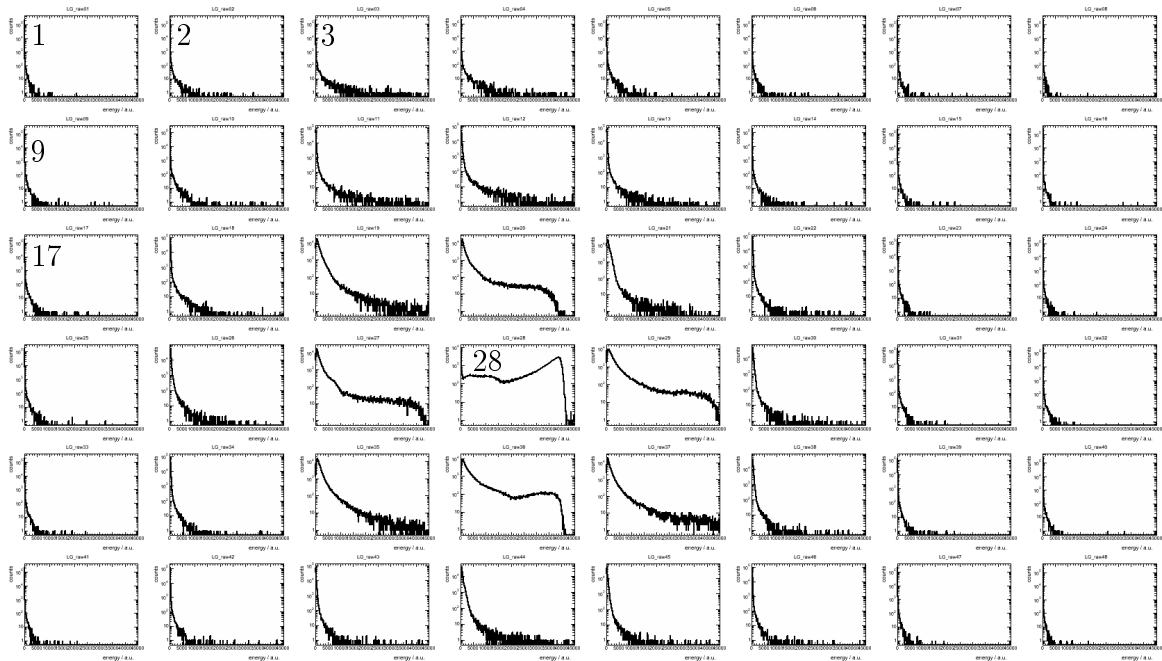


Figure 6.8: Raw data of the measurement with 15 GeV positrons, shot in the center of crystal 28. Plotted are the counts on a logarithmic scale against the energy in arbitrary units.

6.4.2 Calibration

A detailed description of the principle calibration concepts was already given in chapter 5.4.2. In contrast to the read out with peak sensing ADCs, which were used for the experiments at MAMI, the mean noise level is already subtracted due to the previously described energy extraction procedure (chapter 6.2.1). For this experiment, two different measurements are available which can be used for calibration. They will be compared and discussed.

6.4.2.1 Calibration with cosmic radiation

The calibration with cosmic radiation was already described in detail in chapter 5.4.2. It should be noted that the cosmic radiation peak still can be separated from the noise with the increased dynamic range. An overview of all read out modules, fitted with a Landau distribution, is shown in figure 6.9.

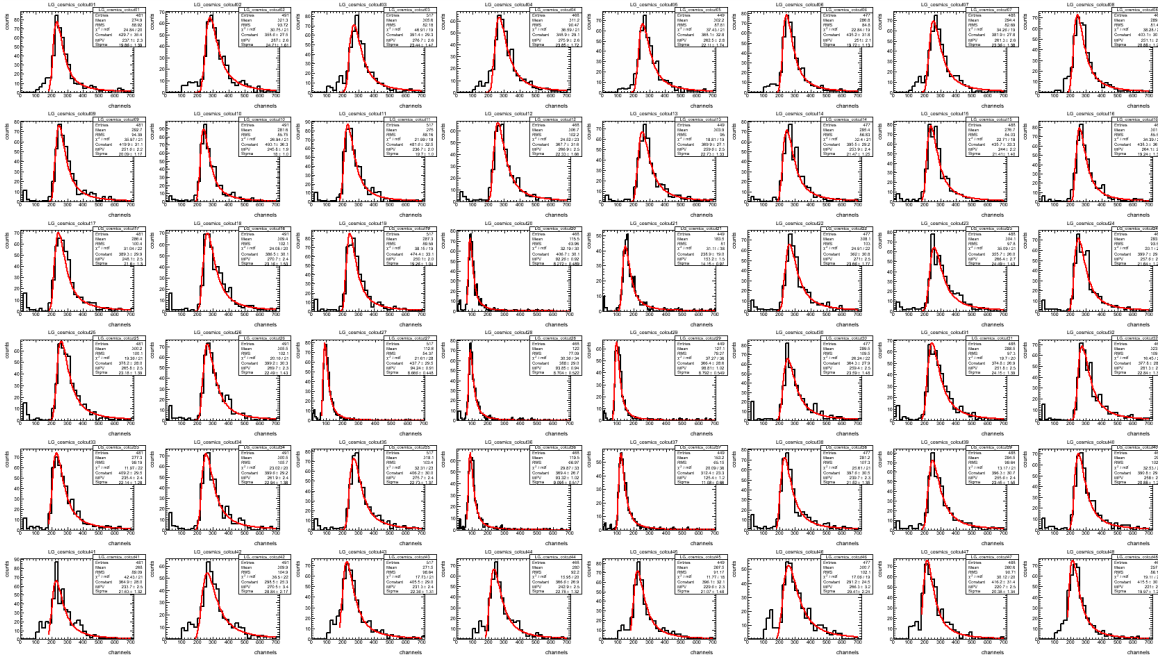


Figure 6.9: Cosmic radiation measured for calibration at CERN. The shown data includes the column cut condition.

6.4.2.2 Calibration with 150 GeV muon beam

In figure 6.10, the combined raw data of the measurements with a 150 GeV muon beam is shown. A peak within the decreasing line-shape can be clearly seen, except in some outer crystals. In order to enhance the structure in all histograms (fig.6.11), two conditions were applied to select those events where a muon went across the full length of the crystals. Only events with a multiplicity of 1 for a threshold of 10 MeV were chosen as a reasonable trade off between background suppression and the amount of remaining events. The absolute threshold value was based on cosmic calibration. The

second condition demands a deposition of more than 100 MeV in one single crystal. A fit with a Landau distribution was applied to determine the peak parameters. Instead of the values of the poorly developed peaks in the most outer crystals, the cosmic calibration was used within the muon beam calibration. For an absolute calibration,

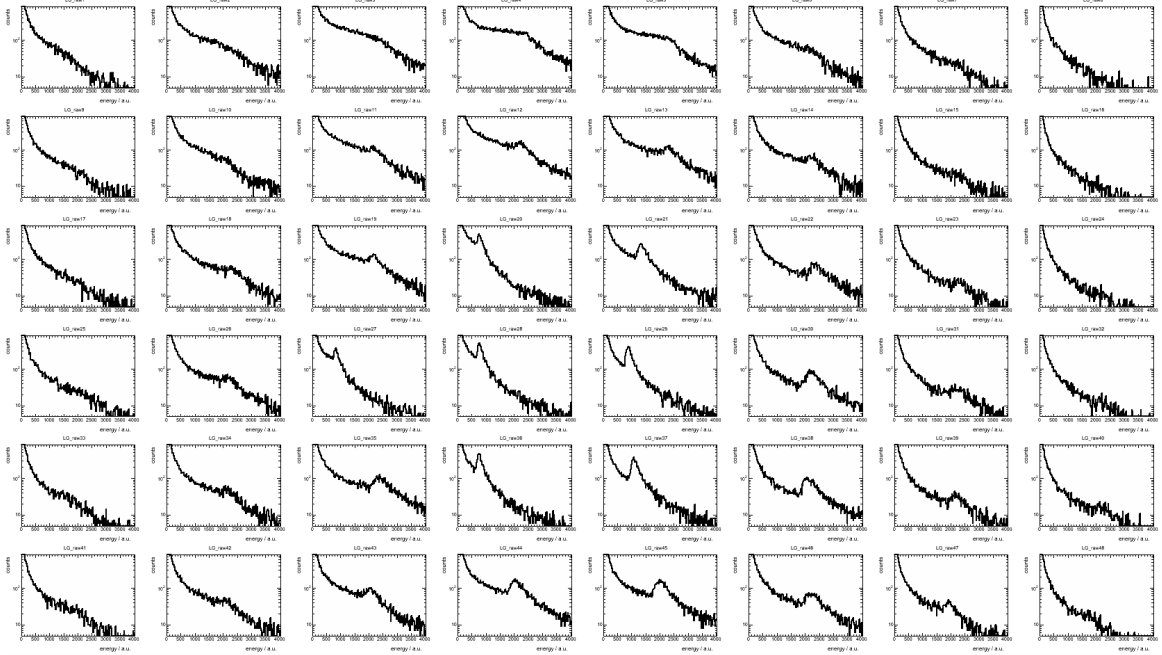


Figure 6.10: Combined raw data of the measurement with 150 GeV muons in several positions. Plotted are the counts on a logarithmic scale against the energy in arbitrary units.

an energy has to be allocated to the peakpositions of the muon beam data. According to equation 2.11 this value corresponds to:

$$\Delta_p(eq) = 234.35 \text{ MeV}, \quad (6.4)$$

calculated for the energy loss in 20 cm lead tungstate. Due to the nonuniform light collection within the crystals, a divergent beam and its passage through the air along an approximated distance of 20 m, a GEANT simulation was performed. In the simulation, an isotropic beam distribution with an opening angle of 0.1 degree, was chosen. The result is shown in figure 6.12. A fit with the Landau function reveals a deposited energy of

$$\Delta_p(sim) = 236.4 \text{ MeV} \quad (6.5)$$

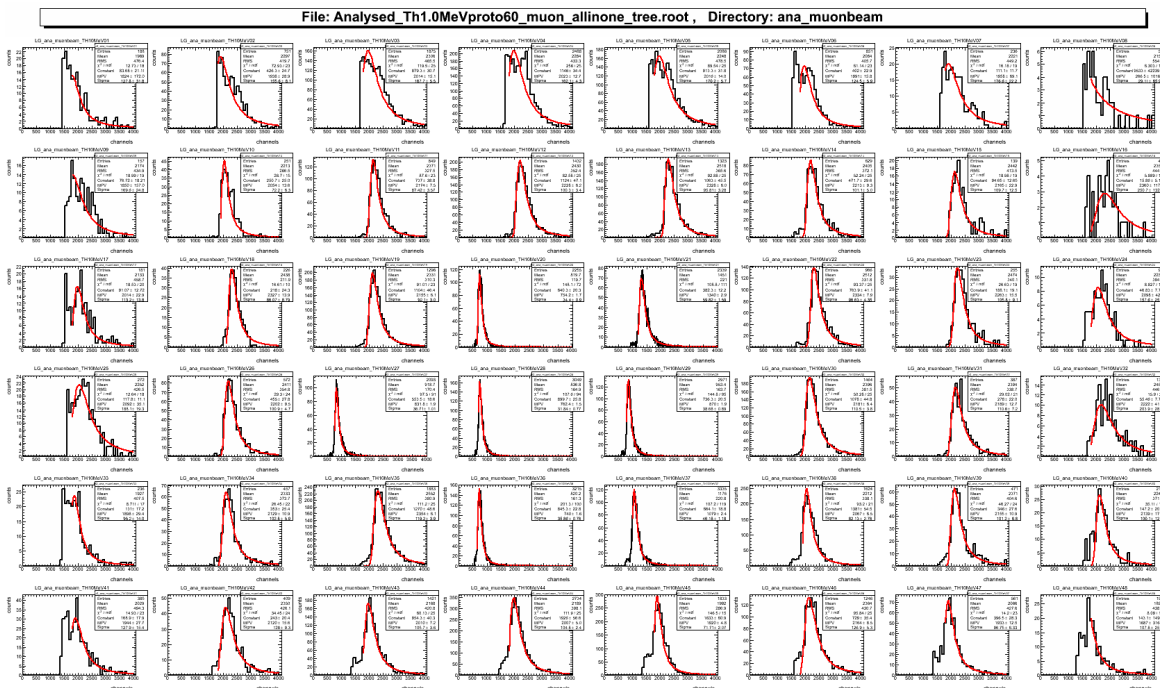


Figure 6.11: Combined data of the measurement with 150 GeV muons in several positions. A energy deposition of more than 100 MeV in one crystal and in all others less than 10 MeV was required. The threshold values were determined with the cosmic radiation calibration.

Chapter 6 Experiment at CERN

within a single crystal of the PROTO60 model. The PROTO60-NUF-NOISE model shows

$$\Delta_p(sim_{nuf}) = 6669 \text{ photo electrons.} \quad (6.6)$$

within the LAAPD. For comparison, this value is equal to a signal of:

$$E_{dep}(0 \text{ cm}) \approx \frac{6669 \text{ phe}}{32.04 \text{ phe/MeV}} = 208.15 \text{ MeV} \quad (6.7)$$

energy deposition within the first mm of the crystal.

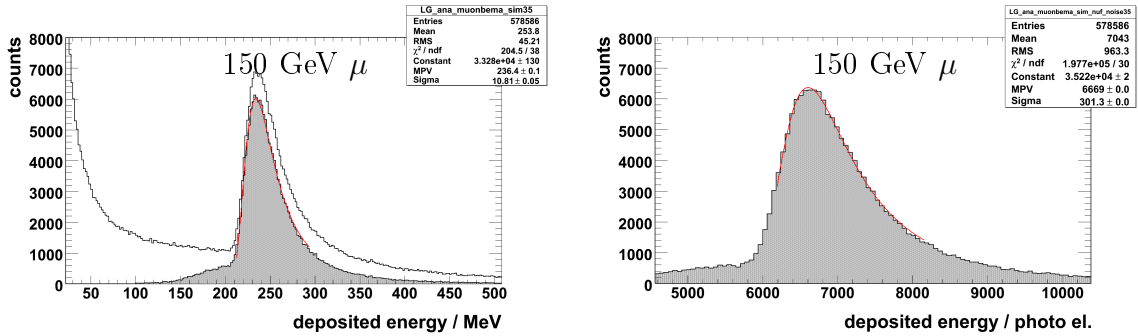


Figure 6.12: GEANT simulation of 150 GeV muons through 20 m of air with the PROTO60 and PROTO60-NUF-NOISE model. The crystal in the beam spot is shown. An energy deposition of more than 100 MeV in one crystal and less than 10 MeV in all others was required for the shaded area.

6.4.2.3 Absolute calibration alignment to GEANT

As mentioned, the reconstructed energy can be aligned to simulations after a relative calibration with the two methods described before. Therefore, a 15 GeV positron beam, at a distance of 20 m, with a radius of 10 mm, together with the PROTO60 model was simulated. Only the same inner 48 crystals, which were read out during the CERN measurements, were considered for the full energy sum. A summation threshold of 0.75 MeV per crystals was used. The peak value of the energy sum corresponds to 1.457 GeV (fig.6.13).

An absolute detector calibration, where the reconstructed energy has the same peak value of the simulation, can be obtained with an additional scaling factor applied on the relative calibration values for eachy detector module. For example, it follows that the muon beam peak needs to be set artificially to a value of $\Delta_p(align) = 227.65 \text{ MeV}$.

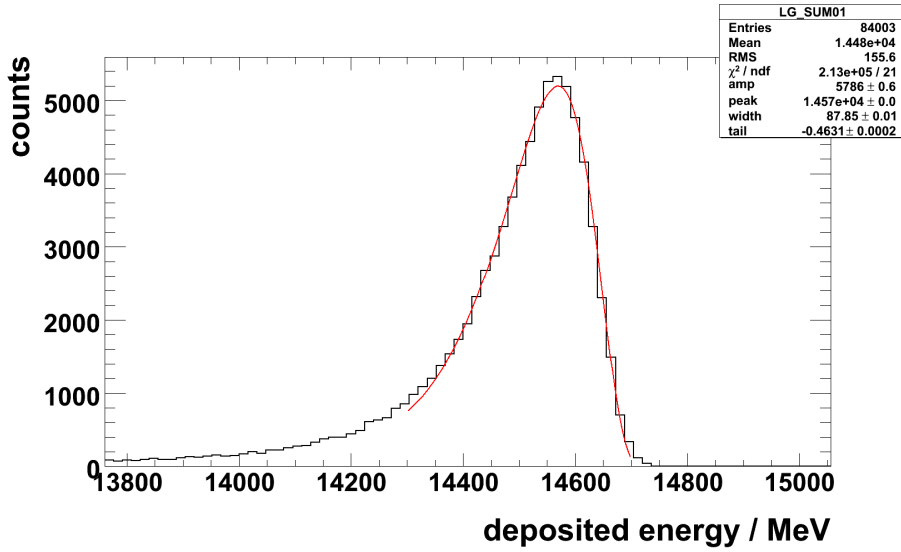


Figure 6.13: GEANT simulation of 15 GeV positrons through 20 m of air with the PROTO60 model. The energy sum of 48 crystals with a summation threshold of 0.75 MeV per crystal is plotted and fitted with a Novosibirsk function.

6.4.3 Line-shapes

In order to illustrate the line-shapes of the deposited energy within the read out crystal matrix, the muon beam calibration with $\Delta_p(sim) = 236.4$ MeV was used. Besides the expected line-shape of the central crystal 28 (fig.6.6), a broad structure between 0 and 5 GeV (fig.6.14) as well as a substructure around 100 MeV in the crystal 20 was observed. Applying a threshold of 5.5 GeV, set for the central crystal, removes the substructure in the crystal 20 (fig.6.15).

For an approximation of the used LAAPD gain, especially of the central sensor with a modified voltage, the peak of the energy sum was aligned to the GEANT simulation, which was shown in figure 6.13. With this calibration, the deposited energy distribution of the central crystal, which is shown in figure 6.16, provides information about the LAAPD gain. Besides the line-shape of the 15 GeV positrons, which ends around 12.5 GeV, a few higher energetic background events are visible peaking at 16.5 GeV. The maximum measured energy ends at 16.7 GeV. This structure could be an artifact caused by saturation of the preamp due to events exceeding the dynamic range. The already shown simulation of 15 GeV positrons with the PROTO60-NUF-NOISE

Chapter 6 Experiment at CERN

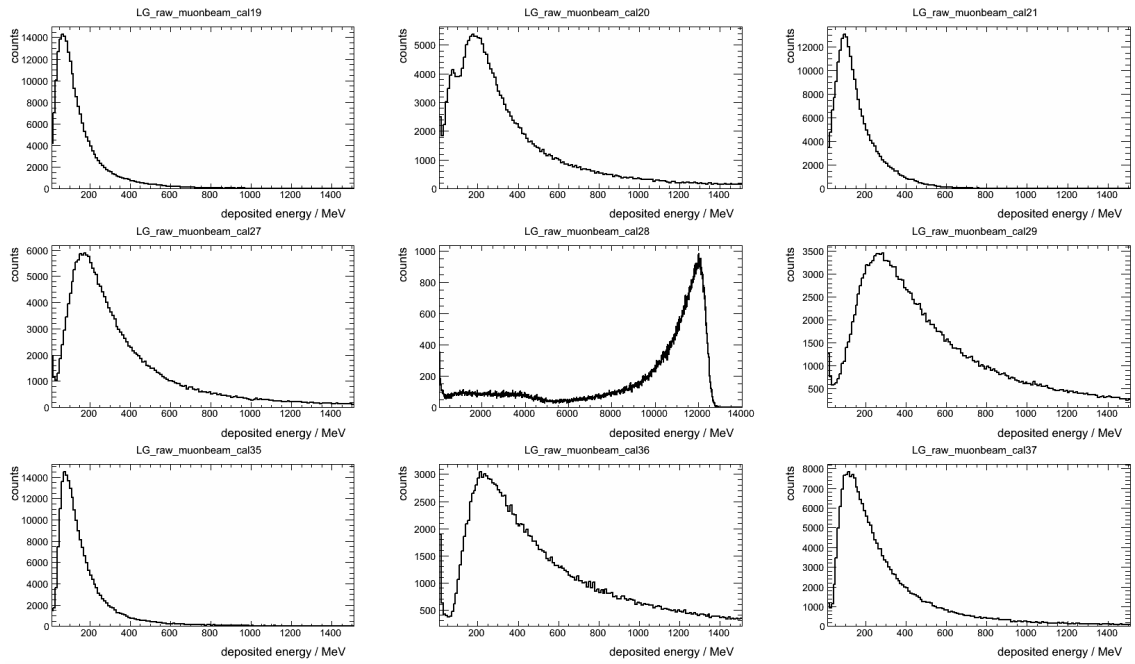


Figure 6.14: Muon beam calibrated raw data of the 15 GeV positron beam.

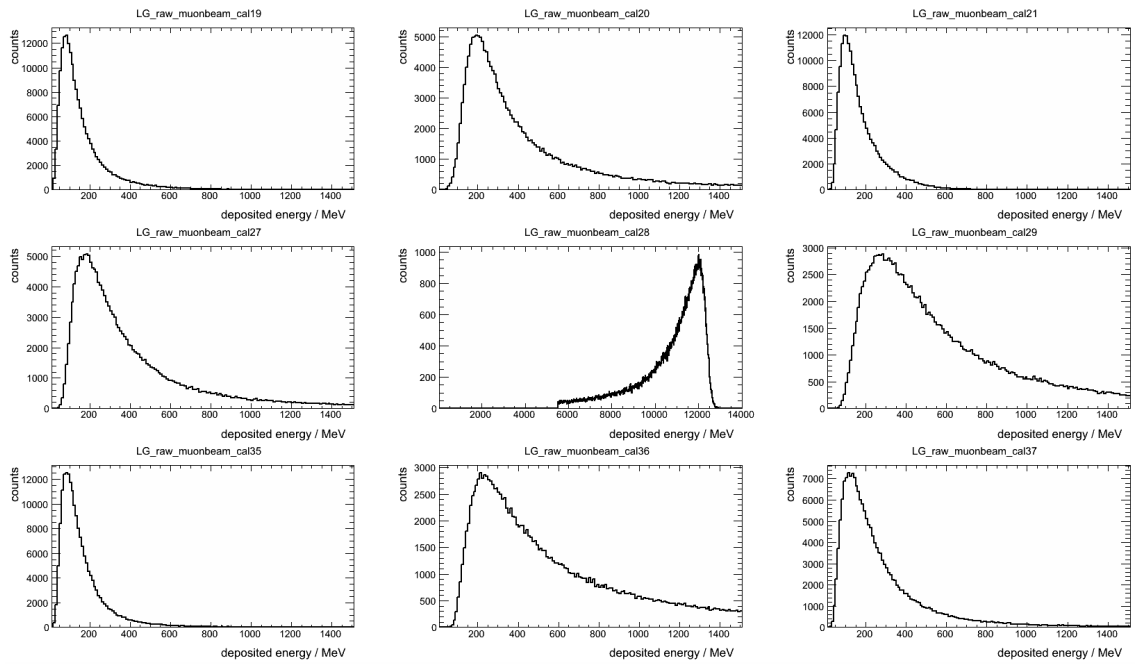


Figure 6.15: Figure 6.14 including an event acceptance threshold of 5.5 GeV, set for the central crystal.

model (fig.6.6) indicates an effective light yield of

$$\frac{3.65 \cdot 10^5 \text{ phe}}{12.4 \text{ GeV}} \approx 29.4 \text{ phe/MeV} \quad (6.8)$$

for high energies. The LAAPD gain can be calculated according to chapter 3.2. Assuming the light yield of equation 6.8, the dynamic range of 16.7 GeV corresponds to a LAAPD gain of 50.9 and 16.5 GeV to 51.5. A relative comparison of the detector calibration values, within the unmodified voltages, shows an average LAAPD gain of 136. Due to a safety margin within the dynamic range of the preamps, these gain values represent only a lower limit.

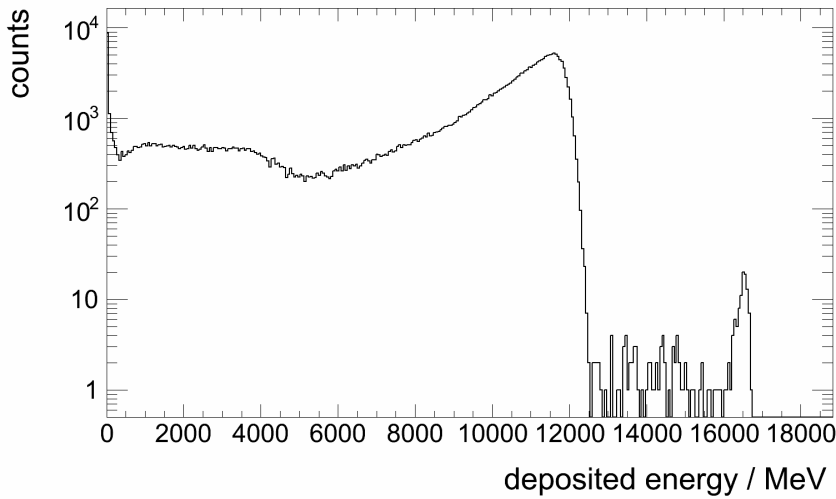


Figure 6.16: Calibrated raw data of the beam impinging crystal for 15 GeV positrons.

6.5 Results

The energy resolution of the CERN data was determined with the Novosibirsk function as well. In comparison, the two different calibration methods show no major difference in the energy resolution (fig.6.17). This indicates an equivalent relative calibration quality. The influence of the chosen fit range has a larger impact on the determined resolution. The result of a fit over the full line-shape is a resolution of $\sigma/E = 1.72\%$ in case of the cosmic radiation calibration and $\sigma/E = 1.69\%$ in case

Chapter 6 Experiment at CERN

of the muon beam calibration. A more restricted fit range delivers $\sigma/E = 1.62\%$ or $\sigma/E = 1.61\%$, respectively. The reconstructed absolute energy depends on the calibration method. The cosmic calibration leads to a peak value of 13.05 GeV and the muon beam calibration a value of 15.33 GeV. As a next step, the muon beam data

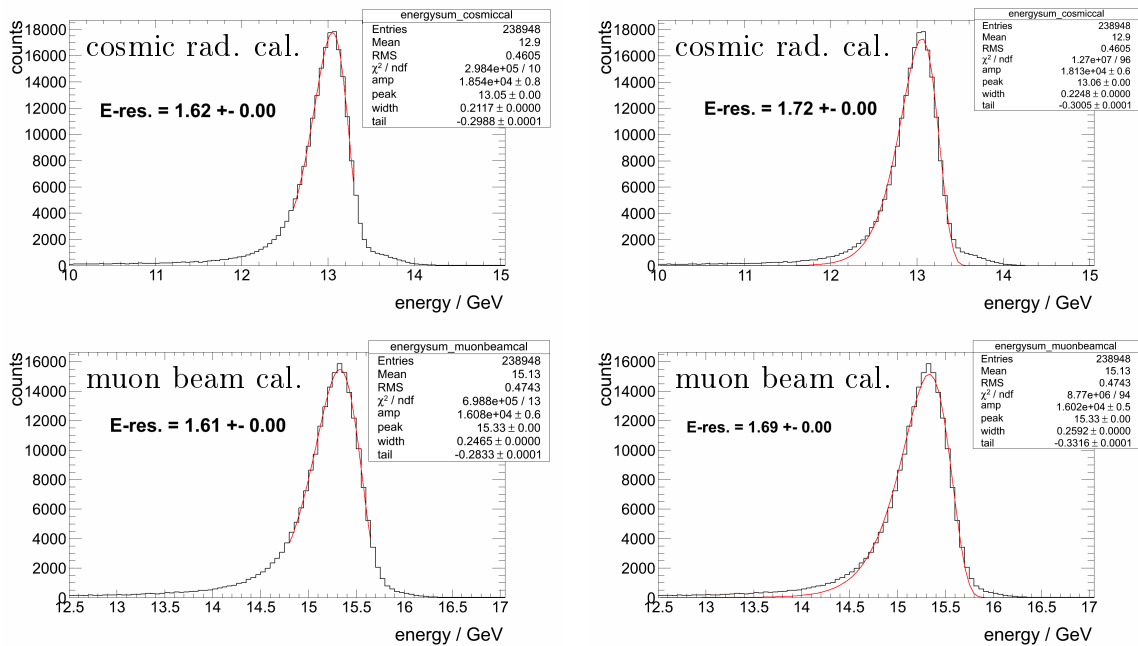


Figure 6.17: Energy sum of all 48 crystals with a threshold of 0.75 MeV and two different calibrations. The determined resolution depends on the fit range.

was used for the relative calibration and the energy sum was aligned to the GEANT simulation. By utilizing the silicon detectors, a beam spot of 2 mm radius was selected and the PROTO 60 scanned in horizontal direction. The fitted line-shapes of the energy sum for the position of the crystal center and the crystal border are shown in figure 6.18. In the center of the crystals' front face, the resolution improves. The full line-shape can be reproduced with the Novosibirsk function. Here a resolution value of $\sigma/E = 1.46\%$ was observed. At the border of two crystals only $\sigma/E = 3.2\%$ can be achieved. The complete scan with 1 mm steps is shown in figure 6.19.

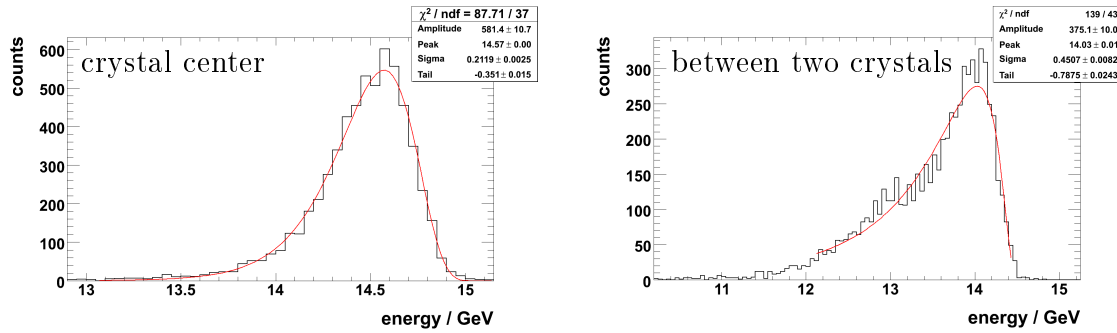


Figure 6.18: Energy sum of all 48 crystals with a threshold of 0.75 MeV. The data was relatively calibrated with the muon beam. The energy sum for the central beam position was aligned to the GEANT simulation for the absolute calibration. A beamspot radius of 2 mm was chosen with the silicon detectors.

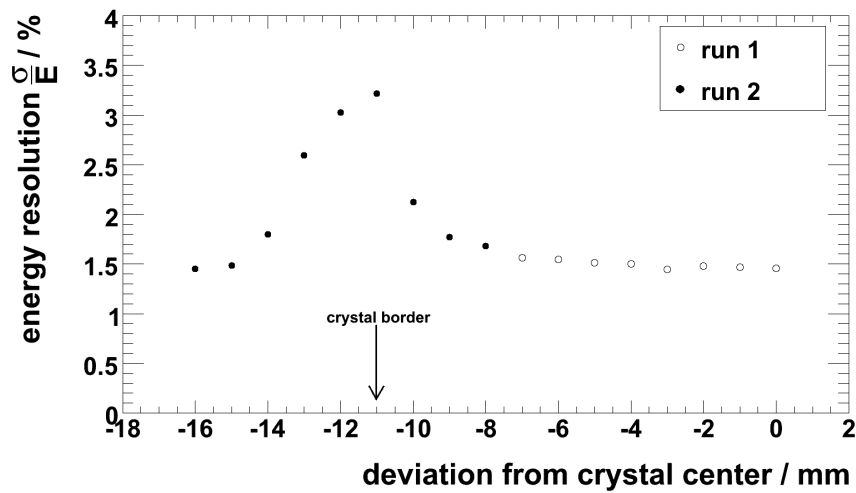


Figure 6.19: Resolutions of the full energy sum, for several positions, measured with 15 GeV positrons. A beamspot radius of 2 mm was chosen with the silicon detectors.

Chapter 7

Optimum APD gain measurements

As indicated in chapter 2.4.1.4 (fig.2.13), the APD gain has to be optimized to achieve the best energy resolution. So far, there was no detailed experience and sufficient knowledge of the APD performance and characterization. Optimum parameters were determined after the performed test measurements with the PROTO 60, the results will be shown in this chapter. All measurements for determining the optimum gain were based on a future Hamamatsu version S11048, $14 \times 6.8 \text{ mm}^2$ with the serial number AA0158 (chapter 2.4.1.4) in combination with the discrete charge preamplifier LNP SP883a (chapter 3.2). Similar measurements were done at $-25 \text{ }^\circ\text{C}$ with a peak sensing ADC and at $+18.5 \text{ }^\circ\text{C}$ with a sampling ADC read out, respectively.

7.1 Voltage to gain relation

The characteristic gain-voltage curve of the AA0158 APD was determined for different temperatures.

In a first study, the utilized APD was measured and tested at the APD laboratory Frankfurt (A. Wilms, Institut für Kernphysik, Goethe-Universität). Amongst other parameters, the corresponding voltages for three selected gains were measured as a function of temperature. Part of the provided data sheet is shown in figure 7.1. For calibration, a unity gain can be assumed at low voltages (20 to 50 V). A stabilized monochromatic LED is used as light source. The gain is determined from the difference of the current of the illuminated (I_{ill}) and not illuminated (I_{dark}) APD current

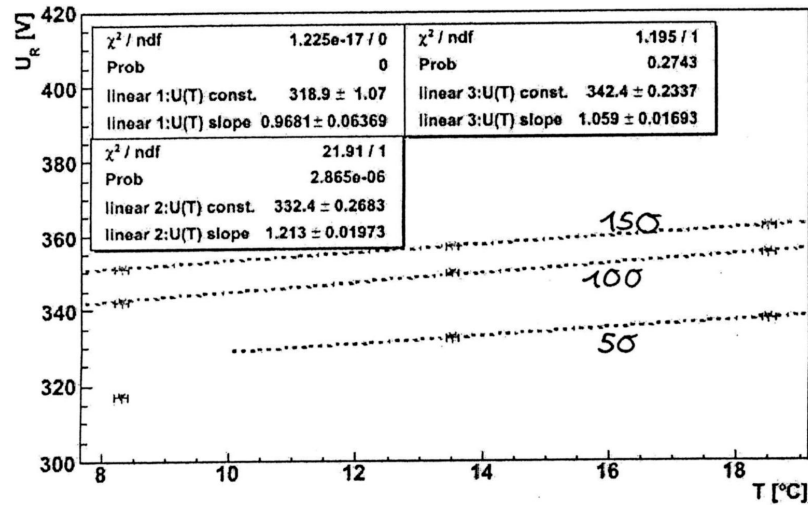


Figure 7.1: Temperature dependence of the necessary voltages for three different gains. Measurement of the AA0158 Hamamatsu LAAPD by the APD laboratory Frankfurt.

measured at different voltages, normalized to the difference observed at low voltages:

$$M(U) = \frac{I_{ill}(U) - I_{dark}(U)}{I_{ill}(20 \text{ V}) - I_{dark}(20 \text{ V})}. \quad (7.1)$$

As a next step, in-house measurements were performed to obtain the complete characteristic gain-voltage correlation of the APD at $-25 \text{ }^\circ\text{C}$. A small BGO¹ crystal, wrapped with Teflon-foil and optically coupled to the APD, detected the response to a ¹³⁷Cs source. The complete setup was placed inside a WT11 Weiss Umwelttechnik (Reiskirchen-Lindenstruth, Germany) climate chamber at $+13.5 \text{ }^\circ\text{C}$ and wrapped with aluminium foil for electric shielding. The output signals of the LNP were actively split (fig.7.2). One branch was fed into an ORTEC (Oak Ridge, USA) 571 Amplifier for signal shaping, followed by an ORTEC AD811 peak sensing ADC. The other branch generated the gate for the ADC. The signals were processed by a 474 ORTEC Timing-Filter-Amplifier (TFA), followed by a CFD² (FCC8 GANELEC, discontinued business operations) and used as a trigger for the DAQ. A gate generator was triggered in case of accepted events to deliver a strobe for the ADC of appropriate length.

According to M. Thiel [THI05], the BGO light yield increases by about 43.6% by

¹BGO = bismuth germanate ($\text{Bi}_4\text{Ge}_3\text{O}_{12}$)

²CFD = constant fraction discriminator

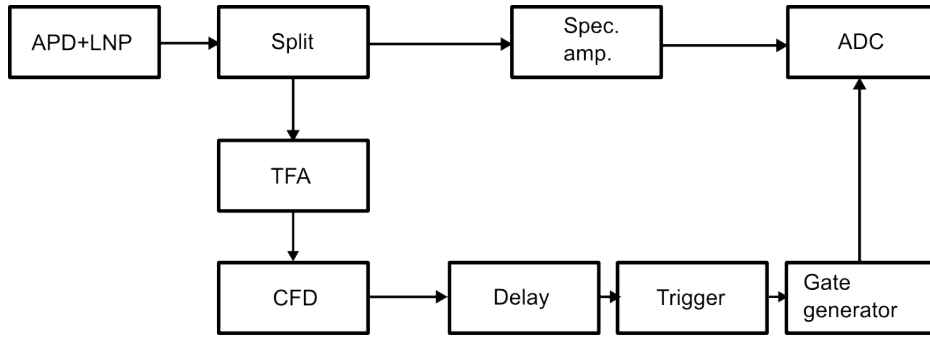


Figure 7.2: Block diagram of the APD readout with peak sensing ADC.

cooling down from +13.5 °C to -25 °C (fig.7.3). Therefore the temperature dependence

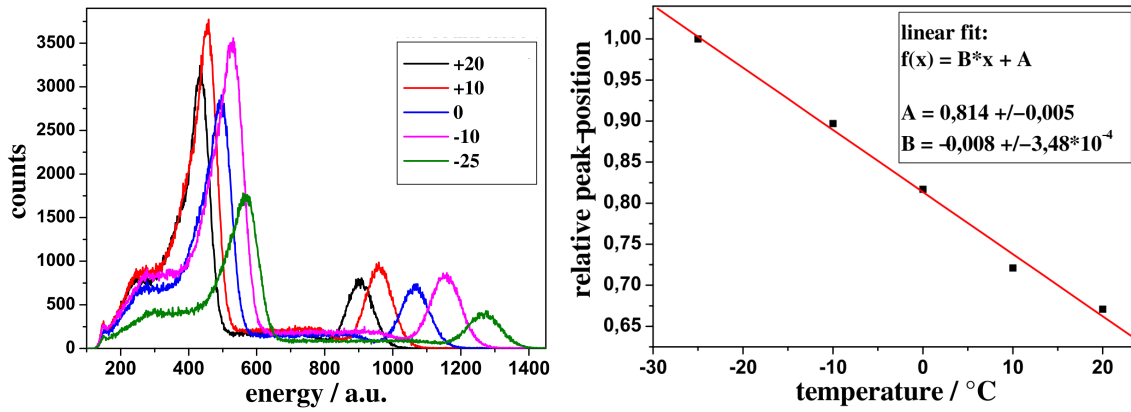


Figure 7.3: Temperature dependent response of a BGO scintillator read out with a PMT. A ^{22}Na source was measured (511 keV, 1275 keV). Pictures taken from [THI05].

of the light yield of the BGO had to be taken into account. A linear fit through the obtained photo peak values, measured with the provided APD gain voltages, delivered the signal to gain relation at 13.5 °C. The signal to gain relation at -25 °C can be obtained by increasing the peak values at 13.5 °C by 43.6% (fig.7.4). The applied relation for -25 °C is shown in fig.7.5. The data-points were fitted with the so-called Miller formula [MEL66]:

$$y(x) = \frac{1}{1 - \left(\frac{x}{p_0}\right)^{p_1}} + p_2. \quad (7.2)$$

For the voltage to gain correlation at +18.5 °C, the given relations for the three different gains could directly be taken from the data sheet (fig.7.1).

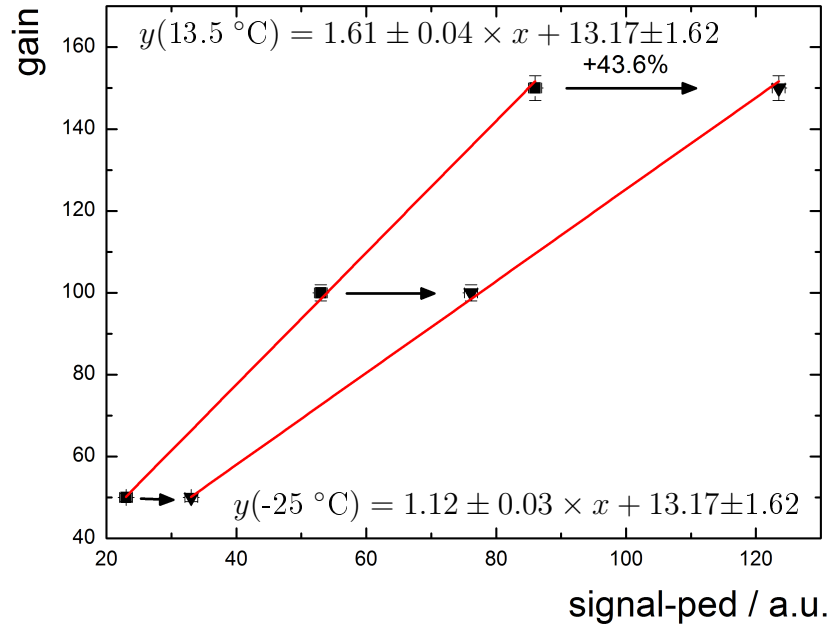


Figure 7.4: BGO signal to APD gain conversion. The data points at $13.5\text{ }^{\circ}\text{C}$ were measured and for $-25\text{ }^{\circ}\text{C}$ calculated.

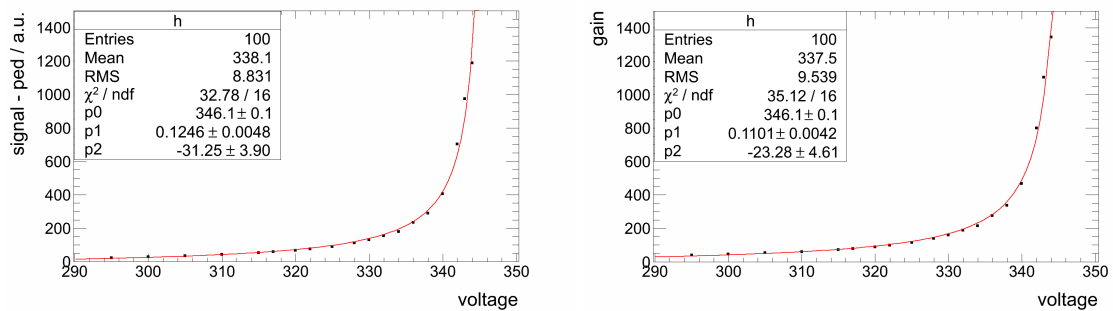


Figure 7.5: Characteristics of the AA0158 Hamamatsu APD at $-25\text{ }^{\circ}\text{C}$.

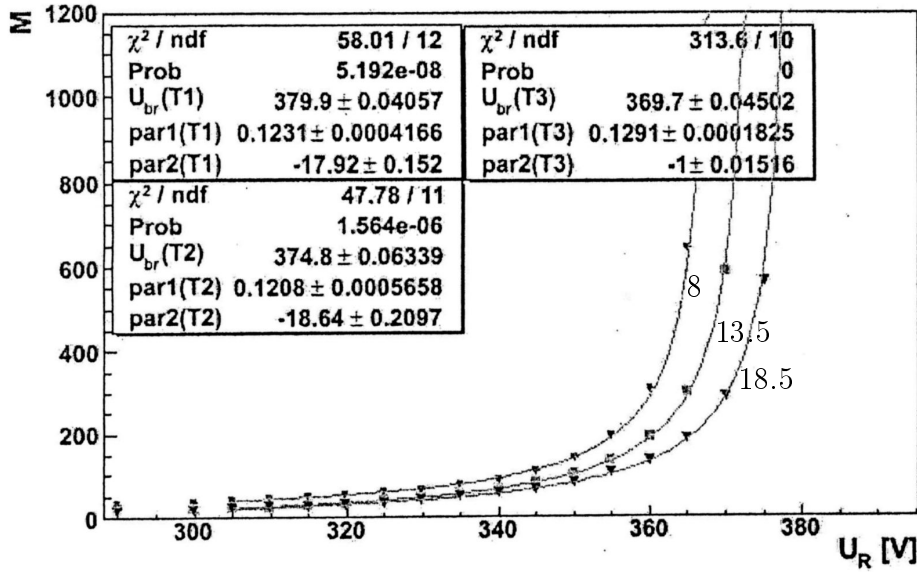


Figure 7.6: Voltage to gain allocation for 8, 13.5 and 18.5 °C. Measurement of the AA0158 Hamamatsu LAAPD by the APD laboratory Frankfurt. U_{br} corresponds to p_0 , $par1$ corresponds to p_1 and $par2$ corresponds to p_2 in equation 7.2.

7.2 Setup

In order to create light pulses, comparable to the scintillation light initiated by high-energy photons in lead tungstate in the range up to several MeV, a stabilized light pulse generator was used which was made by Radiation Instruments & New Components LLC (Minsk, Belarus) (fig.7.7). The light pulses ($\lambda = 460$ nm) were generated with an LED³ and split into two beams. One part was passed to the light output, the other was monitored with a PIN⁴ diode for the intensity stabilization. The variation of the number of emitted photons per pulse is less than 0.1% [LLC04]. A pulse length between 20 ns and 100 ns (*FWHM*) can be chosen at rates between 1 Hz and 1 kHz. The light pulse generator was attached to an optical distribution system (fig.7.8) including a set of 6 different optical attenuators (tab.7.1) located between two focusing lenses. Each filter can be switched independently remote controlled. A bundle of optical fibers was mounted behind the second focusing lens. Some fibers were attached to photomultiplier tubes for a direct measurement of the obtained pulses. The other fibers were placed inside a light tight tube and fed into the climate chamber.

³LED = light-emitting diode

⁴PIN = positive intrinsic negative

Chapter 7 Optimum APD gain measurements

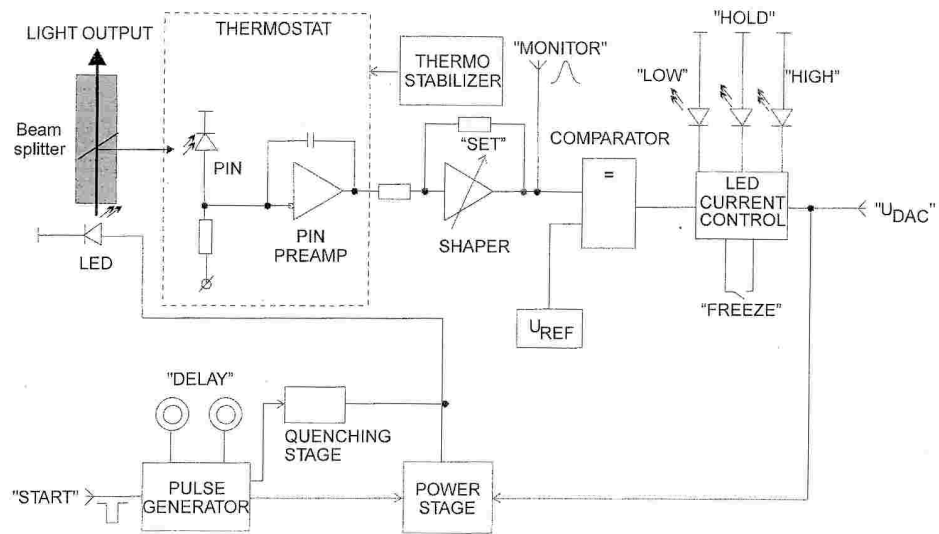


Figure 7.7: Light pulse generator block-diagramm. Picture taken from [LLC04].

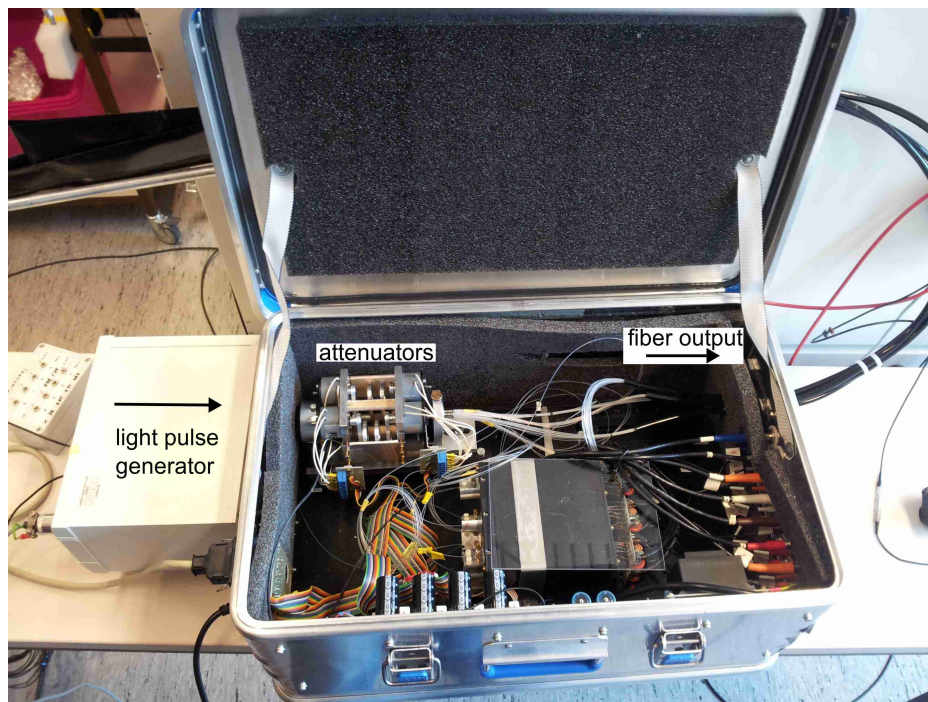


Figure 7.8: Light pulse generator with the distribution system.

Filter number	Transmission / %
1	0.95
2	12.2
3	20.4
4	42
5	65.1
6	77.7

Table 7.1: Selectable optical attenuators inside the distribution system.

To avoid possible local saturation effects in the APD, a light diffuser was used (fig.7.9). It consists of a Plexiglas cuboid with depolished surfaces and holes for attaching up to nine fibers. The block was wrapped with several layers of Teflon foil covered by black adhesive tape. The APD was placed at a cutaway in the wrapping and optically coupled with grease to the diffuser.

The read out with a peak sensing ADC was similar as explained in chapter 7.1. The complementary measurements with a sampling ADC were done in a self triggered mode using a SIS3302 module (Struck Innovative Systeme GmbH Hamburg, Germany). The signals of the preamplifier were directly digitized and afterwards treated with the feature extraction algorithms as explained in chapter 6.2.1.



Figure 7.9: Setup inside the climate chamber. A plastic block with roughened surfaces and wrapped with Teflon foil was used to create diffuse light to avoid saturation effects. The APD was optically coupled to this plastic block.

7.3 Procedure

The light pulse generator was set to produce light pulses with a duration of 42 ns at a rate of 100 Hz. After a warm-up phase of at least 30 minutes, the internal stabilization mechanism was activated. The signal shape of a single fiber measured with a PMT is shown in figure 7.10. The measurements at $-25\text{ }^{\circ}\text{C}$ using the peak sensing ADC as read out were carried out first. The setup inside the climate chamber was cooled down for a few hours in advance. The shaping time of the spectroscopic amplifier was set to $0.5\text{ }\mu\text{s}$. The filter combination 2+4+5, 2+4, 2, 4 and without a filter were chosen (see tab. 7.1). For every light pulse intensity a series of measurements of the light pulse peak with various high voltages were performed and analyzed. Afterwards, the same procedure was repeated at $+18\text{ }^{\circ}\text{C}$ with the sampling ADC.

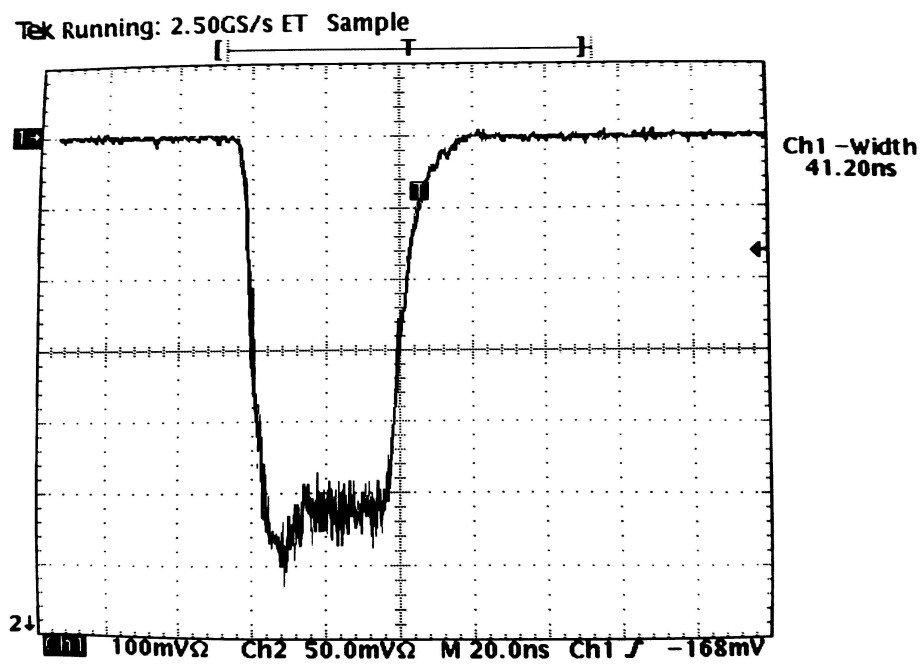


Figure 7.10: Direct measurement of the used light pulses with a PMT and a Tektronix (Beaverton, United States) TDS 540 Oscilloscope.

7.4 Analysis

For the analysis procedure, the measurements with the sampling ADC will be shown exemplary (see also chapter 6.2.1). According to M. Kavatsyuk a *MA* algorithm with 50 ns should be used to reduce the pile up probability within the PANDA experiment. In case, when a low trigger threshold is required, the smoothing length should be increased up to 400 ns to achieve a low noise level [KAV09]. A single light pulse measured with the APD and its processing through the steps of the MWD and MA with 50 ns and 400 ns is shown in figure 7.11. The resolution of the measured pulses

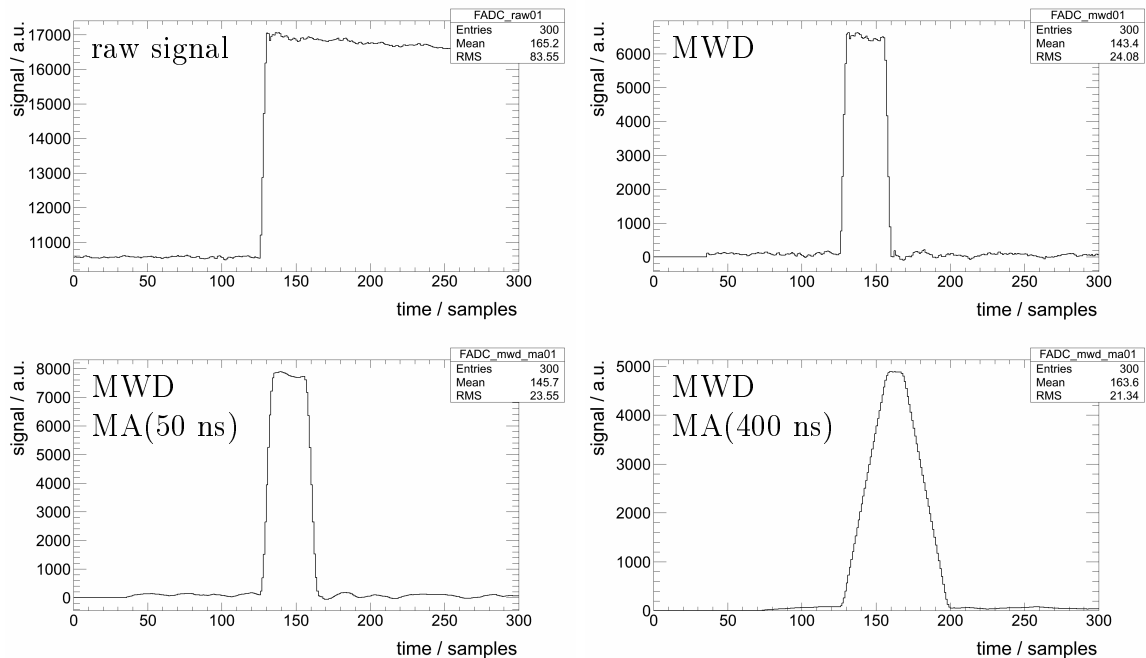


Figure 7.11: Sampling ADC trace of a preamp signal for a light pulse and its development through the steps of the MWD and MA algorithm.

for each voltage and light pulse intensity was determined with a Gaussian distribution (fig.7.12). An overview of the development of the resolution for an MA with 50 ns is shown in figure 7.13. A significant influence of the applied voltage can be seen. For a certain light pulse intensity, the resolution deteriorates from the best measured resolution with increasing and decreasing voltages. Furthermore, the voltage for the best resolution depends on the light pulse intensity (fig.7.13). In case of no optical attenuator, the best measured value can be found at 364 V and in case of the most

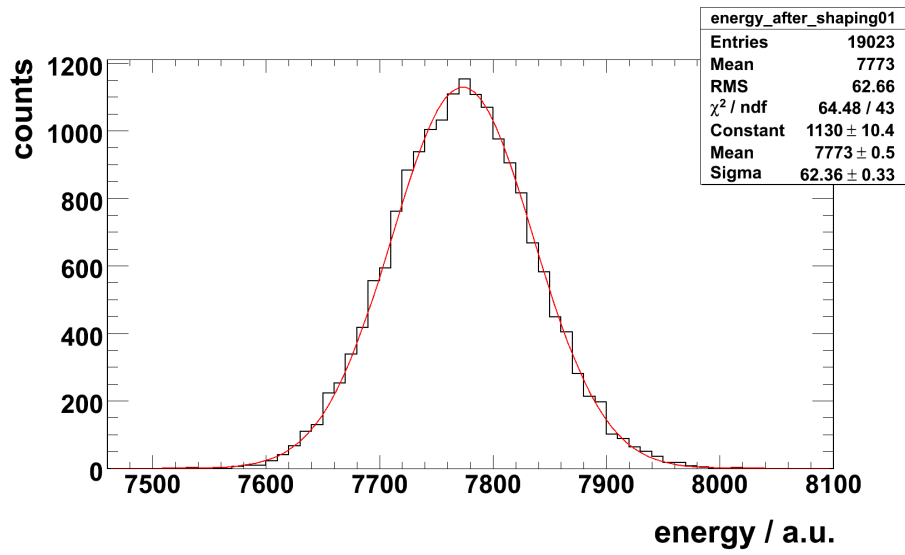


Figure 7.12: Energy distribution of the light pulses, measured with the APD and SADC, without any optical attenuator and fitted with a Gaussian distribution. The APD was operated with 360 V at +18 °C.

attenuated pulses at 374 V.

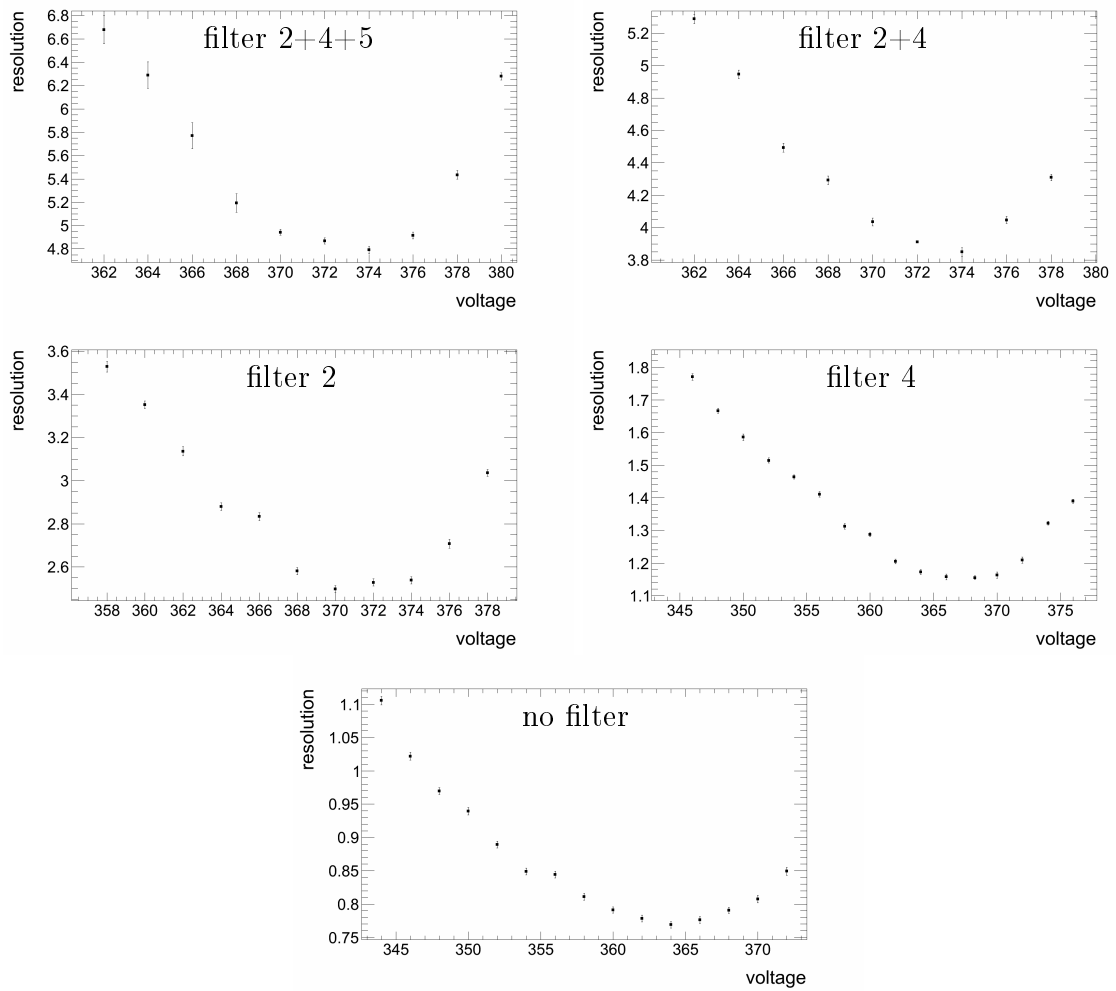


Figure 7.13: Resolution development for different APD voltages and different light pulse attenuations. The SADC measurements after the MWD and MA(50 ns) algorithms are shown.

7.4.1 Equivalent energy determination

The equivalent energy deposition within lead-tungstate was measured with a Hamamatsu R2059-01 PMT (fig.7.14). The digitalization of the signals were done with a V792N QDC⁵ (C.A.E.N Solingen, Germany). For these measurements, the cutaway

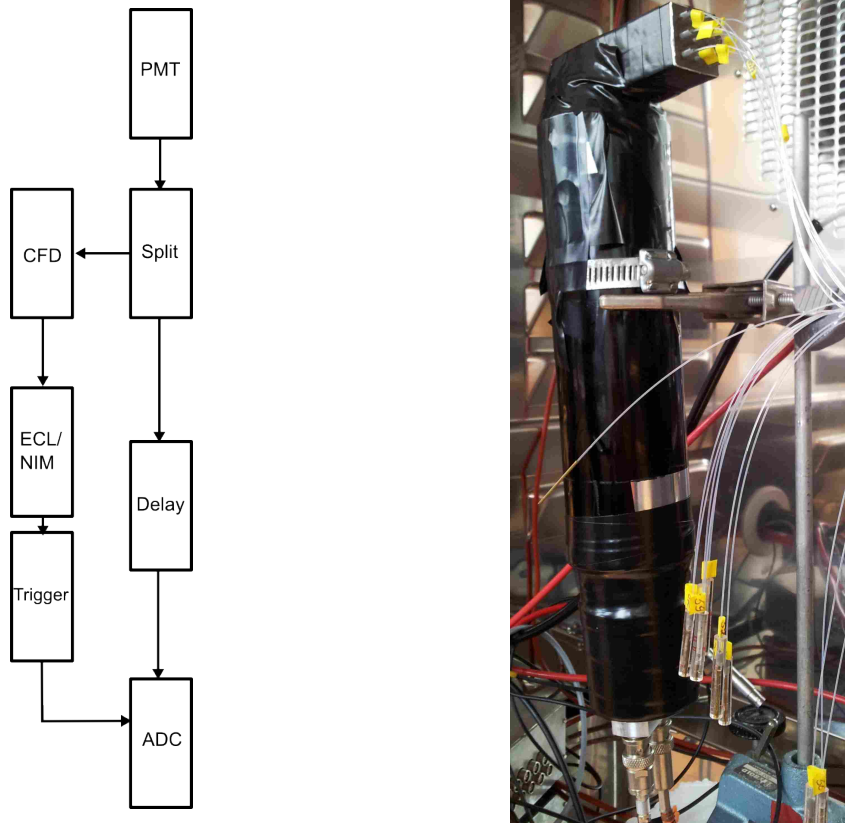


Figure 7.14: Measurement of the light pulse system, to determine the amount of photons. The window in the plastic block wrapping was reduced to the size of the active area of the APD.

in the diffuser wrapping was reduced to the sensitive size of the APD. The reduced window was optically coupled to the PMT. The average light yield of a type 6 PWO-II crystal at the PANDA operation temperature of $-25\text{ }^{\circ}\text{C}$, measured with a 2 inch bialkali photo cathode PMT, was taken into account (67.32 phe/MeV) and reduced to 13.6%. This corresponds to the active area of the APD and leads to 9.16 phe/MeV . The high voltage, and therefore the gain of the PMT was increased until the so called

⁵QDC= Charge (Q) to Digital Converter

Chapter 7 Optimum APD gain measurements

single electron peak could be separated from the noise (pedestal peak). The single electron peak is a distribution of the minimum charge which can be observed at the anode of a photomultiplier, resulting from a single electron emitted from the cathode. A single photon detaches an electron from the cathode with the probability given by the quantum efficiency. Due to the necessary high gain of the PMT for the separation of the single electron peak from the pedestal and the limited dynamic range of the read out, only the most attenuated pulses were measured with the PMT setup (tab.7.2). For all remaining chosen attenuation values for the light pulses, the equivalent energy

filter	ped.	single e ⁻ peak	photo peak	photo el.	equiv. en. dep. / MeV
2+4+5	56.66	63.93	2736.81	368.66	40.25

Table 7.2: Calculation of the equivalent energy deposition within PWO-II at -25 °C for the PMT measurement. The listed values are given in QDC channels unless stated otherwise.

deposition was determined within the APD measurements by comparing the actual peak-value relative to the peak-value of the most attenuated pulses (tab.7.3).

filter	photo-peak / ch.	equivalent energy dep. / MeV
2+4+5	710.81	40.25
4+2	1005.78	56.95
2	1928.86	109.22
4	7069.68	400.32
no filter	14265.30	807.78

Table 7.3: Relative determination of the equivalent energy deposition within PWO-II at -25 °C from the APD measurements with a sampling ADC. The peak values are determined after the *MWD* and *MA*(100 ns) algorithms. The APD was operated with 370 V at +18.5 °C. The first row of the table served as reference for the other energies.

7.5 Results

In order to quantify the development of the resolution for different voltages (gains) and light intensities (energies), the optimum values were taken from an interpolation of the data. Furthermore, the gains for a resolution loss of 0.1% on both sides from

the optimum value were determined to quote a tolerance area for the optimum gain values (fig.7.15). For the peak sensing ADC measurement at -25°C , the optimum APD gain for the most attenuated light pulses, which are equivalent to 40.25 MeV energy deposition inside lead tungstate, corresponds to 270. The 0.1% resolution loss tolerance area is located between a gain of 195 and 451. The optimum gain decreases with increasing amount of photons. Only a gain of 95 is necessary to obtain the optimum value for measuring an energy of 807.78 MeV. Above 109.22 MeV, the 0.1% resolution loss tolerance area becomes broader. For the highest measured energy, it is found between 40 and 452. Comparable developments were seen in the sampling ADC

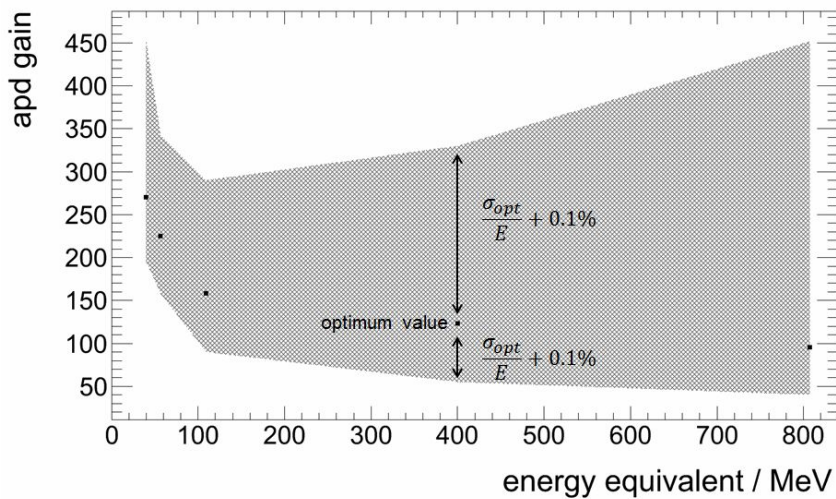


Figure 7.15: Optimum APD gain concerning energy resolution. The shaded area represents a 0.1% resolution loss tolerance band. Analysis of the peak sensing ADC data with an APD at -25°C .

measurements, only the individual values were different. For example, the optimum gain for the lowest energy was found at 372 for the analyzed sampling ADC raw data (fig.7.16), at 423.7 after the feature extraction algorithms with a 50 ns MA and at 238 for a 400 ns MA (fig.7.17).

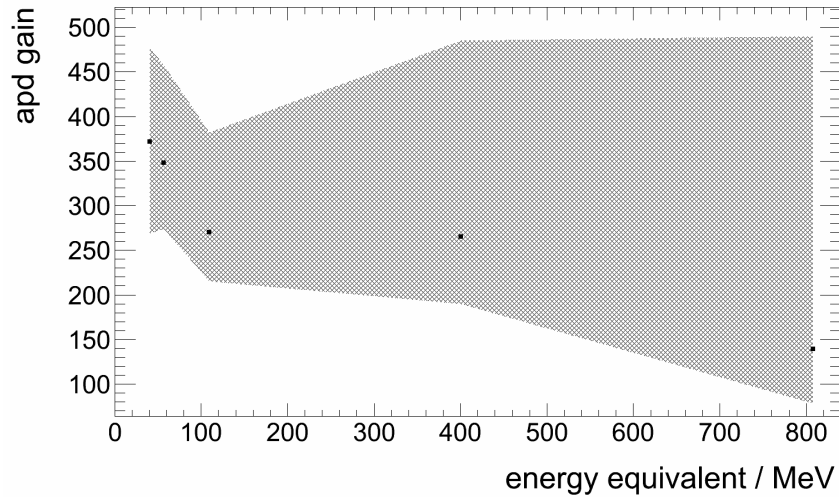


Figure 7.16: Optimum APD gain concerning energy resolution. The shaded area represents a 0.1% resolution loss tolerance band. Analysis of the raw data of a sampling ADC and an APD at +18 °C.

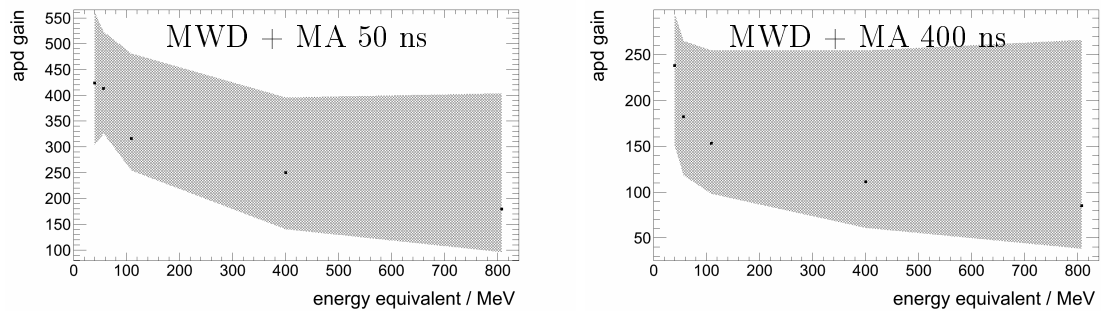


Figure 7.17: Optimum gain for the SADC readout with feature extraction algorithms. The shaded area represents a 0.1% resolution loss tolerance band. Measurement with an ADC at +18 °C.

Chapter 8

Discussion and Outlook

8.1 Discussion

Within the scope of this work aspects of the measurement of electromagnetic probes with the electromagnetic calorimeter of the future \bar{P} ANDA detector were investigated. For the first time, a prototype for the barrel part was used which is designed to measure energies over an extended dynamic range from several GeV down to a few MeV. The concept is based on improved PbWO_4 scintillation crystals cooled down to -25°C in order to increase the light output. For a more efficient scintillation light detection, large area avalanche photo diodes with an increased active surface has been developed. Furthermore, with respect to the large dynamic range, special low noise read out electronics have been developed. For the envisaged physics program, the necessary energy resolution has to be better than

$$\frac{\sigma}{E} = \frac{2\%}{\sqrt{E/\text{GeV}}} \oplus 1\%. \quad (8.1)$$

In this thesis it was shown that this goal can, in principle, be achieved. The energy regime from 52.34 MeV up to 15 GeV was investigated within several experiments. This study verified the principle detector concept and a linear response to photons (see fig.5.42 in sec.5.5.1). An optimum threshold was found at 0.75 MeV for the single module of the detector matrix. This value corresponds to 3σ of the electronic noise distribution. Deviations from this value lead to a deterioration of the energy resolution (see fig.5.35 in sec.5.4.3). It turned out that the parameterization used in equation 8.1 cannot exactly reproduce the measured resolution development over the complete

energy range. With respect to the electronic noise, the total measured response can be described as

$$\frac{\sigma}{E} = \frac{1.86\%}{\sqrt{E/\text{GeV}}} \oplus \frac{0.25\%}{E/\text{GeV}} \oplus 1.46\%. \quad (8.2)$$

and is shown in fig. 8.1.

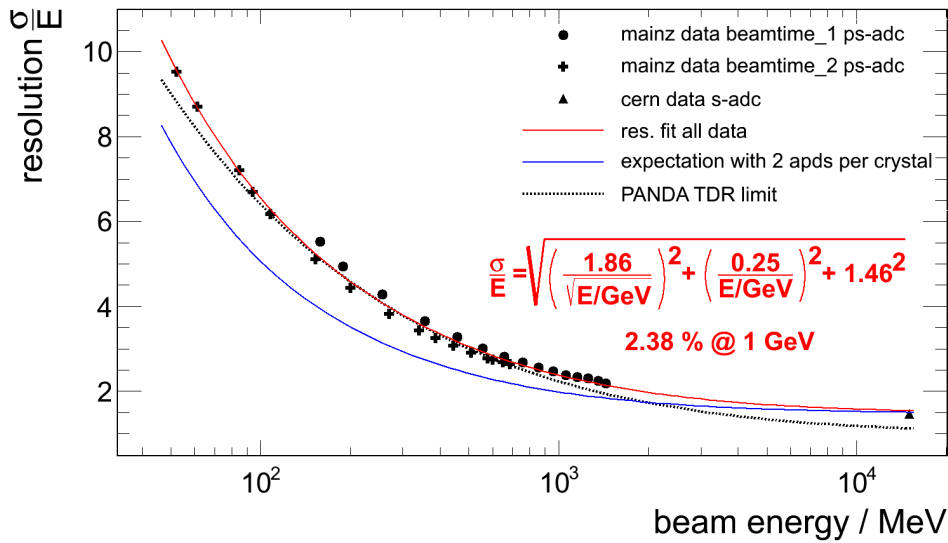


Figure 8.1: Resolution summary of all performed experiments. The resolution of the full PROTO 60 matrix is shown in %.

The difference in the resolution for the overlapping energies between the two beam-times at MAMI can be explained with the size of the beam spot. During the first experiment, the PROTO 60 was located at the very end of the beam-line in contrast to the second experiment at a more forward position. The precise shape of the beam-spot is unknown. A fit through all the data points revealed a resolution slightly worse than the EMC TDR requirement, mainly for high energies approximately above 1 GeV and at low energies below approximately 100 MeV, respectively. Concerning the resolution at low energies, it can be expected that the use of two LAAPDs for the readout of each crystal will improve the response more than necessary. By doubling the collected scintillation light, the photo statistic term will be reduced by up to a

factor of $\sqrt{2}$. This will lead to a response in the order of

$$\frac{\sigma}{E} = \sqrt{\left(\frac{1.32\%}{\sqrt{E/\text{GeV}}}\right)^2 + \left(\frac{0.25\%}{E/\text{GeV}}\right)^2 + 1.46\%^2}, \quad (8.3)$$

being sufficient up to 2 GeV. According to Ingram et al. [ING07], the comparable CMS electromagnetic barrel calorimeter shows a parameter of 2.8% for the photo statistic term. It is designed to measure much higher energies. The used crystals deliver a light yield lower by a factor of 2 [TDREMC] and are operated at room temperature. The PROTO 60 electronics is specially designed to operate at a very low noise level. Together with the larger signals due to the higher light yield and larger APD surfaces, the prototype noise term of 0.25% at 1 GeV corresponds to a single-module noise of about 0.25 MeV. CMS obtained a noise parameter of 12% and a noise level of 40 MeV. The response for different subunits was investigated in detail obtained in the first experiment at MAMI and is given in tab.8.1.

Concerning the resolution for high incident energies, there is room for improvement. At high energies, the response parametrization is mainly influenced by the size of the constant term. For comparison, the CMS electromagnetic calorimeter obtained a constant term in the order of 0.3%. Besides differences in the design due to the much larger energy regime, they roughed one of the the crystal surfaces in order to linearize the light collection. Considering a typical electromagnetic shower within a staggered crystal matrix, the nonlinear light collection becomes relevant. Within a calibrated matrix, the average distribution of the energy deposition is not symmetric for all neighboring crystals with respect to the central one due to the geometrical arrangement as shown in fig.8.2. In case of the neighboring modules the forward shifted crystals obtain an energy deposition shifted closer towards the photo-sensor leading to a decreased number of collected scintillation photons per deposited energy compared to the backward shifted crystals (see also sec. 4.1.1). It should also be mentioned that the diameter of the CMS barrel is larger than the $\bar{\text{P}}\text{ANDA}$ barrel and therefore the crystals are less staggered and less tapered in shape. However, a linearization of the light collection would reduce the total light yield. Unfortunately, the light yield on the enhanced side can only be reduced to match the values obtained near the photo sensor. That would not be in favor of the $\bar{\text{P}}\text{ANDA}$ experiment, since a good energy resolution is needed down to a few MeV. Finally, with two APDs it will be an optimization problem to what extent the non-uniformity could be compensated until the resolution

Chapter 8 Discussion and Outlook

Matrix	TH/MeV	$\frac{\sigma(E)}{E}$ / %	$\frac{\sigma(E)}{E}$ @ 1 GeV / %
3x3	0.75	$\frac{\sigma}{E} = \sqrt{\left(\frac{2.40}{\sqrt{E/\text{GeV}}}\right)^2 + \left(\frac{0.35}{E/\text{GeV}}\right)^2 + 1.50^2}$	2.86
	1	$\frac{\sigma}{E} = \sqrt{\left(\frac{2.41}{\sqrt{E/\text{GeV}}}\right)^2 + \left(\frac{0.36}{E/\text{GeV}}\right)^2 + 1.50^2}$	2.87
	3	$\frac{\sigma}{E} = \sqrt{\left(\frac{2.43}{\sqrt{E/\text{GeV}}}\right)^2 + \left(\frac{0.43}{E/\text{GeV}}\right)^2 + 1.50^2}$	2.88
	5	$\frac{\sigma}{E} = \sqrt{\left(\frac{2.44}{\sqrt{E/\text{GeV}}}\right)^2 + \left(\frac{0.55}{E/\text{GeV}}\right)^2 + 1.51^2}$	2.92
	10	$\frac{\sigma}{E} = \sqrt{\left(\frac{2.66}{\sqrt{E/\text{GeV}}}\right)^2 + \left(\frac{0.78}{E/\text{GeV}}\right)^2 + 1.31^2}$	3.07
5x5	0.75	$\frac{\sigma}{E} = \sqrt{\left(\frac{1.98}{\sqrt{E/\text{GeV}}}\right)^2 + \left(\frac{0.37}{E/\text{GeV}}\right)^2 + 1.48^2}$	2.49
	1	$\frac{\sigma}{E} = \sqrt{\left(\frac{1.88}{\sqrt{E/\text{GeV}}}\right)^2 + \left(\frac{0.45}{E/\text{GeV}}\right)^2 + 1.57^2}$	2.49
	3	$\frac{\sigma}{E} = \sqrt{\left(\frac{2.20}{\sqrt{E/\text{GeV}}}\right)^2 + \left(\frac{0.17}{E/\text{GeV}}\right)^2 + 1.31^2}$	2.56
	5	$\frac{\sigma}{E} = \sqrt{\left(\frac{2.17}{\sqrt{E/\text{GeV}}}\right)^2 + \left(\frac{0.58}{E/\text{GeV}}\right)^2 + 1.40^2}$	2.65
	10	$\frac{\sigma}{E} = \sqrt{\left(\frac{2.38}{\sqrt{E/\text{GeV}}}\right)^2 + \left(\frac{0.90}{E/\text{GeV}}\right)^2 + 1.39^2}$	2.90
6x10	0.75	$\frac{\sigma}{E} = \sqrt{\left(\frac{1.85}{\sqrt{E/\text{GeV}}}\right)^2 + \left(\frac{0.4}{E/\text{GeV}}\right)^2 + 1.55^2}$	2.44
	1	$\frac{\sigma}{E} = \sqrt{\left(\frac{1.88}{\sqrt{E/\text{GeV}}}\right)^2 + \left(\frac{0.39}{E/\text{GeV}}\right)^2 + 1.51^2}$	2.44
	3	$\frac{\sigma}{E} = \sqrt{\left(\frac{2.03}{\sqrt{E/\text{GeV}}}\right)^2 + \left(\frac{0.44}{E/\text{GeV}}\right)^2 + 1.38^2}$	2.50
	5	$\frac{\sigma}{E} = \sqrt{\left(\frac{2.11}{\sqrt{E/\text{GeV}}}\right)^2 + \left(\frac{0.59}{E/\text{GeV}}\right)^2 + 1.42^2}$	2.61
	10	$\frac{\sigma}{E} = \sqrt{\left(\frac{2.57}{\sqrt{E/\text{GeV}}}\right)^2 + \left(\frac{0.77}{E/\text{GeV}}\right)^2 + 1.07^2}$	2.89

Table 8.1: PROTO 60 resolution for different matrices and thresholds for the data of the first experiment at MAMI in the energy range from 158.31 to 1441.06 MeV.

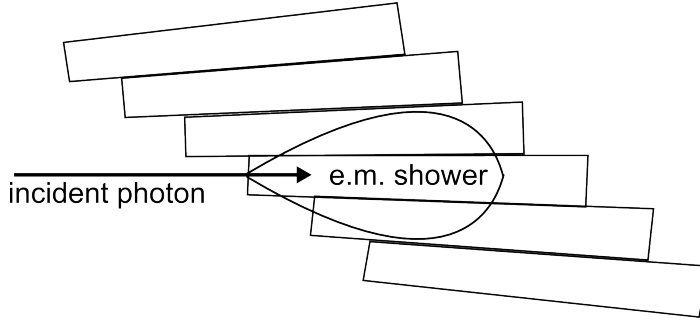


Figure 8.2: Schematic drawing of an electromagnetic shower within the PROTO 60 crystals (not to scale). Due to the dependence of the light collection on the position of the scintillation process, an increased constant term can be expected.

exceeds the TDR requirement for low energies but would improve on the other hand the performance for highest energies. However, one has to take into account that in case of the barrel the dominant part of detected photons will stay below 2 GeV. The influence of the nonuniform light collection on the resolution will be studied in detail by D. Bremer [BRE13], using the PROTO 60 GEANT model (PROTO60-NUF-NOISE) which was introduced in section 4 together with certain experimental measurements. Furthermore, within the next prototype called PROTO 120, a sub-matrix will be equipped with linearized crystals for experimental comparison. According to D. Bremer [BRE13], rectangular crystals have a position independent and therefore uniform response. A first test experiment with lead tungstate crystals in rectangular shape ($20 \times 20 \times 200$ mm), of similar quality (PWO-II) and in combination with a comparable APD read out, achieved in the past a resolution for a 3×3 matrix of

$$\frac{\sigma}{E} = \frac{1.86\%}{\sqrt{E/\text{GeV}}} \oplus 0.65\%. \quad (8.4)$$

with a significant lower constant term [NOV08].

Another contribution to the constant term are inaccuracies of the relative calibration. They will primarily affect the resolution at high energies, where photon statistics becomes negligible. A comparison of two different calibration methods using cosmic muons as well as an impinging muon beam, revealed no significant difference in the energy resolution for the 15 GeV CERN data. The first method utilized cosmic radiation, which irradiates the crystals perpendicularly within restricted volumes. These volumes were defined by the chosen trigger condition and the overlap of all crystals

Chapter 8 Discussion and Outlook

in a column. Due to the staggering, these restricted volumes were slightly different in each row. Cosmic radiation simulations with the PROTO60-NUF-NOISE model revealed a difference in the energy deposition up to 11.8%. The nonlinear light collection compensates these differences down to 1.6% (sec.5.4.2.1). The second calibration method utilized a 150 GeV muon beam in each crystal for calibration. Due to the comparable energy resolution of both methods, significant relative inaccuracies can be excluded.

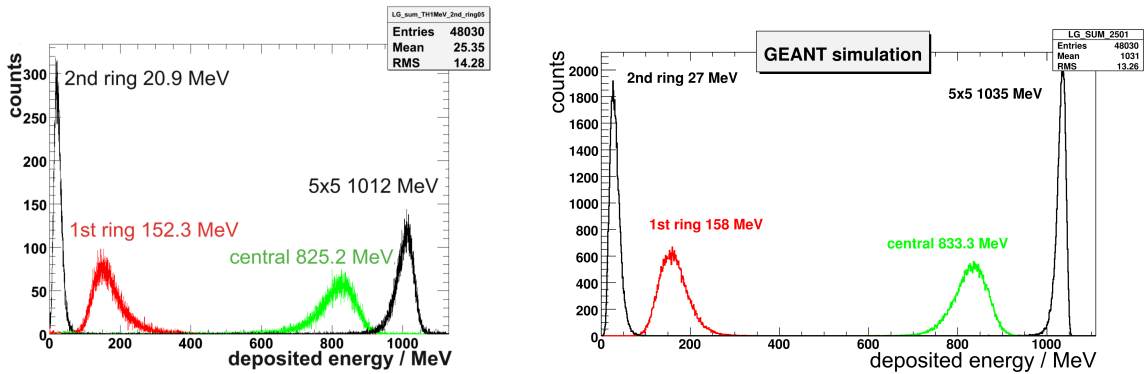


Figure 8.3: Line-shape comparison between experimental data and simulation for 1057.7 MeV photons.

If the nonlinear light collection will not be compensated, an absolute detector calibration require more complex and iterative calibration procedures. For the PANDA calorimeter, it is foreseen to use cosmic radiation for a first rough relative and absolute calibration with an accuracy better than 10%. As a next step, reactions like the reconstruction of neutral pions out of their two photon decay, will be used. For the performed prototype tests, this second option was not applicable due to the limited solid angle. The cosmic radiation simulation with a single type-6 crystal of the PROTO60-NUF-NOISE model revealed a most probable value for the energy deposition in the crystal of 27.87 ± 0.03 MeV and 782.3 ± 0.9 photo-electrons inside the LAAPD. For comparison, the same amount of photo-electrons can be generated by

$$E_{dep}(0 \text{ cm}) \approx \frac{782.3 \text{ phe}}{32.04 \text{ phe/MeV}} = 24.42 \text{ MeV} \quad (8.5)$$

energy deposition within the top of a crystal. With respect to the decreasing light yield with increasing crystal depth, the approximation of 24.51 MeV due to the average perpendicular crystal path length of minimum ionizing particles (sec.5.4.2) seems to

be a reasonable value for an absolute calibration. A comparison of measured and simulated data for 1057.7 MeV photons is shown in figure 8.3. The difference is in the order of 2.3% for the reconstructed energy by summing up a 5×5 matrix and in the order of only 1% for the crystal were the beam was impinging on.

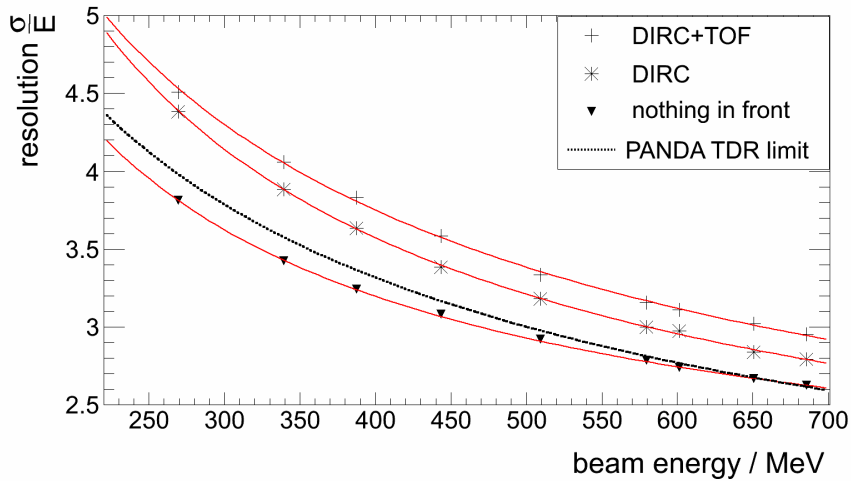


Figure 8.4: Measured energy resolution in % of the PROTO 60 with and without additional absorber material in front. Additionally, the EMC TDR requirement is drawn.

For the first time, the influence of the major part of the material budget due to inner detector components on the $\bar{\text{P}}\text{ANDA}$ electromagnetic calorimeter was investigated experimentally (chapter 5). The combination of absorber material together with the PROTO 60 revealed that in case of γ conversion in the absorber, especially at low energies, the original energy information can only be partly recovered in the matrix of 6×10 crystals. The line-shape of the reconstructed energies was significantly shifted towards lower energies. Even with only a DIRC quartz bar in front, the energy of up to 13% of all gamma events was observed below 3σ of the unaffected line-shape, which leads to a completely wrong reconstruction of the primary photon energy. In order to simulate a proposed TOF detector, a 24.5 mm Plexiglas sheet was added to the DIRC bar. This further increased the total amount of measured events below 3σ up to 16% (fig.5.50). In general, the total energy resolution of the PROTO 60 becomes deteriorated with increasing amount of absorber material and did not meet the TDR requirements (fig.8.4). In order to guarantee the required energy resolution, the proposed SciTil detectors right in front of the EMC appears to be indispensable for the $\bar{\text{P}}\text{ANDA}$ experiment as a Veto detector (sec.2.4.2). Rejecting conversion events, the

Chapter 8 Discussion and Outlook

line-shape and therefore the calorimeter resolution should be preserved. However, the detector efficiency will be reduced. It might require complex simulations to quantify the efficiency for absolute cross section measurements.

Regarding the optimum APD gain setting (sec.7), a gain of 50 was considered so far for the design of the \bar{P} ANDA barrel electronics. However, according to section 5.2.2 and 6.4.3, all shown PROTO 60 measurements were performed with an LAAPD gain in the order of 140-150, except the modules where the 15 GeV beam impinged during the CERN measurement. There, the gain was reduced down to approximately 51 due to the limited dynamic range of the preamplifiers. In the beginning of experiments with PROTO 60 there have not been available detailed specifications in particular when operated at low temperature. The finally performed measurements revealed that the considered gain of 50 does not exploit the full potential concerning the energy resolution, especially at low energies. For example, the energy resolution achieved for light pulses, corresponding to an energy deposition of 40.25 MeV inside a PWO crystal at -25°C , improved from 12.34% at a gain of 73.7 to 3.23% at a gain of 270 (fig.8.5), measured with a peak sensing ADC.

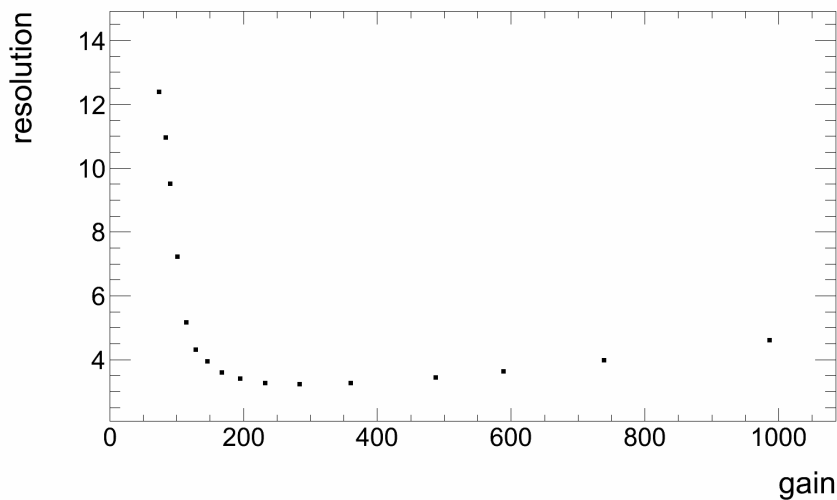


Figure 8.5: Measurement of light pulses with an APD and peak sensing ADC read out. The dependence of the energy resolution $\frac{\sigma}{E}$ in % on the APD gain is drawn. The pulses were comparable to scintillation light caused by 40.25 MeV energy deposition inside a typical \bar{P} ANDA PWO crystal at -25°C .

Referring to the measurements performed with a sampling ADC and feature extraction algorithms (see sec.6.2.1 for explanation), a gain value suitable for both tested moving average lengths (50 & 400 ns), was obtained to be 250 (fig.7.17). In case of a 400 ns MA filter, this value leads to a resolution which stays within a 0.1% resolution loss tolerance band determined for the complete measured energy range. For a 50 ns MA filter, the obtained resolution will remain within a 0.1% resolution loss tolerance band above 100 MeV.

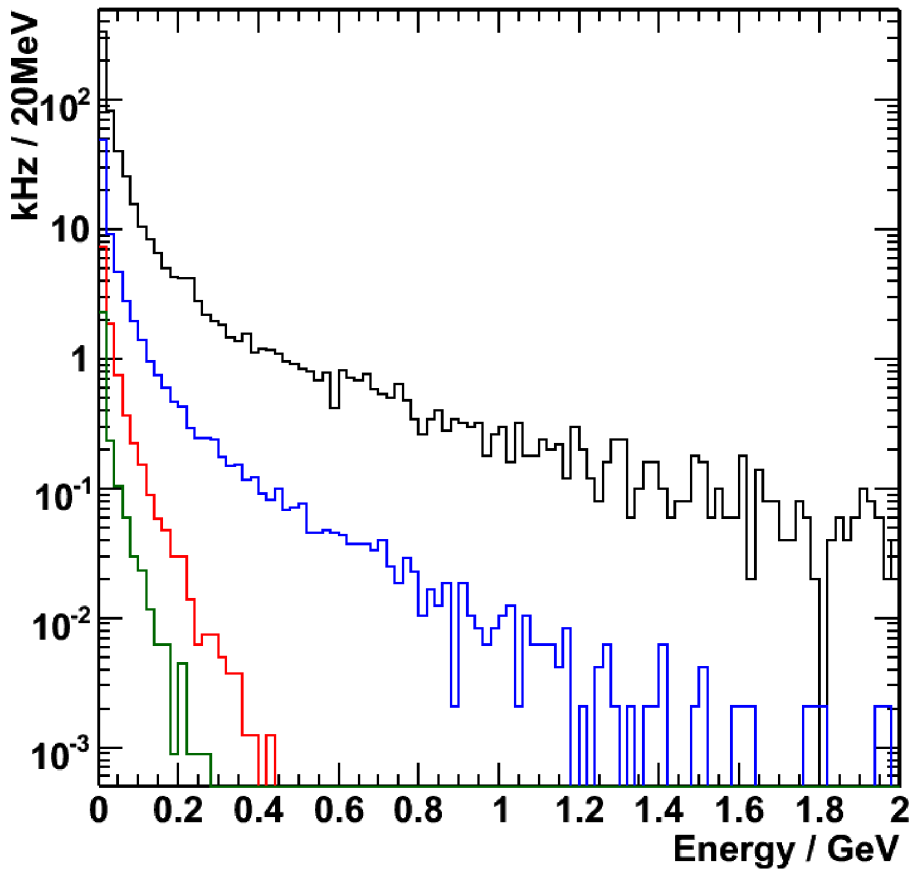


Figure 8.6: Simulation with $\bar{\text{P}}\text{ANDA-Root}$, a branch of FairRoot [FROOT]. Single crystal energy differential rate spectrum of the $\bar{\text{P}}\text{ANDA}$ target calorimeter for polar angles of 5° (black), 25° (blue), 90° (red) and 135° (green) at 15 GeV incident beam momentum. Picture taken from [TDREMC].

For the $\bar{\text{P}}\text{ANDA}$ experiment, the dynamic range limitations of the ASIC developed preamplifier APFEL has to be considered. The present design allows a maximum input

Chapter 8 Discussion and Outlook

charge of 6.31 pC [WIE11]. Therefore, based on the expected light output, quantum efficiency and gain of the APD one has to confirm the applicability over the whole dynamic range of photons to be expected. To quote a general single gain limit for the whole barrel with respect to a safety margin, the highest possible values for light yield and energy deposition should be considered. According to the TDR (tab.2.1), 7.3 GeV energy deposition are expected at maximum in a single crystal of the barrel calorimeter. The highest light yield observed during the quality control of the so far delivered crystals was in the order of 29 phe/MeV at +18 °C, measured with a 2 inch bi-alkali photomultiplier tube [EIS13]. This value corresponds to 51.6 phe/MeV within an APD at -25 °C (see chapter 3.2 for the calculation method) and allows for a maximum APD gain of 104.5 for the measurement of 7.3 GeV with the present ASIC. Considering the expected energy deposition within the different areas of the barrel allows the setting of higher gain values. 7.3 GeV energy deposition within a single crystal is expected only at the very forward part of the barrel calorimeter around a polar angle of 22°. For larger polar angles, the deposited energy will significantly decrease. Even for a slightly larger angle of 25°, figure 8.6 indicates a maximum deposition of less than half of the value at the very forward part and only 0.4 GeV for 90°. With the light yield staying below 29 phe/MeV, the proposed gain compromise of 250 appears applicable over nearly the whole barrel calorimeter. It allows to measure at least 3.05 GeV deposited energy in a single crystal or even more, depending on the crystal quality.

Up to now, it has been shown what has been achieved with the first prototype PROTO 60, what performance can be expected for the future \bar{P} ANDA calorimeter and where there are possibilities for improvements. Another important aspect is the stability during operation, which was not a limiting factor in case of the test experiments.

In order to operate the APDs at a gain of 250, a higher stability for the high voltage supply becomes necessary. A differentiation of the measured APD voltage-to-gain relation at -25°C (fig.7.5 and eq.7.2) shows the sensitivity of the gain with respect to the bias voltage. In order to retain the gain stability at the supposed increased gain of 250 from the foreseen value of 50, an increase in the voltage stability of approximately a factor 12 will be needed (tab.8.2).

The EHQ 8210p-F iseg (Radeberg, Germany) power-supplies which were used for

gain	d/dV gain(V) / %
50	0.63
150	3.05
250	7.3

Table 8.2: Measured sensitivity of the APD gain to the bias voltage at -25°C .

the PROTO 60 have a voltage stability of $\pm 5\text{mV}$ [ISEG]. This creates negligible gain fluctuations in the order of 0.015% at the upper approximation of the used PROTO 60 gain of 150.

Further influences concerning operation stability is the effect of the temperature stability on the APD gain and on the light yield of the crystals. Long term measurements showed a temperature stability of $\pm 0.05^{\circ}\text{C}$ inside the PROTO 60 [KAV11]. The used APDs have a temperature coefficient of $0.78 \text{ V}/^{\circ}\text{C}$ in order to retain a certain gain [HAMP60], which corresponds to a gain variation of $2.38\%/^{\circ}\text{C}$ at a gain of 150. The temperature dependence of the crystal light yield amounts to $3\%/^{\circ}\text{C}$ [TDREMC]. With respect to the temperature and voltage stability, these technical variations are in total in the order of

$$\sqrt{\left(\frac{\Delta\text{gain}}{\Delta V}\%\right)^2 + \left(\frac{\Delta\text{gain}}{\Delta T}\%\right)^2 + \left(\frac{\Delta\text{LY}}{\Delta T}\%\right)^2} \approx 0.19\%. \quad (8.6)$$

The operational stability will be significantly affected by radiation damage in the crystals due to the reduction of the optical transparency which will lead to a light yield loss and a change of the calibration parameters. Therefore, a monitoring system is foreseen which injects stabilized light pulses into the crystals of the $\bar{\text{P}}\text{ANDA}$ experiment in order to correct for light yield losses to be considered in the calibration procedure. All obtained radiation doses during the performed test experiments were negligible compared to the typical $\bar{\text{P}}\text{ANDA}$ operation. The radiation damage was of no relevance and therefore no monitor system was utilized.

8.2 Outlook

Within the scope of this thesis, the response of truncated pyramidal shaped PWO-II crystals was measured for the first time over an extensive energy range from 52.34 MeV up to 15 GeV. The scintillation light of each utilized crystal was read out with one large area avalanche photo-diode in combination with a preamplifier prototype. For all measurements, 60 crystals were used in total within the PROTO 60, a first prototype for the barrel part of the electromagnetic calorimeter of the future PANDA experiment. The obtained results represent only a lower limit for the performance. The final design considers two LAAPDs per crystal and further optimized electronics. The conventional low noise preamplifiers within the PROTO 60 will be replaced by the ASIC APFEL with two different gain stages, optimized signal shaping and a large dynamic range of 10000. The output-signals will be digitized with sampling ADCs with a sampling rate of approximately 100 MHz, being developed within the collaboration as well. Due to the two gain stages of the ASIC, the ratio of signal per channel and therefore the ADC resolution will be better in particular for low energies.

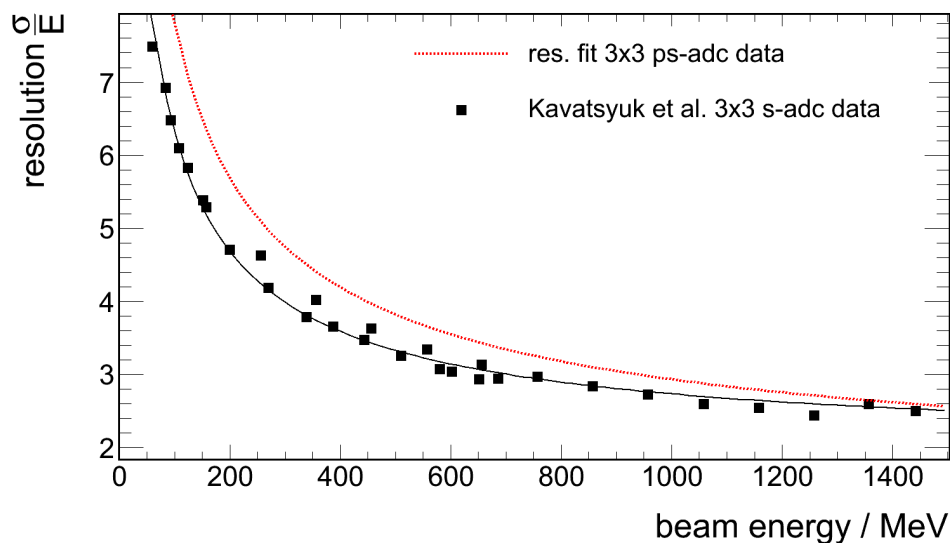


Figure 8.7: Resolution comparison of a 3×3 PROTO 60 matrix read out with different ADC types. The black data points were taken from [KAV11] and obtained via sampling ADC measurements. The parametrization of the red dashed curve is taken out of tab.8.1 for the optimum threshold of 0.75 MeV. The corresponding data were determined with peak sensing ADCs.

The SADCs will be advantageous compared to the peak sensing readout. On one hand, pile-up events at high rates up to 500 kHz in the forward region can be recognized with signal analyzing algorithms and rejected or even separated and recovered. A so called double MWD algorithm allows to reduce the pulse width not achievable with analogue electronics [KAV11]. On the other hand, the analysis of the SADC data provides the possibility of an effective noise reduction. The noise level can be individually determined for each event to determine the baseline. The remaining fluctuations can be reduced with the MA algorithm. As already tested and confirmed in parallel to the described experiments, but analyzed by the collaborators from KVI¹ the sampling ADC readout even improves the resolution compared to standard peak sensing ADC readout (fig. 8.7) due to the higher flexibility having recorded the complete signal shape. A quadratical three parameter resolution fit of the SADC data gives $\sigma(E)/E = 1.9 \text{ \%}/\sqrt{E} \oplus 4.1 \cdot 10^{-4} \text{ \%}/E \oplus 1.97\%$ for the parametrization which shows a negligible noise term.

The adjustments of an optimum APD gain should be repeated and adapted to the final electronics.

The next prototype, called PROTO 120, will include two APDs per crystal and the APFEL-ASIC instead of the analogue LNP as used in the PROTO 60. A sub-matrix will be equipped with linearized crystals in order to estimate experimentally the contribution to the large constant term and the impact on the resolution at low energies.

¹KVI = Kernfysisch Versneller Instituut, Netherlands

Appendix

Crystal	Ped.(M=50)	μ (M=50)	Ped. (M=150)	μ (M=150)	factor
1	107,2	287,5	107,3	290,5	1,02
2	88,6	415,8	89,1	1017,7	2,8
3	105,2	262,8	105,3	556,9	2,8
4	102,8	271,1	102,8	590,4	2,8
5	79,3	254,6	79,4	602,2	2,9
6	95,9	247,5	96,6	538,5	2,9
7	109,4	268,7	109,4	605,5	3,1
8	96,4	268,7	96,5	600,5	2,9
9	103	289,9	103,1	637,4	2,8
10	101,6	186,4	101,6	302,3	2,3
11	103,8	215,8	104	419,5	2,8
12	103,4	268,7	103,4	577	2,8
13	87,4	387,5	88,5	927,2	2,7
14	101,9	278,1	102	615,6	2,9
15	109,1	248,7	109	518,4	2,9
16	79,9	230,2	79,7	510	2,8
17	89,5	271,1	89,7	647,4	3,0
18	85,4	277	85,5	615,6	2,7
19	84,9	233,4	85,1	526,8	2,9
20	88,3	191,1	88,4	372,6	2,7
21	83,5	282,8	83,7	635,7	2,7
22	78	244	78,1	523,4	2,6
23	76	241,7	76,3	607,2	3,2
24	92,6	261,7	93	573,7	2,8
25	94,5	286,4	94,8	660,8	2,9

Appendix

26	91	228,7	91,3	511,7	3,0
27	105,6	278,1	106	662,5	3,2
28	91,7	275,8	92	618,9	2,8
29	81,3	218,1	81,6	518,4	3,1
30	89	241,7	89,4	548,6	3,0
31	89,3	266,4	89,5	575,4	2,7
32	95,4	252,2	95,6	535,2	2,8
33	67,7	213,4	67,8	464,8	2,7
34	65,8	257	66	634	2,9
35	80,1	205,2	80	441,3	2,8
36	78,1	293,4	78,6	712,8	2,9
37	80,8	242,8	81,3	523,4	2,7
38	99,2	279,3	99,6	605,5	2,8
39	71,5	228,7	72,2	508,3	2,7
40	86,4	208,7	87	451,4	2,9
41	77,3	258,1	77,8	620,6	3,0
42	111,4	304	112,1	642,4	2,7
43	56,4	292,2	57,6	737,9	2,8
44	90,1	271,1	91,1	615,6	2,8
45	69,7	238,1	70,5	588,8	3,0
46	107,3	291,1	108	608,9	2,7
47	76,8	249,9	77,4	612,2	3,0
48	92,7	260,5	93,3	540,2	2,6
49	82,1	261,7	82,2	660,8	3,2
50	77	254,6	77,2	608,9	2,9
51	71,6	211,1	71,5	505	3,1
52	78,3	251,1	78,2	582,1	2,9
53	98	224	97,9	488,2	3,0
54	77,5	172,2	77,4	345,8	2,8
55	88,2	265,2	88,2	624	3,0
56	113,3	245,2	113,2	463,1	2,6
57	116,7	265,2	116,6	531,8	2,7
58	109,1	235,8	109	466,5	2,8
59	96,4	211,1	96,4	427,9	2,8
60	108,8	271,1	109	563,6	2,8

Mean value	90,32	256,57	90,58	566,99	2,87
------------	-------	--------	-------	--------	------

Table 8.3: MPV values in ADC channels for the deposited energy of cosmic radiation. The LAAPD gains are determined with a light pulser system.

Appendix

Cr.	MPV / MeV	MPV / ph.el.	Cr.	MPV / MeV	MPV / ph.el.
1	27.9696 ± 0.0008	743.89 ± 0.02	31	27.0891 ± 0.0011	751.62 ± 0.03
3	28.2079 ± 0.0010	746.56 ± 0.02	33	27.0155 ± 0.0013	752.71 ± 0.03
4	27.9051 ± 0.0008	743.13 ± 0.02	34	27.0326 ± 0.0009	751.12 ± 0.03
5	28.0319 ± 0.0008	744.72 ± 0.02	35	27.1436 ± 0.0011	752.44 ± 0.02
6	28.1486 ± 0.0010	744.87 ± 0.02	36	26.9887 ± 0.0012	750.94 ± 0.02
7	28.0119 ± 0.0008	744.05 ± 0.02	37	27.0900 ± 0.0009	752.58 ± 0.03
8	28.0140 ± 0.0008	744.78 ± 0.02	38	27.1144 ± 0.0009	752.59 ± 0.02
9	27.9957 ± 0.0008	744.41 ± 0.02	39	27.0805 ± 0.0009	751.54 ± 0.03
10	27.9816 ± 0.0008	744.08 ± 0.02	40	27.0750 ± 0.0009	751.04 ± 0.02
11	28.0335 ± 0.0009	752.15 ± 0.02	41	26.1400 ± 0.0011	752.74 ± 0.03
12	28.0310 ± 0.0009	752.43 ± 0.02	42	26.1580 ± 0.0011	753.01 ± 0.03
13	28.0720 ± 0.0008	753.47 ± 0.02	43	26.1423 ± 0.0016	753.78 ± 0.03
14	27.9954 ± 0.0009	750.95 ± 0.02	44	26.2265 ± 0.0010	753.05 ± 0.03
15	28.1807 ± 0.0012	752.45 ± 0.02	45	26.1734 ± 0.0011	753.47 ± 0.03
16	28.0152 ± 0.0009	751.64 ± 0.02	46	26.0244 ± 0.0018	754.23 ± 0.03
17	28.0265 ± 0.0009	751.29 ± 0.02	47	26.1677 ± 0.0011	752.85 ± 0.03
18	28.1181 ± 0.0008	754.70 ± 0.02	48	26.2034 ± 0.0015	754.04 ± 0.03
19	27.9307 ± 0.0009	750.52 ± 0.02	49	26.2260 ± 0.0011	754.87 ± 0.03
20	28.0152 ± 0.0009	751.98 ± 0.02	50	26.2230 ± 0.0011	753.72 ± 0.03
21	27.5103 ± 0.0009	749.94 ± 0.02	51	25.3826 ± 0.0014	749.06 ± 0.03
22	27.5583 ± 0.0009	750.50 ± 0.02	52	25.4128 ± 0.0013	749.05 ± 0.03
23	27.5898 ± 0.0012	752.19 ± 0.02	53	25.4205 ± 0.0013	749.58 ± 0.03
24	27.5779 ± 0.0009	751.32 ± 0.02	54	25.2460 ± 0.0021	749.48 ± 0.03
25	27.5821 ± 0.0009	750.79 ± 0.02	55	25.2207 ± 0.0022	749.28 ± 0.03
26	27.5192 ± 0.0012	750.53 ± 0.02	56	25.2861 ± 0.0014	747.94 ± 0.03
27	27.5712 ± 0.0013	751.02 ± 0.02	57	25.2437 ± 0.0014	746.92 ± 0.03
28	27.5673 ± 0.0009	750.89 ± 0.02	58	25.2880 ± 0.0021	749.27 ± 0.03
29	27.6065 ± 0.0012	751.03 ± 0.02	59	25.3196 ± 0.0014	749.59 ± 0.03
30	27.5534 ± 0.0009	751.28 ± 0.024	60	25.4044 ± 0.0012	747.90 ± 0.03

Table 8.4: Summary of the PROTO60 cosmic simulations under the column cut condition. The lines indicating the transition between the rows. The MPVs of the cosmic energy deposition and the non linear response obtained with the PROTO60-NUF model are given.

List of Figures

1.1	Present GSI facility together with the planed FAIR complex.	7
2.1	Overview over the mass and momentum regime. The upper scale represents the antiproton momentum and the lower one the hadron mass. The vertical line shows the upper limit of the former $\bar{p}p$ annihilation experiment at the Low Energy Antiproton Ring (LEAR) at CERN. All states between 1.5 GeV and 15 GeV \bar{p} -momentum are accessible with \bar{P} ANDA.	12
2.2	Main decay channels of the $X(1^{-+})$. Due the high amount of decay products a calorimeter with high energy resolution is necessary.	16
2.3	Schematic view of the HESR ring. Equipment for experiment, stochastic and electron cooling, compensation solenoids, and injection is included. Picture taken from [ACCEL].	17
2.4	One half of the unit cell in the HESR arc. One arc is formed by 6 unit cells. Picture taken from [ACCEL].	19
2.5	The \bar{P} ANDA Detector. Picture taken from [PWEB].	19
2.6	Schematic drawing of the target calorimeter without the backward end cap.	22
2.7	The shape of the barrel scintillator crystals and the definition of geometrical parameters. Pictures taken from [TDREMC].	23
2.8	Schematic view of the barrel calorimeter.	24
2.9	Left picture: LAAPD photo-sensors for the barrel. By using 2 LAAPDs on one crystal, nearly the whole surface is covered. Right picture: considered photo-sensor for the forward end cap.	25
2.10	Exemplary mass attenuation coefficients for lead. With τ/ρ for the photoelectric effect, σ/ρ Compton Scattering, κ/ρ pair production, σ_R/ρ Rayleigh (coherent) scattering and μ/ρ their sum [MIT].	27

List of Figures

2.11	Development of an electromagnetic shower.	28
2.12	Schematic of a APD.	32
2.13	APG gain vs output example for a certain APD. The optimum APD gain depends on the ratio of signal to noise. Picture taken from [HAM].	34
2.14	The microvertex detector has 4 barrel layers and 6 discs of silicon detectors in forward direction around the interaction point. Picture taken from [TDRMVD].	35
2.15	Working principle of a GEM detector: electrons are guided into the holes by the low drift field, where avalanches of electron-ion pairs are generated. The asymmetric field configuration of low drift field and higher extraction field together with the small ion mobility leads to efficient back flow suppression. Adapted from [TDSTPC].	37
2.16	Imaging principle of the DIRC detector. A particle traverses the quartz bar and emits Cherenkov light. The light is reflected internally until it exits the quartz bar where the light is detected [TPR].	38
2.17	The TOF detector between the EMC and the DIRC. It will utilize scintillator-tiles (SCiTil) as active material. Pictures taken from [SCHW13].	39
2.18	Feynman diagram of the Drell-Yan process. A quark of one hadron and an antiquark of another hadron annihilate. This creates a virtual photon or Z boson which decays into a pair of oppositely-charged leptons like e^+e^-	40
2.19	Detector setup for hypernuclear physics. Left picture: beam entering from the left. The backward end cap is replaced by a set of germanium detectors. Right picture: the sandwich structured active secondary target for slow backscattered Ξ s. Pictures taken from [TPR].	41
2.20	Schematic side view of the upper half of the proposed RICH detector. .	42
2.21	A single Shashlyk supermodule is comprised of 4 modules. Each module guides the scintillation light through fibers to a photomultiplier.	43
3.1	The prototype PROTO 60 (lower left picture) is derived from the barrel calorimeter design (upper left picture). The setup of the prototype crystal matrix corresponds to the red circle on the lower right picture. .	47
3.2	Schematic profile view of the PROTO 60 crystal arrangement from the top and front side. Due to the geometry of the barrel calorimeter, the PROTO 60 matrix has a convoluted arrangement.	48

3.3	A group of 4 wrapped crystals is shown. The LAAPDs are hidden behind plastic capsules.	48
3.4	Backside of the opened and partly disassembled PROTO 60.	50
3.5	Circuit diagram of the SP883a. Picture taken from [PREAMP].	51
3.6	Comparison of the luminescence spectrum of lead tungstate with the quantum efficiencies of the $\bar{\text{P}}\text{ANDA}$ LAAPD and the Photomultiplier used for the light yield measurements [HAMP] [HAMP60] [TDREMC].	52
4.1	PROTO60 GEANT model	56
4.2	Measurement of nonuniform light collection of a type 6 crystal at KVI. Adapted from [BRE13].	58
4.3	A laser beam through a $\bar{\text{P}}\text{ANDA}$ PWO-II crystal. The inside scattered photons indicate macro defects within the crystal.	59
4.4	Cosmic shower generated by a high energetic proton interacting with a nucleus of the atmosphere.	60
4.5	All data points showing the velocity spectrum of muons at $\theta = 0^\circ$, except \diamond which are for $\theta = 75^\circ$. Data taken from [PDG12].	62
4.6	Comparison of the full atmosphere simulation of muons and protons at sea level (blue data points) with published data. Pictures are taken from [CRYP].	63
5.1	Floor plan of the MAMI-C accelerator facility including the experimental halls A1, A2, A4 and X1. Picture taken from [JAN06].	66
5.2	Basic setup of a racetrack microtron. Picture taken from [JAN06].	67
5.3	The Glasgow Tagging system. Picture taken from [BERG10].	68
5.4	Experimental setup at MAMI A2. In order to measure the impact of insensitive material on the PROTO 60 energy resolution a 24.5 mm Plexiglas, simulating the material budget of a TOF detector, and an original piece of DIRC quartz are placed between two plastic detectors.	70
5.5	The numbering of the PROTO 60 crystals from the beam perspective.	71
5.6	Schematic of the data acquisition at MAMI during the second beamtime. The only difference during the first beamtime was a coincidence between the tagger and exclusively the central crystal.	72
5.7	Partly assembled PROTO 60 with additional optical fibers. They are fed trough a hole of the crystal's plastic capsules and connected to the crystal's backside.	74

List of Figures

5.8	Raw data of all 60 crystals in run 1.1. The events are plotted in logarithmic scale versus the energy in ADC channels. The crystal number 1 can be found in the upper left corner.	78
5.9	Raw data of all 60 crystals in run 1.3 (beam between crystal 35 and 36). The events are plotted in logarithmic scale versus the energy in ADC channels.	79
5.10	Raw data of all 60 crystals run 2.4, the experiment without any additional dead material in front. The events are plotted in logarithmic scale against the energy in ADC channels.	80
5.11	Raw data of crystal 35 from the second experiment. Run 2.2 with DIRC+TOF in front is plotted in red. Run 2.3 (DIRC only) is plotted in blue and run 2.4, without any additional material in front, in black.	81
5.12	Data from figure 5.11 separated by an individual coincidence with every single tagger channel.	81
5.13	Raw data of the Tagger TDC channel 09 in linear and logarithmic scale from the second experiment run 2.4.	82
5.14	Raw energy data of crystal 35 from run 2.2 for 52.34 MeV (black) and 200.35 MeV (red) photons. For a better comparison of the low energetic peak, the bin-size of the higher energy plot was increased until the photo-peak height becomes comparable.	83
5.15	Exemplary raw data from the TDCs of the plastic detectors from the run 2.3. The DIRC sample was placed between the first and second plastic detector. The data of the first is shown on the left, and of the second plastic detector on the right side.	84
5.16	Exemplary noise distribution of crystal 33 fitted with a Gaussian distribution.	84
5.17	Exemplary raw cosmic data of crystal 33.	85
5.18	Deposited energy spectrum of cosmic radiation radiation in crystal 33 after the column cut. The most probable value Δ_p is determined with a Landau fit-function.	85
5.19	Calibrated cosmic radiation data with the column cut condition. A fit with a Landau distribution (red) is applied in order to verify the alignment.	86

5.20 Cosmic simulation via CRY with a single type 6 crystal. The track of positive charged particles are drawn in blue, negative in red and neutral in green color.	87
5.21 Cosmic radiation simulation of a horizontally aligned type 6 crystal. The data for the red curves are restricted to generated muons. The black curves are obtained by the full simulation. The peak due to muons in the full simulation was fitted with a Landau function in the lower picture.	88
5.22 Cosmic radiation simulation with a single type 6 crystal. Adapted from the PROTO60-NUF-NOISE model.	89
5.23 PROTO60 CRY simulation with 100 events. The track of positive charged particles are drawn in blue, negative in red and neutral in green color.	90
5.24 PROTO60 cosmic radiation simulation. The pure energy deposition for crystals in the middle of the upper, of the middle and the lowest row is shown.	90
5.25 Cosmic simulation for a central crystal out of the PROTO 60 matrix under different trigger conditions. The upper curve represents the raw data, the middle one the result of a coincidence between any crystal out of the top row and any crystal out of the bottom row and the lower curve includes the column cut.	91
5.26 Landau fit of all crystals under simulated cosmic radiation including the column cut.	91
5.27 PROTO 60 cosmic simulation for different trigger conditions. The upper curve in both pictures represents a self triggered DAQ (raw-data). The curves in the middle includes the condition of a coincidence between any crystal from the top and any from the bottom layer. The lowest curves corresponds to the condition, that all crystals in the same column responded simultaneously.	92
5.28 The picture serves to illustrate the mean cosmic paths. It is not true to scale. By applying trigger conditions, the cosmic paths are restricted to the overlapping parts of the crystal volumes.	93

List of Figures

5.29	Summary of the cosmic radiation simulation with the PROTO60 model under the column cut condition. The most probable values of the deposited energy are plotted. The error bars are smaller than the size of the data points. The data can be found in the appendix (tab.8.4). . . .	93
5.30	Summary of the cosmic radiation simulation with the PROTO60-NUF model under the column cut condition. The most probable values are plotted. The error bars are smaller than the size of the data points. 750.31 is the total average of the most probable value and 752.09 for the crystals 11-49. The data can be found in the appendix (tab.8.4). . .	94
5.31	Cosmic radiation simulation with the vertically aligned PROTO 60. The red curves are restricted to muons. The shaded area includes a cut. The conditions are an energy deposition larger than 100 MeV in one crystal and less than 10 MeV in all others.	95
5.32	Cosmic radiation simulation of a vertically aligned PROTO 60. An energy deposition larger than 100 MeV in one crystal and less than 10 MeV in all others was required. The peaks of the pure energy deposition and the PROTO60-NUF-NOISE model are fitted with a Gaussian distribution.	96
5.33	Typical calibrated noise spectrum of the module 19. For the evaluation of $\sigma_{(E,noise)}$, the right picture was fitted with a Gaussian distribution. .	96
5.34	Exemplary energy sum fitted with the Novosibirsk function. The impinging photon had an energy of 200.35 MeV. Data taken from run 2.4.	97
5.35	Determination of the optimum threshold with the data of run 1.1. . .	97
5.36	Lineshape for run 1.1.	98
5.37	Energy sum of the remaining crystals outside the inner 5×5 matrix. . .	99
5.38	Response of different PROTO 60 subunits of run 1.1.	100
5.39	Full energy-sum for different beam positions. 1018 MeV, 1005 MeV and 988 MeV are the peak values. The data is taken from run 1.1, 1.2 and 1.3.	100
5.40	Combined runs of the second experiment. The energy sum over the PROTO 60 is shown (run 2.2: black, run 2.3: blue, run 2.4: red). . . .	101

5.41	Data of run 2.2 (DIRC+TOF in front). The energy sum over the full PROTO 60 is plotted in blue, the sum over the inner 25 crystals in black, the sum over the inner 9 crystals in red and the central crystal in green.	101
5.42	Linear response verification with the energy sum over all 60 crystals. The error bars are smaller than the size of the drawn data points. . . .	102
5.43	Difference between data and fit of run 1.1. The error bars are still within the size of the drawn data points.	103
5.44	Exemplary multiplicity for 685.58 MeV photons.	104
5.45	Multiplicity against the energy. The error-bars are the width σ of the distribution.	104
5.46	Percentage of the number of events with an energy deposition less than 9 MeV in the central crystal for the runs 2.2, 2.3 and 2.4.	105
5.47	Percentage of the number of events with an energy deposition less than 9 MeV in different matrices for run 2.2 (DIRC+TOF in front). The 100% reference is given by the corresponding tagger response.	106
5.48	Energy sum over the 10×6 matrix of run 2.2.	107
5.49	Example for quantifying the line-shape deformation due to the additional material in front. The 10×6 energy sum of run 2.2 is shown. . .	107
5.50	Low energetic histogram entries below 3σ , as shown in figure 5.49. . . .	108
5.51	GEANT simulation of the experiment with the DIRC sample. Only charged particles are drawn. 1000 photons with 52.32 MeV and 500 photons with 1 GeV were simulated.	109
5.52	GEANT simulation of the experiment with the DIRC sample. The energy deposition in the central crystal is plotted. The red curve represents the deposited energy when conversion in the DIRC occurred, the black curve with the shaded area when no conversion occurred and the black curve all events.	109
5.53	GEANT simulation of the experiment with the DIRC sample. The energy sum over 60 crystals is plotted. The red curve represents the deposited energy when conversion in the DIRC occurred, the black curve with the shaded area when no conversion occurred and the black curve all events.	110
5.54	Conversion probability within the DIRC.	111

List of Figures

5.55	Calorimeter efficiency with the SiO ₂ cuboid in front. As a limit, 4 σ of the unaffected line-shaped was considered.	111
5.56	Obtained resolution for the full energy sum from the analysis of the first experiment.	112
5.57	Comparison of the fit accuracy. For low energies, the fit function does not sufficiently reproduce the line shape in case of dead material in front of the detector (run 2.2).	113
5.58	Obtained resolution for the full energy sum from the analysis of the second experiment.	113
6.1	CERN accelerator complex overview. Picture taken from [LEV08].	116
6.2	Detector setup at CERN.	117
6.3	Simplified schematic of the H4 beam-line for the positron beam production. The triangles represents magnets. TAX are motorized beam-dump and collimator modules. Not all available magnets, targets and TAX modules are drawn. Picture taken from [EFT03].	117
6.4	Example of recorded and processed PROTO 60 preamp signal digitized with a SADC.	119
6.5	The numbering of the read out channels from the beam perspective at CERN.	119
6.6	GEANT simulation of 15 GeV positrons with the PROTO60 and PROTO60-NUF-NOISE model. The central crystal is shown.	120
6.7	Beam-spot data of the second silicon detector. Each prototype had an active area of 2 \times 2 cm.	121
6.8	Raw data of the measurement with 15 GeV positrons, shot in the center of crystal 28. Plotted are the counts on a logarithmic scale against the energy in arbitrary units.	122
6.9	Cosmic radiation measured for calibration at CERN. The shown data includes the column cut condition.	123
6.10	Combined raw data of the measurement with 150 GeV muons in several positions. Plotted are the counts on a logarithmic scale against the energy in arbitrary units.	124

6.11 Combined data of the measurement with 150 GeV muons in several positions. A energy deposition of more than 100 MeV in one crystal and in all others less than 10 MeV was required. The threshold values were determined with the cosmic radiation calibration.	125
6.12 GEANT simulation of 150 GeV muons through 20 m of air with the PROTO60 and PROTO60-NUF-NOISE model. The crystal in the beam spot is shown. An energy deposition of more than 100 MeV in one crystal and less than 10 MeV in all others was required for the shaded area.	126
6.13 GEANT simulation of 15 GeV positrons through 20 m of air with the PROTO60 model. The energy sum of 48 crystals with a summation threshold of 0.75 MeV per crystal is plotted and fitted with a Novosibirsk function.	127
6.14 Muon beam calibrated raw data of the 15 GeV positron beam.	128
6.15 Figure 6.14 including an event acceptance threshold of 5.5 GeV, set for the central crystal.	128
6.16 Calibrated raw data of the beam impinging crystal for 15 GeV positrons.	129
6.17 Energy sum of all 48 crystals with a threshold of 0.75 MeV and two different calibrations. The determined resolution depends on the fit range.	130
6.18 Energy sum of all 48 crystals with a threshold of 0.75 MeV. The data was relatively calibrated with the muon beam. The energy sum for the central beam position was aligned to the GEANT simulation for the absolute calibration. A beamspot radius of 2 mm was chosen with the silicon detectors.	131
6.19 Resolutions of the full energy sum, for several positions, measured with 15 GeV positrons. A beamspot radius of 2 mm was chosen with the silicon detectors.	131
7.1 Temperature dependence of the necessary voltages for three different gains. Measurement of the AA0158 Hamamatsu LAAPD by the APD laboratory Frankfurt.	134
7.2 Block diagram of the APD readout with peak sensing ADC.	135

List of Figures

7.3	Temperature dependent response of a BGO scintillator read out with a PMT. A ^{22}Na source was measured (511 keV, 1275 keV). Pictures taken from [THI05].	135
7.4	BGO signal to APD gain conversion. The data points at 13.5 °C were measured and for -25 °C calculated.	136
7.5	Characteristics of the AA0158 Hamamatsu APD at -25°C.	136
7.6	Voltage to gain allocation for 8, 13.5 and 18.5 °C. Measurement of the AA0158 Hamamatsu LAAPD by the APD laboratory Frankfurt. U_{br} corresponds to p_0 , $par1$ corresponds to p_1 and $par2$ corresponds to p_2 in equation 7.2.	137
7.7	Light pulse generator block-diagramm. Picture taken from [LLC04]. . .	138
7.8	Light pulse generator with the distribution system.	138
7.9	Setup inside the climate chamber. A plastic block with roughened surfaces and wrapped with Teflon foil was used to create diffuse light to avoid saturation effects. The APD was optically coupled to this plastic block.	140
7.10	Direct measurement of the used light pulses with a PMT and a Tektronix (Beaverton, United States) TDS 540 Oscilloscope.	141
7.11	Sampling ADC trace of a preamp signal for a light pulse and its development through the steps of the MWD and MA algorithm.	142
7.12	Energy distribution of the light pulses, measured with the APD and SADC, without any optical attenuator and fitted with a Gaussian distribution. The APD was operated with 360 V at +18 °C.	143
7.13	Resolution development for different APD voltages and different light pulse attenuations. The SADC measurements after the MWD and MA(50 ns) algorithms are shown.	144
7.14	Measurement of the light pulse system, to determine the amount of photons. The window in the plastic block wrapping was reduced to the size of the active area of the APD.	145
7.15	Optimum APD gain concerning energy resolution. The shaded area represents a 0.1% resolution loss tolerance band. Analysis of the peak sensing ADC data with an APD at -25 °C.	147
7.16	Optimum APD gain concerning energy resolution. The shaded area represents a 0.1% resolution loss tolerance band. Analysis of the raw data of a sampling ADC and an APD at +18 °C.	148

7.17	Optimum gain for the SADC readout with feature extraction algorithms. The shaded area represents a 0.1% resolution loss tolerance band. Measurement with an ADC at +18 °C.	148
8.1	Resolution summary of all performed experiments. The resolution of the full PROTO 60 matrix is shown in %.	150
8.2	Schematic drawing of a electromagnetic shower within the PROTO 60 crystals (not to scale). Due to the dependence of the light collection on the position of the scintillation process, an increased constant term can be expected.	153
8.3	Line-shape comparison between experimental data and simulation for 1057.7 MeV photons.	154
8.4	Measured energy resolution in % of the PROTO 60 with and without additional absorber material in front. Additionally, the EMC TDR requirement is drawn.	155
8.5	Measurement of light pulses with an APD and peak sensing ADC read out. The dependence of the energy resolution $\frac{\sigma}{E}$ in % on the APD gain is drawn. The pulses were comparable to scintillation light caused by 40.25 MeV energy deposition inside a typical \bar{P} ANDA PWO crystal at -25°C.	156
8.6	Simulation with \bar{P} ANDA-Root, a branch of FairRoot [FROOT]. Single crystal energy differential rate spectrum of the \bar{P} ANDA target calorimeter for polar angles of 5° (black), 25° (blue), 90° (red) and 135° (green) at 15 GeV incident beam momentum. Picture taken from [TDREMC].	157
8.7	Resolution comparison of a 3×3 PROTO 60 matrix read out with different ADC types. The black data points were taken from [KAV11] and obtained via sampling ADC measurements. The parametrization of the red dashed curve is taken out of tab.8.1 for the optimum threshold of 0.75 MeV. The corresponding data were determined with peak sensing ADCs.	160

List of Tables

1.1	Properties of quarks [PDG12].	5
2.1	Overview over the main requirements for the \bar{P} ANDA EMC [TDREMC].	21
2.2	Some properties of PWO-II. The light yield of full size crystals was measured with a photomultiplier with a bi-alkali photocathode (quantum efficiency $\sim 20\%$) [TDREMC].	30
2.3	Some of the S11048(X2) LAAPD properties for \bar{P} ANDA, as written in the data sheet.	31
3.1	PROTO60 LAAPD properties (Hamamatsu S8664-1010SPL) [HAMP60], *[WIL].	49
3.2	Preamp estimations concerning noise and dynamic range.	53
5.1	MAMI procedure overview for the beam experiments.	76
5.2	Chosen energies during the first and second experiment at MAMI. During the first beam-time the wires for the TDC channels 14 and 16 are inverted. TDC channel 15 was not used.	77
7.1	Selectable optical attenuators inside the distribution system.	139
7.2	Calculation of the equivalent energy deposition within PWO-II at $-25\text{ }^\circ\text{C}$ for the PMT measurement. The listed values are given in QDC channels unless stated otherwise.	146
7.3	Relative determination of the equivalent energy deposition within PWO-II at $-25\text{ }^\circ\text{C}$ from the APD measurements with a sampling ADC. The peak values are determined after the <i>MWD</i> and <i>MA</i> (100 ns) algorithms. The APD was operated with 370 V at $+18.5\text{ }^\circ\text{C}$. The first row of the table served as reference for the other energies.	146

List of Tables

8.1	PROTO 60 resolution for different matrices and thresholds for the data of the first experiment at MAMI in the energy range from 158.31 to 1441.06 MeV.	152
8.2	Measured sensitivity of the APD gain to the bias voltage at -25°C . . .	159
8.3	MPV values in ADC channels for the deposited energy of cosmic radiation. The LAAPD gains are determined with a light pulser system. .	IX
8.4	Summary of the PROTO60 cosmic simulations under the column cut condition. The lines indicating the transition between the rows. The MPVs of the cosmic energy deposition and the non linear response obtained with the PROTO60-NUF model are given.	X

Bibliography

- [PDG12] J. BERINGER ET AL. (PARTICLE DATA GROUP): *Phys.Rev. D 86*, 010001, 2012.
- [TDREMC] PANDA COLLABORATION: *Technical Design Report for the PANDA Elektromagnetic Calorimeter*. arXiv:0810.1216 [physics.ins-det], 2008.
- [BTDR] HELMHOLTZZENTRUM FÜR SCHWERIONENFORSCHUNG: *FAIR - An International Accelerator Facility for Beams of Ions and Antiprotons*. Baseline technical report, 2006. [Online] Available: <http://www.gsi.de/fair/reports/btr.html>.
- [HEN08] W. F. HENNING: *FAIR - recent developments and status*. Nucl. Instr. Meth., A805:502c-510c, 2008.
- [ACCEL] HELMHOLTZZENTRUM FÜR SCHWERIONENFORSCHUNG: *FAIR - Baseline Technical Report, Volume 2, Accelerator and Scientific Infrastructure*, 2006. [Online] Available: <http://www.fair-center.de/de/fuer-nutzer/publikationen/fair-publikationen.html>.
- [PPR] PANDA COLLABORATION: *Physics Performance Report for PANDA. Strong Interaction Studies with Antiprotons*, 2009. [Online] Available: <http://www.fair-center.eu/for-users/publications/experiment-collaboration-publications.html>.
- [CMSWEB] CMS COLLABORATION: *Webpage* [Online] Available: <http://cms.web.cern.ch>.
- [LE09] C. LEROY & P.G. RANCOITA: *Principles of Radiation Interaction in Matter and Detection*, 2nd Edition. World Scientific, 2009.
- [MIT] MIT OPEN COURSE WARE: *Interactions of Photons with Mater*. Webpage [Online] Available: http://ocw.mit.edu/courses/nuclear-engineering/22-01-introduction-to-ionizing-radiation-fall-2006/lecture-notes/energy_dep_photo.pdf.

Bibliography

- [PDG08] C. AMSTER ET AL. (PARTICLE DATA GROUP): *Particle Physics Booklet*. Physics Letters B 667,1 2008.
- [INT66] MCINTRYRE: *Multiplication Noise in Uniform Avalanche Diodes*, IEEE Trans. Electron Devices, ED-13, pp. 164-168 (1966).
- [HAM] HAMAMATSU: *Technical Information, Characteristics and use of Si APD* [Online] Available: http://www.sales.hamamatsu.com/assets/applications/SSD/Characteristics_and_use_of_SI_APD.pdf.
- [ABEL96] A.ABELE ET AL. (CRYSTAL BARREL COLLABORATION): *Nucl. Phys. A 609* (1996) 562.
- [ACH12] P. ACHENBACH ET AL: *Hypernuclear Physics at PANDA Experimental Challenges*, arXiv:1206.3149v1 [nucl-ex], 2012.
- [PWEB] PANDA COLLABORATION: *Webpage* [Online] Available: <http://www-panda.gsi.de/framework/detector.php>.
- [CHOI02] S. CHOI ET AL.: Phys. Rev. Lett. 89, 102001 (2002).
- [CHOI03] S. CHOI ET AL.: Phys. Rev. Lett. 91, 262001 (2003).
- [BOCA] PANDA COLLABORATION: *The PANDA experiment: physics and goals and experimental setup*, Gianluigi Boca.
- [TDRMVD] PANDA COLLABORATION: *Technical Design Report for the PANDA Micro Vertex Detector*. arXiv:1207.6581 [physics.ins-det], 2012.
- [TDRSTT] PANDA COLLABORATION: *Technical Design Report for the PANDA Straw Tube Tracker*. arXiv:1205.5441 [physics.ins-det], 2012.
- [COY94] P. COYLE ET AL.: *The DIRC counter: a new type of particle identification device for B factories*. Nuclear Instruments and Methods in Physics Research A 343 (1994) 292-299.
- [TDSTPC] PANDA COLLABORATION: *Technical Design Study for the PANDA Time Projection Chamber*. arXiv:1207.0013 [physics.ins-det], 2012.
- [SCHW13] C.SCHWARZ ET AL., ON BEHALF ON THE SiPM GROUP AT GSI: *The Scintillation Tile Hodoscope* SiPM workshop EU(HP3), Vienna, 16. Feb. 2013.

- [TPR] PANDA COLLABORATION: *Technical Progress Report for PANDA. Strong Interaction Studies with Antiprotons*, 2009. [Online] Available: <http://www.fair-center.eu/for-users/publications/experiment-collaboration-publications.html>. 2005.
- [ATO08] G.S. ATOIAN ET AL.: *An improved Shashlyk calorimeter*. Nuclear Instruments and Methods in Physics Research A 584 (2008) 291-303.
- [ATO04] G. S. ATOIAN ET AL.: *Development of Shashlyk calorimeter for KOPIO*. Nuclear Instruments and Methods in Physics Research, A 531 (2004).
- [PREAMP] W. ERNI: *Technical Design Report for discrete Preamplifier for APD Readout, LNP Preamplifier Version SP 883A02*, 2008 [Online] Available: <http://panda-wiki.gsi.de/cgi-bin/view/DCS/SupportedHardware>.
- [WIL] A. WILMS: *Privat discussion*.
- [BRE13] D. BREMER: Phd Thesis, Justus-Liebig-Universität Gießen, 2013.
- [CRY] HAGMANN, C. LANGE, D. WRIGHT, D. LAWRENCE LIVERMORE NAT. LAB., LIVERMORE: *Conference Record, 2007 IEEE Nuclear Science Symposium*, Honolulu, HI, Oct. 26 2007-Nov. 3 2007, 10.1109/NSSMIC.2007.4437209 (<http://ieeexplore.ieee.org>).
- [CRYP] C. HAGMANN ET AL.: *Monte Carlo Simulation of Proton-induced Cosmic-ray Cascades in the Atmosphere* [Online] Available: http://nuclear.llnl.gov/simulation/doc_cry_v1.7/cry_physics.pdf, 2012.
- [CO83] D. J. COOK: Physical Rev. Lett., Vol 51 No 4, (1983).
- [DO09] L. DORMAN: *Cosmic Rays in Magnetospheres of the Earth and other Planets*. Astrophysics and Space Science Library 358 (2009).
- [HAMPM] HAMAMATSU: *PHOTOMULTIPLIER TUBE R1828-01, R2059* [Online] Available: http://www.hamamatsu.com/resources/pdf/etd/R1828-01_R2059_TPMH1259E04.pdf.
- [HAMP60] HAMAMATSU: *Datasheet PHOTODIODE Si APDS8664 series*, [Online] Available: http://www.hamamatsu.com/resources/pdf/ssd/s8664_series_kapd1012e04.pdf.
- [JAN06] A. JANKOWIAK: *The Mainz Microtron MAMI - Past and future*, Eur. Phys. J. A 28, s01, 149-160 (2006).

Bibliography

- [BERG10] H. BERGHAUESER: *Investigation of the Dalitz decays and the electromagnetic form factors of the η and π^0 -meson*, Phd Thesis, 2010.
- [KRU95] B.KRUSCHE: *Photoproduction of π^0 and η mesons from nucleons and nuclei in the second resonance region*, Habilitationsschrift, Justus-Liebig-Universität Gießen, 1995.
- [KNU06] K. H. KNUTH: *Optimal Data-Based Binning for Histograms*, arXiv:physics/0605197v1, 2006.
- [LEV08] C. LEVEFRE: *A collection of facts and figures about the Large Hadron Collider*, CERN-Brochure-2008-001-Eng, 2008.
- [LHC1] O. S. BRÜNING ET AL.: *LHC Design Report, v.1 : the LHC Main Ring* CERN-2004-003-V-1, 2004.
- [LHC2] O. S. BRÜNING ET AL.: *LHC Design Report, v.2 : the LHC Infrastructure and General Services* CERN-2004-003-V-2, 2004.
- [LHC3] M. BENEDIKT ET AL.: *LHC Design Report, v.3 : the LHC Injector Chain* CERN-2004-003-V-3, 2004.
- [NA57] NA57 COLLABORATION: *The WA97 and NA57 experiments*, [Online] Available: <http://wa97.web.cern.ch/WA97/main.html>.
- [BE11] M. BECKER ET AL.: *FPGA-based readout for double-sided silicon strip detectors*, JINST 6 C01008, 2011.
- [KAV11] M. KAVATSYUK ET AL., ON BEHALF OF THE PANDA COLLABORATION: *Performance of the prototype of the electromagnetic calorimeter for PANDA*, Nuclear Instruments and Methods in Physics Research Section A: Accelerators, Spectrometers, Detectors and Associated Equipment, Volume 648, Issue 1, 21 August 2011, Pages 77-91, ISSN 0168-9002, 10.1016/j.nima.2011.06.044.
- [EFT03] I. EFTHYMIPOULOS: *AB/ATB-EASPS/EA Training Lecture Program*, 2003.
- [THI05] M. THIEL: *Die Auslese von $PbWO_4$ -Szintillatoren mit Large Area Avalanche Photo-Dioden*, Diploma Thesis, 2005.
- [LAB] PANDA COLLABORATION, APD laboratory, http://www.uni-frankfurt.de/fb/fb13/ikf/Arbeitsgruppen/Peters/PANDA_APD-Labor/.

- [LLC04] RADIATION INSTRUMENTS AND NEW COMPONENTS LLC: *Stabilized LED-based pulsed light source*, Operation manual, Minsk 2004.
- [MEL66] H. MELCHIOR, W.T. LYNCH: IEEE Trans. Electron Devices ED-13 (12) 829, 1966.
- [KAV09] M. KAVATSYUK ET AL., ON BEHALF OF THE PANDA COLLABORATION: *Feauter-extraction algorithms for the PANDA electromagnetic calorimeter*, IEEE Nuclear Science Symposium Conference Record, 2009.
- [WIE11] P. WIECZOREK, ON BEHALF OF THE PANDA COLLABORATION: *Low noise preamplifier ASIC for the PANDA experiment*, topical workshop on electronics for particle physics, IOPscience JINST 6 C12055, 2011.
- [EIS13] T. EISSNER: Phd Thesis, Justus-Liebig-Universität Gießen, 2013.
- [FROOT] PANDA COLLABORATION: *The FairRoot framework*, [Online] Available: <http://fairroot.gsi.de>.
- [ING07] Q. INGRAM ET AL.: *Energy resolution of the barrel of the CMS Electromagnetic Calorimeter* IOPscience JINST 2 P04004, 2007.
- [ISEG] ISEG SPEZIALELEKTRONIK GMBH: *EHS High Precision HV Modules 8 Channels with Single Channel Floating-GND Operator's manual*. [Online] Available: http://productspice.iseg-hv.com/media/production/MAN_EHS_HP_FG_08_EN-20110610.pdf.
- [NOV08] R.NOVOTNY: IEEE Trans. on Nucl. Sci. 55, 1207 (2008).

Danksagung

Bereits kurz nach meinem Vordiplom wurde ich von Herrn Dr. Rainer Novotny als Betreuer für das Physikpraktikum für Mediziner engagiert. Aus den vielen Gesprächen während des Praktikums ergab sich im Laufe meines Hauptstudiums recht schnell eine wissenschaftliche Mitarbeit am II. Physikalischen Institut (AG Prof. (em) Dr. V. Metag) aus der schließlich später meine Diplomarbeit und nun diese Doktorarbeit hervorgegangen sind. Rückblickend kommen so einige Jahre in diesem Institut zusammen in denen ich sehr viel gelernt, erlebt und natürlich auch sehr gerne gearbeitet habe. Dazu beigetragen haben alle jetzigen sowie ehemaligen Mitarbeiter. Mein ganz besonderen Dank gilt aber vor allem Dr. Rainer Novotny und Prof. Dr. Volker Metag welche beide zusammen mir dies überhaupt ermöglicht haben.

Besonderen dank gehört auch Dr. Peter Drexler für seine Unterstützung und Hilfe mit der Ausleselektronik und bei Programmierfragen.

Meinen Mitdoktoranden sowie Bürokollegen Daniel Bremer und Tobias Eißner danke ich für die erstklassige Zusammenarbeit. Wie bereits in der Dissertation angedeutet, wurden einige Messungen sowie Analysen zusammen geplant, durchgeführt und besprochen. Die gemeinsam gewonnenen Erkenntnisse wurden erst unmittelbar vor dem Verfassen den jeweiligen Arbeiten zugeordnet und entsprechend im Detail aufbereitet. Für die Unterstützung beim Erstellen des PROTO60 GEANT Modells möchte ich Dr. Valera Dormenev danken.

Stefan Diehl danke ich für seine fleißige Hilfe bei den APD Messungen.

Bedanken möchte ich mich auch bei den vielen Helfern die bei den durchgeführten Strahlzeiten direkt oder indirekt beteiligt waren. Neben Allen die bereits vorher namentlich genannt wurden gehören Till Kuske, Rene Schubert sowie Marcel Straube aus der Arbeitsgruppe dazu. Vielen dank für eure Hilfe. Ferner nicht zu vergessen sind alle sonstigen Beteiligten aus der PANDA Kollaboration sowie an den Beschleunigern in Mainz sowie CERN.

Für die mühevollen Arbeit des Korrekturlesens möchte ich mich herzlich bedanken bei

Danksagung

Nadine Löschmann, Dr. Eric Gutz, Dr. Rainer Novotny, Dr. Henning Berghäuser
sowie meiner Schwester Anja Moritz-Zimmermann.

Erklärung der Urheberschaft

Ich erkläre: Ich habe die vorgelegte Dissertation selbständig und ohne unerlaubte fremde Hilfe und nur mit den Hilfen angefertigt, die ich in der Dissertation angegeben habe. Alle Textstellen, die wörtlich oder sinngemäß aus veröffentlichten Schriften entnommen sind, und alle Angaben, die auf mündliche Auskünften beruhen, sind als solche kenntlich gemacht. Bei den von mir durchgeführten und in der Dissertation erwähnten Untersuchungen habe ich die Grundsätze gute wissenschaftlicher Praxis, wie sie in der "Satzung der Justus-Liebig-Universität Gießen zur Sicherung guter wissenschaftlicher Praxis" niedergelegt sind, eingehalten.

Ort, Datum

Unterschrift